

**Illuminating Sunscreens:  
Probing the Intrinsic Absorption  
Properties of Ionic UV Filters *via*  
Laser Photodissociation  
Action Spectroscopy**

**Natalie G. K. Wong**

**Ph.D.**

**University of York**

**Chemistry**

**July 2021**



# Abstract

Few studies have explored the fundamental mechanisms that govern how sunscreens function at the molecular level until recently. Here, we apply the novel approach of UV laser photodissociation action spectroscopy to measure how the intrinsic absorption properties of commercially-available organic sunscreen molecules are affected at the molecular level by pH (*i.e.*, protonation or deprotonation).

In several systems, we observe that protonation state has a substantial effect on the UV absorption profile of common sunscreens. Deprotonated oxybenzone, for instance, displays a remarkably modified absorption spectrum and photogenerates both electrons and free radicals. Likewise, deprotonated 2-phenylbenzimidazole-5-sulfonic acid yields anionic and neutral free radicals *via* all photodissociation routes. Importantly, these experiments allow us to characterize their photophysical behavior, through analysis of the photofragments generated and comparison of these to the fragment ions produced upon the thermal breakdown of the ground electronic state molecule.

We further report, for the first time in a study of an anionic UV filter, high-level *ab initio* potential energy surfaces for the popular sunscreen benzophenone-4 in conjunction with brand-new results from gas-phase laser photodissociation and higher-energy collisional dissociation studies for the deprotonated species, which would be present under alkaline conditions. The *ab initio* calculations confirm the implied photophysics that we deduced in the earlier studies on oxybenzone and 2-phenylbenzimidazole-5-sulfonic acid.

Using a series of new solution-phase irradiation setups which couple home-built photolysis cells with electrospray ionization mass spectrometry, we use a model system (*i.e.*, riboflavin) to exemplify how gas-phase photofragmentation of this UV chromophore is mirrored by its solution-phase behavior. Broader application of this approach to identifying photoproducts of other photoactive molecules, *i.e.*, sunscreens, is discussed.

These findings, at the molecular level, address the issues surrounding the suitability of existing sunscreens and demonstrate the utility of laser-interfaced mass spectrometry for fundamental studies for sunscreen photochemistry.



*“Do you have any wisdom for today?” asked the boy.*

*“Yes,” said the mole.*

*“What is it?”*

*“Don’t put off ‘til tomorrow... the cake you could eat today.”*

*– Charlie Mackesy*



# Contents

Abstract.....	iii
List of Figures.....	x
List of Tables.....	xii
List of Schemes.....	xiii
Acknowledgements.....	xv
Author's Declaration .....	xvii
Chapter 1.....	1
Introduction.....	1
1.1    Insight into Sunscreens.....	1
1.2    Laser Spectroscopy of Organic Sunscreens.....	11
1.2.1    Solution-Phase Laser Spectroscopy of Organic Sunscreens.....	11
1.2.2    Gas-Phase Laser Spectroscopy of Organic Sunscreens .....	20
1.3    Laser Photodissociation Mass Spectrometry .....	32
1.3.1    Electrospray Ionization Mass Spectrometry .....	33
1.3.2    Quadrupole Ion Trap Mass Spectrometry .....	35
1.3.3    Gas-Phase UV-visible Photodissociation Spectroscopy .....	37
1.3.4    Collision-Induced Dissociation.....	49
1.4    Thesis Overview .....	50
References.....	53
Chapter 2.....	67
Mapping the Intrinsic Absorption Properties and Photodegradation Pathways of the Protonated and Deprotonated Forms of the Sunscreen Oxybenzone.....	67
2.1    Declaration.....	67

2.2	Paper I: Mapping the Intrinsic Absorption Properties and Photodegradation Pathways of the Protonated and Deprotonated Forms of the Sunscreen Oxybenzone	68
Chapter 3	.....	80
	Direct Observation of Photochemical Free Radical Production from the Sunscreen 2-Phenylbenzimidazole-5-Sulfonic Acid via Laser-Interfaced Mass Spectrometry	.....80
3.1	Declaration.....	80
3.2	Paper II: Direct Observation of Photochemical Free Radical Production from the Sunscreen 2-Phenylbenzimidazole-5-Sulfonic Acid <i>via</i> Laser-Interfaced Mass Spectrometry	.....81
Chapter 4	.....	89
	Linking Electronic Relaxation Dynamics and Ionic Photofragmentation Patterns for the Deprotonated UV Filter Benzophenone-4.....	89
4.1	Declaration.....	89
4.2	Paper III: Linking Electronic Relaxation Dynamics and Ionic Photofragmentation Patterns for the Deprotonated UV Filter Benzophenone-4..	91
Chapter 5	.....	98
	Photodegradation of Riboflavin under Alkaline Conditions: What can Gas-Phase Photolysis Tell Us About What Happens in Solution? .....	98
5.1	Declaration.....	98
5.2	Paper IV: Photodegradation of Riboflavin under Alkaline Conditions: What can Gas-Phase Photolysis Tell Us About What Happens in Solution? .....	99
Chapter 6	.....	117
	The Present and the Future.....	117
6.1	Contributions.....	117
6.2	Future directions .....	119
6.3	Final remarks.....	120
Appendices	.....	121

A1	Supplementary Information – Mapping the Intrinsic Absorption Properties and Photodegradation Pathways of the Protonated and Protonated Forms of the Sunscreen Oxybenzone .....	121
A2	Supplementary Material – Direct Observation of Photochemical Free Radical Production from the Sunscreen 2-Phenylbenzimidazole-5-Sulfonic Acid <i>via</i> Laser-Interfaced Mass Spectrometry.....	132
A3	Supporting Information – Linking Electronic Relaxation Dynamics and Ionic Photofragmentation Patterns for the Deprotonated UV Filter Benzophenone-4	140
A4	Supplementary Information – Photodegradation of Riboflavin under Alkaline conditions: What can Gas-Phase Photolysis Tell Us About What Happens in Solution? .....	164

# List of Figures

**Figure 1.** Representative examples of the 8 chemical classes of organic UV filters that form most FDA-approved sunscreens: **(a)** benzophenones (e.g., oxybenzone and sulisobenzone), **(b)** dibenzoyl methanes (e.g., avobenzone), **(c)** benzimidazoles (e.g., 2-phenylbenzimidazole-5-sulfonic acid), **(d)** salicylates (e.g., octyl salicylate) **(e)** camphors (e.g., 4-methylbenzylidene camphor), **(f)** para-aminobenzoates (e.g., para-aminobenzoic acid), **(g)** anthranilates (e.g., menthyl anthranilate), and **(h)** cinnamates (e.g., octyl methoxycinnamate).....5

**Figure 2.** Schematic structure of **(a)** ethylhexyl triazone (EHT; MW: 823.07 g/mol), **(b)** bisoctrizole (MW: 658.88 g/mol), and **(c)** bemotrizinol (MW: 627.81 g/mol)..... 14

**Figure 3.** Pictorial summary of the two photorelaxation mechanisms of diethylamino hydroxylbenzoyl hexyl benzoate (DHHB) under the influence of **(a)** non-polar and **(b)** polar solvent environments. Adapted from Ref <sup>[118]</sup>. ..... 17

**Figure 4.** Schematic structure of **(a)** methyl salicylate and **(b)** homomethyl salicylate (HMS). Notably, ESIPT is found to occur at their enol-keto point(s) to allow for barrierless tautomerization. .... 19

**Figure 5.** Schematic structures of **(a)** methyl sinapate (MS), **(b)** sinapoyl malate (SM), and **(c)** sinapic acid (SA).....25

**Figure 6.** Schematic structures of **(a)** octyl methoxycinnamate (OMC) and its precursor **(b)** methyl-4-methoxycinnamate (MMC). .....26

**Figure 7.** Schematic structures of the **(a)** phenoxide [i.e., pCEs<sup>-</sup>] and **(b)** carboxylate [i.e., pCEt<sup>-</sup>] deprotomers, and **(c)** para-coumaric acid.....29

**Figure 8.** Schematic structures of **(a)** menthyl anthranilate (MenA) and its precursor **(b)** methyl anthranilate (MA).....30

**Figure 9.** Diagram of the key components found within the nebulizer-assisted Bruker amaZon quadrupole ion trap (QIT) mass spectrometer. Image taken from the Bruker Daltonics amaZon series User Manual (Revision 1), November 2009.<sup>[210]</sup> .....33

**Figure 10.** Labelled photographs of the laser bench housing the optics, required for UV and visible-NIR wavelengths, located on top of our modified amaZon mass spectrometer. The laser path from the OPO laser to the ion trap is outlined in **(a)** for UV where **[i]** the incoming laser beam is first adjusted in height using a pair of right-angled UV-fused silica prisms and then **[ii]** hits a right-angled prism, allowing for the beam to be reflected by 90° into either **[iii]** an adjustable right-angled prism (situated on a motorized flip mount) which allows for the redirection of the beam towards the power meter, or **[iv]** into the QIT. The route the visible/NIR beam takes are mapped in **(b)** where the laser is first wrought to overlap with that of the UV path using **[i]** a right-angled prism. The beam is then redirected into **[ii]** a corresponding right-angled prism (situated on a motorized flip mount). Following that of the UV route, the height of the incoming visible/NIR laser beam is adjusted at **[iii]** and reflected at **[iv]**, allowing for the laser to directly hit either the power meter or the QIT at **[v]** and **[vi]**, respectively. In both instances continuing on to **[vi]** will allow for the laser to pass via an optomechanical laser shutter and a transparent window that bridges the QIT..... 45

# List of Tables

**Table 1.** FDA-approved organic UV filters listed alongside their maximum approved concentrations and UV spectral coverage.<sup>[81,83]</sup> .....6

**Table 2.** FDA-approved inorganic (nanoparticulate) UV filters listed alongside their maximum approved concentrations and spectral coverage.<sup>[81,83]</sup> .....7

# List of Schemes

<b>Scheme 1.</b> Schematic depiction of the electrospray ionization (ESI) process in the positive ion mode. ....	34
<b>Scheme 2.</b> Schematic cross-section of the quadrupole ion trap (QIT) mass spectrometer as adapted from the Bruker amaZon manual. <sup>[210]</sup> Notably, A = entrance of the end cap; B = ring electrode(s); C = exit end cap; and D = ion cloud and buffer gas (i.e., helium). ....	36
<b>Scheme 3.</b> Schematic of the recent modifications made to the quadrupole ion trap (QIT) mass spectrometer to allow for gas-phase photodissociation spectra to be recorded. The location of the tapered hole (upper flange: 6 mm; center of QIT: 2 mm) drilled through the ring electrode of the QIT, to allow for the coupling of the laser, is illustrated within. Other notable components include: the Nd <sup>3+</sup> :YAG pumped OPO tunable laser source; a UV fused silica lens (LE4467-UV, Thorlabs Inc); a mechanical optical laser shutter (Model SH05, Thorlabs Inc.); flange mounted uncoated UV fused silica windows (WG41050, Thorlabs, Inc.); a pair of aluminum mirrors (PF05-03-F01, Thorlabs, Inc.), and a UV-visible spectrometer (USB2000+ UV-VIS, Ocean Optics Inc.). Scheme adapted from Reference <sup>[224]</sup> .....	38
<b>Scheme 4.</b> Schematic of the energy levels involved in the emission of 1064 nm light by a Nd <sup>3+</sup> :YAG laser. ....	40
<b>Scheme 5.</b> Schematic of the Q-switch used to produce laser pulses in the Surelite Nd:YAG laser. H = Horizontal polarization; V = Vertical polarization; and C = Circular polarization. Image adapted from the Surelite manual. ....	41
<b>Scheme 6.</b> Optical layout of the Horizon™ Optical Parametric Oscillator (OPO) laser. [1, 3] mirror, dichroics (355 nm); [2a, 8, 15, 25a, 30] half wave plate; [2b, 14, 25b] polarizer (355 nm); [4, 5] lens; [6, 13, 16, 21] window; [7] porro prism; [9] injection pump mirror; [10] #1 Crystal BBO Type-1; [11] #2 Crystal BBO Type-1; [12, 19] mirror; [17, 20, 23, 24, 29] crystal, BBO; [18] waveplate; [22, 35] Pelin Broca prism; [26] beam dump assy; [38, 39] prism 90°. Notably, commercial software is available to accompany the Horizon, used to control the output wavelength of the laser and tune the laser power at	

each wavelength. Step motors are available to control BBO crystal orientation and the Pelin Broca prisms. Image adapted from the Continuum® Horizon™ I and II OPO Operation and Maintenance Manual (P/N: 996-0034, Revision C, 2014).<sup>[225]</sup> .....42

**Scheme 7.** Simplified schematic highlighting the now-automated workflow of the laser-interfaced mass spectrometry experimental set up. ....48

# Acknowledgements

First and foremost, I would like to massively thank my supervisors, Prof. Caroline Dessent and Dr. Martin Cockett, for their encouragement and guidance throughout my Ph.D.

I would also like to thank Dr. Edward Matthews, Dr. Ed Bergstrom, and Dr. Rosaria Cercola for patiently training me to use and troubleshoot mass spectrometers; Dr. Jacob Berenbeim for first training me to use our lasers; and Dr. Chris Rhodes in Electronics Workshops for bringing my photolysis designs to life.

I am largely grateful to the Leverhulme Trust for funding my Ph.D. studentship and for funding my attendance and travel to all the amazing international conferences that I have been ever so fortunate to attend over the past three years.

Well, if this Ph.D. has taught me anything, it is that “*you’re the product of your own environment*”. Surround yourself with the best. Over the last 3.5 years, I have genuinely been fortunate enough to have met some wonderfully-unique individuals at York. Special shout-outs go to Michi Burrow, Tomas Lock-Feixas, Pete Howe, Sam Daly, Dr. Conor Rankine, and Dr. Fiona Whiting from the PhysChem office for always coming up with witty, sarcastic comments that would often make my day; odd whiteboard illustrating sessions; traumatizing rounds of ‘What Do You Meme’; incredible escapes to Naples, Girona, and Paris; and in providing invaluable advice, both scientific and personal.

The events of 2020 were tolling. SFY, OYW, KAW, MWRH, and HRJH – merci d’avoir veillé sur moi. Joe – thank you for enabling all my late-night McDonald’s runs and for tolerating me being an absolute goblin whilst writing up. Andrianna – we are stronger than we think. Devaney – this world just is not the same without you.

Lastly, I would like to thank my parents for their love, patience, and generosity throughout the entirety of my undergraduate and postgraduate studies. I know for a fact I would not have gotten to where I am today in my career without their support. I can’t wait to see where I’ll adventure off to next.



## Author's Declaration

I declare that this thesis is a presentation of original work, and I am the sole author. This work has not previously been presented for an award at this, or any other, University. All sources are acknowledged as References.

This thesis is based on four peer-reviewed publications where I am the lead author. The details of the articles are outlined below:

### ***Chapter 2 (Paper I) has been published:***

“Mapping the Intrinsic Absorption Properties and Photodegradation Pathways of the Protonated and Deprotonated Forms of the Sunscreen Oxybenzone”

N. G. K. Wong, J. A. Berenbeim, M. Hawkrige, E. Matthews and C. E. H. Dessent, *Phys. Chem. Chem. Phys.*, 2019, **21**, 14311-14321. <https://doi.org/10.1039/C8CP06794E>.

### ***Chapter 3 (Paper II) has been published:***

“Direct Observation of Photochemical Free Radical Production from the Sunscreen 2-Phenylbenzimidazole-5-Sulfonic Acid *via* Laser-Interfaced Mass Spectrometry”

N. G. K. Wong, J. A. Berenbeim and C. E. H. Dessent, *ChemPhotoChem*, 2019, **3**, 1231-1237. <https://doi.org/10.1002/cptc.201900149>.

***Chapter 4 (Paper III) has been published:***

“Linking Electronic Relaxation Dynamics and Ionic Photofragmentation Patterns for the Deprotonated UV Filter Benzophenone-4”

N. G. K. Wong, C. D. Rankine and C. E. H. Dessent, *J. Phys. Chem. Lett.*, 2021, **12**, 2831–2836. <https://doi.org/10.1021/acs.jpcclett.1c00423>.

***Chapter 5 (Paper IV) has been submitted for peer review:***

“Photodegradation of Riboflavin under Alkaline Conditions: What can Gas-Phase Photolysis Tell Us About What Happens in Solution?”

N. G. K. Wong, C. Rhodes and C. E. H. Dessent, 2021 [submitted to *Molecules*]



Signed          Natalie G. K. Wong

# Chapter 1

## Introduction

### 1.1 Insight into Sunscreens

Ultraviolet (UV) radiation derived from sunlight is now considered the most prominent and prevalent carcinogen found within our natural environment,<sup>[1]</sup> despite the wealth of benefits which have been largely attributed to UV radiation over the years – such as its ability to stimulate vitamin D production;<sup>[2-5]</sup> decrease blood pressure and inflammation;<sup>[6,7]</sup> and enhance one's mood *via* the ensuing increase in serotonin levels in the brain with sunlight.<sup>[8]</sup> Though a form of non-ionizing radiation (like that of visible, infrared, microwave, and radiowave radiation), UV radiation has profound immunosuppressive properties and the ability to induce cell damage through the formation of pyrimidine dimers,<sup>[9,10]</sup> photoproducts,<sup>[11,12]</sup> and reactive oxygen species.<sup>[13]</sup> However, it is nodus to equipoise the benefits that sunlight provides against its destructive properties.<sup>[14]</sup>

The UV region of the electromagnetic spectrum encompasses three bands: UV-A (400-320 nm), UV-B (320-280 nm), and UV-C (280-100 nm). Whilst short-wavelength UV-C is the most damaging band within the UV spectrum, it is the least prevalent given its tendency to be mostly absorbed by the atmosphere.<sup>[15]</sup> Biologically-harmful UV-B radiation penetrates and damages the outermost layers of human skin and is responsible for delayed tanning effects and sunburn, along with consequences like skin ageing.<sup>[16]</sup> All UV-C and most UV-B is absorbed by the ozone layer. Ozone is a naturally-occurring gas produced in the upper stratosphere by short-wavelength sunlight where 'ordinary' conditions in the stratosphere act to sustain a dynamic equilibrium between the destruction

and reformation of the ozone required to shield the Earth from the detrimental impact of UV-B.<sup>[17]</sup> The amount of absorption largely depends on a number of natural phenomena (*i.e.*, time of year or day, latitude, altitude, cloud coverage and haze, and ground reflection), but is also highly affected by human activity.<sup>[18]</sup> The uncontrolled growth in the usage of ozone-depleting substances (*e.g.*, hydrochlorofluorocarbons and chlorofluorocarbons used in refrigeration and air conditioning;<sup>[19,20]</sup> halons used as fire suppression agents;<sup>[21]</sup> methyl bromide used for fumigation and soil treatment,<sup>[22]</sup> etc.) in industry in the mid-1970s heavily disturbed this dynamic balance of ozone, eradicating ozone much more quickly than it could be replaced.<sup>[23–26]</sup> The signing of the landmark Montreal Protocol in 1987 has since curbed the use of such chemicals, and more than 30 years on, scientists have now reported the first direct proof that the Antarctic ozone hole has started to recover as a direct result.<sup>[27–34]</sup> Finally, deeply penetrating UV-A accounts for 95% of the total solar radiation incident on human skin. Contrary to earlier beliefs where it was assumed that chronic exposure to UV-A did not contribute towards any lasting damage,<sup>[35–37]</sup> cumulative evidence from more recent studies now reveal its role beyond that of the immediate tanning effect, further enhancing the development of skin cancers and photoaging, cutaneous photooxidative stress, photoallergic dermatoses, and photoimmunosuppression.<sup>[38–40]</sup> Its ability to penetrate far beyond superficial layers of skin now warrant further means of photoprotection against UV-A radiation.

Clearly excessive exposure to UV rays, whether obtained from the direct exposure of the sun or from other more deliberate sources like artificial sunlamps and sunbeds, can cumulatively contribute to a plethora of side-effects including skin damage, skin ageing, DNA mutations, and erythema – all of which can progress into skin cancer.<sup>[41]</sup> In 2021, melanoma is one of the top 5 leading cancer types for new cancer cases in the US, with modeled projections showing 106,110 expected new cases in 2021 alone.<sup>[42]</sup> Notably, melanoma skin cancer often develops as a consequence of the intermittent exposure of human skin to bursts of high-intensity UV radiation emitted from the sun,<sup>[43]</sup> and though there are natural photoprotective mechanisms which aim to protect against UV-induced DNA damage, the increasing prevalence of skin cancers worldwide makes it clear that such preventive mechanisms are inadequate, and that sun protection interventions, and thus the use of artificial sun protection is very necessary.<sup>[44]</sup>

By understanding how the body works to protect itself from the adverse effects of UV radiation, we can develop new and improved means of photoprotection based on the same principles. Naturally, human skin has its own photoprotective mechanisms that serve to

protect it from harmful UV rays. Melanin, a protective skin pigment, is naturally found in most organisms and in particular, in human skin. Eumelanin is one form of melanin that allows us to develop a suntan and ultimately gives color to black and brown hair. Whilst novel studies on the skin and its building blocks have found eumelanin to, in fact, convert harmful UV radiation into heat with almost 100% efficiency,<sup>[45]</sup> it is recognized that endogenous melanin in most phenotypes is not enough for full photoprotection.<sup>[45-47]</sup>

Historical evidence has conveyed the various ways in which humans have protected themselves against the sun.<sup>[48]</sup> From the use of veils and brim hats to parasols, protection from the sun were first considered marks of honor before later becoming more of a fashion statement in the 18th century. Whilst it is easy to attempt to simply reduce excessive exposure to UV radiation, it has become apparent in recent times that this approach is not at all that easy to implement.<sup>[49,50]</sup> Now, dermatologists heavily advocate the use of commercially-available sunscreens as one of the many effective ways one can reduce their exposure to UV.

Alongside that of UV light, both visible and infrared (IR) rays also form major components of natural sunlight, with IR-A wavelengths (750-1400 nm) making up *ca.* 30% of the total solar irradiance that reaches the surface of the Earth.<sup>[51,52]</sup> With most modern-day sunscreens marketed to protect solely against UV radiation, studies have traditionally focused on developing our understanding of UV-induced reactions. Diffey and Cadar have argued that it is perhaps premature to incorporate IR protection into topical sunscreens as there is not compelling evidence to demonstrate that observable, deleterious cutaneous effects are occurring at doses of solar IR-A radiation commensurate with those experienced by the common population under normal environmental circumstances.<sup>[53-55]</sup> However, for the sake of completeness, the photoprotective projections of existing sunscreens against IR-A damage will be fleetingly reviewed.<sup>[56-58]</sup> In recent times, studies addressing IR-A-induced skin damage have been on the rise, and it is now well inferred that chronic exposure to wavelengths in the IR-A can too inflict skin damage, premature photoaging and is linked to photocarcinogenesis, similar to that found of UV rays.<sup>[59-66]</sup> With IR-A rays capable of deeply penetrating human skin, to an extent they are responsible for the increase in skin temperature and contribute towards the free radical and metalloproteinases-1 production in the dermis that manifests towards the formation of rhytides (or wrinkles, as they are more commonly known),<sup>[64]</sup> a perturbation of extracellular matrix homeostasis by degradation of the dermal connective tissue. Studies evaluating the topical application of antioxidants to achieve IR-A photoprotection have

too garnered much attention over the past few years, many of which have claimed physiological relevance;<sup>[67]</sup> however, even in some well-respected studies, the extreme dosages applied point towards a less compelling argument (*i.e.*, where IR-A is applied at a dose of 360-720 J/cm<sup>2</sup> over 57-114 minutes, such dosages represent a range equivalent to an individual spending hours lying horizontally across an unshaded surface on a clear day).<sup>[64]</sup> Others have worked to address the effectiveness of supplementing cosmetics (*e.g.*, sunscreens) with doses of antioxidants that can functionalize to quench free radicals within the epidermis and dermis.<sup>[68-70]</sup> Still, whilst it is obvious we still need to think far beyond that of just UV rays and continue to rationalize the development of sunscreens that offer a practical ‘blend’ of UV and IR photoprotection, we now await a quantitative analysis of the benefits, if any, of incorporating agents into sunscreens that reduce cutaneous IR-A damage.<sup>[53]</sup>

Whilst sunscreens are now widely employed to alleviate the adverse effects of UV radiation, relatively few studies have investigated the fundamental mechanisms that govern how sunscreens function at the molecular level until very recently. A model sunscreen system should ideally demonstrate a range of photophysical properties including, but notwithstanding, (i) a broad absorption cross-section within the UV-A and UV-B regions, combined with (ii) the ability for the resulting excited-state population to decay *via* non-radiative means of internal conversion (IC) to its ground state, and later (iii) relax back to reform its original ground state geometry. Other desirable characteristics of such formulations should include (iv) prolonged skin resistance with exposure time, (v) minimal skin penetration and systemic availability, and (vi) absence of any subsequent phototoxic products. Thus, given the vast significance and need for the ‘ideal’ – high-performing,<sup>[71]</sup> “jack of all trades” – sunscreen, and to ensure that its formulation complies with established regulations,<sup>[72]</sup> a commercial sunscreen will typically embrace the properties of an assortment of active ingredients, solvents,<sup>[73]</sup> fragrances,<sup>[74]</sup> emollients,<sup>[75]</sup> emulsifiers,<sup>[76-78]</sup> thickeners,<sup>[79]</sup> and stabilizers.<sup>[80]</sup>

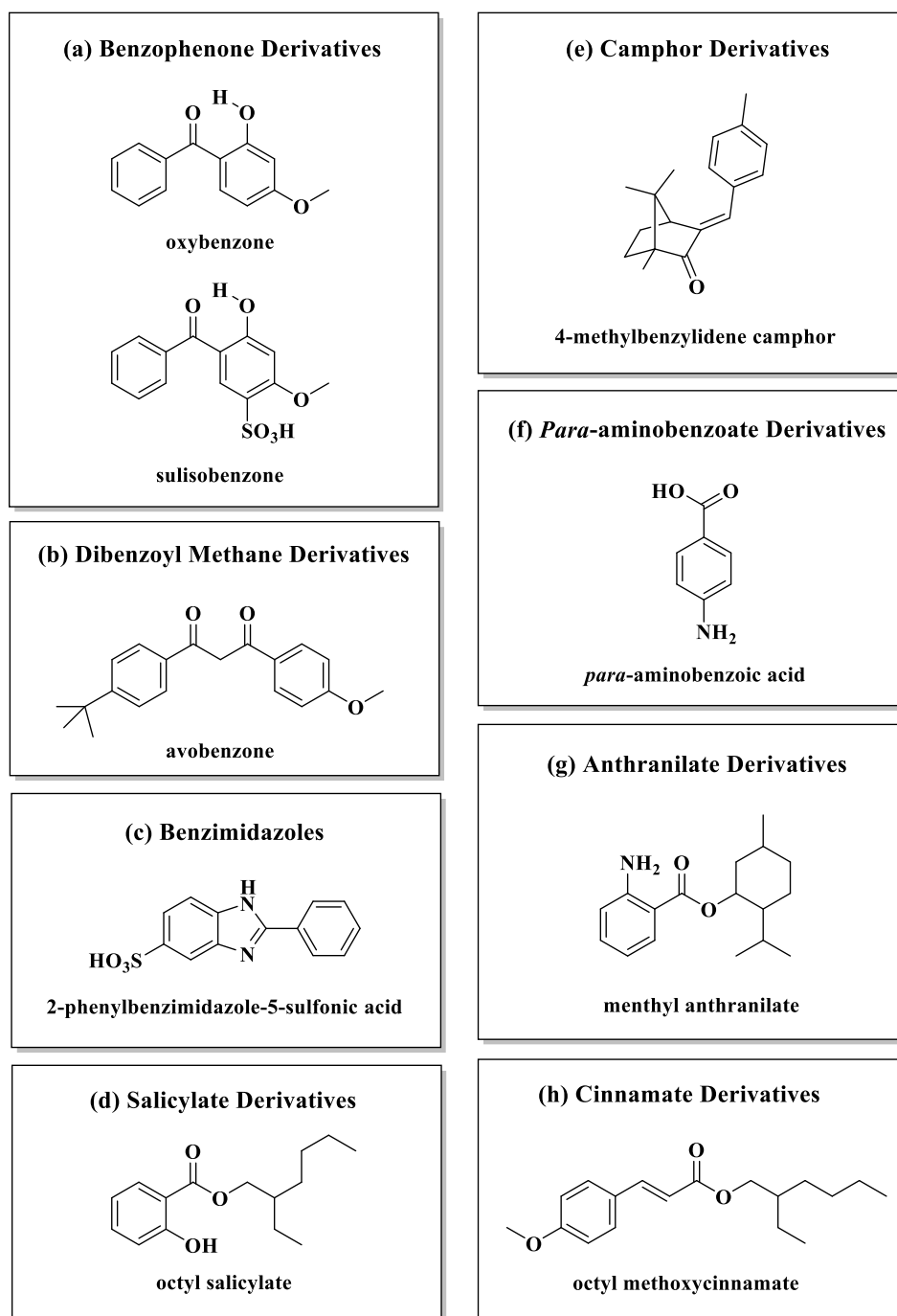


**Figure 1.** Representative examples of the 8 chemical classes of organic UV filters that form most FDA-approved sunscreens: **(a)** benzophenones (*e.g.*, oxybenzone and sulisobenzonate), **(b)** dibenzoyl methanes (*e.g.*, avobenzone), **(c)** benzimidazoles (*e.g.*, 2-phenylbenzimidazole-5-sulfonic acid), **(d)** salicylates (*e.g.*, octyl salicylate) **(e)** camphors (*e.g.*, 4-methylbenzylidene camphor), **(f)** para-aminobenzoates (*e.g.*, para-aminobenzoic acid), **(g)** anthranilates (*e.g.*, menthyl anthranilate), and **(h)** cinnamates (*e.g.*, octyl methoxycinnamate).

The UV active ingredients found within contemporary sunscreen formulations can often be categorized into two main groups: organic and inorganic particulate filters. Organic (chemical) filters generally present as conjugated UV chromophores which can absorb UV radiation through resonant  ${}^1\pi\pi^*$  transitions and rapidly (sub-picosecond) dissipate any excess energy through non-destructive pathways (*i.e.*, via IC; as heat to the surroundings), without dissociating into photofragments or free radicals. An example of the organic UV filters recurrently used within commercial formulations are outlined in Figure 1 and can be further divided to fit within the 8 structural classes highlighted therein (*i.e.*, benzophenones, dibenzoyl methanes, benzimidazoles, salicylates, camphors, para-aminobenzoates, anthranilates, and cinnamates). Examples of the array of Food and Drug Administration (FDA)-approved UV filters are outlined in Tables 1 and 2.<sup>[81,82]</sup>

**Table 1.** FDA-approved organic UV filters listed alongside their maximum approved concentrations and UV spectral coverage.<sup>[81,83]</sup>

UV Filter	Maximum Approved Concentration (%)	UV Spectral Coverage		
		UV-A (I)	UV-A (II)	UV-B
p-Aminobenzoic acid	15			✓
Avobenzene	3	✓		
Cinoxate	3			✓
Dioxybenzone	3		✓	✓
Encamsule	3	✓	✓	
Ensulizole	4			✓
Homosalate	15			✓
Menthyl Anthranilate	5		✓	
Octyl methoxycinnamate	7.5			✓
Octyl salicylate	5			✓
Octocrylene	10			✓
Oxybenzone	6		✓	✓
Padimate O	8			✓
Sulisobenzene	10		✓	✓
Trolamine salicylate	12			✓

Strikingly, despite the wealth of organic filters being marketed to date, not one is able to provide consistent photoprotection across the entire UV-A and UV-B spectral range. Particulate (physical) filters are formed of nanoparticles which remain at the surface of the skin (*cf.* organic sunscreens which are often toxically absorbed into the blood stream);<sup>[84]</sup> however, like that of the organic filters, such filters aptly display broad absorption across the UV spectral region but can also scatter incoming radiation away from the upper epidermis of the skin. Earlier apprehensions regarding the tendency for these nanoparticles (namely TiO<sub>2</sub> and ZnO) to penetrate the skin fueled extensive studies, but have since, in several instances, shown their inability to pass the stratum corneum of healthy skin or the epidermis.<sup>[85,86]</sup>

**Table 2.** FDA-approved inorganic (nanoparticulate) UV filters listed alongside their maximum approved concentrations and spectral coverage.<sup>[81,83]</sup>

UV Filter	Maximum Approved Concentration (%)	UV Spectral Coverage		
		UV-A (I)	UV-A (II)	UV-B
Titanium dioxide (TiO <sub>2</sub> )	25			✓
Zinc Oxide (ZnO)	25	✓	✓	✓

The efficacy of a sunscreen tends to be historically linked with its sun protection factor (SPF) value, a parameter that outlines the potency of (photo)protection from erythema (*i.e.*, sunburn) caused primarily through exposure to UV-B. SPF is a figure that relies on the independence of the SPF value to both UV radiation dose and irradiance. Markedly, the level of UV absorbance of a sunscreen is not directly proportional to the SPF of a marketed sunscreen product – transmission is instead observed as 1/SPF, such that a sunscreen with an SPF of 25 will block out 96% of UV-B light etc. In an effort to uniform UV protection, SPF has since become the standard to benchmark the level of UV-B photoprotection provided by a sunscreen when applied *in vivo* (*i.e.*, on skin samples) at an even distribution of 2 mg/cm<sup>2</sup>,<sup>[87]</sup> and employs Eq. 1.1 to formally assess the ratio of UV radiation transmitted with/without photoprotection:<sup>[88,89]</sup>

$$\text{SPF} = \frac{\sum_{290}^{\lambda_{400}} E(\lambda)S(\lambda)\Delta\lambda}{\sum_{290}^{\lambda_{400}} E(\lambda)S(\lambda)T(\lambda)\Delta\lambda} \quad (\text{Eq. 1.1})$$

where  $E(\lambda)$  is the spectral power distribution at a wavelength ( $\lambda$ ; nm) of the radiation source used in the determination;  $S(\lambda)$  is the erythema action spectrum; and  $T(\lambda)$  is the spectral transmission through the sunscreen.

Likewise, the FDA defines the SPF *via* Eq. 1.2:

$$\text{SPF} = \frac{\text{MED} [\text{protected skin (PS)}]}{\text{MED} [\text{unprotected skin (US)}]} \quad (\text{Eq. 1.2})$$

where MED (PS) is the Minimal Erythema Dose for Protected Skin (*i.e.*, skin by which 2 mg/cm<sup>2</sup> of sunscreen has been applied) and MED (US) is the Minimal Erythema Dose for Unprotected Skin (*i.e.*, skin in the absence of any suncreening product).

As it stands, existing SPF testing methods are limited in that manufacturers are not required to test the intrinsic photostability properties of these marketed formulations, and therefore their inclination to form photoproducts and long-lived excited states has been overlooked. In essence, sunscreen behavior (and hence, performance) could be greatly compromised should the existence of long-lived excited states (and corresponding photoproducts) alter the SPF under more inherent conditions (*i.e.*, natural solar radiation) in comparison to that of lab simulated conditions used previously in SPF standardized tests. In view of recent studies, it is overtly apparent that labelled SPFs may not necessarily mirror (but overestimate) the extent of photoprotection offered by sunscreens in natural sunlight.<sup>[88]</sup> Still, in absence of fundamental data examining how erythema sensitivity of the skin changes in wavelength in the visible region and the tendency of sunscreen formulations to irreversibly photodegrade from longer-lived molecular states, the heavily popularized interpretation of SPF values is not a viable means under differing dose and irradiance conditions.<sup>[87,88]</sup>

As it stands, the COLIPA group (European Cosmetic Trade Association ‘In Vitro Sun Protection Methods’ group) have largely worked to standardize claims of UV-A protection. This COLIPA method has since been adapted from its *in vivo* practice for *in vitro* quantification of UV-A protection (*i.e.*, whereby a film of sunscreen is applied to an artificial test substrate and evaluated using a spectrophotometer that analyzes the amount of UV-R passing through the film of product).<sup>[90]</sup> This is guided through monitoring the suppression of Persistent Pigment Darkening (PPD), which is a visual cutaneous response

following 2 to 24 hours of UV-A exposure thought to stem from the photooxidation of pre-formed melanin and its precursors. Analogous to SPF readings, a PPD rating of 2 suggests that the sunscreen allows a two-fold increase in UV-A prior to PPD suppression.

Alternately, the FDA make use of an *in vitro* ‘critical wavelength’ alternative to interpret the quality of broad-spectrum photoprotection. This critical parameter is indicative of the wavelength at which > 90% of the sunscreen’s spectral coverage occurs and must value over 370 nm. Remarkably, the FDA does not require an *in vivo* test to demonstrate broad spectrum protection.<sup>[91,92]</sup> In the UK, especially, sunscreen labels regularly print a Boots UV-A star rating; it is assumed that the higher the star rating, the better the protection against UV-A rays. Here, broad spectrum photoprotection is indicated through the percentage of UV-A radiation afforded by the sunscreen versus UV-B radiation, as measured applied on a sunscreen film (*i.e.*, *in vitro*). Notably, to claim this ‘broad-spectrum’ label in the EU, a suncreening product should demonstrate usage of both UV-A and UV-B filters and must achieve at least a ratio of 1/3 UV-A protection.<sup>[91,92]</sup>

Whilst most UV filters introduced above are approved for use as photoprotective agents worldwide (*i.e.*, in Australia, Japan, US, UK, and the EU), some approved UV filters, namely PABA and trolamine salicylate, have now become defunct as a result of their questionable spectral coverage, photostabilities, phototoxicities, and bioavailability.<sup>[93–96]</sup> Moreover, a number of them have been recently identified as an emerging organic pollutant due to their widespread use in cosmetics and sunscreen products and are regarded as hazardous for aquatic environments.<sup>[97,98]</sup> In response to the growing research demonstrating the detrimental impact of sunscreen-linked contamination of the ocean – in particular, concomitant coral death – it is vital to explore how the alkalinity of surface and salt-water lakes affect a UV filter’s performance both in its role as a sunscreen and as a pollutant. Towards this end, in 2018, the state of Hawaii in the US became the first in the nation to sign a legislative bill (SB 2571) banning the sale and distribution of sunscreens containing two of the most popular sunscreen agents oxybenzone and octinoxate, which has been in place since Jan 1<sup>st</sup>, 2021.<sup>[99]</sup> There now remains the need to determine the ecological behavior of sunscreen products in order to allow for the development of highly innovative and least hazardous filters. In line with this, more recently, new tools (*i.e.*, the EcoSun Pass) have been developed by BASF,<sup>[100]</sup> designed with the potential to evaluate the ecofriendliness of individual sunscreen components in order to make informed decisions and select components with the best ecological footprint.

Other efforts have also been extended to formulate skincare products utilizing a newly formulated mineral-based coating applied to particles of inorganic UV filters (*i.e.*, zinc oxide and titanium dioxide) which provide broad protection against a range of environmental insults and are ecologically safe.<sup>[101]</sup> Such developments again act to address the issues concerning the dermal uptake of UV filters like oxybenzone through clothing, plastics, and coatings.<sup>[84,102–104]</sup> Very recent work has also shown nanoparticulate UV filters like TiO<sub>2</sub> to be a potential pollutant of recreational waters, with its surface coating and sunscreen formulation type observed to drive environmental disparage.<sup>[105]</sup> This again is especially concerning but links heavily with that of recent gas-phase studies mapping the photofragmentation profiles of sunscreens in alkaline environments.<sup>[106–108]</sup>

As with any cosmetic product, there is no “one-size-fits-all” sunscreen formulation available in the market. In the 21<sup>st</sup> century, brands are increasingly having to rely on digital (*i.e.*, social media trends) and influencer marketing strategies to distinguish themselves from the likes of other brands. And as efficacy claims for sunscreen products are becoming more uniformed and increasingly controlled (*i.e.*, the EU currently regulates the SPF claims that can be used),<sup>[91,92]</sup> there are often limited means to differentiate between two products at face value. There is now such a collection of sunscreens on the market that consumers can afford to be more selective in their choice of photoprotection, ultimately allowing one’s sensory experience with the sunscreen to come into play. Aesthetic elements of a sunscreen such as its on-skin appearance, fragrance, and skin feel during/after application are most frequently cited by consumers reasoning their underuse (or lack thereof) of sunscreen products.<sup>[109]</sup> With current crisis calling for a paradigm shift towards the delivery of sustainable, ecofriendly, and ‘natural’ sunscreens,<sup>[110–112]</sup> formulators now more than ever are having to think creatively “outside the box” in order to navigate the challenging standards for product efficacy whilst also meeting aesthetic considerations warranted from the modern-day consumer.

The understanding of the photophysical properties of organic sunscreen molecules at the molecular level is therefore becoming of great relevance and may deliver a progressive perspective to revolutionize the development of the next generation of sunscreens. Such work will be a concerted effort towards addressing the impact and commercialization of these cosmetic suncreening agents in the near future.

## 1.2 Laser Spectroscopy of Organic Sunscreens

Laser spectroscopy is a powerful technique that has been increasingly applied over the years to probe the intrinsic properties of UV filters and deliver essential insights into the detailed mechanisms by which sunscreen molecules operate.<sup>[113,114]</sup> Now, in the search towards tailoring the development of the next generation of UV filters, a string of fundamental high-level quantum-chemical calculations<sup>[115–117]</sup> and recent advanced spectroscopic studies<sup>[118–122]</sup> have been conducted on such systems both in the solution and gas phases. Nevertheless, whilst solution-phase experiments can account for the conditions that closely mimic that of the surroundings by which these sunscreen molecules can be found (*i.e.*, in that of a commercial sunscreen formulation),<sup>[113,123]</sup> gas-phase interpretations undeniably better demonstrate a fundamental molecular-level understanding of their photophysical behavior,<sup>[124–129]</sup> and merit data that can be readily elucidated by theoretical investigations.

### 1.2.1 Solution-Phase Laser Spectroscopy of Organic Sunscreens

Contemporary excited-state dynamic measurements and laser spectroscopic studies have been widely performed to explore the fundamental photodynamics of sunscreens in solution. This work further provides insight into how bulk solvation influences intrinsic sunscreen photophysics and reckons just how information attained from gas-phase experiments can guide the interpretation of the intrinsic dynamics of their solution-phase counterparts.<sup>[130–134]</sup> Undoubtedly, as solution-phase laser studies are less removed from that of gas-phase interpretations, such techniques have reaped much attention over the years, with the aim of providing more realistic environmental model. The processes underpinning how solvent and solute molecules interact therefore prove fundamental. This subchapter will stand to review the laser spectroscopic studies of organic UV filters carried out in solution over the last 10 years.

Given the most conventional means of photoprotection is generally found to be that of sunscreen formulations, such solutions will undoubtedly be solvated, held under the aforementioned ‘bulk’ phase at the surface of the skin. Still, as solvation is still so poorly understood in experiment, such complications have extended over to theoretical approaches where solute-solvent interactions of these systems have also proven challenging to model. It is therefore of great importance to continue unravel the contributions of the solute and solvent in the relaxation dynamics of such systems as well

as any coupled solute/solvent interactions. Currently, transient absorption (*i.e.*, electronic and vibrational; TEAS and TVAS, respectively) and two-dimensional infrared (2D-IR) spectroscopies stand as two of the most established solution-phase techniques used to explore the photophysical behavior behind our repertoire of sunscreens.

2D-IR spectroscopy is based upon a typical pump-probe experimental setup, utilizing a short laser excitation pulse – an IR pump – and a second broad-band IR probe pulse. Wavelength is selected by either using a tunable Fabry-Perot filter or a pulse shaper which alter the IR pump pulse that imposes onto the sample.<sup>[135]</sup> After a specified delay time, the IR probe pulse is overlapped spatially with the pump beam in the sample and a downstream array detector records the signal and residual probe light to generate the probe frequency. Through varying pump frequencies, a 2D array of data is mapped and its ability to provide IR spectroscopy with refined time resolution aids to provide information on its structural fluctuations, a detail previously inaccessible *via* methods like nuclear magnetic resonance spectroscopy.<sup>[135,136]</sup> The acquisition of 2D-IR data has evolved down two paths – that of frequency-domain double resonance 2D-IR, and that of a time-domain (Fourier transform) route.<sup>[135,137]</sup> By insertion of a programmable pulse shaper in the pump beam, either path can be taken; filtering the incident broad band pulse into a two-pulse sequence allows for time-domain spectroscopy to lead, whereas formation of a tunable narrow-band pulse leads to frequency-domain spectroscopy. Whilst the results of both routes provide identical peaks in a 2D-IR spectrum, there are inert differences which have been focused on in great detail elsewhere.<sup>[135,137]</sup> Both methods have since been extended to explore the 2D-IR of transient species through the introduction of a UV(-visible) pump pulse which functions as a “phototrigger”, perturbing the equilibrium of the system. Should the delay between the UV and IR pulses be sufficiently short, the transient 2D-IR map will reflect the vibrational states of the electronic excited state(s); the system’s relaxation processes can then be studied by altering the delay between the UV pulse and IR pump-probe. Transient 2D-IR spectroscopy is hence a direct and valuable approach for probing the intrinsic vibrational spectra of solvated electronically-excited molecules over time and largely acts to complement techniques such as TEAS and TVAS, both of which will be introduced anon. Nevertheless, 2DIR is thus key for studying the molecular structure, reactivity (*i.e.*, solvent-solute interactions), and vibrational dynamics of compounds that hone functional groups that strongly absorb IR,<sup>[138–140]</sup> like that of the carbonyl within benzophenones (*e.g.*, organic UV filters benzophenone-3 and benzophenone-4).<sup>[141]</sup>

Lately, TEAS has become one of the most popularly applied laser experimental solution-phase techniques used for studying organic sunscreen molecules in the UV-visible regions. Effectively, TEAS is the time-resolved study of the absorption spectrum of a small fraction of the sample molecules following their photoexcitation with a femtosecond laser pulse.<sup>[142]</sup> In line with the typical ultrafast (< 100 fs) pump-probe setups mentioned previously in this Review, the pump pulse (habitually tuned within the *ca.* 235-1600 nm spectral range) excites a molecule to an electronically excited state after which a broadband white pulse (*ca.* 300-800 nm) probes its excited state absorption profile. To avoid multiphoton processes, weak probe pulses are usually used, led through the sample with a delay with respect to the pump pulse.<sup>[142]</sup> Varying the time delay (*i.e.*, the difference between the arrival times of the pump relative to the probe pulse) even with interludes of *ca.* 10 fs allows one to build a dynamic absorption profile for the molecule through a series of “snapshots”.<sup>[143]</sup> A difference absorption spectrum (*i.e.*, a transient absorption spectrum) is then calculated from monitoring the change in optical density measured for each wavelength at each specified time delay. Excellent reviews detailing the experimental methodology behind the transient absorption spectroscopy of sunscreens have been better addressed elsewhere.<sup>[143,144]</sup> The vastness of the literature on the ultrafast photochemistry of an array of sunscreen families largely extends to the mass application of transient absorption techniques (*viz* the anthranilates,<sup>[145]</sup> benzophenones,<sup>[121,146]</sup> cinnamates,<sup>[147-153]</sup> octocrylenes,<sup>[154]</sup> and salicylates,<sup>[119]</sup> to name but a few). Accordingly, transient absorption techniques have now become a workable tool necessary to vitally explain the photorelaxation dynamics and mechanisms of a wide range of suncreening applications and technologies.<sup>[155,156]</sup>

Broadband infrared pulses may also be used in lieu of white light pulses, instead probing the vibrational modes of a system in what now has been coined as TVAS, which when run in conjunction with TEAS measurements, provide the complete vibrational and electronic absorption spectral package needed to follow the evolution of an UV-excited species. In taking TVAS measurements, the formation and/or destruction of important bonds can be followed and any repopulation of the ground state of the molecule to be monitored and identified through changes in the intensity and features of the ground state bleach.<sup>[142]</sup>

From a safety standpoint, high molecular weight UV filters make for attractive suncreening candidates, contingent upon the assumption that such systems cannot penetrate the skin and thereby reduce cutaneous absorption.<sup>[157,158]</sup> One example of such a system is that of the UV filter ethylhexyl triazone (EHT; Figure 2a), which stands at *ca.*

2-3 times greater in mass than most sunscreen molecules, and bears a close structural resemblance to several other larger sunscreens (*e.g.*, bisoctrizole [MW: 658.88 g/mol], bemotrizinol [MW: 627.81 g/mol], silatrizole [MW: 501.849 g/mol], and diethylhexyl butamido triazone [MW: 765.981 g/mol]). Schematic structures of bisoctrizole and bemotrizinol are outlined in Figures 2b-c for ease of comparison with that of EHT. In solution, EHT (MW: 823.07 g/mol) generally offers a broad absorption profile across the UV-B region and EHT possesses excellent photostability. Whilst it is yet to be approved for use by the FDA, it is used broadly in Europe within various water-resistant formulations. In light of this, TEAS has been used to study the ultrafast photodeactivation mechanisms available to the EHT.<sup>[159]</sup>

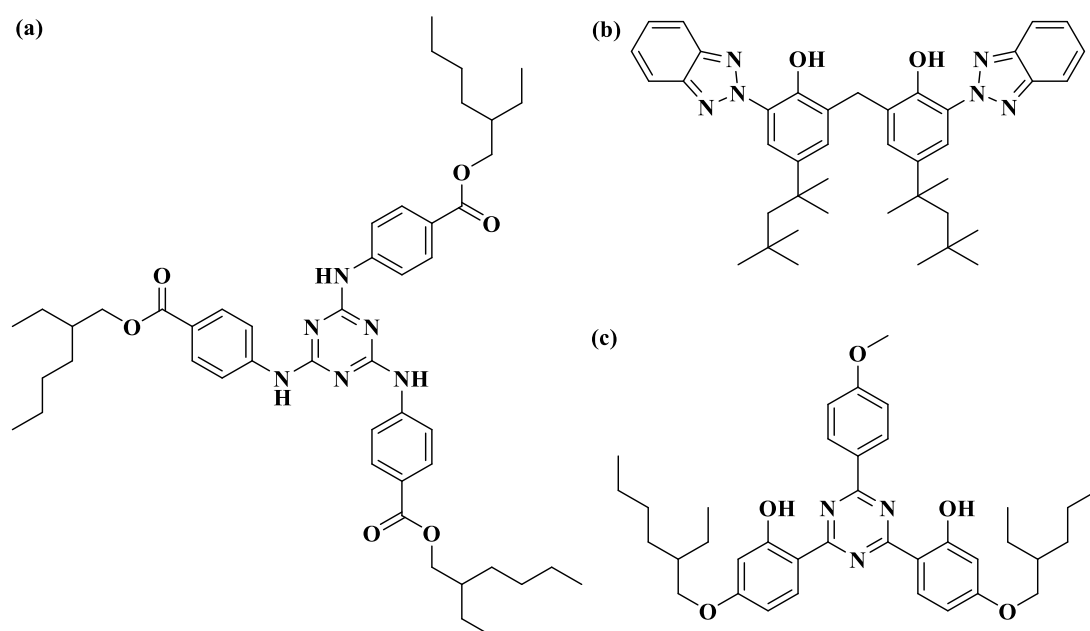


**Figure 2.** Schematic structure of (a) ethylhexyl triazone (EHT; MW: 823.07 g/mol), (b) bisoctrizole (MW: 658.88 g/mol), and (c) bemotrizinol (MW: 627.81 g/mol).

Here, Baker *et al.* propose that following UV-B photoexcitation to the initial high-lying  $n^1\pi\pi^*$  state, EHT will undergo ultrafast ( $\sim 400$  fs) IC to the  $S_1(1^1\pi\pi^*)$  state followed by subsequent vibrational relaxation ( $\sim 20$  ps) to the ground  $S_0$  state through a  $1^1\pi\pi^*/S_0$  conical intersection (CI).<sup>[159]</sup> The dominant deactivation mechanism for EHT is thus again that of internal conversion, as had been confirmed previously using steady-state fluorescence and phosphorescence techniques.<sup>[160]</sup> Notably, in these earlier experiments,

whilst ultrafast mechanisms were suggested, further measurements were beyond the means of the study. However, using ultrafast TEAS, it was observed that such repopulation of the ground vibrational state sanctions uninterrupted cycles of EHT absorption/recovery to ensue, a desirable quality for an efficient sunscreen – and one that has been previously observed for OB.<sup>[121,146]</sup> The long-lived excited state features observed in their transient absorption studies in both dioxane and methanol confirm the presence of long-lived photoproducts attributed to metastable transient states (*i.e.*, where the peaks at *ca.* 350 and 450 nm reveal the excited-state populations trapped in S<sub>1</sub> and T<sub>1</sub> states, respectively) and that ISC to a low-lying triplet state is highly probable channel. Such channels are markedly supported *via* their electronic structure calculations. In understanding the photodeactivation mechanisms behind EHT, this work offers a means to synthetically optimize the photostability of EHT and its structural UV-absorbing analogues through various substitutions of functional groups, or work to fully functionalize the chromophore itself.<sup>[159]</sup> This study also brings about the practicality of aggregating UV filters of lower mass (*i.e.*, dimerizing or trimerizing) to elicit systems with an greater overall molecular mass.

As a popular building block used considerably in organic synthesis, the classic benzophenone {(C<sub>6</sub>H<sub>5</sub>)<sub>2</sub>CO} backbone can also be found within several FDA-approved sunscreen ingredients (*i.e.*, oxybenzone (OB) and sulisobenzene, which are otherwise aptly named benzophenone-3 and benzophenone-4, respectively; see Figure 1a). UV-excited benzophenone is understood to partake in ultrafast conversion from its singlet to triplet states and has proven somewhat handy for a selection of technological applications.<sup>[161]</sup> Notably over the years, one of the key mechanisms by which an organic system (*i.e.*, benzophenone-derivatives) access CIs is *via* an H-atom donor and acceptor that facilitate ultrafast intramolecular hydrogen transfer. OB is a classic example of a system that utilizes this route, partaking in the barrierless electron-driven H-atom transfer pathway from the S<sub>1</sub> CI to the S<sub>0</sub>, as tracked both through a series of gas- and solution-phase studies.<sup>[108,117,143,162,163]</sup> For the most part, the ‘subensemble-selective’ photophysical nature of benzophenone in a protic solvent (*i.e.*, methanol) had been centered around exploiting the red-edge excitation effect (REEE).<sup>[141]</sup> Here, using a combination of TEAS/TVAS and Raman spectroscopy, it was observed that selectively UV photoexciting in the long-wavelength region or near the maximum of a  $\pi^* \leftarrow n$  absorption band of benzophenone respectively excites benzophenone molecules with their carbonyl group non-coordinated, or predominantly coordinated to a molecule of methanol solvent through hydrogen bonding. Strikingly, hydrogen-bonding interactions are seen to increase the ISC

time constant from  $< 200$  fs to *ca.* 1.7 ps in methanol, evidencing that the preferred ISC channel is from the  $S_1(n\pi^*)$  to the  $T_2(\pi\pi^*)$  intermediate state, with IC from the  $T_2(\pi\pi^*)$  to  $T_1(n\pi^*)$  controlled by solvent quenching of excess vibrational energy.<sup>[164]</sup> There has been limited work on the use of 2D-IR spectroscopy on sunscreens; nonetheless, in this instance 2D-IR spectroscopy has more aptly been used to support TEAS and TVAS in studying the model system of benzophenone, delving into the exchange between various solvent environments with a sub-picosecond time resolution.<sup>[141]</sup> Again, here, REEE was exploited to demonstrate the acceleration of an H-atom abstraction reaction (*ca.* by a factor of 40) through subensemble (solvation-environment) photoselective excitation of benzophenone molecule, either coordinated or non-coordinated to a coreactant (*i.e.*, phenol) through hydrogen bonding in polar environments (*i.e.*, in DCM solution). TEAS/TVAS spectra reveal H-atom abstraction reaction between the triplet excited state benzophenone and phenol. Conventional FTIR on benzophenone-phenol identifies three significant benzophenone carbonyl peaks which are (i) uncoordinated, (ii) hydrogen bonded to a single phenol, and (iii) hydrogen bonded to a phenol which consequently accepts a H-bond from at least one further phenol molecule. 2D-IR spectra of these such distinct benzophenone-phenol environments support the assignment of the picosecond nature of the exchange dynamics between H-bonded and non-H-bonded structures. Subsequently, the authors propose that in the static limit following photoexcitation of hydrogen-bonded BP( $S_0$ )-phenol complexes, accelerated hydrogen atom transfer from the phenol to BP( $T_1$ ) occurs from molecules of vibrationally-thermalized BP( $T_1$ ), and that the weaker BP( $T_1$ )-phenol hydrogen bonds break before H-atom transfer can occur.<sup>[141]</sup>

As much as ‘denatured alcohols’ are used to help dissolve various sunscreen actives in a sunscreen and make the solution less greasy, their polar counterparts are also used within cosmetics (*e.g.*, ethanol in hand sanitizers and isopropanol in rubbing alcohol);<sup>[165]</sup> it is therefore consequential to see how UV filters behave under similar environmental conditions. In line with this, the influence of solvent environment(s) on the excited state dynamics of photoexcited diethylamino hydroxybenzoyl hexyl benzoate (DHHB; Figure 3), a widely used UV-A absorber found in a range of sunscreens sold worldwide. DHHB differs from OB only through the addition of an auxochrome nitro group located meta to the hydroxy group on one phenyl ring, and the addition of an ester group on the neighboring ring. Kao *et al.*, using complementary TEAS/TVAS techniques, reported a difference in the ultrafast transient absorption spectra of DHHB when solvated in non-polar (cyclohexane) and polar (*i.e.*, methanol, dimethyl sulfoxide, and acetonitrile)

solvents at 360 and 345 nm.<sup>[118]</sup> In cyclohexane, excited-state hydrogen transfer (ESHT) was found to occur from the  $S_1$  Franck-Condon region within  $< 200$  fs and as the  $S_1$ -*enol* form of DHHB twists from its initially excited form, its energy decreases and the energy of the corresponding  $S_1$ -*keto* structure increases, fostering its most preferred relaxation pathway. TVAS evidences that the ground state bleach recovery of DHHB photoexcited at 345 nm in cyclohexane approaches 98%, with a  $\sim 10$  ps time constant.

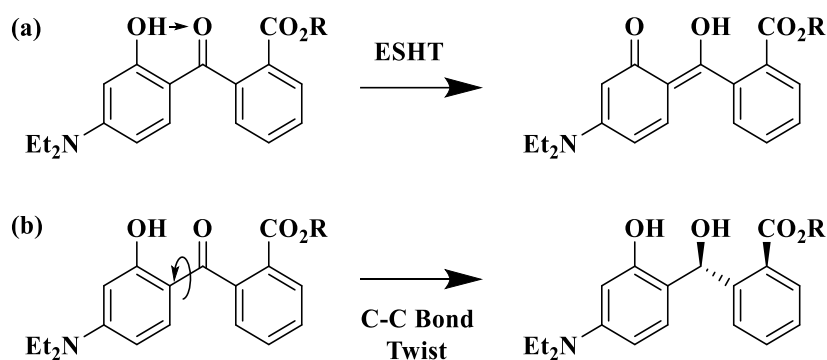


**Figure 3.** Pictorial summary of the two photorelaxation mechanisms of diethylamino hydroxylbenzoyl hexyl benzoate (DHHB) under the influence of (a) non-polar and (b) polar solvent environments. Adapted from Ref<sup>[118]</sup>.

As for three polar solvents studied, it would appear that ESHT is inhibited through the disruption of the intramolecular hydrogen bond. The  $S_1$ -*enol* character is retained as a result and  $\sim 95\%$  of photoexcited DHHB is found to relax through torsion of the C–C bond that quenches stimulated emission and is suggested to lead to internal conversion to  $S_0$  via a CI. A small proportion of the twisted  $S_1$ -*enol* intermediates then undergoes ISC into the  $T_1$ -*enol*, as observed by TEAS. The formation of such species is highly undesirable and can yield singlet oxygen upon quenching by  $O_2$ . The synergistic filter-filter aggregation effects of DHHB have previously been studied with avobenzone where it failed to present a photostabilizing effect on the mixture.<sup>[166–168]</sup> In the spirit of offering a DHHB within a (more) favorable blend, this study was advanced through the aggregation of DHHB with octocrylene, a well-known photosensitizing UV filter with a similar triplet state energy to DHHB.<sup>[169,170]</sup> Strikingly, this mixture resulted in the quenching of the undesirable triplet DHHB.<sup>[118]</sup> Therefore this study strappingly reinforces the importance of employing a manifold of UV filters within formulations to counteract various challenging properties (*i.e.*, prevention of destabilization of multiple UV filters within formulations)<sup>[168,171]</sup> and

backs the potential directions for future sunscreen formulations functionalizing DHHB. Together, the two transient absorption techniques have delivered a completely feasible relaxation mechanism for photoexcited DHHB in various solvent environments, with TVAS, in particular, allowing for the assignment of the minor photoproducts (*i.e.*, the metastable *trans-enol* DHHB) in polar solvents. Notably, it is not always so that the solvent environment will dramatically influence that of the behavior of a sunscreen molecule. In particular, in the case of methyl anthranilate (MA) and its sunscreen analogue menthyl anthranilate (MenA), the ultrafast dynamics of such molecules are barely altered upon solvation or as their gas-phase species.<sup>[145,172]</sup> Using a series of TR-IY, TR-PES, and TEAS, both systems are shown to be long-lived (> 1.2 ns), and photoexcitation to their S<sub>1</sub> state result in the trapping of the excited state population, with no accessible CIs with the pump energies utilized. The case for MA and MenA will be addressed more relevantly anon, in line with their gas-phase significance.

Naturally a preservative produced by food and plants, salicylates have also proven to be a safe and attractive choice for inclusion in sunscreen formulations.<sup>[173,174]</sup> In the same way as the benzophenones (*i.e.*, OB and DHHB) mentioned above, salicylates present the same hydroxybenzoate moiety that proclaim the *enol-keto* point necessary to undergo excited-state intramolecular proton transfer (ESIPT) followed by molecular rotation and decay to the ground state. Much work has focused on methyl salicylate over the years, with a large proportion of experimental and computational studies conducted to investigate the mechanism of its dual fluorescence and ESIPT.<sup>[175–179]</sup> Surprisingly, the (experimental) ultrafast relaxation dynamics of salicylates have received very little attention over the years. Femtosecond depletion techniques were conducted on methyl salicylate by Herek *et al.* (1992),<sup>[180]</sup> identifying ESIPT to occur within 60 fs, with a longer decay channel of 120 ps. Ling *et al.* more recently utilized femtosecond time-resolved ion yield (TRIIY) and photoelectron spectroscopy (TR-PES) to reveal ESIPT to occur (on a 100 fs timescale) followed by IVR (sub-ps) and IC (ps).<sup>[181]</sup> Computational efforts have been much more fruitful and support this interpretation, with Chang *et al.* (2021) having more recently addressed the excited-state relaxation paths and photophysical mechanisms of methyl salicylate,<sup>[115]</sup> identifying three S<sub>1</sub> excited-state non-radiative relaxation pathways to the ground state. Whilst the photostability of popular choice UV filter homomethyl salicylate (homosalate; HMS; Figure 4) has been widely contested over the years, it is somewhat notoriously included in as many as *ca.* 45% of the sunscreens approved for sale in the US. Recent work by Holt *et al.* employed a bottom-up approach to investigate the ultrafast molecular dynamics of HMS upon excitation with UV-B radiation.<sup>[119]</sup> Using a diverse

blend of laser techniques, from laser-induced fluorescence and steady-state absorption spectroscopy, to a combination of time-resolved laser spectroscopies both in the solution and gas phase (*i.e.*, TEAS and TRIY, respectively), the authors show that, as would be expected, the *enol* tautomer of HMS undergoes ultrafast ESIPT upon photoexcitation in the UV-B.

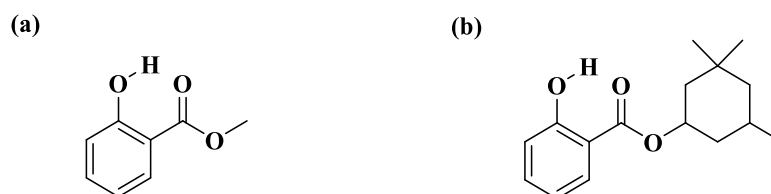


**Figure 4.** Schematic structure of (a) methyl salicylate and (b) homomethyl salicylate (HMS). Notably, ESIPT is found to occur at their *enol-keto* point(s) to allow for barrierless tautomerization.

Following barrierless *enol-keto* tautomerization, the  $S_1$ -*keto* effectively undergoes fast IC to the ground  $S_0$  state sided with the occurrence of low quantum yields of fluorescence and ISC. The studies in solution and *in vacuo* agree the ultrafast decay of HMS is due to the ESIPT process, a verdict sought to be in line with several other sunscreen studies (*i.e.*, OB and DHHB).<sup>[118,146]</sup> The authors also propose the presence of a ‘trapped’ photoexcited *enol* conformer in solution which is unable to undergo ESIPT, explaining the fluorescence seen in their LIF spectra; still, given their (diminutive) yield in gas-phase TRIY measurements, further gas-phase hole burning experiments are warranted to confirm their existence. Such methods are gas-phase techniques that will be addressed in Chapter 1.2.2. Within the bounds of this investigation, it emerges that HMS, for the most part, decays non-radiatively *via* sunscreen-favorable routes (*i.e.*, IC and ESIPT). Though the (undesirable) generation of HMS triplet states necessitate the need for additional investigation, this study is an excellent example of a concerted regimen of the experimental gas- and solution-phase techniques needed to formulate more optimized artificial sunscreen products.

## 1.2.2 Gas-Phase Laser Spectroscopy of Organic Sunscreens

Between the sheer volume of gas- and solution-phase studies published in recent years, it is markedly clear that the excited state dynamics of such molecules first need to be fully defined in the gas phase – where a system can be fully isolated – before the intricacies of ‘bulk’ effects can be fully assessed and manipulated.<sup>[114,126,129,182]</sup> A widespread range of techniques have been employed over the years to explore the intrinsic photophysical properties of UV filters in the gas phase, incorporating techniques such as time-resolved ion yield (TR-IY), UV-UV holeburning (HB), depletion (ion dip), resonance-enhanced multiphoton ionization (REMPI), photoelectron (PES) spectroscopies, and finally, that of laser-interfaced mass spectrometry (LIMS; see Chapter 1.3).

Time-resolved ion yield (TRIY) spectroscopy is another technique that has been used in close conjunction with a range of the aforementioned (*i.e.*, 2D-IR, TEAS, and TVAS) and upcoming laser spectroscopy techniques looking into the ultrafast dynamics of sunscreen molecules. As a gas-phase method, samples are typically vaporized *via* heating and seeded into a buffer gas (*i.e.*, helium) where the mixture is expanded into vacuum to create the sample molecular beam. This technique again closely follows the typical pump-probe setup where the pump photoexcites the sample at the laser-molecular beam intersection upon which the probe subsequently photoionizes the excited molecule. In line with that of characteristic mass spectrometric techniques, the ion signal (*i.e.*, of the precursor molecule and fragment ions) here is wholly representative of the ion yield. Changes in ion yield, measured as a function of the time delay between the two pulses, provides fundamental information concerning the relaxation of electronic states in the gas-phase sample as it relaxes from its excited state and as the excited state population decays.<sup>[126,183]</sup>

Another popular gas-phase technique used to study neutral UV filters to date is that of REMPI. Primarily developed as a relatively efficient ‘soft’ ionization technique, REMPI is often used to investigate high-lying excited states, for which dissociation is more likely. It is generally performed in a two-photon process, where the molecule is excited (pumped) by the first photon to an intermediate electronic state, and then is ionized (probed) from the excited state by the absorption of the second photon. As multiple photons are able to resonantly excite and ionize the molecule, REMPI is hereby referred to as  $(n + m)$  scheme, where both  $n$  and  $m$  are integers, and correspond to the number of single-color photons that are used to pump and probe the system, respectively. Fittingly,  $(n + m')$  is commonly used when different colors are used for the pump and probe stages. Whilst the excited states can be adequately accessed *via* a 1+1 REMPI scheme (*i.e.*, resonant two-photon

ionization or R2PI), multiphoton processes are also common, and follow an  $I^n$  power dependence where  $n$  corresponds to the number of photons absorbed. Information stemming from the vibronic excited states of the system can thereby be obtained by scanning the wavelength of the initial photon and measuring the number of ions formed in the ionization stage. The ionization potential of the molecule can also be determined through monitoring the total ion signal as a function of the probe wavelength. This technique has been used extensively to successfully probe the photochemistry of various biomolecules such as the purine nucleobase, tryptophan, and dipeptides, just to name a few.<sup>[184–186]</sup> Detection of these ions is usually achieved using time-of-flight (TOF) mass spectrometry,<sup>[187–189]</sup> which offers great sensitivity, spectral quality, speed, and stability.

In principle, TOF mass analyzers separate ions of different mass-to-charge ( $m/z$ ) based on their velocity as they travel down the flight tube.<sup>[190]</sup> Generally, in TOF, ions are directly introduced from the source of an instrument or as a pulse from an earlier analyzer. As the analyte ions travel through the field-free flight zone, they are separated by their masses. This level of mass selectivity will also enable the separation of the parent ion from the resulting fragments, aiding their identification *via* their  $m/z$  ratio. A TOF trace is typically collected through measuring the time it takes for an ion to reach the detector at a known distance following photoexcitation. From this ‘time’ and other established experimental parameters, one is able to determine the mass-to-charge ratio of the ion.<sup>[191–192]</sup> Upon colliding with a microchannel plate (MCP), the particle (with any given  $m/z$ ) generates a surge of electrons, amplifying electronic ion signal detection and providing spatial resolution. Outputs are recorded gated in ion flight time over mass channel of the parent ion, as depicted on a digital oscilloscope. REMPI has often been used alongside other time-resolved (*i.e.*, TRIY) and frequency-resolved (*i.e.*, UV-UV HB) techniques available in the gas phase to study sunscreen components.

Velocity map imaging (VMI) is another simple, yet highly-successful method used for studying the dynamics of molecular photodissociation processes. This technique was originally developed by Chandler and Houston,<sup>[193]</sup> and later advanced by Eppink and Parker.<sup>[194]</sup> By linking this technique using charged products (*i.e.*, anions) with processes like photoionization, photodetachment, photodissociation, and/or bimolecular collisions, information on their respective neutral systems can be unveiled. There have been many demonstrations of VMI, with REMPI-VMI, for example, allowing for the simultaneous measurement of the internal energy and velocity of reaction products. Paired with anion PES, VMI detectors can obtain photoelectron spectra, where 2D images of both the

velocity and angular distribution of the photodetached electrons can be simultaneously acquired, providing sufficient information about the character of the molecular orbital from which the photoelectron was detached from. The idea of VMI is to intersect a molecular beam *via* a pump pulse to disrupt the molecular bond whilst a probe laser ionizes the resulting fragment. The potential between the electrodes would be such that a spherical ionic cloud (classically termed a Newton sphere) would be accelerated towards the VMI detector by three-electrode electrostatic lens, akin to a Wiley-McLaren TOF-MS setup.<sup>[192]</sup> Upon passing through a field-free flight tube similar to that from a TOF set up, the 3D Newton sphere will eventually reach the MCP assembly detector and compacted into a 2D feature. Following this, a charged-coupled device camera captures the 2D image pictured by the phosphor screen attached to the VMI detector.<sup>[192]</sup> The 3D sphere can subsequently be reconstructed from its fine-tuned 2D projection in order to achieve detailed information on the 3D distribution of the Newton sphere, as has been detailed elsewhere.<sup>[152]</sup>

As we drive towards abstracting a ‘bottom up’ approach necessary to probe the intrinsic properties of sunscreens,<sup>[126]</sup> the interrogation of systems of varying size and flexibility are inevitable. It is therefore likely that multiple conformations will be present within the molecular jet/beam or TOF mass spectrometer. For this reason, double resonance methods, namely UV-UV holeburning (HB) and depletion (ion dip) spectroscopies, are especially useful when measuring the UV spectroscopy of neutral species in that they are able to measure conformation-specific spectra,<sup>[195,196]</sup> especially since TOF mass spectrometry (*i.e.*, used with REMPI) will be unable to differentiate between such conformers. HB has been used on occasion to supplement that of R2PI spectra to attain insightful conformation-specific electronic spectra of organic sunscreen systems.<sup>[125]</sup> Such double resonance techniques generally utilize three laser pulses – a hole-burn, a pump, and a probe pulse – and again rely on detection of the ions by TOF or laser-induced fluorescence (LIF). Typically for photochemical UV-UV HB, the narrow band laser will induce selective UV excitation at the frequency of holeburning, which in turn saturates the absorption of a class of system; the laser is spatially overlapped, and its timing tuned to allow for it to intersect the jet/beam at a given time before the probe. The second UV pulse (probe) will photoionize the selected species from the excited state. The corresponding ‘hole’ (*i.e.*, in the ground state population) is then monitored by the probe pulse. The difference in the ion signals with and without hole-burn laser influence is recorded. It is unlikely for two (or more) conformers to be identically resonant with the excitation (pump) pulse; thus, if a particular conformer is resonant with a transition at the

same ground state as the hole-burning pulse, a ‘dip’ in the ion yield of the UV-excited system is observed and will come about in the form of either a depletion in the ion signal for TOF, or a fluorescence signal for LIF. In HB spectroscopy, the signal intensity depends on both the absorption cross section and the excited state dynamics. Similarly, for depletion (ion dip) spectroscopy, the depletion in the ion signal occurs in the event of the hole-burn laser being in resonance with a conformer’s vibronic state. As before, this method measures the change in the ion signals as a function of the hole-burn laser versus the standard pump-probe intensities, with ion signals dependent on the absorption cross section of the transition accessed by the hole-burn laser. Whilst UV pulses are typically used for the hole-burning and pump steps, IR pulses can be used instead to attain conformer-selective IR spectra.

The photoelectric effect is the emission of electrons from matter upon the absorption of electromagnetic radiation (*e.g.*, UV, visible, or x-ray). Analogous to the photoelectric effect, photoelectron spectroscopy (PES) is duly the measurement of the kinetic energy of liberated (photo)electrons ejected from atoms or molecules upon photoabsorption. Extending this principle, gas-phase anion PES – where an anion is ionic species that holds a net negative charge – has, through the years, become a multifaceted spectroscopic technique that allows the neutral form of a species to be investigated following photodetachment from its parent anion. Advantageously, like that of the gas-phase REMPI-VMI, TRIY, and laser-interfaced photodissociation mass spectrometry (see Chapter 1.2.3) methodologies outlined within this Review, anion PES employs mass spectrometric techniques that allow for the anion precursors to be easily selected, isolated, manipulated, and mass-analyzed *via* means of mass spectrometry.<sup>[197]</sup> This coupling of techniques allows for a detailed analysis of the ions and observing the presence of potential exotic gas-phase clusters not typically seen in bulk environments. As the excess electron of an anion is more weakly bound, the photophysics of their anionic and consequent neutral forms will be sufficiently probed with UV-visible energy. Upon photodetachment, anion PES is able to directly measure the electron affinity (EA) of the neutral species, where the EA is the minimum energy required to produce a photoelectron (or ADE). The ADE is found to be the difference in energy between the incident UV-visible photon ( $h\nu$ ) and the electron kinetic energy of the electron detached between the neutral and the corresponding anion, both in their vibrational ground states. Useful vibrational information of the neutral systems can therefore be derived from anion PES experiments and is capable of also measuring the transitions between its electronic states of different spin multiplicity, providing there is sufficient means for photodetachment.

The corresponding geometry of the neutral is altered as an electron is removed from the parent anion at variable incident photon energies, allowing the investigation into its varying energies. The energy difference between the anion and the neutral at the optimal geometry of the anion is therefore the vertical detachment energy (VDE), whereby a positive VDE value is indicative of energy being required to detach an electron from the anion to the neutral. PES is powerful for its sensitivity to both the binding energy of the electron in an anionic state and the time dynamics of that anionic state. Notably, whilst all the experimental configurations of PES center around the photoelectric effect, the field of PES is extremely broad and there are therefore a number of techniques that exploit this phenomenon (*e.g.*, x-ray PES; angle-resolved PES; and gas- and liquid-phase PES). But in the interest of brevity and relevance towards ionic UV filters, we shall only delve into the technique of PES most applied on potential sunscreens to date – time-resolved PES (TR-PES) where the dynamics of anionic resonances can be explored in the time domain. Again, like the other ultrafast spectroscopic techniques mentioned within, TR-PES follows a standard pump-probe setup, and its methodology can be summarized as follows. At a previously-selected  $h\nu$ , an ultrafast femtosecond laser pump pulse is applied to photoexcite the anion ground state to an excited state. After some time, an ultrafast probe pulse is applied to photodetach an electron. Temporal resolution of the photoelectron spectra is available upon varying the delay time between the two pulses, with the photoelectron spectrum consequential of the difference in energy between the neutral ground state and the excited potential energy surfaces as a function of the nuclear dynamics. Though TR-PES has proven to be a very sensitive technique necessary to study the electronic configuration and vibrational dynamics of a range of systems,<sup>[197]</sup> sunscreens in their ionic states have been relatively less studied to date.

In first aligning with the idea of devising a ‘bottom-up’ approach to uncover the excited state features of such natural photoprotective systems, the study progresses to ‘deconstruct’ the molecule, providing insight into the intrinsic properties of the primary class of sinapate esters (or sinapates), and later increasing the complexity of the ester side chain attached to the sinapate group, towards that of the structure of sinapoyl malate. Methyl sinapate (MS; Figure 5a), a chromophore also known to protect plants from UV-B radiation, is perhaps one of the most well studied of the systems in our repertoire of artificial and natural sunscreens. All considered, MS has been explored on a number of occasions in comparative gas- and solution-phase studies designed to uncover the structure-dynamics-function relationships of such plant sunscreen derivatives.<sup>[124,150,198–</sup>

<sup>200]</sup> Gas-phase TRIY transients of MS have shown a three-component deactivation process

after photoexcitation that occurs within a 1.3 ns timescale: internal vibrational energy redistribution (IVR) following photoexcitation to the  $S_1$  state ( $< 3$  ps); intersystem crossing (ISC) between the  $S_1$  and  $T_1$  states (30 ps); and relax preferentially back to the ground  $S_0$  state at a timescale beyond the means of the experiment ( $> 1$  ns).<sup>[150]</sup> Complementary transient absorption studies subsequently show that MS is likely excited to the  $S_1$  ( $1^1\pi\pi^*$ ) state where both the MS geometry and solvent shell undergo geometry rearrangement.<sup>[150]</sup> Notably, MS then predominantly undergoes *trans-cis* isomerization along the aliphatic C=C bond of MS *via* a  $1^1\pi\pi/S_0$  CI (3 ps) before vibrationally cooling to give the ground-*cis* state. Excess populations of MS (that do not follow the isomerization route) relax *via* vibrational energy transfer to the surrounding solvent (9 ps) to reform the *trans*-isomer. These experiments, having been applied *via* both gas- and solution-phase techniques, allow us to fully appreciate the influence environment can have on the photoprotective properties of a UV filter, and allow us to understand the potential relaxation mechanisms that a sunscreen undergoes in more ‘simplistic’ isolated environments.

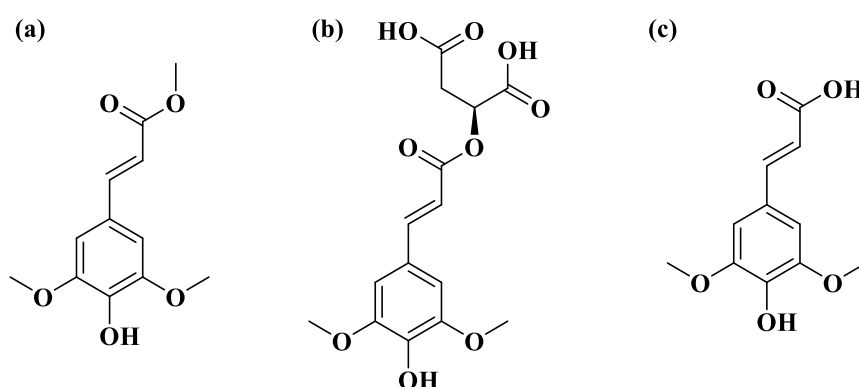


**Figure 5.** Schematic structures of (a) methyl sinapate (MS), (b) sinapoyl malate (SM), and (c) sinapic acid (SA).

R2PI on MS has also been performed by Fan *et al.* (2021),<sup>[124]</sup> which closely links to that of earlier work conducted by Tan *et al.* (2014) on octyl methoxycinnamate (OMC; Figure 6a) and its precursor methyl-4-methoxycinnamate (MMC; Figure 6b) which have been comprehensively reviewed,<sup>[125,201]</sup> but will be again addressed in passing to support the comparative nature of more recent literature on MS. Using a two-color R2PI excitation scheme, the authors propose that the electronically excited  $V(\pi\pi^*)$  state is the lowest

excited singlet state in MS, with ISC likely occurring by spin-orbit coupling of the  $V(\pi\pi^*)$  {HOMO  $\rightarrow$  LUMO} state to a higher lying  $^3n\pi^*$  state.<sup>[124]</sup> This heavily contradicts the picture previously painted for cinnamate-based systems (*i.e.*, OMC and MMC) where the  $S_3$  ( $^1n\pi^*$ ) state is found to be an adiabatically lower electronically excited state, with the higher  $^3\pi\pi^*$  state lying close in energy.<sup>[125]</sup>

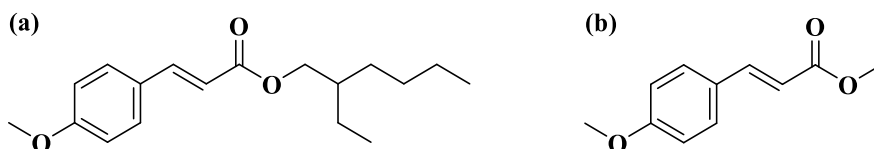


**Figure 6.** Schematic structures of (a) octyl methoxycinnamate (OMC) and its precursor (b) methyl-4-methoxycinnamate (MMC).

(Such orderings of the states allow for ISC to occur on a picosecond timescale *via* a  $^1n\pi^*$  to  $^3\pi\pi^*$  channel that is available following the IC of the “bright”  $^1\pi\pi^*$  to the optically “dark” excited  $^1n\pi^*$  state.)<sup>[153,202]</sup> This route is a major decay pathway in OMC and MMC which impedes the fast electronic energy dissipation required from that of an effective sunscreen molecule. In both investigations, (micro)solvation of the molecule(s) in question have provided valuable insights into how the electronic structure and excited-state relaxation mechanisms of such systems are influenced by solvent-solute interactions. This  $n\pi^*$  bottleneck is ostensibly removed upon microsolvation of MMC (*i.e.*, MMC–H<sub>2</sub>O), revealing that the ordering of the  $n\pi^*$  and  $V'(\pi\pi^*)$  states can be reversed by their solvatochromatic properties, where polar solvents stabilize  $^1\pi\pi^*$  states but destabilize  $^1n\pi^*$ . MMC–H<sub>2</sub>O thus undergoes rapid IC from the  $^1\pi\pi^*$  state to the electronic ground state, somewhat mediated by isomerization of the *cis-trans* double bond occurring on a picosecond timescale. Still, MS displays similar decay rates (*ca.* 20-30 ns) to what has been reported for sinapate-, coumarate-, ferulate-based systems, in line with the idea that decay occurs from the lowest triplet state which arises from the HOMO  $\rightarrow$  LUMO excitation and adopts perpendicular vinyl bond geometry.<sup>[124]</sup> Consequently, the authors also observe considerably slower decay rates of  $V(\pi\pi^*)$  vibronic levels (*ca.*  $10^9$  s<sup>-1</sup>) and competition with direct IC pathways to the ground state. Large shifts in excitation energy show MS–H<sub>2</sub>O to favorably form complex hydrogen bonds of with the carbonyl group and the CH of the propenyl group. Photoexcitation of MS–H<sub>2</sub>O is revealed to lead to the

rapid dissociation of MS from its  $V(\pi\pi^*)$  state to populate the lowest triplet state which decays on a nanosecond timescale to the electronic ground state (as also seen for isolated MS). Insight from ultrafast TEAS infer that the absence of a triplet nanosecond transient in solution is the result of ISC being a relatively inefficient decay pathway when MS is solvated in one single water solvent molecule (*i.e.*, microsolvation) than when it is in isolated ‘gas-phase’ conditions.<sup>[124]</sup> Notably, this notion that any harmful long-lived reactive electronically excited states observed in the gas phase are likely quenched in “bulk” sunscreen environments afford the intuitive use of MS within such formulations. Collectively, the studies by Tan *et al.* and Fan *et al.* adopt a great combination of time- and frequency-resolved methods needed to highlight the dramatic influence that the addition of just one water of molecule can do to the excited-state lifetimes of UV filters. Such work alludes the future directions for sunscreen research, including investigations of which address the behavior of multiple sunscreen aggregates, and which inform the behavior of such molecules following complexation with common cosmetic solvents (to in time successfully rationalize that of the solute-solvent interactions found within marketable formulations).

Further gas-phase studies of OMC employing transient TRIY have also demonstrated the presence of a long-lived lifetime upon UV photoexcitation, associated with a long-lived  $^1n\pi^*$  state, with Peperstraete *et al.* having extended such studies to show the influence of non-polar (*i.e.*, cyclohexane) solvents effectively reorder the excited states to allow for ultrafast photoisomerization,<sup>[153]</sup> an idea similarly depicted in studies of ethyl ferulate.<sup>[151,152]</sup>

Justly, earlier efforts principally from Dean *et al.* (2014) utilizing vibrationally-resolved UV spectroscopy, afforded by cooling the molecules in a supersonic expansion, largely inspired a whole of array of laser spectroscopy work done in the field as of late.<sup>[122]</sup> Parallel gas-phase methods have been extended to encompass a wider scope of UV filters, with R2PI spectroscopy, UV-UV HB spectroscopy, and resonant ion-dip infrared IR spectroscopy (RIDIRS) collectively applied to explore the UV spectroscopy of linked natural sunscreens namely sinapic acid (SA) and sinapoyl malate (SM), as structurally depicted in Figure 5, highlighting the potential of their isolated forms to exhibit properties that rationalize their ability to function as a natural ‘plant’ UV-B suncreening agent. Relevantly, SM is the major sinapate ester found in the leaf epidermis of adult Arabidopsis flowering plants, is shown to exhibit a distinctly broad, featureless spectrum extending to  $> 1000 \text{ cm}^{-1}$  in the UV-B. On increasing the intricacy of the simpler analogues, it becomes

evident that the excited state nature of SM likely results from the excited state (vibronic) mixing of the bright  $V(\pi\pi^*)$  state with the nearby (background)  $n\pi^*$  state which inherently demonstrates significant charge-transfer character in the UV-B spectral region.<sup>[122]</sup> Complementary condensed-phase studies (*i.e.*, in aqueous solution) also show that their gas-phase observations are also seen in solution. The  $\pi\pi^*$  transition of SM allows for a broad absorption efficiency, and produce a geometry change between the  $S_0$  and  $S_1$  states that leads to long Franck-Condon progressions involving low-frequency modes to produce excitation spectra that favorably extends across the UV-B. By upping the complexity of the ester side chain, the excited state mixing of the  $V(\pi\pi^*)$  and  $n\pi^*$  states, coupled with the congested UV spectrum of sinapates) encourages such the broadening of their UV spectra. Baker *et al.* have since gone on to uncover the relaxation mechanisms of SM and SA in the solution phase (*i.e.*, TEAS) across a range of solvents, leading the demonstrating towards the idea that the primary relaxation mechanisms of such derivatives first requires the internal conversion of the photoexcited  $1^1\pi\pi^*$  state along a *trans-cis* photoisomerization coordinate.<sup>[150]</sup> Luo *et al.* later reapplied TEAS and TD-DFT calculations on their deprotonated equivalents (to account for more physiological environmental conditions), finding that their  $\pi\pi^*$  states again relax to their ground states *via* an ultrafast barrierless *trans-cis* isomerization pathway.<sup>[203]</sup>

Chromophore systems with a *para*-hydroxycinnamate moiety are often found in nature, either as a photoswitching unit in photoactive yellow protein (PYP), or more fittingly, as a sunscreen in the leaves of plants. Cinnamates are commonly able to absorb UV radiation, and safely convert the absorbed energy *via* an ultrafast IC pathway (along an  $E \rightarrow Z$  coordinate).<sup>[147,151,153]</sup> Lately, anion PES combined with frequency- and angle-resolved photoelectron imaging has been employed to probe the higher lying excited-state dynamics of the methyl ester anions ( $p\text{CEs}^-$ ) of deprotonated *para*-coumaric acid ( $p\text{CA}$ ),<sup>[204]</sup> notably the simplest of the *para*-hydroxycinnamate family. Deprotonation of  $p\text{CA}$  forms either the monoanion (a) phenoxide [*i.e.*,  $p\text{CEs}^-$ ], or the (b) carboxylate [*i.e.*,  $p\text{CEt}^-$ ] deprotomer as illustrated in Figure 7.

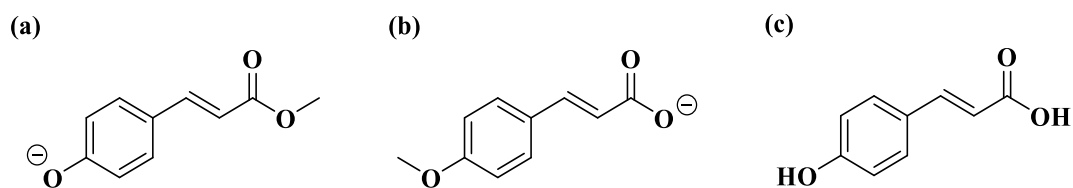


**Figure 7.** Schematic structures of the (a) phenoxide [*i.e.*,  $pCEs^-$ ] and (b) carboxylate [*i.e.*,  $pCEt^-$ ] deprotonomers, and (c) *para*-coumaric acid.

Photodetachment action spectra of the deprotonomers reveal deprotonation site significantly effects the fingerprint of the excited-state dynamics. Firstly, the  $pCEs^-$  deprotonomer (with absorption bands observed at *ca.* 2.88, 3.30, and 4.1 eV for its  $S_1(\pi\pi^*)$ ,  $S_2(n\pi^*)$ , and  $2^1(\pi\pi^*)$  states, respectively) is unable to return to its ground electronic state *via* IC and cannot subsequently undergo  $E \rightarrow Z$  tautomerization *via* a CI. Frequency-resolved PES measurements of  $pCEs^-$  reveal photon energies above the  $S_1(\pi\pi^*)$  state exhibit vibrational autodetachment, with some autodetachment arising from a dipole-bound state. (Briefly, autodetachment is a multi-step process whereby an anion absorbs a photon to an excited anionic state which lies above the threshold for electron detachment, ejecting an electron in the process whilst transferring to the neutral ground electronic state.) They show that the  $S_2(n\pi^*)$  state can undergo efficient IC to the  $S_1(\pi\pi^*)$  state at photon energies resonant with the Franck-Condon and Herzberg-Teller modes. Excitation to the  $2^1(\pi\pi^*)$  state also shows *ca.* 20-40% of its population internally converting to the  $S_1(\pi\pi^*)$  state and conclude that the barriers on the  $S_1(\pi\pi^*)$  state hinder the manifestation of IC to the electronic ground state and associated  $E \rightarrow Z$  tautomerization to needed provide a stable photoisomer. The excess vibrational energy deposited on the  $S_1(\pi\pi^*)$  state upon photoexcitation and IC from either the  $S_2(n\pi^*)$  or  $2^1(\pi\pi^*)$  state is inefficient at helping overcome such barriers prior to autodetachment, with the ground state recovery of  $pCEs^-$  proving inefficient relative to autodetachment occurring in the gas phase.  $pCEt^-$ , on the other hand, reveals efficient ground-state recovery dynamics when photoexcited over the first two absorption bands [at *ca.* 3.6 { $S_1(\pi\pi^*)$ } and 3.93 eV { $S_2(\pi\pi^*)$ }, respectively]. In supposing that  $pCEs^-$  have the same excited-state dynamics as the PYP thioester chromophore in the gas phase, the lack of ground-state recovery suggests that the protein's binding pocket environment in PYP is the major source of PYP photochemistry.

The photophysics of the UV-A sunscreen menthyl anthranilate (MenA; Figure 8a) and its precursor methyl anthranilate (MA; Figure 8b) have also been probed using TR-IY and TR-PES spectroscopies (*in vacuo*) and supported by TEAS (in solution).<sup>[145,172]</sup> Photoexcited MenA and MA have been observed to (undesirably) relax *via* radiative decay, questioning the mass inclusion of MenA within commercial sunscreen formulations on the market today.

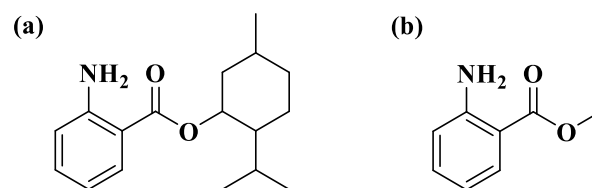


**Figure 8.** Schematic structures of (a) menthyl anthranilate (MenA) and its precursor (b) methyl anthranilate (MA).

Gas-phase experiments yield mono-exponential TR-IY transients for both molecules, confirming their long-lived decay lifetimes ( $> 1.2$  ns) *in vacuo*. In solution, they show a similar decay mechanism, with the existence of triplet states in both MA and MenA implicating dominant instances of luminescence (*i.e.*, fluorescence). Regardless of environment (gas/solution, and thus any resulting solvent-solute interactions), pump wavelength (315 nm *vs.* 330 nm, and 300 nm for MA), or solvent polarity (cyclohexane *vs.* methanol), both MA and MenA are seen to display long-lived excited states for  $> 1$ -2 ns. Fast relaxation pathways from the  $S_1$  state are not present, as shown by the long-lived photodynamics, in line with the idea that the  $S_1$  state “trapped” the photoexcited population. Molecular quantum beat spectroscopy, used in conjunction with TR-PES, often provides useful information on intramolecular state couplings, as well as the dynamics of the energy redistributions on polyatomic molecules. Using TR-PES to observe the quantum beats of MA and probe the energy redistribution mechanisms upon photoexcitation, intramolecular vibrational energy redistribution (IVR) / ISC was found responsible for “trapping” the excited state population of MA (and by structural resemblance, MenA) in the  $S_1$  state, thwarting its efficient coupling to the overall reaction coordinate. Specifically, such observations revealed that MA was unable to overcome the energy barrier (*ca.* 0.4 eV) enroute the possible  $S_1/S_0$  CI, as shown previously in related time-resolved studies of MA.<sup>[145]</sup> Ordinarily upon accessing the  $S_1$  state, excited-state

hydrogen migration along the N–H---O hydrogen bond into the tautomeric form of MA ensues, followed by the internal rotation around the out-of-plane  $C_{\text{ring}}=C_{\text{carbonyl}}$  twist coordinate. Where only the lowest vibrational levels of MA are populated at  $\lambda_{\text{pump}} = 348$  nm, IVR is not observed. Comparably, at  $\lambda_{\text{pump}} = 330$  nm, the long excited-state lifetimes observed at wavelengths above the excited state barrier are sought to be the result of IVR (as justified through a rapid ‘dampening’ of beats), and IVR is thereby expected to allow for the prompt redistribution of population on the  $S_1$  state. In line with this, increasing the density of states (*i.e.*, through the addition of a methyl to achieve the sunscreen analogue MenA) in turn is observed to decrease the IVR lifetime. The efficient relaxation ( $S_1 \rightarrow S_0$ ) of MA’s electronic excited states is thereby heavily hindered by ultrafast IVR mechanisms at the shorter wavelengths of the UV-A region, with compelling evidence stressing that MA is unable to facilitate any means of rapid, non-radiative decay necessary to afford adequate photoprotection within a sunscreen. VMI is often employed to monitor any hydrogen atom elimination following photoexcitation and in the case of MA, VMI (utilizing a 243 nm probe wavelength) was used to confirm the lack of formation of a single-photon-induced N–H<sub>free</sub> bond fission along a dissociative excited state.<sup>[172]</sup> This was further backed by computational studies which confirmed a large barrier to the N–H<sub>free</sub> bond fission relative to the  $S_1$  state minimum.

### 1.3 Laser Photodissociation Mass Spectrometry

Whilst the specific experimental particulars regarding each of the studies included in this thesis will be relayed in their relevant manuscripts and with their respective decks of supporting information, it is important to first offer an abridged description of the technique of laser-interfaced mass spectrometry (LIMS).

The experimental aspects of the articles presented within Chapters 2-5 were performed primarily on an amaZon SL dual funnel electrospray ionization quadrupole ion trap (ESI-QIT) mass spectrometer (Bruker Daltonics, GmbH, Germany). This commercially-available amaZon mass spectrometer is coupled with an ESI source, and provides the ultimate ion trap mass resolving power, with up to 20,000 in full scan mode, across the  $m/z$  50-3000 window. ESI thereby allows for the analysis of small, polar ions (*e.g.*, sunscreens, vitamins, and nucleobases) with very high levels of sensitivity, a considerable extension from its initial success in earlier studies where Fenn *et al.* (who later shared the 2002 Nobel Prize in mass spectrometry with Koichi Tanaka and Kurt Wuthrich) groundbreakingly utilized ESI to show that multiply charged ions were obtained from proteins.<sup>[205]</sup> Whilst sustaining all the benefits of a commercial mass spectrometer, the amaZon has since been modified to allow for the integration of a tunable pulsed laser.<sup>[206,207]</sup> This laser is set up to pass through the QIT, permitting the recording of gas-phase UV-visible absorption and photodissociation spectra, as will be outlined in greater detail in Chapters 1.3.2-1.3.3.

Solutions are generally introduced into the amaZon using a syringe (1.0 mL; Gastight Syringe Model 1001 TLL, PTFE Luer Lock from Hamilton, Reno, Nevada, US, or SGE Analytical Science, Trajan Scientific and Medical, Victoria, Australia), and a single syringe infusion pump (KDS 100 Legacy Syringe Pump, KD Scientific, MA, USA), whereon the mass selected ions (and/or complexes) are subjected into the gas phase *via* ESI. The ion signal intensity on a mass spectrum is conventionally optimized for a particular  $m/z$  ratio using the automated tuning capabilities available *via* trapControl (version 7.2; Bruker Daltonics). This commercially software can also be used to govern the conditions of the ESI source (*e.g.*, ESI voltages; nebulizing gas pressure; drying gas flow rate; and drying-gas temperature), the operation of the QIT (*e.g.*, ion accumulation time; mass isolation), the ion optics, and the settings of its ion fragmentation capabilities. As will be drawn upon later, the trapControl software (version 7.2; Bruker Daltonics) has also lately been adapted to allow for LabVIEW to automate the collation of photodissociation data.

### 1.3.1 Electrospray Ionization Mass Spectrometry

ESI-MS is a soft ionization technique used extensively to produce the gas-phase ions of large, thermally labile molecules.<sup>[208]</sup> Soft ionization techniques, in this sense, allow for the ionization of molecules without fragmenting them, allowing weak non-covalent interactions to be presented when introduced into the gas phase.<sup>[209]</sup> An ESI ion source is used here within our amaZon mass spectrometer, operating under atmospheric conditions. Notably, as depicted in Figure 9, four differentially-pumped vacuum stages are necessary to account for the difference in pressure in the QIT region of the mass spectrometer which tends to operate at a pressure of  $\sim 10^{-6}$  mbar. Once inside the spray chamber, analyte ions move towards the vacuum chamber and on towards the QIT through a double-stage ion funnel, two multipole ion guides, and two ion lenses. Such ions are then methodically exploited *via* means of photo- or thermal dissociation in the QIT, and mass-selectively ejected. A Daly conversion dynode detector is subsequently used to detect the ions.

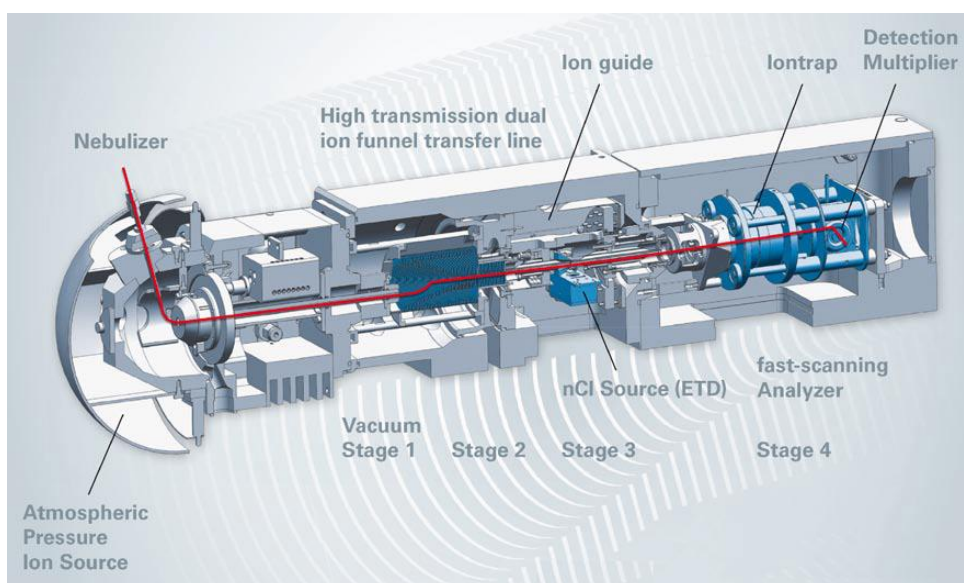
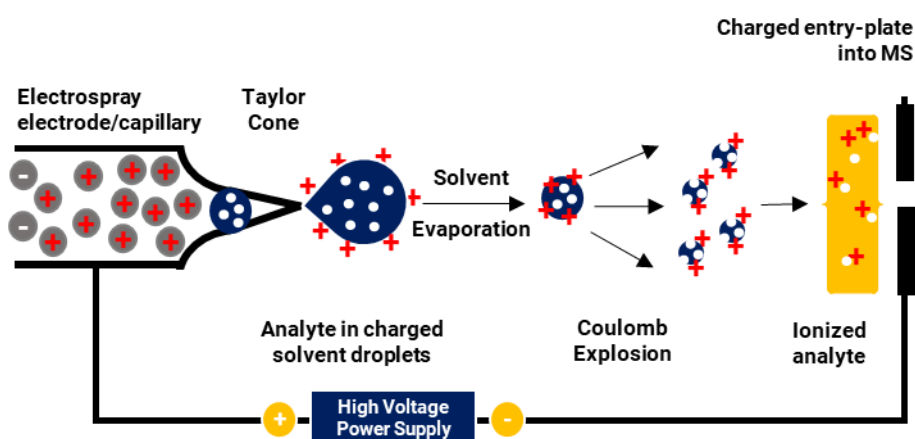


**Figure 9.** Diagram of the key components found within the nebulizer-assisted Bruker amaZon quadrupole ion trap (QIT) mass spectrometer. Image taken from the Bruker Daltonics amaZon series User Manual (Revision 1), November 2009.<sup>[210]</sup>

In practice, ionic species in their solution-phase are first infused into an inlet capillary with a weak flux (*ca.* 1-10  $\mu\text{L}/\text{min}$ ) where the tip of the metal capillary is held at an electric

potential of between  $\pm 2\text{-}6$  kV, generating an electrostatic field (on the order of  $10^6$  V/m) in the electrospray chamber.<sup>[211]</sup> As a solution travels through the charged needle, the needle will proceed to attract and accumulate ions of a particular polarity at the liquid surface located at the tip of the capillary and repel oppositely-charged ions. Ions repelled from the needle become increasingly charged-concentrated as it passes through the needle. Scheme 1 presents a schematic depiction of the conventional nebulizer-assisted ESI source.



**Scheme 1.** Schematic depiction of the electrospray ionization (ESI) process in the positive ion mode.

At the tip of the electrospray capillary, the charge-concentrated analyte solution is distorted into a so-called Taylor cone (see Scheme 1),<sup>[212,213]</sup> which subsequently emits a fine spray of highly-charged droplets, with a nebulizing gas (*i.e.*, dry nitrogen) injected coaxially at a low flow rate to assist droplet formation and direct the spray towards the mass spectrometer. The droplet inevitably explodes when the force of Coulomb repulsion exceeds the surface tension, producing smaller droplets which are liable to evaporate further. Where the total Coulombic repulsion reaches the same level as the surface tension of the droplets is defined as the Rayleigh limit.<sup>[214]</sup> Notably, Gomez and Tang have advocated that the breakdown of such droplets can take place prior to this limit, given that these droplets are mechanically ‘deformed’, reducing the repulsion necessary to disturb the droplets. Such droplets undergo fast solvent evaporation in a region maintained in a vacuum, causing the charge density of the droplet to increase as the droplets shrink. A drying gas (*i.e.*, nitrogen) is used to heat the highly-charged droplets in the gas phase. As

the solvent molecules evaporate, the distance between ions of the same polarity decreases, and in turn increase the level of Coulombic stress within the droplet, subsequently resulting in the exploding of the droplets again. Repeated evaporation and fission eventually yield the formation of a collection highly-charged ESI droplets, which allow for the analyte ions of such species to be detected *via* the mass spectrometer and be introduced into the gas phase.<sup>[215,216]</sup> It is also important to note that when working in the positive ion mode, only positively charged aerosols are formed (*i.e.*, protonated ions); conversely, negatively charged aerosols are produced in the negative ion mode (*i.e.*, deprotonated ions).<sup>[211]</sup>

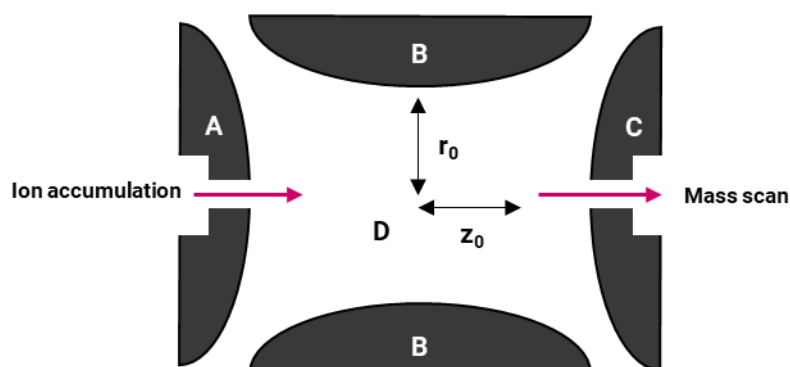
Low-mass analyte ions are notably considered to be transferred into the gas phase *via* the well-established ion evaporation model (IEM);<sup>[216–218]</sup> notably, the systems studied within the following Chapters are considered to be relatively low in mass and are thought to follow that of the IEM.<sup>[219]</sup> This model, proposed by Iribarne and Thomson,<sup>[216,218]</sup> is based on the notion that the electric field originating from the Rayleigh-charged nanodroplet is high enough to cause the ejection of solvated ions from the surface of the droplet. Distinctly, heavier globular species (*i.e.*, natively folded proteins) are thought to follow the charge residue model (CRM) into the gas phase.<sup>[220–222]</sup>

### 1.3.2 Quadrupole Ion Trap Mass Spectrometry

Our amaZon QIT mass spectrometer provides a highly sensitive and reliable tool for studying the photodissociation of photoactive systems. The quadrupole itself homes four parallel cylindrical metal rods (electrodes with a hyperbolic interior surface), as sketched in Scheme 2. Within this system, the opposite ring electrodes demonstrate the same polarity (*i.e.*,  $\Phi$ ) and adjacent end cap electrodes, the opposite polarity (*i.e.*,  $-\Phi$ ), and house a constant direct potential ( $U$ ) and an alternating radio frequency (RF) potential ( $V_0 \cos \omega t$ ). The equations of motion that classically govern the path of the ions within the ion trap describe a series of oscillations in the electric field used to (de)stabilize ions as they pass through the RF quadrupole field and are notably  $U$ - and  $V$ -dependent.<sup>[223]</sup>

By operating the quadrupole in a “stable” region, the ions follow the path set out between the rods until they approach that of the detector. A typical mass spectrum is scanned through varying  $U$  and  $V_0$ , allowing for the ratio of  $U/V_0$  to remain constant.<sup>[223]</sup> Unambiguously, the QIT in the amaZon mass spectrometer uses only an RF voltage (*i.e.*,  $U = 0$ ). In this sense, as only ions with a selected  $m/z$  value exhibit a stable ion trajectory

(*i.e.*, where the position of the ion does not axially or radially exceed the distance between the center of the QIT and the electrodes), QITs will typically offer a  $m/z$  range to which this can be achieved (*i.e.*, the introduction of a low mass cut off).



**Scheme 2.** Schematic cross-section of the quadrupole ion trap (QIT) mass spectrometer as adapted from the Bruker amaZon manual.<sup>[210]</sup> Notably, A = entrance of the end cap; B = ring electrode(s); C = exit end cap; and D = ion cloud and buffer gas (*i.e.*, helium).

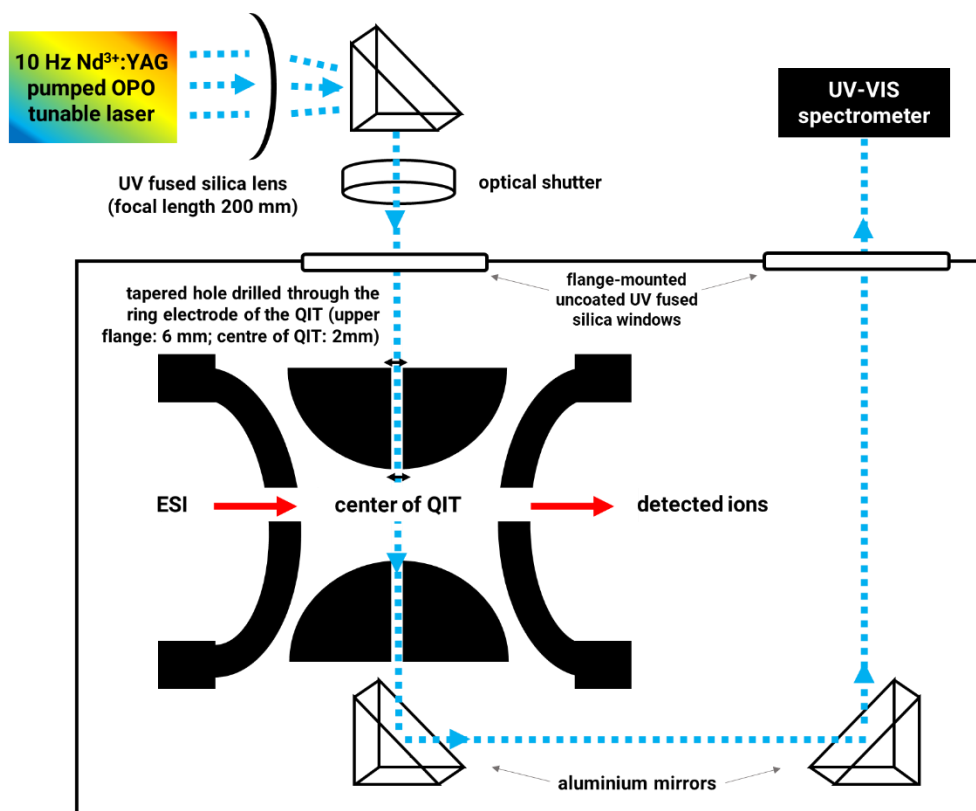
In practice, a mass spectrum is generated after the ions produced in the ESI source enter the QIT *via* its entrance end cap electrode. For the most part, the trapControl software controls the experimental conditions optimized for each experiment, responsible for the clearing of the trap, accumulation, isolation, fragmentation, and finally the mass analysis steps. As ion trap operations are controlled by varying voltages of primary and auxiliary RFs, various voltages are next applied to each of these electrodes, forming a void within the 3D multipolar field where the ions are accumulated and trapped. Due to the collisions of such ions with buffer gas (*i.e.*, helium), the ions themselves then lose kinetic energy and become primarily focused within the center of the trap. Such ions oscillate within the center and produce an ion cloud typically *ca.* 2 mm in diameter. To eject the ions from the trap, the ring electrode RF potentials proceed to produce a 3D quadrupolar RF potential which enables ions to travel in the  $z$ -direction with an oscillatory motion in the  $xy$  plane, allowing ions to be scanned by varying DC/RF quadrupole voltages. Such voltages can be adjusted to ensure that the amplitudes of oscillation for target  $m/z$  ratios are stable within the ions travelling along the  $z$ -axis and can reach the detector of the mass spectrometer. This largely boosts sensitive and reliable mass selectivity, especially since only ions with a select  $m/z$  ratio will reach the appropriate resonance amplitude and demonstrate the correct oscillatory pathway in the RF field.

### 1.3.3 Gas-Phase UV-visible Photodissociation Spectroscopy

As it has been alluded to earlier, the gas-phase UV-visible laser photodissociation experiments highlighted within the upcoming Chapters were conducted in an amaZon ESI-QIT mass spectrometer, which has specially been adapted to allow for laser-coupling. The modifications made to the QIT that enable the linking of a pulsed laser to our amaZon mass spectrometer have been drawn up in great detail elsewhere,<sup>[224]</sup> but a fleeting drive-by of the modifications will be issued here.

Two holes were bored through the edge of the QIT ring electrode designed to sit directly underneath two uncoated UV fused silica windows situated on the upper vacuum flange of the mass spectrometer, and sealed by a KF-16 centering ring, O-ring, and vacuum flange to avert air from escaping in/out of the high-vacuum chamber of the amaZon mass spectrometer (Scheme 3). Here, the first of the two windows lie directly above the QIT, aligning with the first tapered hole machined into the ring electrode. This allows for the laser beam to pass through the first window, and into the QIT. The tapering of both holes, as depicted in Scheme 3, allows for the flow of the buffer gas (*i.e.*, helium) out of the QIT to be optimized.

To simplify the alignment of the laser beam through the QIT, an aluminum mirror (PF05-03-F01, Thorlabs, Inc.) that reflects across the 200-2000 nm spectral range is conveniently positioned below the QIT and stands to reflect the incoming laser beam towards a partnering mirror which then reflects the photons out of the vacuum chamber and through the second window. Accordingly, a laser bench housing the optical components of our setup was fitted to park on the top of the mass spectrometer to allow for our approach of gas-phase laser-interfaced mass spectrometry (LIMS) to be employed. Other apparatuses will be outlined shortly.



**Scheme 3.** Schematic of the recent modifications made to the quadrupole ion trap (QIT) mass spectrometer to allow for gas-phase photodissociation spectra to be recorded. The location of the tapered hole (upper flange: 6 mm; center of QIT: 2 mm) drilled through the ring electrode of the QIT, to allow for the coupling of the laser, is illustrated within. Other notable components include: the  $\text{Nd}^{3+}$ :YAG pumped OPO tunable laser source; a UV fused silica lens (LE4467-UV, Thorlabs Inc.); a mechanical optical laser shutter (Model SH05, Thorlabs Inc.); flange mounted uncoated UV fused silica windows (WG41050, Thorlabs, Inc.); a pair of aluminum mirrors (PF05-03-F01, Thorlabs, Inc.), and a UV-visible spectrometer (USB2000+ UV-VIS, Ocean Optics Inc.). Scheme adapted from Reference <sup>[224]</sup>.

In solution-phase absorption spectroscopy, absorbance is routinely recorded on a commercial optical spectrophotometer, where the intensity of monochromatic light that passes through the cuvette is measured as each wavelength of light ( $\lambda$ ) passes through the sample. Here, the Beer-Lambert law (Eq. 1.3) aptly states the linear relationship between the absorbance ( $A$ ) and the concentration of a solution ( $c$ ), and molar absorption coefficient ( $\epsilon$ ) and optical coefficient of the solution ( $l$ ):

$$A(\lambda) = \varepsilon(\lambda) \times c \times l = \ln\left(\frac{I_0}{I}\right) \quad (\text{Eq. 1.3})$$

where  $I_0$  and  $I$  represent the intensities of monochromatic light without and upon passing through the sample, respectively. Whilst the abundance of ions (*ca.*  $10^{18}$ ) in a solution allows for one to easily measure the absorption of light from the source, the limitations of the ion trap in the gas phase make for the numbers of ions present to be several orders of magnitudes less than that of solution (*ca.*  $10^5$ ). Upon taking into consideration of the background noise of the laser, it is apparent through gas-phase dissociation experiments that one cannot directly nor easily measure the electronic absorption of a system *via* the depletion intensity of the excitation laser. Instead, the absorption cross sections of the system (Eq. 1.4) are measured by means of “action spectroscopy” – a term notably coined by Kawai *et al.* – where absorption is measured by the photodepletion of gaseous ion intensity, induced by ionic photofragmentation or electron detachment, as a function of the wavelength of incident light:

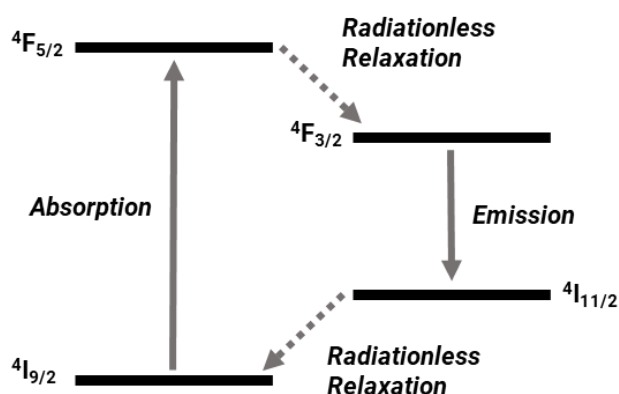
$$I(t) = I_0 e^{-tf \int \sigma(\lambda) \rho(\lambda) d(\lambda)} \quad (\text{Eq. 1.4})$$

where  $I_0$  and  $I(t)$  are the intensity of the ion without irradiation influence and after  $t$  durations of irradiation, respectively;  $f$  is the geometrical overlap factor between the light beam and the ions;  $\sigma(\lambda)$  is the absorption cross section at a defined wavelength; and  $\rho(\lambda)$  is the photon flux as approximated by the average number of photons per laser pulse (and which is proportional to the product of the laser pulse energy and the wavelength of the laser). The integral is over the spectral range of wavelengths used to photodissociate the ions. Should the overlap between the ion packet and a single laser pulse be sufficiently constant across the spectral range, Eq. 1.4 can be simplified and rearranged to give Eq. 1.5:

$$\sigma(\lambda) = \frac{\ln\left(\frac{I_0}{I}\right)}{\lambda \times \rho} \quad (\text{Eq. 1.5})$$

Accordingly,  $I_0$  and  $I$  can be determined through the recording of the parent (precursor) analyte ion(s) without and with irradiation, respectively. Eq. 1.5 has therefore been adapted for use in several instances in Chapters 2-5 as a measure of photodepletion (*i.e.*, the gaseous absorption coefficient) intensity. Laser power measurements are routinely for each new system, carried out to ensure that the ions are only ‘softly’ ionized so that only one-photon absorption takes place. Such measurements are addressed in greater detail within the Supporting Information for each manuscript.

The UV-visible photons optically focused through the ion trap of our amaZon mass spectrometer are selectively generated by a 10 Hz Surelite™ (Continuum) neodymium-doped yttrium aluminum garnet (Nd<sup>3+</sup>:YAG) pumped Horizon™ (Continuum) optical parametric oscillator (OPO). Conventionally, Nd<sup>3+</sup> is in control of the lasing properties of the YAG rod; Scheme 4 highlights the energy levels involved in the emission of NIR (1064 nm) light from the Nd<sup>3+</sup>:YAG laser. Nowadays, flashlamps that surround the YAG rod are often used as an energy source used to supply energy to the active medium (*i.e.*, the crystal of the Nd:YAG).

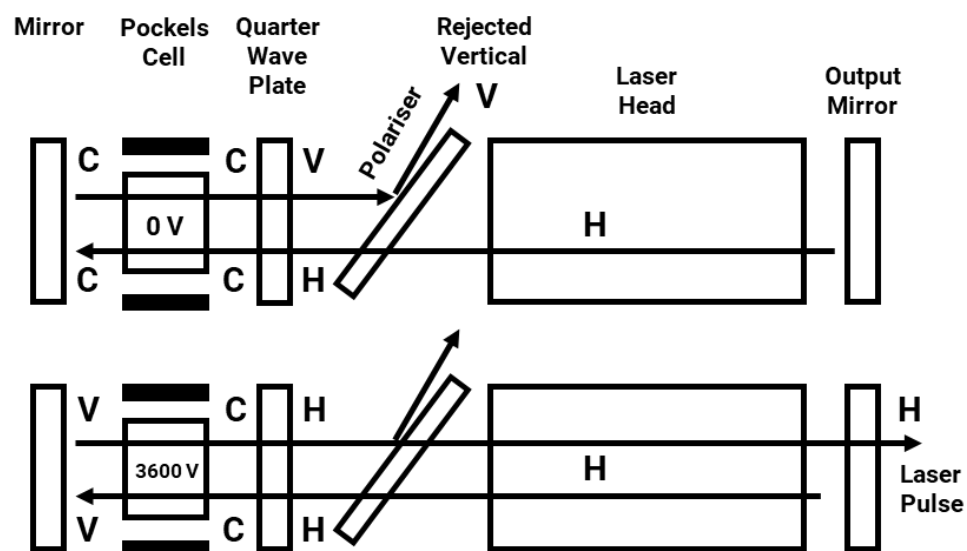


**Scheme 4.** Schematic of the energy levels involved in the emission of 1064 nm light by a Nd<sup>3+</sup>:YAG laser.

Here, the electronic ground state ( $4I_{9/2}$ ) is the lowest energy state and upon absorption of light, the Nd<sup>3+</sup> ions become electronically excited, and moves to the highest electronically-excited energy level ( $4F_{5/2}$ ). As this level is that of an unstable state, and exhibits a short lifespan, the electrons will undergo radiationless relaxation into another (metastable) excited state ( $4F_{3/2}$ ) before emitting that of the 1064 nm photon to reach the  $4I_{11/2}$  state. It

is at this stage where a population inversion is created between these two electronic states in the YAG rod and is where the lasing properties of the Nd:YAG rods originates from. After, since this level ( ${}^4I_{11/2}$ ) exhibits a shorter lifespan, the electrons will once again undergo radiationless relaxation back to the  ${}^4I_{9/2}$  ground state.

The conceptual flow of the Q-switch, which holds the YAG rod and the flashlamps that surround it, controls the release of the laser, as is shown in Scheme 5. A laser pulse is therefore released upon the application of a voltage (*i.e.*, at 3600 V, as depicted in Scheme 5). Frequency doubling is often used to produce a wavelength that is half (or one third etc.) of the fundamental wavelength of a laser (1064 nm); in essence, given this would be that of the wavelengths of 532 and 355 nm, or the second and third harmonics, respectively. The output can often be optimized manually through reorientating the crystals that generate the laser harmonic frequencies. The tunable Horizon OPO can generate mid-band radiation within the visible and near-infrared (IR) regions, pumped by 355 nm light from the Nd:YAG laser, with the UV-visible module of the Horizon offering complete wavelength coverage across from 2750-193 nm (0.45-6.42 eV). The apparatus used within is specially designed to be pumped with a Surelite Nd:YAG, offering the full digital motor control of crystals and wavelength separation for a consistently optimal output. A schematic optical layout of the Horizon OPO is outlined in Scheme 6.



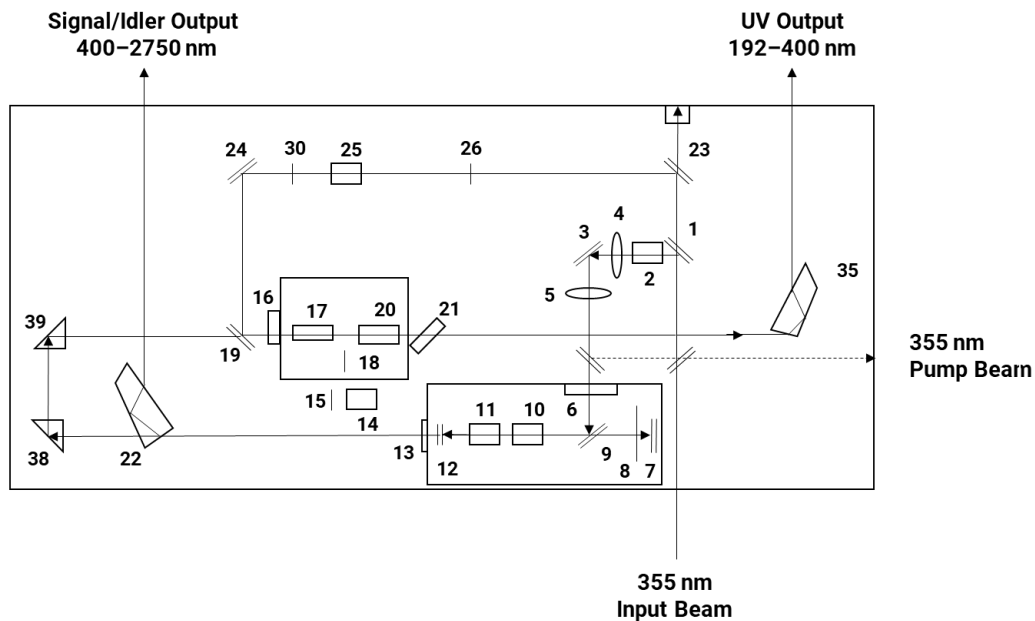
**Scheme 5.** Schematic of the Q-switch used to produce laser pulses in the Surelite Nd:YAG laser. H = Horizontal polarization; V = Vertical polarization; and C = Circular polarization. Image adapted from the Surelite manual.

The optical parametric process is a three-photon interaction whereby a single (pump) photon is split into two low-energy photons. Notably, the higher-energy photon is the signal, and the lower-energy photon is the idler. Eqs. 1.6-1.7 show that the energy of the photon ( $E$ ) and the initial photon's momentum vector ( $k$ ) must be conserved between the two photons that are produced:

$$E_{\text{pump}} = E_{\text{signal}} + E_{\text{idler}} \text{ (Eq. 1.6)}$$

$$k_{\text{pump}} = k_{\text{signal}} + k_{\text{idler}} \text{ (Eq. 1.7)}$$

This process can occur in non-linear optics, where  $\beta$ -barium borate (BBO) crystals are used specifically in the Horizon OPO laser. The angle by which the pump beam makes with respect to the optical axis of the crystal determines the frequencies of the signal and idler that are possible for momentum to be observed. Control of BBO crystal rotation allows for the Horizon OPO to function as a tunable laser source.



**Scheme 6.** Optical layout of the Horizon™ Optical Parametric Oscillator (OPO) laser. [1, 3] mirror, dichroics (355 nm); [2a, 8, 15, 25a, 30] half wave plate; [2b, 14, 25b]

polarizer (355 nm); [4, 5] lens; [6, 13, 16, 21] window; [7] porro prism; [9] injection pump mirror; [10] #1 Crystal BBO Type-1; [11] #2 Crystal BBO Type-1; [12, 19] mirror; [17, 20, 23, 24, 29] crystal, BBO; [18] waveplate; [22, 35] Pelin Broca prism; [26] beam dump assay; [38, 39] prism 90°. Notably, commercial software is available to accompany the Horizon, used to control the output wavelength of the laser and tune the laser power at each wavelength. Step motors are available to control BBO crystal orientation and the Pelin Broca prisms. Image adapted from the Continuum® Horizon™ I and II OPO Operation and Maintenance Manual (P/N: 996-0034, Revision C, 2014).<sup>[225]</sup>

The laser beam is as has been previously described,<sup>[108,206,207,224]</sup> and the optical route taken by the UV (400-193 nm) and visible/NIR (2750-400 nm) photons in the abovementioned experiments between the OPO laser and the optical interface of the amaZon mass spectrometer is as depicted in Figure 10a. To mimic the irradiation wavelengths typically exerted by the sun for sunscreens, the spectral range of this experiment will generally be within the UV-A to UV-C and visible regions, optimized for a sunscreen molecule's absorption maximum as determined *via* steady-state UV-visible spectroscopy.<sup>[107,108]</sup>

In the first instance, following the UV path (Figure 10a), such photons are directed onto the optical bench through a tube connected to the OPO laser, with the height of the horizontal laser beam notably altered accordingly with right-angled UV fused silica prisms to enable for a more practical setup upon re-alignment of the laser. The visible/NIR path (Figure 10b) is similarly adjusted in height to accommodate for user ease and practicality, with the incoming laser beam entrained for the visible/NIR route subsequently overlapped with that of the UV route using a pair of right-angled prisms.

Figures 10a and 10b further outlines the aspect of the setup which permits a power meter to monitor the power of the laser. The movement of the motorized flip mount (re)directing the laser beam towards the power meter or out of the beam is controlled by a home-written LabVIEW virtual instrument (VI), which additionally provides a digital read-out of the laser power throughout the laser experiment.

The mechanical laser beam shutter (Model SH05, Thorlabs Inc.) is triggered by an external transistor-transistor logic (TTL) signal and is connected to a benchtop shutter controller (Model SC10, Thorlabs Inc.) which provides the TTL signal (*i.e.*, 5 or 0 V) necessary to block/transmit the laser beam from the OPO laser into the QIT, respectively.

Typically, the shutter controller is operated in its external gate mode and receives a TTL signal from external interface of the amaZon mass spectrometer.

Other apparatuses include the spectrometer (USB2000+ UV-VIS, Ocean Optics Inc.), which is used to verify the wavelength of the laser at set stages of each run, and two motorized flip mounts (ModelMFF001, ThorLabs Inc.) – one of which is used to redirect the laser beam towards the power meter (Power Detector UP19K-15S-VR, Monitor is a Gentec-EO Tuner) and another which moves a right-angled prism to enable the transmission of UV or visible/NIR light and brings the beam through the main path set out on the laser table.

To effectually generate gaseous absorption coefficients, the mass spectrometer is set to selectively output a signal to open the optical shutter within the fragmentation stage of the QIT cycle, which is optimized and programmed to occur for single isolation (MS) and multiple isolations (MS/MS and MS<sup>n</sup>) of the analyte ion(s). Assuming perfect alignment, this ensures that the laser is only entrained into the QIT at the point where the ion(s) have been adequately isolated and the ion packet stowed for fragmentation, so that the resulting photodepletion and production of photofragments are directly consequential from that of the laser photodissociation process. The fragmentation step is programmed for a 100 ms duration, ensuring that only a single laser shot from the 10 Hz Nd:YAG pumped OPO laser is used to photodissociate the intended ion(s).

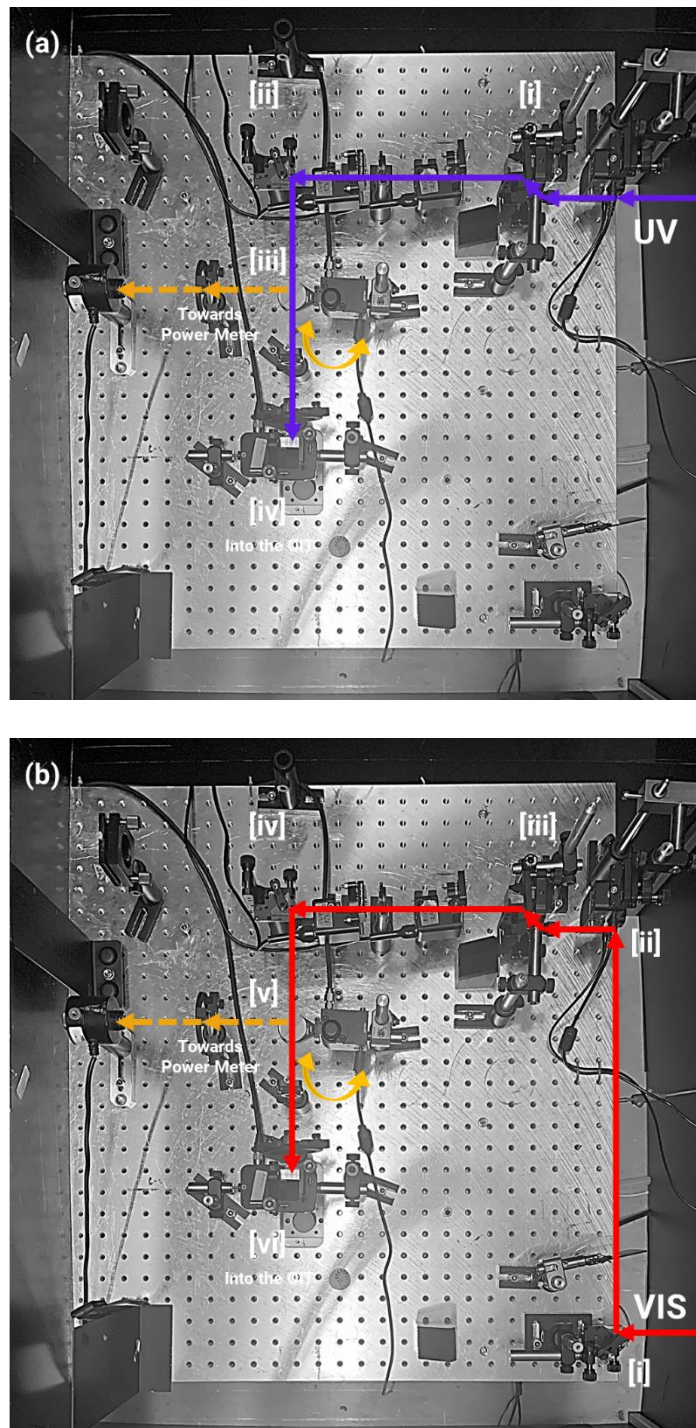
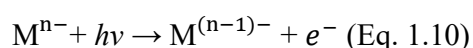
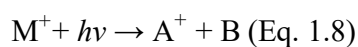


**Figure 10.** Labelled photographs of the laser bench housing the optics, required for UV and visible-NIR wavelengths, located on top of our modified amaZon mass spectrometer. The laser path from the OPO laser to the ion trap is outlined in (a) for UV where [i] the incoming laser beam is first adjusted in height using a pair of right-angled UV-fused silica prisms and then [ii] hits a right-angled prism, allowing for the beam to be reflected by  $90^\circ$  into either [iii] an adjustable right-angled prism (situated on a motorized flip mount) which

allows for the redirection of the beam towards the power meter, or [iv] into the QIT. The route the visible/NIR beam takes are mapped in (b) where the laser is first wrought to overlap with that of the UV path using [i] a right-angled prism. The beam is then redirected into [ii] a corresponding right-angled prism (situated on a motorized flip mount). Following that of the UV route, the height of the incoming visible/NIR laser beam is adjusted at [iii] and reflected at [iv], allowing for the laser to directly hit either the power meter or the QIT at [v] and [vi], respectively. In both instances continuing on to [vi] will allow for the laser to pass *via* an optomechanical laser shutter and a transparent window that bridges the QIT.

As will be discussed comprehensively in the upcoming Chapters, the gas-phase ionic fragmentation patterns of cationic or anionic systems often provide detailed insights into their structural properties. Befittingly, techniques such as photodissociation action spectroscopy (*i.e.*, LIMS) and collision-induced dissociation (CID; see Chapter 1.3.4) are frequently employed to link the intrinsic absorption properties and photodegradation pathways of their ionic forms. Briefly, in LIMS, one is able to derive the gaseous absorption spectrum (*i.e.*, gas-phase photodepletion) of a system through obtaining two mass spectra, *e.g.*, one where the laser is focused into the ion trap (*i.e.*, laser on) enabling fragmentation, and one where the shutter is closed (*i.e.*, laser off). The means by which depletion in the ion intensity of the mass-selected precursor ion induced by the laser is signified by Eqs. 1.8-1.10, representative of the ionic photofragmentation of a cation and anion, and that of electron detachment, respectively.



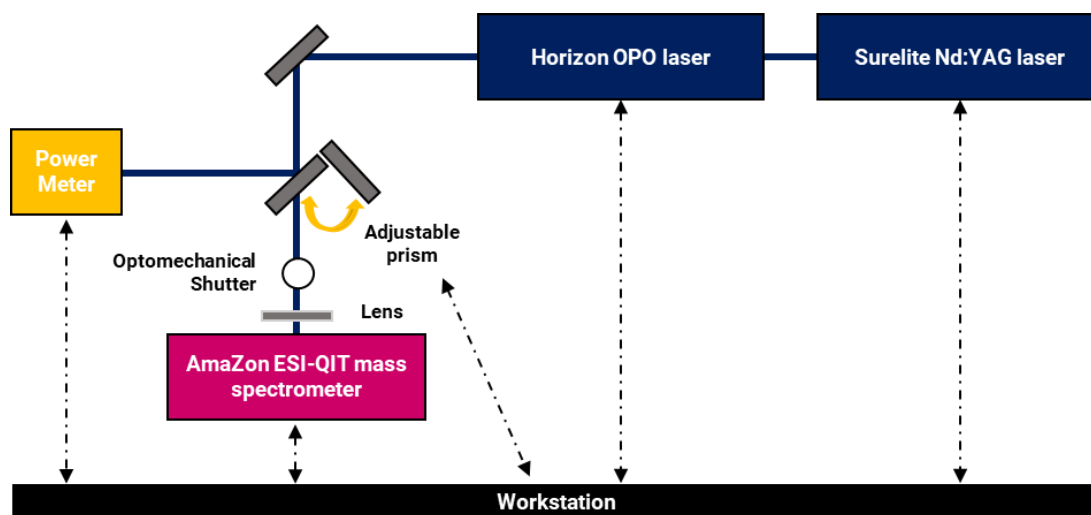
Notably, the production spectra of the ionic photofragments can be mapped to determine their dependence on wavelength (or photon energy). Upon electronic excitation in the gas phase, the ionic fragmentation of such systems can come about *via* two distinct channels. Firstly, either through a dissociative excited-state surface (*i.e.*, accessed vertically or

following relaxation *via* a CI), or secondly, on the hot ground-state surface, accessed *via* ultrafast relaxation from an electronically-excited state through a CI.

Notably, whilst electron detachment can largely contribute towards the gas-phase photodepletion of a system, the extent of electron detachment (*i.e.*, the loss of electrons) is not directly measurable within our amaZon mass spectrometer, given that the resultant photoproducts are not charged ions. Therefore, the electron detachment yield (ED\*) can be indirectly derived, fully assuming that any photodepletion ions that are not detected as ionic photofragments are instead losing an electron, as per Eq. 1.11. As alluded to earlier, fragment ions with a  $m/z < 50$  are not measurable in our experimental set up, as such masses fall outside the mass window of the QIT.

$$ED^* = \frac{(Int_{OFF} - Int_{ON}) - Int_{PFT}}{\lambda \times P} \quad (\text{Eq. 1.11})$$

Whilst the nature of obtaining the ‘laser on’ and ‘laser off’ ion spectra of a single wavelength is considerably accessible, the recording of data across the entire UV and visible spectral region, *i.e.*, from 214-700 nm in 2 nm step sizes, can be laborious. Automation of the main routine for data collection and processing of spectra has been progressively adapted over the years, and now exists as a LabVIEW VI now responsible for the efficient recording of the data, and the repetitive nature of extracting new data alleviated using Bruker Daltonic’s commercial DataAnalysis/AutomationEngine packages (version 4.2) and that of a python script written to oversee such systematic processes. Schemes 7 and 8 are presented to accompany the overarching outline of experimental process utilized to obtain consistently reproducible photodissociation spectra using our instrument.



**Scheme 7.** Simplified schematic highlighting the now-automated workflow of the laser-interfaced mass spectrometry experimental set up.

To scan across a range of wavelengths, the starting wavelength is set *via* the software operating the Horizon OPO laser. Once adjusted, the motorized prism will guide that of the laser beam into the path of the power meter, and the output of the OPO laser adjusted to attune for a suitable laser power (*e.g.*, for the sunscreen systems, laser powers of *ca.* 0.1-0.4 mJ have been sufficient, supported through a series of independent laser power dependence measurements and laser power readings that are recorded at each wavelength to compensate for the depletion in ion intensity for photon flux within the QIT; see Appendices 1-4). Accordingly, once the targeted laser power is met, the adjustable prism will move to allow for the beam to continue on into the path of the QIT where the photodissociation process will ensue. Upon the acquisition of the required ‘laser on’ and ‘laser off’ mass spectra, the adjustable prism will again be adjusted to allow for the power reading of the next wavelength. When the OPO output power is too high, the Q-switch timing (*i.e.*, attenuation time) can also be adjusted using the LabVIEW VI. Alternately, neutral density (ND) filters can be interchangeably utilized to obtain better stability. The ensuing delay times and shot stability can be easily monitored as outlined above. Often if the OPO power is too low (*e.g.*, when the Q-switch delay value no longer produces enough pulse power or shot stability is > 15%), the non-linear optics (NLOs) of the laser will need to be reoptimized. Using the LabVIEW VI (which has been designed to bear the necessary settings of the Horizon software), the second and third harmonic crystals can be adjusted whilst monitoring the output of the Horizon. In most instances, only small adjustments of the third harmonic phase angle are required to reoptimize the output power of the Horizon.

The user-interface of the automated LabVIEW VI is currently set in place to record and monitor our laser photodissociation experiment whilst also efficiently tabulating the experimental parameters used (*i.e.*, laser power and shot stability at a particular wavelength) automatically and systematically. Essentially, the practical design of the front panel of this VI allows for the laser and Q-switch to be turned on/off and timings to be adjusted (*i.e.*, attenuation time); the mechanical shutter to be opened/closed; the output of the Horizon (*i.e.*, stability of the wavelength and amount of laser power) to be read and managed accordingly; the mechanical ND filters to be interchanged; and the motor on the adjustable prism (guiding the laser beam into the path of either the QIT or the power meter) to be activated. Additionally, this LabView VI now incorporates the use of trapControl's front external (auxiliary) interface, which has been automated to trigger particular stages of the QIT cycle (*i.e.*, fragmentation) when deemed necessary (*e.g.*, once the wavelength of the laser has stepped and when a suitable power reading has been obtained and recorded).

### 1.3.4 Collision-Induced Dissociation

Collision-induced dissociation (CID) or collision-activated dissociation (CAD) experiments are an 'ergodic' ion activation method often conducted largely to complement our gas-phase UV photodissociation studies, with its resultant dissociation products (*i.e.*, fragments) aiding in the structural elucidation of our ground-state gaseous ions. Here, tandem mass spectrometry (MS/MS) allows for a mass-selected precursor ion to be 'activated' in a collision cell through sequentially increasing its internal energy. This in turn promotes the homolytic or heterolytic cleavage of the chemical bonds within a system, allowing for the production of various resulting fragment ions. An excitation quadrupolar alternating current (AC) voltage is commonly applied to the end caps of the collision cell (*i.e.*, QIT) to allow the trapped ions to collide with sufficient energy with the buffer gas (*i.e.*, helium). The energy gained is redistributed among different vibrational degrees of freedom within the precursor. More specifically, within that of experiments that incorporate ion traps (*e.g.*, QIT), the kinetic energy of the precursor ion is only able to increase to a level by which stable ion motion is still in place, as defined by the Mathieu equation. As QIT instruments commonly have a projectile translation energy of *ca.* 10-100 eV, low-energy CID is often obtained in such experiments.

Aligning with this concept, higher-energy collisional dissociation (HCD) experiments have also been conducted within this thesis – especially in Chapters 3 and 4 for which the ionic fragmentation patterns of deprotonated 2-phenylbenzimidazole-5-sulfonic acid and benzophenone-4 are explored.<sup>[107]</sup> Though named “higher energy”, HCD is generally performed in the regime of < 100 eV and is fundamentally still classed as low-energy CID. However, in such instances, such HCD experiments typically employ a mass spectrometer with an Orbitrap mass analyzer (*e.g.*, the Thermo Fisher Orbitrap Fusion™, as used in Chapters 3 and 4) whereby its two outer electrode and central electrode system allows for it to act both as a mass analyzer and a detector and for fragmentation to take place external to the trap.<sup>[226,227]</sup> Typically in an orbitrap mass analyzer, pulsed packets of ions produced by a curved linear trap (C-trap) are introduced and captured into the analyzer to get spectral data. For HCD experiments, ions are passed through the C-trap into the HCD collision cell to enable for MS/MS experiments to occur. Rather applicably, HCD measurements have pertinently enabled for us to identify that of secondary products, formed when a precursor species fragments at high internal energy as well as differentiating between that of purely photochemical or thermal fragments.<sup>[107]</sup>

## 1.4 Thesis Overview

This thesis uses four peer-reviewed journal articles as stand-alone chapters, with the details pertaining to each publication addressed in the Author’s Declaration. The contents of the chapters are true to the accepted and published articles; however, minor formatting changes have been made for the sake of completeness and consistency to support the inclusion of the published Supplementary/Supporting Information within the Appendices. In several instances, the references presented within such Chapters will align with the journal’s referencing format at the time of publishing.

Chapter 2 presents the electronic study of the protonated and deprotonated analogues of the model UV filter oxybenzone, which are introduced into the gas phase *via* electrospray ionization mass spectrometry (ESI-MS). The paper offered within represents one of the first studies carried out on an organic sunscreen molecule where we explore in great detail the extent to which the pH environment alters its effectiveness to function as a means of photoprotection. A combination of results from our laser photodissociation studies, collision-induced (thermal) dissociation experiments, and subsequent *ab initio* calculations reveal that the protonation state truly has a dramatic effect on the absorption

and photodissociation properties of oxybenzone in the UV-A to UV-C spectral region and thereby strongly warranted the continuation of research exploring the implications of ionization on sunscreen performance.

Building upon the findings conveyed from that of protonated and deprotonated oxybenzone, Chapter 3 is redirected to focus on the sunscreen molecule 2-phenylbenzimidazole-5-sulfonic acid, a well-known UV-B absorber known to exhibit strong photosensitizing behavior. This work delivers an insight into its 'native' gas-phase deprotonated form and reveals three ionic photoproducts with distinctive wavelength-dependent production profiles. The direct photochemical production of free radicals is observed *via* one channel whilst other pathways establish the characteristics of non-statistical photofragmentation associated with non-ergodic excited-state decay. Such observations ultimately expose its unsuitability to function as an optimal sunscreen molecule.

In recognizing the value of fully understanding how deprotonation influences the photophysical behavior of organic UV filters, Chapter 4 details the measurement of the intrinsic electronic absorption spectra of benzophenone-4 in alkaline environments comparable to that of surface waters, swimming pools, and coral reefs. Seamlessly, benzophenone-4 structurally blends the benzophenone backbone of oxybenzone (Chapter 2) together with the strongly-acidic sulfonic acid group found in 2-phenylbenzimidazole-5-sulfonic acid (Chapter 3), where this hybrid unfalteringly dots the photofragmentation behavior of all three aforementioned UV filters. For the first time for an ionic sunscreen, high-level *ab initio* potential energy surfaces are presented alongside high-energy collisional activation findings and UV laser-interfaced mass spectrometry to map and interpret the relaxation pathways of deprotonated benzophenone-4.

The current position of the on-line UV photolysis cell developed by the author for this Ph.D. is evaluated in Chapter 5, where riboflavin (vitamin B<sub>2</sub>) is used as a prototypical system in the journey to establish a viable means of routinely mapping the solution-phase photodegradation and photofragmentation channels of chromophore systems in real time using high-powered UV light emitting diodes (LEDs) and ESI-MS techniques. Here, the author is able to actively compare the gas-phase LIMS photofragments of deprotonated riboflavin to its solution-phase equivalents, offering exclusive recommendations necessary for the on-going development and promising future of this newly-built device. Fittingly, this proof-of-principle design will additionally form a strong foundation for the

rapid development of more powerful photolysis devices, optimized for the photolysis of organic UV filters that are evidently more photostable in solution than this modeled prototype.

## References

- [1] S. E. Mancebo, S. Q. Wang, *Rev. Environ. Health* **2014**, *29*, 265–273.
- [2] J. J. Neville, T. Palmieri, A. R. Young, *JBMR Plus* **2021**, *5*, 1–15.
- [3] A. A. Brożyna, R. M. Hoffman, A. T. Slominski, *Anticancer Res.* **2020**, *40*, 473–489.
- [4] W. G. M. De Silva, M. Abboud, C. Yang, K. M. Dixon, M. S. Rybchyn, R. S. Mason, **2020**, pp. 227–253.
- [5] O. Engelsens, *Nutrients* **2010**, *2*, 482–495.
- [6] R. B. Weller, Y. Wang, J. He, F. W. Maddux, L. Usvyat, H. Zhang, M. Feelisch, P. Kotanko, *J. Am. Heart Assoc.* **2020**, *9*, e013837.
- [7] V. Kapil, A. K. Gupta, *J. Am. Heart Assoc.* **2020**, *9*, e015627.
- [8] B. I. Veleva, R. L. van Bezooijen, V. G. M. Chel, M. E. Numans, M. A. A. Caljouw, *Photodermatol. Photoimmunol. Photomed.* **2018**, *34*, 288–297.
- [9] G. P. Pfeifer, *Genome Instab. Dis.* **2020**, *1*, 99–113.
- [10] N. Goto, G. Bazar, Z. Kovacs, M. Kunisada, H. Morita, S. Kizaki, H. Sugiyama, R. Tsenkova, C. Nishigori, *Sci. Rep.* **2015**, *5*, 11808.
- [11] S. Premi, S. Wallisch, C. M. Mano, A. B. Weiner, A. Bacchiocchi, K. Wakamatsu, E. J. H. Bechara, R. Halaban, T. Douki, D. E. Brash, *Science* **2015**, *347*, 842–847.
- [12] R. P. Rastogi, Richa, A. Kumar, M. B. Tyagi, R. P. Sinha, *J. Nucleic Acids* **2010**, *2010*, 1–32.
- [13] S. E. Ullrich, *Mutat. Res. Mol. Mech. Mutagen.* **2005**, *571*, 185–205.
- [14] L. Alfredsson, B. K. Armstrong, D. A. Butterfield, R. Chowdhury, F. R. de Gruijl, M. Feelisch, C. F. Garland, P. H. Hart, D. G. Hoel, R. Jacobsen, et al., *Int. J.*

- Environ. Res. Public Health* **2020**, *17*, 5014.
- [15] F. R. de Gruijl, J. C. van der Leun, *CMAJ* **2000**, *163*, 851–5.
- [16] J. D’Orazio, S. Jarrett, A. Amaro-Ortiz, T. Scott, *Int. J. Mol. Sci.* **2013**, *14*, 12222–12248.
- [17] F. R. de Gruijl, J. C. van der Leun, *CMAJ* **2000**, *163*, 851–5.
- [18] B. Diffey, *Int. J. Environ. Res. Public Health* **2018**, *15*, 1112.
- [19] M. K. Vollmer, D. Young, C. M. Trudinger, J. Mühle, S. Henne, M. Rigby, S. Park, S. Li, M. Guillevic, B. Mitrevski, et al., *Atmos. Chem. Phys.* **2018**, *18*, 979–1002.
- [20] M. B. McElroy, R. J. Salawitch, S. C. Wofsy, J. A. Logan, *Nature* **1986**, *321*, 759–762.
- [21] G. Taylor, *Report of the Halons Technical Options Committee.*, Nairobi, Kenya, **1991**.
- [22] S. C. Wofsy, M. B. McElroy, Y. L. Yung, *Geophys. Res. Lett.* **1975**, *2*, 215–218.
- [23] A. F. Bais, R. M. Lucas, J. F. Bornman, C. E. Williamson, B. Sulzberger, A. T. Austin, S. R. Wilson, A. L. Andrady, G. Bernhard, R. L. McKenzie, et al., *Photochem. Photobiol. Sci.* **2018**, *17*, 127–179.
- [24] J. C. Farman, B. G. Gardiner, J. D. Shanklin, *Nature* **1985**, *315*, 207–210.
- [25] M. J. Molina, F. S. Rowland, *Nature* **1974**, *249*, 810–812.
- [26] R. S. Stolarski, R. J. Cicerone, *Can. J. Chem.* **1974**, *52*, 1610–1615.
- [27] M. P. Chipperfield, R. Hossaini, S. A. Montzka, S. Reimann, D. Sherry, S. Tegtmeier, *Nat. Rev. Earth Environ.* **2020**, *1*, 251–263.
- [28] S. S. Dhomse, W. Feng, S. A. Montzka, R. Hossaini, J. Keeble, J. A. Pyle, J. S. Daniel, M. P. Chipperfield, *Nat. Commun.* **2019**, *10*, 5781.
- [29] S. E. Strahan, A. R. Douglass, M. R. Damon, *J. Geophys. Res. Atmos.* **2019**, *124*, 8837–8850.
- [30] R. G. Prinn, R. F. Weiss, J. Arduini, T. Arnold, H. L. DeWitt, P. J. Fraser, A. L. Ganesan, J. Gasore, C. M. Harth, O. Hermansen, et al., *Earth Syst. Sci. Data* **2018**, *10*, 985–1018.

- [31] S. Solomon, D. J. Ivy, D. Kinnison, M. J. Mills, R. R. Neely, A. Schmidt, *Science* **2016**, *353*, 269–274.
- [32] E.-S. Yang, D. M. Cunnold, M. J. Newchurch, R. J. Salawitch, M. P. McCormick, J. M. Russell, J. M. Zawodny, S. J. Oltmans, *J. Geophys. Res.* **2008**, *113*, D20308.
- [33] M. J. Newchurch, *J. Geophys. Res.* **2003**, *108*, 4507.
- [34] S. A. Montzka, J. H. Butler, R. C. Myers, T. M. Thompson, T. H. Swanson, A. D. Clarke, L. T. Lock, J. W. Elkins, *Science* **1996**, *272*, 1318–1322.
- [35] E. Sage, P.-M. Girard, S. Francesconi, *Photochem. Photobiol. Sci.* **2012**, *11*, 74–80.
- [36] E. C. De Fabo, F. P. Noonan, T. Fears, G. Merlino, *Cancer Res.* **2004**, *64*, 6372–6376.
- [37] C. Kielbassa, *Carcinogenesis* **1997**, *18*, 811–816.
- [38] N. C. Moreno, T. A. de Souza, C. C. M. Garcia, N. Q. Ruiz, C. Corradi, L. P. Castro, V. Munford, S. Ienne, L. B. Alexandrov, C. F. M. Menck, *Nucleic Acids Res.* **2020**, *48*, 1941–1953.
- [39] C. Marionnet, S. Nouveau, V. Hourblin, K. Pillai, M. Manco, P. Bastien, C. Tran, C. Tricaud, O. de Lacharrière, F. Bernerd, *J. Invest. Dermatol.* **2017**, *137*, 1184–1187.
- [40] C. Marionnet, C. Pierrard, C. Golebiewski, F. Bernerd, *PLoS One* **2014**, *9*, e105263.
- [41] C. Chang, E. C. Murzaku, L. Penn, N. R. Abbasi, P. D. Davis, M. Berwick, D. Polsky, *Am. J. Public Health* **2014**, *104*, e92–e99.
- [42] R. L. Siegel, K. D. Miller, H. E. Fuchs, A. Jemal, *CA. Cancer J. Clin.* **2021**, *71*, 7–33.
- [43] J. M. Hands, L. Moy, *Ski. J. Cutan. Med.* **2020**, *4*, 200–220.
- [44] B. Diffey, *Int. J. Cosmet. Sci.* **2020**, *42*, 1–4.
- [45] A. Corani, A. Huijser, T. Gustavsson, D. Markovitsi, P.-Å. Malmqvist, A. Pezzella, M. D’Ischia, V. Sundström, *J. Am. Chem. Soc.* **2014**, *136*, 11626–11635.
- [46] F. Solano, *Molecules* **2020**, *25*, 1537.

- [47] M. Brenner, V. J. Hearing, *Photochem. Photobiol.* **2008**, *84*, 539–549.
- [48] A. Haynes, A. Nathan, H. Dixon, M. Wakefield, S. Dobbinson, *Prev. Med. (Baltim)*. **2020**, *139*, 106230.
- [49] J. Krutmann, T. Passeron, Y. Gilaberte, C. Granger, G. Leone, M. Narda, S. Schalka, C. Trullas, P. Masson, H. W. Lim, *J. Eur. Acad. Dermatology Venereol.* **2020**, *34*, 447–454.
- [50] B. Diffey, *Int. J. Cosmet. Sci.* **2020**, *42*, 1–4.
- [51] L. Hudson, E. Rashdan, C. A. Bonn, B. Chavan, D. Rawlings, M. A. Birch-Machin, *FASEB J.* **2020**, *34*, 3874–3883.
- [52] K. Sondenheimer, J. Krutmann, *Front. Med.* **2018**, *5*, 162.
- [53] B. Diffey, B. Cadars, *Photochem. Photobiol. Sci.* **2016**, *15*, 361–364.
- [54] E. Lydahl, A. Glansholm, M. Levin, *Health Phys.* **1984**, *46*, 529–536.
- [55] A. LYDAHL, B. PHILIPSON, *Acta Ophthalmol.* **2009**, *62*, 976–992.
- [56] S. Grether-Beck, A. Marini, T. Jaenicke, J. Krutmann, *Photodermatol. Photoimmunol. Photomed.* **2014**, *30*, 167–174.
- [57] E. Dupont, J. Gomez, D. Bilodeau, *Int. J. Cosmet. Sci.* **2013**, *35*, 224–232.
- [58] J. Krutmann, A. Morita, J. H. Chung, *J. Invest. Dermatol.* **2012**, *132*, 976–984.
- [59] C. Robert, M. Bonnet, S. Marques, M. Numa, O. Doucet, *Skin Pharmacol. Physiol.* **2015**, *28*, 196–204.
- [60] M. C. Meinke, S. F. Haag, S. Schanzer, N. Groth, I. Gersonde, J. Lademann, *Photochem. Photobiol.* **2011**, *87*, 452–456.
- [61] M. E. Darvin, S. F. Haag, J. Lademann, L. Zastrow, W. Sterry, M. C. Meinke, *J. Invest. Dermatol.* **2010**, *130*, 629–631.
- [62] P. Schroeder, C. Calles, T. Benesova, F. Macaluso, J. Krutmann, *Skin Pharmacol. Physiol.* **2010**, *23*, 15–17.
- [63] L. Zastrow, N. Groth, F. Klein, D. Kockott, J. Lademann, R. Renneberg, L. Ferrero, *Skin Pharmacol. Physiol.* **2009**, *22*, 31–44.
- [64] P. Schroeder, J. Lademann, M. E. Darvin, H. Stege, C. Marks, S. Bruhnke, J.

- Krutmann, *J. Invest. Dermatol.* **2008**, *128*, 2491–2497.
- [65] S. Cho, M. J. Lee, M. S. Kim, S. Lee, Y. K. Kim, D. H. Lee, C. W. Lee, K. H. Cho, J. H. Chung, *J. Dermatol. Sci.* **2008**, *50*, 123–133.
- [66] M.-S. Kim, Y. K. Kim, K. H. Cho, J. H. Chung, *Mech. Ageing Dev.* **2006**, *127*, 875–882.
- [67] H. Piazena, D. K. Kelleher, *Photochem. Photobiol.* **2010**, *86*, 687–705.
- [68] A. Hubner, F. Sobreira, A. Vetore Neto, C. A. S. de O. Pinto, M. F. Dario, I. E. C. Díaz, F. R. Lourenço, C. Rosado, A. R. Baby, E. M. Bacchi, *Antioxidants* **2019**, *8*, 530.
- [69] D. L. Compton, K. O. Evans, M. Appell, J. R. Goodell, *J. Am. Oil Chem. Soc.* **2019**, *96*, 999–1009.
- [70] G. Petruk, R. Del Giudice, M. M. Rigano, D. M. Monti, *Oxid. Med. Cell. Longev.* **2018**, *2018*, 1–11.
- [71] Ngoc, Tran, Moon, Chae, Park, Lee, *Cosmetics* **2019**, *6*, 64.
- [72] G. Pirotta, in *Sunscreens In Coastal Ecosystems* (Eds.: A. Tovar-Sánchez, D. Sánchez-Quiles, J. Blasco), Springer International Publishing, Cham, **2020**, pp. 15–35.
- [73] K. M. Hanson, M. Cutuli, T. Rivas, M. Antuna, J. Saoub, N. T. Tierce, C. J. Bardeen, *Photochem. Photobiol. Sci.* **2020**, *390–398*, 390–398.
- [74] A. Steinemann, *Air Qual. Atmos. Heal.* **2019**, *12*, 891–897.
- [75] M. Sohn, L. Amorós-Galicia, S. Krus, K. Martin, B. Herzog, *J. Photochem. Photobiol. B Biol.* **2020**, *205*, 111818.
- [76] N. D. Bikiaris, G. Michailidou, M. Lazaridou, E. Christodoulou, E. Gounari, A. Ofrydopoulou, D. A. Lambropoulou, S. Vergkizi-Nikolakaki, S. Lykidou, N. Nikolaidis, *Polymers* **2020**, *12*, 1542.
- [77] S. Ntohogian, V. Gavriadiou, E. Christodoulou, S. Nanaki, S. Lykidou, P. Naidis, L. Mischopoulou, P. Barmpalexis, N. Nikolaidis, D. Bikiaris, *Molecules* **2018**, *23*, 2107.
- [78] S. Smaoui, H. Ben Hlima, I. Ben Chobba, A. Kadri, *Arab. J. Chem.* **2017**, *10*,

- S1216–S1222.
- [79] S. E. Cross, M. S. Roberts, R. Jiang, H. A. E. Benson, *J. Invest. Dermatol.* **2001**, *117*, 147–150.
- [80] B. Herzog, J. Giesinger, V. Settels, *Photochem. Photobiol. Sci.* **2020**, *19*, 1636–1649.
- [81] S. Narla, H. W. Lim, *Photochem. Photobiol. Sci.* **2020**, *19*, 66–70.
- [82] N. Sabzevari, S. Qiblawi, S. A. Norton, D. Fivenson, *Int. J. Women's Dermatology* **2021**, *7*, 28–44.
- [83] N. Sabzevari, S. Qiblawi, S. A. Norton, D. Fivenson, *Int. J. Women's Dermatology* **2021**, *7*, 28–44.
- [84] S. Song, Y. He, Y. Huang, X. Huang, Y. Guo, H. Zhu, K. Kannan, T. Zhang, *Sci. Total Environ.* **2020**, *726*, 138503.
- [85] T. Smijs, Pavel, *Nanotechnol. Sci. Appl.* **2011**, *2011*, 95–112.
- [86] J. Xu, Y. Sagawa, M. Futakuchi, K. Fukamachi, D. B. Alexander, F. Furukawa, Y. Ikarashi, T. Uchino, T. Nishimura, A. Morita, et al., *Food Chem. Toxicol.* **2011**, *49*, 1298–1302.
- [87] A. Bacardit, X. Cartoixà, *J. Phys. Chem. Lett.* **2020**, *11*, 1209–1214.
- [88] B. Diffey, U. Osterwalder, *Photochem. Photobiol. Sci.* **2017**, 1519–1523.
- [89] U. Osterwalder, B. Herzog, *Br. J. Dermatol.* **2009**, *161*, 13–24.
- [90] M. Pelizzo, E. Zattra, P. Nicolosi, A. Peserico, D. Garoli, M. Alaibac, *ISRN Dermatol.* **2012**, *2012*, 1–4.
- [91] S. Q. Wang, H. Xu, J. W. Stanfield, U. Osterwalder, B. Herzog, *J. Am. Acad. Dermatol.* **2017**, *77*, 42–47.
- [92] S. Bielfeldt, E. Klette, M. Rohr, B. Herzog, J. Grumelard, C. Hanay, U. Heinrich, P. Hansen, D. Kockott, J. Lademann, et al., *J. Photochem. Photobiol. B Biol.* **2018**, *189*, 185–192.
- [93] A. A. Shaw, L. A. Wainschel, M. D. Shetlar, *Photochem. Photobiol.* **2008**, *55*, 657–663.
- [94] F. P. Gasparro, M. Mitchnick, J. F. Nash, *Photochem. Photobiol.* **1998**, *68*, 243–

- [95] H. Flindt-Hansen, P. Thune, C. J. Nielsen, *Photodermatol.* **1989**, *6*, 263–7.
- [96] J. C. Sutherland, K. P. Griffin, *Photochem. Photobiol.* **1984**, *40*, 391–394.
- [97] J. C. DiNardo, C. A. Downs, *J. Cosmet. Dermatol.* **2018**, *17*, 15–19.
- [98] C. A. Downs, E. Kramarsky-Winter, R. Segal, J. Fauth, S. Knutson, O. Bronstein, F. R. Ciner, R. Jeger, Y. Lichtenfeld, C. M. Woodley, et al., *Arch. Environ. Contam. Toxicol.* **2016**, *70*, 265–288.
- [99] The Hawaii State Legislature, “SB2571 SD2 HD2 CD1,” **2018**.
- [100] S. Pawlowski, B. Herzog, M. Sohn, M. Petersen-Thiery, S. Acker, *Int. J. Cosmet. Sci.* **2020**, ics.12681.
- [101] E. F. Bernstein, H. W. Sarkas, P. Boland, D. Bouche, *J. Cosmet. Dermatol.* **2020**, *19*, 407–415.
- [102] G. C. Morrison, G. Bekö, C. J. Weschler, T. Schripp, T. Salthammer, J. Hill, A.-M. Andersson, J. Toftum, G. Clausen, H. Frederiksen, *Environ. Sci. Technol.* **2017**, *51*, 11371–11379.
- [103] C. G. Benevenuto, L. O. Guerra, L. R. Gaspar, *Eur. J. Pharm. Sci.* **2015**, *68*, 127–136.
- [104] J. F. Nash, P. R. Tanner, *Photodermatol. Photoimmunol. Photomed.* **2014**, *30*, 88–95.
- [105] D. L. Slomberg, R. Catalano, V. Bartolomei, J. Labille, *Environ. Pollut.* **2021**, *271*, 116263.
- [106] N. G. K. Wong, C. D. Rankine, C. E. H. Dessent, *J. Phys. Chem. Lett.* **2021**, *12*, 2831–2836.
- [107] N. G. K. Wong, J. A. Berenbeim, C. E. H. Dessent, *ChemPhotoChem* **2019**, *3*, 1231–1237.
- [108] N. G. K. Wong, J. A. Berenbeim, M. Hawkrige, E. Matthews, C. E. H. Dessent, *Phys. Chem. Chem. Phys.* **2019**, *21*, 14311–14321.
- [109] J. P. Hewitt, in *Princ. Pract. Photoprotection*, Springer International Publishing, Cham, **2016**, pp. 289–302.

- [110] V. Geraldes, E. Pinto, *Pharmaceuticals* **2021**, *14*, 63.
- [111] J. M. Woolley, M. Staniforth, M. D. Horbury, G. W. Richings, M. Wills, V. G. Stavros, *J. Phys. Chem. Lett.* **2018**, *9*, 3043–3048.
- [112] S. C. M. Fernandes, A. Alonso-Varona, T. Palomares, V. Zubillaga, J. Labidi, V. Bulone, *ACS Appl. Mater. Interfaces* **2015**, *7*, 16558–16564.
- [113] E. L. Holt, V. G. Stavros, *Int. Rev. Phys. Chem.* **2019**, *38*, 243–285.
- [114] N. D. N. Rodrigues, V. G. Stavros, *Sci. Prog.* **2018**, *101*, 8–31.
- [115] X.-P. Chang, T.-S. Zhang, Y.-G. Fang, G. Cui, *J. Phys. Chem. A* **2021**, *125*, 1880–1891.
- [116] C.-X. Li, W.-W. Guo, B.-B. Xie, G. Cui, *J. Chem. Phys.* **2016**, *145*, 074308.
- [117] T. N. V. Karsili, B. Marchetti, M. N. R. Ashfold, W. Domcke, *J. Phys. Chem. A* **2014**, *118*, 11999–12010.
- [118] M.-H. Kao, R. K. Venkatraman, M. Sneha, M. Wilton, A. J. Orr-Ewing, *J. Phys. Chem. A* **2021**, *125*, 636–645.
- [119] E. L. Holt, K. M. Krokidi, M. A. P. Turner, P. Mishra, T. S. Zwier, N. d. N. Rodrigues, V. G. Stavros, *Phys. Chem. Chem. Phys.* **2020**, *22*, 15509–15519.
- [120] R. R. Losantos, I. Funes-Ardoiz, J. Aguilera, E. Herrera-Ceballos, C. García-Iriepa, P. J. Campos, D. Sampedro, N. D. N. N. Rodrigues, N. C. Cole-Filipiak, M. A. P. P. Turner, et al., *J. Chem. Phys.* **2018**, *515*, 744–752.
- [121] L. A. Baker, M. D. Horbury, S. E. Greenough, P. M. Coulter, T. N. V. Karsili, G. M. Roberts, A. J. Orr-Ewing, M. N. R. Ashfold, V. G. Stavros, *J. Phys. Chem. Lett.* **2015**, *6*, 1363–1368.
- [122] J. C. Dean, R. Kusaka, P. S. Walsh, F. Allais, T. S. Zwier, *J. Am. Chem. Soc.* **2014**, *136*, 14780–14795.
- [123] L. A. Baker, S. E. Greenough, V. G. Stavros, *J. Phys. Chem. Lett.* **2016**, *7*, 4655–4665.
- [124] J. Fan, W. Roeterdink, W. J. Buma, *Mol. Phys.* **2021**, *119*, e1825850.
- [125] E. M. M. Tan, M. Hilbers, W. J. Buma, *J. Phys. Chem. Lett.* **2014**, *5*, 2464–2468.
- [126] M. Staniforth, V. G. Stavros, *Proc. R. Soc. A Math. Phys. Eng. Sci.* **2013**, *469*,

20130458.

- [127] S. J. Harris, D. Murdock, Y. Zhang, T. A. A. Oliver, M. P. Grubb, A. J. Orr-Ewing, G. M. Greetham, I. P. Clark, M. Towrie, S. E. Bradforth, et al., *Phys. Chem. Chem. Phys.* **2013**, *15*, 6567.
- [128] J. R. R. Verlet, *Chem. Soc. Rev.* **2008**, *37*, 505–517.
- [129] M. S. de Vries, P. Hobza, *Annu. Rev. Phys. Chem.* **2007**, *58*, 585–612.
- [130] M. Sugita, I. Onishi, M. Irida, N. Yoshida, F. Hirata, *Molecules* **2021**, *26*, 271.
- [131] E. M. Adams, O. Lampret, B. König, T. Happe, M. Havenith, *Phys. Chem. Chem. Phys.* **2020**, *22*, 7451–7459.
- [132] R. Cabot, C. A. Hunter, *Chem. Soc. Rev.* **2012**, *41*, 3485.
- [133] V. Amenta, J. L. Cook, C. A. Hunter, C. M. R. Low, J. G. Vinter, *J. Phys. Chem. B* **2012**, *116*, 14433–14440.
- [134] S. Ebbinghaus, S. J. Kim, M. Heyden, X. Yu, U. Heugen, M. Gruebele, D. M. Leitner, M. Havenith, *Proc. Natl. Acad. Sci.* **2007**, *104*, 20749–20752.
- [135] N. T. Hunt, *Chem. Soc. Rev.* **2009**, *38*, 1837–1848.
- [136] R. Fritzsche, S. Hume, L. Minnes, M. J. Baker, G. A. Burley, N. T. Hunt, *Analyst* **2020**, *145*, 2014–2024.
- [137] V. Cervetto, J. Helbing, J. Bredenbeck, P. Hamm, *J. Chem. Phys.* **2004**, *121*, 5935–5942.
- [138] N. K. Preketes, J. D. Biggs, H. Ren, I. Andricioaei, S. Mukamel, *Chem. Phys.* **2013**, *422*, 63–72.
- [139] J. Bredenbeck, J. Helbing, R. Behrendt, C. Renner, L. Moroder, J. Wachtveitl, P. Hamm, *J. Phys. Chem. B* **2003**, *107*, 8654–8660.
- [140] S. Mukamel, *Annu. Rev. Phys. Chem.* **2000**, *51*, 691–729.
- [141] R. K. Venkatraman, A. J. Orr-Ewing, *J. Am. Chem. Soc.* **2019**, *141*, 15222–15229.
- [142] R. Berera, R. van Grondelle, J. T. M. Kennis, *Photosynth. Res.* **2009**, *101*, 105–118.
- [143] L. A. Baker, V. G. Stavros, *Sci. Prog.* **2016**, *99*, 282–311.

- [144] E. T. J. Nibbering, H. Fidder, E. Pines, *Annu. Rev. Phys. Chem.* **2005**, *56*, 337–367.
- [145] N. D. N. Rodrigues, N. C. Cole-Filipiak, M. D. Horbury, M. Staniforth, T. N. V. Karsili, Y. Peperstraete, V. G. Stavros, *J. Photochem. Photobiol. A Chem.* **2018**, *353*, 376–384.
- [146] L. A. Baker, M. D. Horbury, S. E. Greenough, M. N. R. R. Ashfold, V. G. Stavros, *Photochem. Photobiol. Sci.* **2015**, *14*, 1814–1820.
- [147] K. M. Krokidi, M. A. P. Turner, P. A. J. Percy, V. G. Stavros, *Mol. Phys.* **2021**, *119*, e1811910.
- [148] L. A. Baker, M. Staniforth, A. L. Flourat, F. Allais, V. G. Stavros, *ChemPhysChem* **2020**, *21*, 2006–2011.
- [149] X. Zhao, J. Luo, Y. Liu, P. Pandey, S. Yang, D. Wei, K. Han, *J. Phys. Chem. Lett.* **2019**, *10*, 5244–5249.
- [150] L. A. Baker, M. Staniforth, A. L. Flourat, F. Allais, V. G. Stavros, *ChemPhotoChem* **2018**, *2*, 743–748.
- [151] M. D. Horbury, L. A. Baker, N. D. N. Rodrigues, W. D. Quan, V. G. Stavros, *Chem. Phys. Lett.* **2017**, *673*, 62–67.
- [152] N. D. N. Rodrigues, M. Staniforth, J. D. Young, Y. Peperstraete, N. C. Cole-Filipiak, J. R. Gord, P. S. Walsh, D. M. Hewett, T. S. Zwier, V. G. Stavros, *Faraday Discuss.* **2016**, *194*, 709–729.
- [153] Y. Peperstraete, M. Staniforth, L. A. Baker, N. D. N. Rodrigues, N. C. Cole-Filipiak, W.-D. D. Quan, V. G. Stavros, *Phys. Chem. Chem. Phys.* **2016**, *18*, 28140–28149.
- [154] L. A. Baker, M. D. Horbury, V. G. Stavros, *Opt. Express* **2016**, *24*, 10700.
- [155] T. T. Abiola, N. d. N. Rodrigues, C. Ho, D. J. L. Coxon, M. D. Horbury, J. M. Toldo, M. T. do Casal, B. Rioux, C. Peyrot, M. M. Mention, et al., *J. Phys. Chem. Lett.* **2021**, *12*, 337–344.
- [156] L. A. Baker, L. C. Grosvenor, M. N. R. Ashfold, V. G. Stavros, *Chem. Phys. Lett.* **2016**, *664*, 39–43.
- [157] S. Tampucci, S. Burgalassi, P. Chetoni, D. Monti, *Cosmetics* **2017**, *5*, 1.

- [158] C. Puglia, E. Damiani, A. Offerta, L. Rizza, G. G. Tirendi, M. S. Tarico, S. Curreri, F. Bonina, R. E. Perrotta, *Eur. J. Pharm. Sci.* **2014**, *51*, 211–217.
- [159] L. A. Baker, S. L. Clark, S. Habershon, V. G. Stavros, *J. Phys. Chem. Lett.* **2017**, *8*, 2113–2118.
- [160] T. Tsuchiya, A. Kikuchi, N. Oguchi-Fujiyama, K. Miyazawa, M. Yagi, *Photochem. Photobiol. Sci.* **2015**, *14*, 807–814.
- [161] G. Dormán, H. Nakamura, A. Pulsipher, G. D. Prestwich, *Chem. Rev.* **2016**, *116*, 15284–15398.
- [162] J. A. Berenbeim, N. G. K. Wong, M. C. R. Cockett, G. Berden, J. Oomens, A. M. Rijs, C. E. H. Dessent, *Phys. Chem. Chem. Phys.* **2020**, *22*, 19522–19531.
- [163] L. A. Baker, *Understanding Electronic Energy Transport in Biologically Relevant Systems*, University of Warwick, **2017**.
- [164] R. K. Venkatraman, S. Kayal, A. Barak, A. J. Orr-Ewing, S. Umaphathy, *J. Phys. Chem. Lett.* **2018**, *9*, 1642–1648.
- [165] A. Bekatorou, in *Encycl. Food Heal.*, Elsevier, **2016**, pp. 88–96.
- [166] Y.-T. Cho, H. Su, S.-J. Lin, B.-H. Wu, C.-Y. Lai, I.-C. Huang, *Rapid Commun. Mass Spectrom.* **2016**, *30*, 2315–2322.
- [167] C. M. Kawakami, L. N. C. Máximo, B. B. Fontanezi, R. S. da Silva, L. R. Gaspar, *Eur. J. Pharm. Sci.* **2017**, *99*, 299–309.
- [168] V. Lhiaubet-Vallet, M. Marin, O. Jimenez, O. Gorchs, C. Trullas, M. A. Miranda, *Photochem. Photobiol. Sci.* **2010**, *9*, 552.
- [169] E. Berardesca, T. Zuberbier, M. Sanchez Viera, M. Marinovich, *J. Eur. Acad. Dermatology Venereol.* **2019**, *33*, 25–33.
- [170] Y. Shamoto, M. Yagi, N. Oguchi-Fujiyama, K. Miyazawa, A. Kikuchi, *Photochem. Photobiol. Sci.* **2017**, *16*, 1449–1457.
- [171] E. Chatelain, B. Gabard, *Photochem. Photobiol.* **2007**, *74*, 401–406.
- [172] N. D. N. Rodrigues, N. C. Cole-Filipiak, M. A. P. Turner, K. Krokidi, G. L. Thornton, G. W. Richings, N. D. M. Hine, V. G. Stavros, *Chem. Phys.* **2018**, *515*, 596–602.

- [173] Urek, *Glob. J. Pathol. Microbiol.* **2013**, *1*, 7–11.
- [174] Cosmetic Ingredient Review Expert Panel, *Int. J. Toxicol.* **2003**, *22 Suppl 3*, 1–108.
- [175] P. Zhou, M. R. Hoffmann, K. Han, G. He, *J. Phys. Chem. B* **2015**, *119*, 2125–2131.
- [176] J. Catalán, *Phys. Chem. Chem. Phys.* **2012**, *14*, 8903.
- [177] A. Mitsuzuka, A. Fujii, T. Ebata, N. Mikami, *J. Phys. Chem. A* **1998**, *102*, 9779–9784.
- [178] L. Heimbrook, J. E. Kenny, B. E. Kohler, G. W. Scott, *J. Phys. Chem.* **1983**, *87*, 280–289.
- [179] J. Goodman, L. E. Brus, *J. Am. Chem. Soc.* **1978**, *100*, 7472–7474.
- [180] J. L. Herek, S. Pedersen, L. Bañares, A. H. Zewail, *J. Chem. Phys.* **1992**, *97*, 9046–9061.
- [181] F. Ling, D. Liu, S. Li, W. Li, B. Zhang, P. Wang, *J. Chem. Phys.* **2019**, *151*, 094302.
- [182] V. G. Stavros, J. R. R. Verlet, *Annu. Rev. Phys. Chem.* **2016**, *67*, 211–232.
- [183] N. D. N. Rodrigues, M. Staniforth, V. G. Stavros, *Proc. R. Soc. A Math. Phys. Eng. Sci.* **2016**, *472*, 20160677.
- [184] E. Nir, K. Kleinermanns, L. Grace, M. S. de Vries, *J. Phys. Chem. A* **2001**, *105*, 5106–5110.
- [185] F. Piuze, I. Dimicoli, M. Mons, B. Tardivel, Q. Zhao, *Chem. Phys. Lett.* **2000**, *320*, 282–288.
- [186] R. Cohen, B. Brauer, E. Nir, L. Grace, M. S. de Vries, *J. Phys. Chem. A* **2000**, *104*, 6351–6355.
- [187] T. Streibel, K. Hafner, F. Mühlberger, T. Adam, R. Zimmermann, *Appl. Spectrosc.* **2006**, *60*, 72–79.
- [188] L. Cao, F. Mühlberger, T. Adam, T. Streibel, H. Z. Wang, A. Kettrup, R. Zimmermann, *Anal. Chem.* **2003**, *75*, 5639–5645.
- [189] R. Zimmermann, H. J. Heger, A. Kettrup, U. Boesl, *Rapid Commun. Mass Spectrom.* **1997**, *11*, 1095–1102.

- [190] N. Mirsaleh-Kohan, W. D. Robertson, R. N. Compton, *Mass Spectrom. Rev.* **2008**, *27*, 237–285.
- [191] U. Boesl, *Mass Spectrom. Rev.* **2017**, *36*, 86–109.
- [192] W. C. Wiley, I. H. McLaren, *Rev. Sci. Instrum.* **1955**, *26*, 1150–1157.
- [193] D. W. Chandler, P. L. Houston, *J. Chem. Phys.* **1987**, *87*, 1445–1447.
- [194] A. T. J. B. Eppink, D. H. Parker, *Rev. Sci. Instrum.* **1997**, *68*, 3477–3484.
- [195] H. de Vries, D. A. Wiersma, *Phys. Rev. Lett.* **1976**, *36*, 91–94.
- [196] J. Friedrich, D. Haarer, **1986**, pp. 149–198.
- [197] A. Henley, H. H. Fielding, *Int. Rev. Phys. Chem.* **2019**, *38*, 1–34.
- [198] X. Zhao, J. Luo, S. Yang, K. Han, *J. Phys. Chem. Lett.* **2019**, *10*, 4197–4202.
- [199] Y. Liu, X. Zhao, J. Luo, S. Yang, *J. Lumin.* **2019**, *206*, 469–473.
- [200] M. D. Horbury, A. L. Flourat, S. E. Greenough, F. Allais, V. G. Stavros, *Chem. Commun.* **2018**, *54*, 936–939.
- [201] V. G. Stavros, *Nat Chem* **2014**, *6*, 955–956.
- [202] X.-P. Chang, C.-X. Li, B.-B. Xie, G. Cui, *J. Phys. Chem. A* **2015**, *119*, 11488–11497.
- [203] J. Luo, Y. Liu, S. Yang, A. L. Flourat, F. Allais, K. Han, *J. Phys. Chem. Lett.* **2017**, *8*, 1025–1030.
- [204] J. N. Bull, C. S. Anstöter, J. R. R. Verlet, *J. Phys. Chem. A* **2020**, *124*, 2140–2151.
- [205] J. Fenn, M. Mann, C. Meng, S. Wong, C. Whitehouse, *Science* **1989**, *246*, 64–71.
- [206] A. Sen, E. M. Matthews, G.-L. Hou, X.-B. Wang, C. E. H. Dessent, *J. Chem. Phys.* **2015**, *143*, 184307.
- [207] E. Matthews, A. Sen, N. Yoshikawa, E. Bergström, C. E. H. Dessent, *Phys. Chem. Chem. Phys.* **2016**, *18*, 15143–15152.
- [208] S. Banerjee, S. Mazumdar, *Int. J. Anal. Chem.* **2012**, *2012*, 1–40.
- [209] M. Przybylski, M. O. Glocker, *Angew. Chemie Int. Ed. English* **1996**, *35*, 806–826.
- [210] Bruker Daltonik GmbH, *AmazOn Series User Manual*, Germany, **2009**.

- [211] R. Cole, *Electrospray and MALDI Mass Spectrometry: Fundamentals, Instrumentation, Practicalities, and Biological Applications*, John Wiley & Sons, New Jersey, NJ, USA., **2010**.
- [212] M. S. Wilm, M. Mann, *Int. J. Mass Spectrom. Ion Process.* **1994**, *136*, 167–180.
- [213] G. Taylor, *Proc. R. Soc. London. Ser. A. Math. Phys. Sci.* **1964**, *280*, 383–397.
- [214] Lord Rayleigh, *London, Edinburgh, Dublin Philos. Mag. J. Sci.* **1882**, *14*, 184–186.
- [215] P. Kebarle, L. Tang, *Anal. Chem.* **1993**, *65*, A972–A986.
- [216] J. V Iribarne, B. A. Thomson, *J. Chem. Phys.* **1976**, *64*, 2287–2294.
- [217] M. Karas, U. Bahr, T. Dülcks, *Fresenius. J. Anal. Chem.* **2000**, *366*, 669–676.
- [218] B. A. Thomson, J. V Iribarne, *J. Chem. Phys.* **1979**, *71*, 4451–4463.
- [219] L. Konermann, E. Ahadi, A. D. Rodriguez, S. Vahidi, *Anal. Chem.* **2013**, *85*, 2–9.
- [220] S. Nguyen, J. B. Fenn, *Proc. Natl. Acad. Sci.* **2007**, *104*, 1111–1117.
- [221] G. Schmelzeisen-Redeker, L. Bütfering, F. W. Röllgen, *Int. J. Mass Spectrom. Ion Process.* **1989**, *90*, 139–150.
- [222] M. Dole, L. L. Mack, R. L. Hines, R. C. Mobley, L. D. Ferguson, M. B. Alice, *J. Chem. Phys.* **1968**, *49*, 2240–2249.
- [223] N. V. Konenkov, M. Sudakov, D. J. Douglas, *J. Am. Soc. Mass Spectrom.* **2002**, *13*, 597–613.
- [224] E. Matthews, Photodissociation Spectroscopy of Gaseous Bio-Ions in a Commercial Quadrupole Ion Trap Mass Spectrometer, University of York, **2018**.
- [225] Continuum, *Continuum® Horizon<sup>TM</sup> I and II OPO Operation and Maintenance Manual*, San Jose, CA, USA, **2014**.
- [226] R. A. Zubarev, A. Makarov, *Anal. Chem.* **2013**, *85*, 5288–5296.
- [227] R. H. Perry, R. G. Cooks, R. J. Noll, *Mass Spectrom. Rev.* **2008**, *27*, 661–699.

## Chapter 2

# Mapping the Intrinsic Absorption Properties and Photodegradation Pathways of the Protonated and Deprotonated Forms of the Sunscreen Oxybenzone

### 2.1 Declaration

This work was originally published in the *Physical Chemistry Chemical Physics* on 17 January 2019.

All experimental work in this paper was carried and processed by myself, with the laser experimental work conducted under the supervision of Dr. Jacob A. Berenbeim. The computational analysis presented within was a joint effort by myself and Dr. Jacob A. Berenbeim. Mathew Hawkrige and Dr. Edward Matthews are also acknowledged for their contributions to the preliminary scans on protonated oxybenzone taken prior to the start of my tenure as a Ph.D. researcher within the group.

I wrote a complete first draft of the manuscript, which was revised through multiple reiterations involving Prof. Caroline E. H. Dessent, Dr. Jacob A. Berenbeim, and myself.



Signed Prof. Caroline E. H. Dessent (University of York, U.K.)

**2.2 Paper I: Mapping the Intrinsic Absorption Properties and Photodegradation Pathways of the Protonated and Deprotonated Forms of the Sunscreen Oxybenzone**

Cite this: *Phys. Chem. Chem. Phys.*, 2019, 21, 14311

# Mapping the intrinsic absorption properties and photodegradation pathways of the protonated and deprotonated forms of the sunscreen oxybenzone†

Natalie G. K. Wong,<sup>id</sup> Jacob A. Berenbeim,<sup>id</sup> Mathew Hawkridge, Edward Matthews and Caroline E. H. Dessent<sup>id</sup>\*

Sunscreens provide vital protection against the photodamaging effects of UV radiation, however, many fundamental questions remain about the detailed mechanisms by which they dissipate UV energy. One such issue is the extent to which the pH environment of an organic sunscreen molecule alters its effectiveness, both in terms of ability to absorb UV radiation, and also its potential to photodegrade. Here, we use gas-phase laser photodissociation spectroscopy for the first time to measure the intrinsic UVA–UVC absorption spectra and associated photodegradation products of protonated and deprotonated oxybenzone, away from the complications of bulk mixtures. Our results reveal that protonation state has a dramatic effect on the absorption and photodissociation properties of this sunscreen. While the UV absorption profile of oxybenzone is only modestly affected by protonation across the range from 400–216 nm, deprotonated oxybenzone displays a significantly modified absorption spectrum, with very low photoabsorption between 370–330 nm. Protonated oxybenzone primarily photofragments by rupture of the bonds on either side of the central carbonyl group, producing cationic fragments with  $m/z$  151 and 105. Additional lower mass photofragments (e.g.  $m/z$  95 and 77) are also observed. The production spectra for the photofragments from protonated oxybenzone fall into two distinct categories, which we discuss in the context of different excited state decay pathways. For deprotonated oxybenzone, the major photofragments observed are  $m/z$  211 and 212, which are associated with the ejection of methane and the methyl free radical from the parent ion, respectively. Implications for the suitability of oxybenzone in its protonated and deprotonated forms as an optimum sunscreen molecule are discussed.

Received 1st November 2018,  
Accepted 16th January 2019

DOI: 10.1039/c8cp06794e

rsc.li/pccp

## 1. Introduction

In order that the skin can be protected against the photo-damaging effects of UV exposure, considerable effort has been put into the development of effective sunscreens.<sup>1–4</sup> Given the very widespread adoption of sunscreens, it is surprising that many questions remain regarding the detailed mechanisms by which they function.<sup>5–8</sup> Over recent years, a number of advanced laser spectroscopic studies have been conducted on sunscreen molecules under highly-controlled conditions.<sup>1,6,9–16</sup> These measurements can provide a detailed picture of the fundamental properties of the sunscreen molecule away from the complicated and dense environment of a real sunscreen lotion. For example, “isolated” gas-phase sunscreen molecules

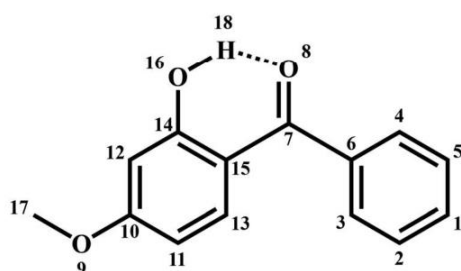
have been studied to provide information on the intrinsic molecular properties.<sup>14,15,17–19</sup> A second group of investigations have involved highly-simplified mixtures, *i.e.* one sunscreen in one solvent, with transient absorption spectroscopy being applied to probe relaxation dynamics.<sup>1,9–11,13</sup> Both of these distinctive approaches have been complemented by high-level quantum chemical calculations,<sup>20–25</sup> and have provided important insights into the detailed mechanism by which a sunscreen molecule operates.

One fundamental issue that appears to have been largely ignored to date, particularly in fundamental studies, is the way in which the pH environment of the sunscreen can affect its performance,<sup>6,26,27</sup> *i.e.* how do the properties of the protonated or deprotonated sunscreen molecule differ from those of the neutral. Recently, Li *et al.* showed through a series of photolysis studies performed in pure water that while neutral forms of oxybenzone do not photodecay over long timescales, the anionic form does.<sup>26</sup> This is potentially an important issue since commercial sunscreens typically involve complex mixtures

Department of Chemistry, University of York, Heslington, York, YO10 5DD, UK.

E-mail: caroline.dessent@york.ac.uk

† Electronic supplementary information (ESI) available. See DOI: 10.1039/c8cp06794e



Scheme 1 Schematic diagram of oxybenzone (OB) with atom labels.

including water and alcoholic solvents. Moreover, in common usage, sunscreens are exposed to acidic and alkaline environments, with human skin and sweat being typically mildly acidic,<sup>28,29</sup> while chlorinated swimming pools are alkaline.<sup>30</sup>

In this work, we perform the first UV laser spectroscopy measurements on protonated and deprotonated oxybenzone, to probe the potential impact of pH on the UVA–UVB absorption profile and photodegradation products of oxybenzone (Scheme 1). Experiments are conducted on isolated, gas-phase oxybenzone ions within a novel laser-interfaced mass spectrometer. This allows us to unambiguously measure the intrinsic UV absorption profile and any associated ionic photodegradation products of the mass-selected ion,<sup>31–33</sup> away from any complications of the bulk-phase environment.

Oxybenzone (OB) is an active ingredient that has been widely used in commercial sunscreens, and in its neutral form, is thought to be photostable even following several hours of irradiation.<sup>4,5,34–36</sup> Oxybenzone was selected for study in this work as it has been the subject of several recent fundamental studies.<sup>6,9,10,21,25</sup> Quantum chemical studies of OB have indicated that the basis of its sunscreen functionality can be traced to ultrafast decay dynamics following photoexcitation.<sup>25</sup> Excited state intramolecular proton transfer (ESIPT) is understood to yield the keto form of OB which can undergo fast picosecond internal conversion.<sup>9</sup> Recent transient absorption studies of OB in solution by Stavros and co-workers have produced experimental results that are consistent with these calculations, thus establishing OB as the prototype organic sunscreen for fundamental studies.<sup>9,10</sup>

## 2. Methods

Gas-phase UV photodissociation experiments were conducted in an Amazon SL dual funnel electrospray ionization quadrupole ion-trap (ESI-QIT) mass spectrometer (Bruker Daltonics Inc., Billerica, MA, USA), which was modified to allow laser interfaced mass spectrometry (LIMS).<sup>37,38</sup> This instrument has the advantages of a commercial mass spectrometer (flexible ion sources, mass selection, isolation of primary and secondary ions *via* MS<sup>n</sup> schemes, *etc.*), coupled with the ability to record UV photodissociation spectra in a routine manner.

OB was purchased from Alfa Aesar (Ward Hill, MA, USA) and HPLC-grade MeOH was purchased from Fisher Scientific, Inc. (Pittsburg, PA, USA), both used as received. Solutions of OB

( $1 \times 10^{-4}$  mol dm<sup>-3</sup>) in MeOH were introduced to the mass spectrometer by ESI using typical instrumental parameters: nebulizing gas pressure of 10.0 psi, an injection rate of 0.33 mL h<sup>-1</sup>, a drying gas flow rate of 8.0 L min<sup>-1</sup>, and run in positive/negative ion mode at capillary temperatures of 140 °C and 100 °C to form protonated and deprotonated oxybenzone, respectively.

[OB + H]<sup>+</sup> and [OB – H]<sup>-</sup> were mass selected and isolated in the ion-trap prior to laser irradiation. UV-Vis photons were produced by a 10 Hz Nd:YAG (Surelite™, Amplitude Laser Group, San Jose, CA, USA) pumped OPO (Horizon™, Amplitude Laser Group) laser, giving ~1.0 mJ across the range 400–216 nm (3.10–5.74 eV) for [OB + H]<sup>+</sup> and ~0.3 mJ across the range 500–216 nm (2.48–5.74 eV) for [OB – H]<sup>-</sup>. Laser step sizes used for [OB + H]<sup>+</sup> and [OB – H]<sup>-</sup> were that of 1 and 2 nm, respectively. 2 nm laser step sizes were used to record the photofragment depletion spectra of [OB + H]<sup>+</sup> photofragments. The laser beam was focused as described in ref. 37 and 38.

Photofragmentation experiments were conducted with ion accumulation times between 10–50 ms and a fragmentation time of 100 ms, thereby ensuring that each mass-selected ion packet interacted with one laser pulse to minimize the likelihood of multiphoton events. When fluorescence is negligible,<sup>39</sup> the UV excited gaseous ion will fragment upon excited state relaxation, yielding an action absorption spectrum by photodepletion.<sup>37,40,41</sup> Photodepletion (PD) of [OB + H]<sup>+</sup> and [OB – H]<sup>-</sup> was measured as a function of the scanned wavelength, with the photofragment production (PF) also recorded simultaneously at each wavelength:

$$\text{Photodepletion intensity} = -\frac{\ln\left(\frac{\text{Int}_{\text{OFF}}}{\text{Int}_{\text{ON}}}\right)}{\lambda \times P} \quad (1)$$

$$\text{Photofragmentation intensity} = \frac{\left(\frac{\text{Int}_{\text{FRAG}}}{\text{Int}_{\text{OFF}}}\right)}{\lambda \times P} \quad (2)$$

where Int<sub>OFF</sub> and Int<sub>ON</sub> are the peak intensities with laser off and on respectively; Int<sub>FRAG</sub> is the fragment intensity with the laser on;  $\lambda$  is the excitation wavelength (nm); and  $P$  is the tunable laser pulse energy (mJ). The photodepletion intensities were taken from an average of three runs at each wavelength of the ranges studied. We note that fragment ions with  $m/z < 50$  are not detectable in our mass spectrometer since low masses fall outside the mass window of the ion trap. The UV photodepletion (absorption) spectra of the major OB photofragments produced upon the photoexcitation of protonated and deprotonated oxybenzone were also recorded using the MS<sup>n</sup> scheme and mass-isolation feature available on the trapControl version 7.2 (Bruker Daltonics Inc.) software.

Low-energy collision induced dissociation (CID) was employed to determine the ground state thermal fragmentation productions of [OB + H]<sup>+</sup> and [OB – H]<sup>-</sup>. This technique was performed by applying an excitation AC voltage to the end caps of the trap to induce collisions of the trapped ions with the He buffer gas, as also described in detail previously.<sup>42,43</sup>

Solution-phase UV absorption spectra of OB ( $3 \times 10^{-5} \text{ mol dm}^{-3}$ ) in MeOH were recorded using a UV-1800 UV-Visible spectrophotometer (Shimadzu, Kyoto, Japan) with a 10 mm UV quartz cuvette, using MeOH as the baseline solvent. To achieve a UV spectrum for  $[\text{OB} + \text{H}]^+$  and  $[\text{OB} - \text{H}]^-$ , solutions of OB in MeOH were acidified with HCl (3.0 M) and alkalinized with NaOH (2.0 M). The  $\text{pH}^*$  is not directly measured for these methanol solutions, however, comparison to methanol-aqueous mixtures is included in Section S5 of the ESI† where the pH of the aqueous buffer solution is known. Acidic, neutral, and basic methanol solution conditions yield UV-Visible spectra which are comparable to those methanol-aqueous mixtures of pH 2.95, 7.0, and 13.0 buffered solutions, respectively.

Calculations were performed using density functional theory at the  $\omega\text{B97XD/6-311++G}^{**}$  level as implemented in Gaussian 09.<sup>44</sup> All reported structures correspond to true minima as confirmed by frequency calculations.

## 3. Results

### 3.1 Deprotonated oxybenzene

**3.1A Gas-phase and solution-phase UV absorption spectra of deprotonated oxybenzene.** Fig. 1a displays the photodepletion (gas-phase absorption) spectra of  $[\text{OB} - \text{H}]^-$  ( $m/z$  227) over

the range 2.48–5.74 eV. The low-intensity band centered close to the VIS–UVA crossover region has been labeled  $\text{I}_\text{D}$  ( $\lambda_{\text{max}} = 3.0 \text{ eV}$ ) and does not fully approach zero photodepletion signal at 2.48 eV, the lowest energy scanned in this study. The UVA–UVB crossover point at 3.8 eV marks the onset of an intense broad photodepletion region which we label as containing two bands,  $\text{II}_\text{D}$  ( $\lambda_{\text{max}} = 4.0 \text{ eV}$ ) and  $\text{III}_\text{D}$  ( $\lambda_{\text{max}} = 4.9 \text{ eV}$ ), to allow us to straightforwardly identify different spectral regions, with **D** indicating the deprotonated system. Photodepletion increases strongly into the UVC region.

Fig. 1b presents the solution-phase absorption spectrum of OB obtained under basic conditions. Comparison of the Fig. 1a and b spectra reveals that the gaseous ion spectrum is very similar to the solution-phase spectrum. In solution, the UVA band,  $\text{I}_\text{D}$ , appears with  $\lambda_{\text{max}} = 3.4 \text{ eV}$ , and the UVB/UVB crossover length bands,  $\text{II}_\text{D}$  and  $\text{III}_\text{D}$  with  $\lambda_{\text{max}} = 4.3 \text{ eV}$  and  $5.1 \text{ eV}$ , respectively. Notably, each gas-phase band blue-shifts by  $\sim 0.3 \text{ eV}$  on going to solution.

The similarity of the  $[\text{OB} - \text{H}]^-$  gaseous spectrum (Fig. 1a) and the solution spectrum (Fig. 1b) demonstrates unambiguously that the species giving rise to the solution-phase spectrum is the  $[\text{OB} - \text{H}]^-$  moiety. In this context, it is instructive to compare the  $[\text{OB} - \text{H}]^-$  solution-phase absorption spectra with that of neutral OB (Fig. 1c). The neutral and deprotonated forms of OB display significantly different absorption profiles, with the deprotonated form providing absorption across a wider range of the UVA. In contrast, the deprotonated form absorbs significantly less UVB compared to the neutral, particularly in the vicinity of 320 nm (3.87 eV).

Finally, we note that computational chemistry calculations of the structures of  $[\text{OB} - \text{H}]^-$  presented in Section 3.1C indicate that only single deprotonation isomers dominate the gas-phase (Fig. 1a) and solution-phase spectra (Fig. 1b).

**3.1B Photofragmentation of deprotonated oxybenzene.** We next turn to investigating the wavelength-dependent photofragments that are produced following photoabsorption of deprotonated oxybenzene between the range 2.48–5.74 eV. Fig. 2 displays the difference (laser on–laser off) photofragment mass spectra of  $[\text{OB} - \text{H}]^-$  irradiated at the maxima of bands  $\text{I}_\text{D}$ ,  $\text{II}_\text{D}$ , and  $\text{III}_\text{D}$  (3.0, 4.0, and 4.9 eV, respectively). The dominant photofragments are  $m/z$  212 (loss of  $m/z$  15) (3a) and  $m/z$  211 (loss of  $m/z$  16 from parent ion) (3b), with photofragments being produced with relatively low intensity compared to the parent ion depletion. This indicates that the major photodissociation channel across the spectral range studied is electron loss (3c):



Both the  $m/z$  184 and 183 ions are also observed as minor photofragments. These correspond to the loss of 28 Da from  $m/z$  212 and 211, respectively, and are therefore assigned as secondary fragment ions produced by the loss of CO from hot  $m/z$  212 and 211. We note that collision-induced dissociation of  $[\text{OB} - \text{H}]^-$  in the quadrupole ion trap of our instrument also

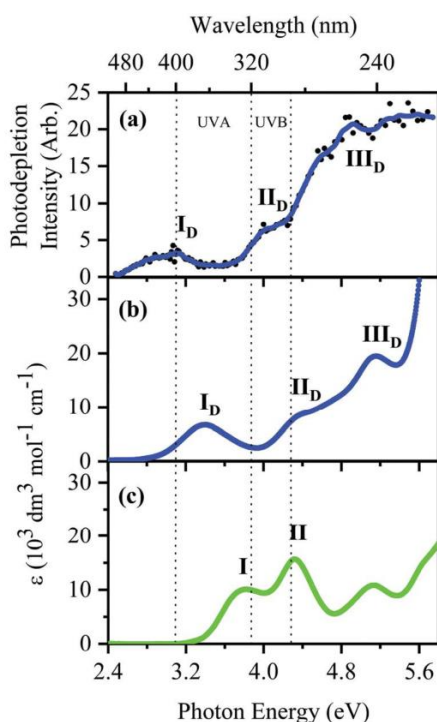


**Fig. 1** (a) Gas-phase photodepletion spectrum of deprotonated oxybenzene ( $[\text{OB} - \text{H}]^-$ ). The solid line is a five-point adjacent average of the data points. (b) Solution-phase absorption spectrum of OB under basic conditions. (c) Solution-phase absorption spectrum of OB under neutral conditions.

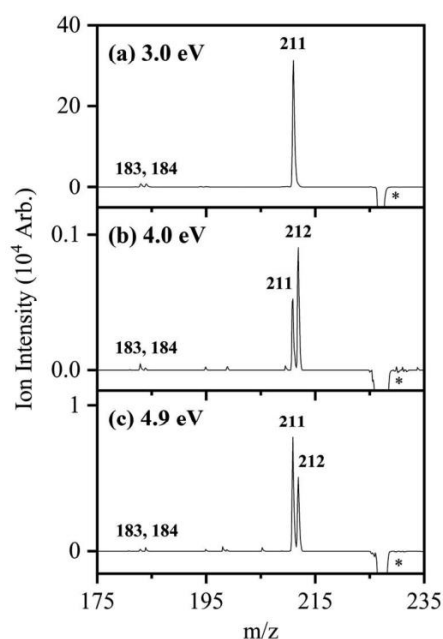


Fig. 2 Photofragment difference (laser on–laser off) mass spectrum of  $[\text{OB} - \text{H}]^-$ , excited at three (a–c) photodepletion maxima (bands  $\text{I}_D$ ,  $\text{II}_D$ , and  $\text{III}_D$ ) of (a) 3.0, (b) 4.0, and (c) 4.9 eV. \* Represents the depleted parent ion signal at  $m/z$  227.

produces  $m/z$  211 and 212 as the dominant fragment ions. The loss of  $m/z$  16 from  $[\text{OB} - \text{H}]^-$  was confirmed as being associated with ejection of  $\text{CH}_4$  (and not an oxygen atom) from the parent ion by performing exact mass analysis by time of flight mass spectrometry. Whether  $\text{CH}_4$  is ejected by a concerted release or by stepwise ejection of  $\bullet\text{CH}_3 + \bullet\text{H}$  cannot be determined in our photodissociation experiment, but the fact that  $m/z$  211 is produced by CID as well as photoexcitation strongly suggests that  $\text{CH}_4$  is being lost in a single step. Unimolecular

thermal decomposition studies of methoxybenzene have been conducted previously and have shown that methoxybenzene dissociates into methyl and phenoxy radicals,<sup>45–47</sup> consistent with production of the  $m/z$  212 fragment for  $[\text{OB} - \text{H}]^-$  observed here. The phenoxy radical is also known to lose CO under secondary dissociation to produce the cyclopentadienyl radical, again in line with the fragmentation patterns observed here. Table 1 lists the  $[\text{OB} - \text{H}]^-$  photofragment ions, along with tentative structural assignments. It is notable that all fragmentation routes result in the production of free radicals, some being diradical in nature.

Photofragment action spectra are acquired simultaneously with the photodepletion spectrum in our instrument, providing a complete picture of the wavelength-dependent fragmentation products. Fig. 3b and c display the action spectra of the dominant  $m/z$  211 and 212 photofragments of  $[\text{OB} - \text{H}]^-$ , with the parent  $[\text{OB} - \text{H}]^-$  photodepletion spectrum presented in Fig. 3a for ease of comparison. The action spectrum of the  $m/z$  211 fragment (Fig. 3b) shows a broad band centered around 3.0 eV, with two lower-intensity peaks in fragment production visible at  $\sim 4.7$  and  $\sim 5.4$  eV. The  $m/z$  212 fragment (Fig. 3c) is produced at a lower intensity than the  $m/z$  211 fragment, with peaks in fragment ion production at 2.6 and 4.5 eV. In contrast to  $m/z$  211, the  $m/z$  212 fragment intensity falls away rapidly above 4.8 eV, probably due to dissociation of  $m/z$  212 into a secondary fragment ion. The same pattern is also evident across the lower energy band  $\text{I}_D$  region, with  $m/z$  211 fragment production continuing to energies above those at which the  $m/z$  212 fragment is produced. Overall, the production profiles of  $m/z$  211 and 212 are enhanced through bands  $\text{I}_D$  and  $\text{III}_D$ , while photofragment ion production in region of band  $\text{II}_D$  is very low.

To obtain an approximate spectrum for the electron detachment profile (3c), it is possible to subtract the photofragment intensities from the photodepletion signal. This spectrum is included in Section S1 of the ESI† and reveals that at the lowest-energy scanned (2.48 eV) the electron detachment cross-section

Table 1 Proposed structures for the low-intensity ionic fragments of  $[\text{OB} - \text{H}]^-$  ( $m/z$  227) produced during CID and laser photoexcitation

Fragment mass ( $m/z$ )	Proposed structure of fragment	$m/z$ lost from $[\text{OB} - \text{H}]^-$	Fragment results from loss of neutral	Observed in CID <sup>a</sup>	Observed in laser photoexcitation <sup>a</sup>
212		15	$\bullet\text{CH}_3$	✓ (s)	✓ (w)
211		16	$\text{CH}_4$ (or $\bullet\text{CH}_3 + \bullet\text{H}$ )	✓ (s)	✓ (m)
184		43	$\bullet\text{CH}_3 + \text{CO}$		✓ (vw)
183		44	$\text{CH}_4 + \text{CO}$ (or $\bullet\text{CH}_3 + \bullet\text{H} + \text{CO}$ )		✓ (vw)

<sup>a</sup> s (strong), m (medium), w (weak), and vw (very weak).

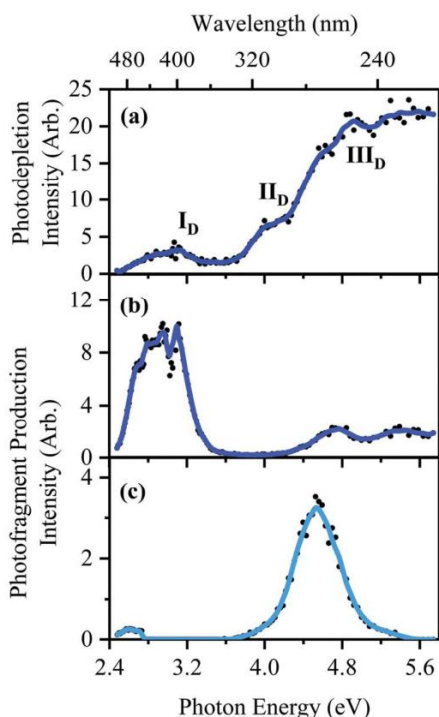
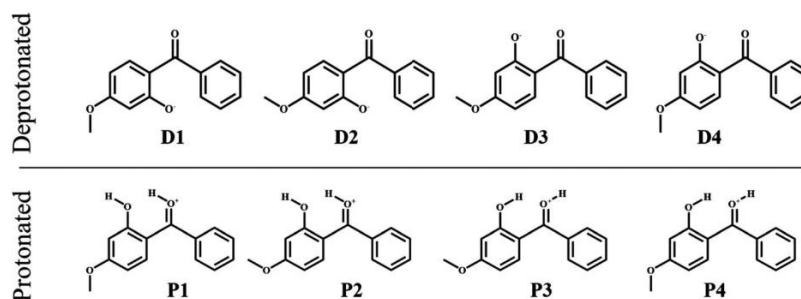


Fig. 3 (a) Gas-phase UV absorption (photodepletion) spectra of  $[\text{OB} - \text{H}]^-$ . (b and c) Photofragment production spectrum of two major photofragments at  $m/z$  211 and  $m/z$  212, respectively. The solid line is a five-point adjacent average of the data points.

is  $\sim 50\%$  of the photodepletion signal, while at energies corresponding to band  $\text{II}_D$  and above, electron detachment represents  $\sim 100\%$  of the photodepletion intensity.

**3.1C Quantum chemical calculations of deprotonated oxibenzene.** DFT geometry optimization established two forms of neutral OB, from which a search for geometric minima of the deprotonated species was initiated, with protons being removed from the hydroxyl, methoxyl, or benzoyl positions.  $[\text{OB} - \text{H}]^-$  was allowed to freely rotate during optimization. Four relatively low-energy isomers (within  $30 \text{ kJ mol}^{-1}$  of the minimum for the gaseous structures) were identified and are shown in Scheme 2.



Scheme 2 Low energy isomers of  $[\text{OB} - \text{H}]^-$  and  $[\text{OB} + \text{H}]^+$  obtained at the  $\omega\text{B97XD}/6\text{-311++G}^{**}$  level.

Table 2 Calculated relative energies and physical properties of oxibenzene dependent on pH. Calculated at the  $\omega\text{B97XD}/6\text{-311++G}^{**}$  level

	Structure	Relative energy <sup>a,b</sup> ( $\text{kJ mol}^{-1}$ )	VDE <sup>c</sup> (eV)
$[\text{OB} - \text{H}]^-$	<b>D1</b>	0.0 (0.0)	3.00
	<b>D2</b>	8.2 (5.1)	3.00
	<b>D3</b>	21.0 (3.8)	2.89
	<b>D4</b>	29.8 (8.7)	2.87
$[\text{OB} + \text{H}]^+$	<b>P1</b>	0.0 (1.0)	
	<b>P2</b>	1.8 (0.0)	
	<b>P3</b>	9.9 (9.8)	
	<b>P4</b>	16.6 (12.7)	

<sup>a</sup> Relative electronic energies are zero-point energy corrected. <sup>b</sup> Values in parentheses are calculated in methanol. <sup>c</sup>  $\text{VDE} = E(\text{neutral at optimized anion geometry}) - E(\text{anion})$ .

The structures are labelled numerically in order of increasing relative energy. Table 2 displays the relative energies, with further structures being included in Section S2 of the ESI.†

The  $[\text{OB} - \text{H}]^-$  structures can be classed into two groups associated with the deprotonated oxygen O16 either remaining adjacent to the  $\text{C}_7\text{O}_3$  carbonyl group (**D3** and **D4**), or rotating by  $\sim 180$  degrees so that the deprotonated oxygen is adjacent to the benzene ring (**D1** and **D2**). In the gas-phase, isomers **D1** and **D2** are significantly lower in energy than **D3** and **D4**, but in methanol solution, the relative energy ordering of **D2** and **D3** switch, and isomers **D2**, **D3**, and **D4** become significantly lower in relative energy. A Boltzmann distribution calculation at  $T = 400 \text{ K}$  predicts that **D1** accounts for 93% of an equilibrated gaseous mixture, and 64% in solution. Under the ESI conditions used here (protic solvent), we anticipate that the ion ESI populations will be overwhelmingly **D1**.<sup>31,32,38</sup> This is important as it means that the gaseous photodepletion and solution-phase absorption spectra discussed above could be assigned to just a single isomer, which considerably simplifies the analysis of the spectra presented.<sup>31,32,38</sup>

The vertical electron detachment energy (VDE) was calculated for all  $[\text{OB} - \text{H}]^-$  structures, including those shown in Section S2 the ESI,† with values of  $\sim 2.95 \text{ eV}$  being obtained for all of the low-energy conformers. This value agrees well with that of the isolated phenoxide moiety which has a VDE of  $2.25 \text{ eV}$ .<sup>48,49</sup> From the calculated VDE, it is likely that any absorbance in the UVA–UVC range for gaseous  $[\text{OB} - \text{H}]^-$  will

result in some electron detachment, in line with the strong propensity for electron detachment discussed in Section 3.1B.

### 3.2 Protonated oxybenzone

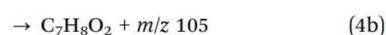
**3.2A Gas-phase and solution-phase UV absorption spectra of protonated oxybenzone.** Fig. 4a presents the  $[\text{OB} + \text{H}]^+$  photodepletion spectra, which displays three distinct bands, labeled  $\text{I}_\text{P}$ – $\text{III}_\text{P}$ , with  $\lambda_{\text{max}}$  values at 3.50, 4.27, and 5.17 eV, respectively (P denotes the protonated system). Bands  $\text{I}_\text{P}$  and  $\text{II}_\text{P}$  are of similar intensity and are centered within the UVA and UVB spectral regions, respectively. Band  $\text{I}_\text{P}$  is a dominant feature of the photodepletion spectrum having a FWHM of 0.68 eV which accounts for broad absorption across the entire UVA region and into the higher-energy UVB. Band  $\text{II}_\text{P}$  is slightly more intense than  $\text{I}_\text{P}$ , but narrower with a FWHM of 0.4 eV. Band  $\text{III}_\text{P}$  is the least intense feature of the  $[\text{OB} + \text{H}]^+$  photodepletion spectrum, with a FWHM similar to that of band  $\text{II}_\text{P}$ . Bands  $\text{II}_\text{P}$  and  $\text{III}_\text{P}$  are separated by a deep spectral valley (270–230 nm), with very low photodepletion over this UVC region.

Comparison of the measured gaseous photodepletion (absorption) spectrum of  $[\text{OB} + \text{H}]^+$  to the solution-phase absorption spectrum (Fig. 4b) obtained under acidic conditions, illustrates that the spectra agree well over both the UVA and UVB regions. In solution, bands  $\text{I}_\text{P}$  and  $\text{II}_\text{P}$  peak at  $\lambda_{\text{max}} = 3.78$  and 4.29 eV, with band  $\text{I}_\text{P}$  being blue-shifted on going from the gas-phase to solution,

while the position of band  $\text{II}_\text{P}$  is relatively insensitive to solvation. The solution-phase spectrum obtained under neutral conditions is displayed in Fig. 4c and displays a very similar profile across the UVA and UVB regions to the acidic spectrum. This indicates that the absorption properties of solvated OB is only modestly affected by low pH, with the sunscreen still being able to act as a strong and broad UVA and UVB absorber upon protonation. (We note that the solution-phase absorption spectrum shown here matches the previously published spectra.<sup>50</sup>)

Finally, we note that computational chemistry calculations of the structures of  $[\text{OB} + \text{H}]^+$  presented in Section 3.1C indicate that only single protonation isomers dominate the gas-phase (Fig. 4a) and solution-phase spectra (Fig. 4b).

**3.2B Photofragmentation of protonated oxybenzone.** The difference (laser on–laser off) photofragment mass spectra of  $[\text{OB} + \text{H}]^+$  obtained following photoexcitation at the maxima of bands  $\text{I}_\text{P}$ ,  $\text{II}_\text{P}$ , and  $\text{III}_\text{P}$  at 3.50, 4.27, and 5.17 eV, respectively, are shown in Fig. 5. Photofragmentation is extensive, with the major photofragments at each energy being  $m/z$  151 and 105 (4a) and (4b). The  $m/z$  95, and 77 fragments occur with significant intensity at all three excitation wavelengths, along with a number of lower intensity photofragments.



We note that low-energy CID of  $[\text{OB} + \text{H}]^+$  also results in production of the  $m/z$  151 and 105 ions as the dominant fragments,

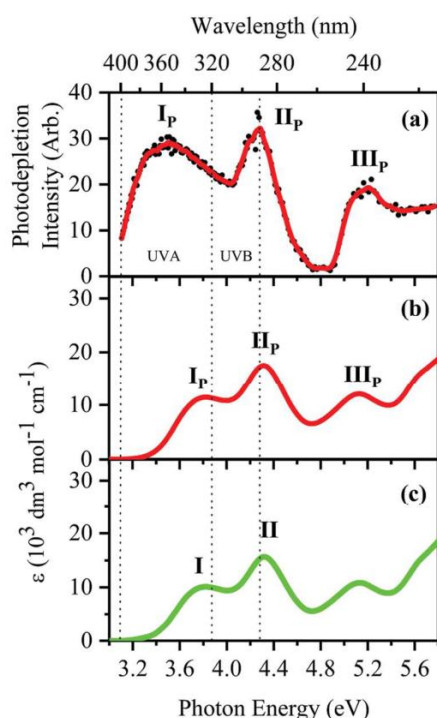


Fig. 4 (a) Gas-phase photodepletion spectrum of protonated oxybenzone ( $[\text{OB} + \text{H}]^+$ ). The solid line is a five-point adjacent average of the data points. (b) Solution-phase absorption spectra of OB under acidic conditions. (c) Solution-phase absorption spectra of OB under neutral conditions.

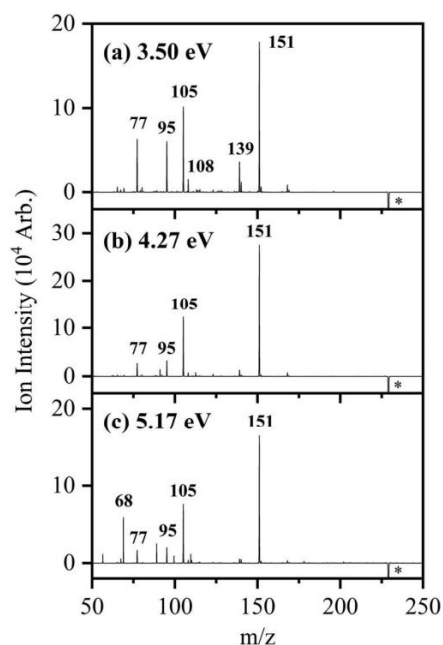


Fig. 5 Photofragment difference (laser on–laser off) mass spectrum of  $[\text{OB} + \text{H}]^+$ , excited at the photodepletion maxima (bands  $\text{I}_\text{P}$ ,  $\text{II}_\text{P}$ , and  $\text{III}_\text{P}$ ) of (a) 3.50, (b) 4.27, and (c) 5.17 eV. \* Represents the depleted parent ion signal at  $m/z$  229.

**Table 3** Proposed structures for the low-intensity ionic fragments of  $[\text{OB} + \text{H}]^+$  ( $m/z$  229) produced during CID and laser photoexcitation

Fragment mass ( $m/z$ )	Proposed structure of fragment	$m/z$ lost from $[\text{OB} + \text{H}]^+$	Fragment results from loss of neutral	Observed in CID <sup>a</sup>	Observed in laser photoexcitation <sup>a</sup>
151		78		✓ (vs)	✓ (vs)
139		90	—	—	✓ (w)
108		121	—	—	✓ (vw)
105		124		✓ (m)	✓ (s)
95 <sup>b</sup>		—	—	✓ (vw)	✓ (m)
77		152		✓ (vw)	✓ (m)

<sup>a</sup> vs (very strong), s (strong), m (medium), w (weak), and vw (very weak). <sup>b</sup>  $m/z$  95 likely  $m/z$  77 + 18.

with the  $m/z$  95 and  $m/z$  77 ions being produced as very minor fragments at higher collision energies. Table 3 presents assignments of all the  $[\text{OB} + \text{H}]^+$  fragment ions and highlights that the major fragments are produced through dissociation on either side of the central carbonyl group. Our structural assignment of  $m/z$  151 and 105 match previously reported CID results of  $[\text{OB} + \text{H}]^+$ .<sup>51</sup> The  $m/z$  77 and  $m/z$  95 ions are common organic cations in mass spectrometry, corresponding to the benzyl cation and its complex with a water molecule.<sup>52–54</sup>

To further investigate the photofragmentation of  $[\text{OB} + \text{H}]^+$ , we turn to considering the photofragment production spectra across the region from 3.10–5.74 eV. Two distinctive spectral profiles are observed for the various photofragment ions, with the  $m/z$  151 and 105 photofragments displaying identical spectral profiles (illustrated in Fig. 6b for  $m/z$  151), and  $m/z$  77, 95, 108 and 139 also displaying an identical profile (illustrated in Fig. 6c for  $m/z$  77). The photodepletion spectrum for  $[\text{OB} + \text{H}]^+$  is reproduced in Fig. 6a, for ease of comparison. Notably, the  $m/z$  151 photofragment is produced much more strongly through band  $\text{II}_p$  than band  $\text{I}_p$ , whereas this trend is reversed for the  $m/z$  77 photofragment spectrum. Overall, all of the photofragments are produced across the photodepletion region studied here, with very low photofragmentation or photodepletion in the “hole” region centered at 260 nm (4.77 eV). However, the relative intensities of the different photofragments change significantly across the spectral range. The complete set of photofragmentation action spectra are provided in Section S4 of the ESI.†

To further investigate the relationship between the  $m/z$  151/105 photofragments and the  $m/z$  77/95 photofragments, we performed

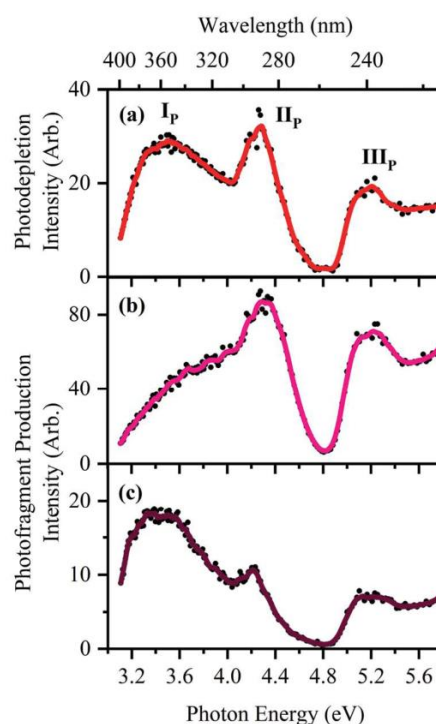


**Fig. 6** (a) Gas-phase UV absorption (photodepletion) spectra of  $[\text{OB} + \text{H}]^+$ . (b and c) Photofragment production spectra of the photofragments at  $m/z$  151 and  $m/z$  77, respectively. The solid line is a five-point adjacent average of the data points.

a series of experiments where each of the dominant  $m/z$  151 and 105 photofragments were isolated in the ion trap, and subjected to laser excitation. This allowed us to acquire their photodepletion spectra, as well as identify their primary photofragments. Fig. 7 presents the results obtained for the  $m/z$  151 ion. This ion displays a very broad absorption between 340–260 nm (3.65–4.77 eV), with further absorption towards the high-energy region. The most intense photofragments observed from  $m/z$  151 are  $m/z$  123, 95, 80 and 52. Fig. 8 displays the corresponding data for the  $m/z$  105 ion, which can be seen to display one absorption band between 340–280 nm and a second, stronger band, from 270–230 nm. The main photofragments produced

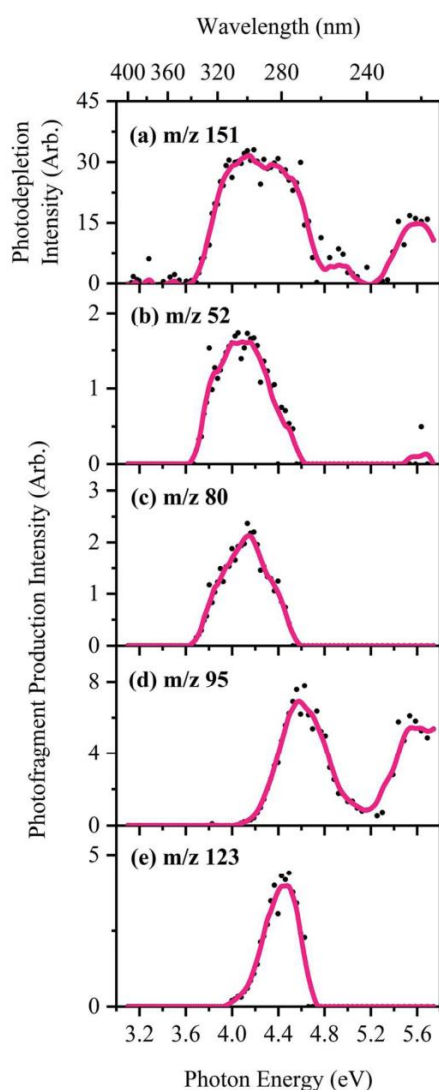


Fig. 7 The photodepletion spectrum (absorption) of photofragment ion  $m/z$  151 (a), along with the photofragment action spectra of its primary photofragments (b)  $m/z$  52, (c)  $m/z$  80, (d)  $m/z$  95, and (e)  $m/z$  123. The solid line is a five-point adjacent average of the data points.

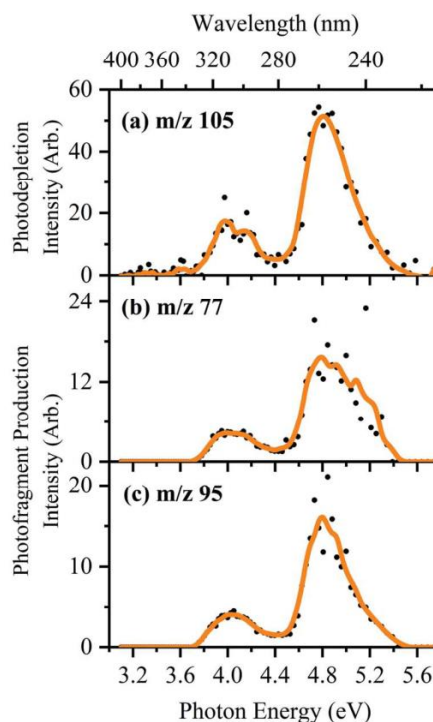


Fig. 8 The photodepletion spectrum (absorption) of photofragment ion  $m/z$  105 (a), along with the photofragment action spectra of its primary photofragments (b)  $m/z$  77 and (c)  $m/z$  95. The solid line is a five-point adjacent average of the data points.

across these two bands are  $m/z$  95 and 77. For both  $m/z$  151 and 105, it is evident that  $m/z$  95 and 77 can therefore be produced as secondary photofragments at energies above 300 nm. However, for both  $m/z$  151 and  $m/z$  105, absorption is negligible across the key band  $I_P$  region, *i.e.* at wavelengths longer than 340 nm. This leads us to conclude that the  $m/z$  77, 95, 108 and 139 primary photofragments from  $[\text{OB} + \text{H}]^+$  are being produced in this VIS–UVA region through a different pathway (evident in the distinctive production spectrum) from the  $m/z$  151 and 105 photofragments.

**3.2C Further discussion of the photodissociation dynamics of protonated oxybenzone.** While a detailed mapping of the photodissociation dynamics of  $[\text{OB} + \text{H}]^+$  will require time-resolved measurements of the production of the various photofragments, some initial insight can be gained from considering whether excited state decay is statistical or non-statistical. In general, excited state decay can be classified as statistical when the observed photofragments match those obtained when the ground electronic state is subjected to thermal dissociation, as in CID. Non-statistical (or non-ergodic) processes occur when dissociation proceeds directly from the excited state without significant involvement of a conical intersection to bring the system back to the ground electronic state in the vicinity of the starting geometry.<sup>55</sup> For non-statistical decay, the photofragments will differ significantly in relative intensity

and identity from those observed under thermal fragmentation conditions.

Our measurements on  $[\text{OB} + \text{H}]^+$  have revealed that the photofragments produced in the region of band **I<sub>D</sub>** display relative intensities that are significantly different from those observed upon CID, *i.e.* the intensities of the  $m/z$  139, 108, 95, and 77 ions are considerably more intense than in CID, suggesting that the excited state surface accessed in this region is not simply evolving through a conical intersection back to the ground state in the region of the vertical transition. A non-statistical pathway appears to be dominant in this region, with direct dissociation from the excited state. Such a situation is highly undesirable for a sunscreen molecule, and merits further investigation in dynamical studies in condensed-phase media.

**3.2D Quantum chemical calculations of protonated oxybenzene.**  $[\text{OB} + \text{H}]^+$  isomers were identified by attaching a proton to each oxygen atom on neutral OB prior to optimization, and allowing the ion to rotate freely during optimization. Four relatively low-energy isomers (within  $30 \text{ kJ mol}^{-1}$  of the minimum for the gaseous structures) were identified (Scheme 2), with the relative energies being displayed in Table 2. Comprehensive structures are included in Section S2 of the ESI.†

The lowest energy  $[\text{OB} + \text{H}]^+$  isomers are closer in relative energy than those of  $[\text{OB} - \text{H}]^-$ , as well as in average nuclear displacement. The lowest energy **P1** and **P2** structures, which are only distinguished by a methyl group rotation, and are close enough in energy that their combined Boltzmann population accounts for more than 90% of the gaseous population (66% and 31% respectively). This trend is carried over in methanol conditions where **P1** accounts for 41% and **P2** for 55% of the average population. We anticipate that the ESI ion ensemble will be dominated by a mixture of **P1** and **P2** in our experiment (protic spray solvent).<sup>31,32,38</sup> (These rotamers are expected to produce identical photodepletion spectra at the resolution of our spectrometer.<sup>36</sup>) It is important that our calculations reveal the presence of effectively just a single isomer, as it means that the gaseous photodepletion and solution-phase absorption spectra discussed above could be assigned to just a single isomer, simplifying the analysis of the spectra compared to similar systems where distinctive multiple protonation isomers are present.<sup>31,32,38</sup>

## 4. Concluding remarks

The photodepletion spectra of  $[\text{OB} - \text{H}]^-$  and  $[\text{OB} + \text{H}]^+$  obtained in this work clearly illustrate the effect that protonation state can have on the absorption properties of a typical organic sunscreen molecule. While the effect of protonation is relatively modest (primarily associated with shifting of the UVA region absorption), deprotonation has a more significant effect, with photoabsorption being significantly decreased between 370–330 nm compared to the neutral system. Our comparison of the solution-phase and gas-phase spectra indicates that these differences occur both in solution and in the gas-phase, so will be important even within the complex environment of a sunscreen mixture.

One of the novel aspects of our gas-phase experiment is that it allows us to obtain a full picture of the photofragments produced following excitation.  $[\text{OB} - \text{H}]^-$  and  $[\text{OB} + \text{H}]^+$  photodissociate by very distinct pathways, with  $[\text{OB} - \text{H}]^-$  primarily fragmenting *via* pathways associated with loss of the anisole methyl group, while  $[\text{OB} + \text{H}]^+$  dissociates by rupture of the molecule on either side of the central carbonyl group. For  $[\text{OB} - \text{H}]^-$ , the fragmentation pathway appears to follow those of neutral anisoles and negatively charged flavinoids,<sup>57</sup> which are known to eject methyl radicals and hydrogen atoms. For  $[\text{OB} + \text{H}]^+$ , the dissociation pathways branch from the central protonated carbonyl, in line with the known mass spectrometric fragmentation behavior of such ions.<sup>58</sup>

For  $[\text{OB} - \text{H}]^-$ , it is important to note that it produces large quantities of electrons following photoexcitation, as well as generating free radicals by all of its dissociation routes. This is a highly undesirable property for a sunscreen molecule, which leads to the question of how this behavior will be modified on going to the condensed phase. It is well established that the propensity of an anionic molecule to photodetach will be quenched upon solvation,<sup>59</sup> so that the photofragmentation pathways are likely to become relatively more important in condensed media. Recent work by Li *et al.* has found that oxybenzone photodegrades in aqueous alkaline solutions made from pure water.<sup>26</sup> The authors were broadly concerned with indirect photodegradation of oxybenzone in surface and salt waters (due to environmental and wastewater management implications) by transient photosensitizers such as the triplet excited states of dissolved organic matter (<sup>3</sup>DOM), hydroxy radicals ( $\bullet\text{OH}$ ), and singlet oxygen (<sup>1</sup>O<sub>2</sub>). Their experiments confirmed the presence of free  $\bullet\text{OH}$  in their photolytic systems as well and the ability for  $\bullet\text{OH}$  and <sup>3</sup>DOM to photodegrade oxybenzone. The gas-phase work conducted here is in line with these observations and provides further information on the details on the active photodegradation pathways.

In considering how well the protonated and deprotonated forms of OB behave as sunscreen molecules, it is also important to consider the ability of the ionic forms of the molecule to undergo ultrafast excited state decay back to the electronic ground state from where excess energy can be dissipated as heat energy. This process is now well understood for neutral oxybenzone, following detailed quantum chemical calculations by Domecke and co-workers, who found that excited state decay involves proton transfer from the enol to keto forms, followed by rapid internal conversion.<sup>25</sup> Our calculations predict that the keto–enol site of oxybenzone is the protonation/deprotonation location, so it would be unsurprising to discover that the neutral ultrafast decay mechanism is significantly perturbed in the presence of acid or base. In  $[\text{OB} + \text{H}]^+$ , we have found evidence for two distinctive decay pathways in the UVA region, which is notable since it is well documented that locally excited states (such as a UVA  $\pi$ – $\pi^*$  transition) can couple with nearby charge-transfer states.<sup>60–62</sup> Interestingly, Dean *et al.* have demonstrated that this situation occurs for sinapoyl malate,<sup>15</sup> a photoprotection molecule found in plants. Future time-resolved measurements are warranted to more fully investigate this.

In conclusion, we report the first gas-phase laser photodissociation of the protonated and deprotonated forms of the model sunscreen, oxybenzone. The results presented provide important new insights into how protonation behavior can affect the intrinsic properties of an organic sunscreen and demonstrate the utility of laser-interfaced mass spectrometry for mapping the photodegradation pathways of such systems.

## Conflicts of interest

There are no conflicts to declare.

## Acknowledgements

This work was funded through the Leverhulme Trust Research Project Grant RPG-2017-147. We thank the University of York and the Department of Chemistry at the University of York for provision of funds for the Horizon OPO laser system, as well as the York Advanced Research Computing Cluster (YARCC) for access to computational resources.

## References

- L. A. Baker, B. Marchetti, T. N. V. Karsili, V. G. Stavros and M. N. R. Ashfold, *Chem. Soc. Rev.*, 2017, **46**, 3770–3791.
- R. Losantos, I. Funes-Ardoiz, J. Aguilera, E. Herrera-Ceballos, C. Garcia-Iriepa, P. J. Campos and D. Sampedro, *Angew. Chem., Int. Ed. Engl.*, 2017, **56**, 2632–2635.
- N. D. Rodrigues, M. Staniforth and V. G. Stavros, *Proc. R. Soc. A*, 2016, **472**, 20160677.
- S. Forestier, *J. Am. Acad. Dermatol.*, 2008, **58**, S133–138.
- V. G. Stavros, *Nat. Chem.*, 2014, **6**, 955–956.
- M. T. Ignasiak, C. Houee-Levin, G. Kciuk, B. Marciniak and T. Pedzinski, *ChemPhysChem*, 2015, **16**, 628–633.
- M. E. Burnett and S. Q. Wang, *Photodermatol., Photoimmunol. Photomed.*, 2011, **27**, 58–67.
- M. Loden, H. Beitner, H. Gonzalez, D. W. Edstrom, U. Akerstrom, J. Austad, I. Buraczewska-Norin, M. Matsson and H. C. Wulf, *Br. J. Dermatol.*, 2011, **165**, 255–262.
- L. A. Baker, M. D. Horbury, S. E. Greenough, M. N. Ashfold and V. G. Stavros, *Photochem. Photobiol. Sci.*, 2015, **14**, 1814–1820.
- L. A. Baker, M. D. Horbury, S. E. Greenough, P. M. Coulter, T. N. Karsili, G. M. Roberts, A. J. Orr-Ewing, M. N. Ashfold and V. G. Stavros, *J. Phys. Chem. Lett.*, 2015, **6**, 1363–1368.
- L. A. Baker, M. Staniforth, A. L. Flourat, F. Allais and V. G. Stavros, *ChemPhotoChem*, 2018, **2**, 743–748.
- J. Luo, Y. Liu, S. Yang, A. L. Flourat, F. Allais and K. Han, *J. Phys. Chem. Lett.*, 2017, **8**, 1025–1030.
- Y. Peperstraete, M. Staniforth, L. A. Baker, N. D. Rodrigues, N. C. Cole-Filipiak, W. D. Quan and V. G. Stavros, *Phys. Chem. Chem. Phys.*, 2016, **18**, 28140–28149.
- E. M. Tan, M. Hilbers and W. J. Buma, *J. Phys. Chem. Lett.*, 2014, **5**, 2464–2468.
- J. C. Dean, R. Kusaka, P. S. Walsh, F. Allais and T. S. Zwier, *J. Am. Chem. Soc.*, 2014, **136**, 14780–14795.
- S. R. Domingos and M. Schnell, *J. Phys. Chem. Lett.*, 2018, **9**, 4963–4968.
- Y. Miyazaki, K. Yamamoto, J. Aoki, T. Ikeda, Y. Inokuchi, M. Ehara and T. Ebata, *J. Chem. Phys.*, 2014, **141**, 244313.
- N. D. Rodrigues, M. Staniforth, J. D. Young, Y. Peperstraete, N. C. Cole-Filipiak, J. R. Gord, P. S. Walsh, D. M. Hewett, T. S. Zwier and V. G. Stavros, *Faraday Discuss.*, 2016, **194**, 709–729.
- C. P. Rodrigo, W. H. James, 3rd and T. S. Zwier, *J. Am. Chem. Soc.*, 2011, **133**, 2632–2641.
- Y. G. Fang, C. X. Li, X. P. Chang and G. Cui, *ChemPhysChem*, 2018, **19**, 744–752.
- C. X. Li, W. W. Guo, B. B. Xie and G. Cui, *J. Chem. Phys.*, 2016, **145**, 074308.
- L. B. Assis Oliveira, T. L. Fonseca, B. J. Costa Cabral, K. Coutinho and S. Canuto, *J. Chem. Phys.*, 2016, **145**, 084501.
- B. Marchetti and T. N. Karsili, *Phys. Chem. Chem. Phys.*, 2016, **18**, 3644–3658.
- X. P. Chang, C. X. Li, B. B. Xie and G. Cui, *J. Phys. Chem. A*, 2015, **119**, 11488–11497.
- T. N. Karsili, B. Marchetti, M. N. Ashfold and W. Domcke, *J. Phys. Chem. A*, 2014, **118**, 11999–12010.
- Y. Li, X. Qiao, C. Zhou, Y. N. Zhang, Z. Fu and J. Chen, *Chemosphere*, 2016, **153**, 494–499.
- E. De Laurentiis, M. Minella, M. Sarakha, A. Marrese, C. Minero, G. Mailhot, M. Brigante and D. Vione, *Water Res.*, 2013, **47**, 5943–5953.
- E. Proksch, *J. Dermatol.*, 2018, **45**, 1044–1052.
- H. Lambers, S. Piessens, A. Bloem, H. Pronk and P. Finkel, *Int. J. Cosmet. Sci.*, 2006, **28**, 359–370.
- K. Kulthanan, P. Nuchkull and S. Varothai, *Asian Pac. J. Allergy Immunol.*, 2013, **3**, 155–160.
- E. Matthews and C. E. Dessent, *J. Phys. Chem. A*, 2016, **120**, 9209–9216.
- E. Matthews and C. E. H. Dessent, *J. Phys. Chem. Lett.*, 2018, **9**, 6124–6130.
- E. Matthews, R. Cercola and C. E. H. Dessent, *Molecules*, Basel, Switzerland, vol. 23, 2018.
- R. Kumasaka, A. Kikuchi and M. Yagi, *Photochem. Photobiol.*, 2014, **90**, 727–733.
- N. Serpone, A. Salinaro, A. V. Emeline, S. Horikoshi, H. Hidaka and J. Zhao, *Photochem. Photobiol. Sci.*, 2002, **1**, 970–981.
- Y.-S. Liu, G.-G. Ying, A. Shareef and R. S. Kookana, *Environ. Chem.*, 2011, **8**, 581–588.
- E. Matthews, A. Sen, N. Yoshikawa, E. Bergstrom and C. E. Dessent, *Phys. Chem. Chem. Phys.*, 2016, **18**, 15143–15152.
- E. Matthews and C. E. H. Dessent, *Phys. Chem. Chem. Phys.*, 2017, **19**, 17434–17440.
- S. M. Wellman and R. A. Jockusch, *J. Phys. Chem. A*, 2015, **119**, 6333–6338.
- A. Sen, T. F. Luxford, N. Yoshikawa and C. E. Dessent, *Phys. Chem. Chem. Phys.*, 2014, **16**, 15490–15500.
- R. Antoine and P. Dugourd, *Phys. Chem. Chem. Phys.*, 2011, **13**, 16494–16509.

- 42 W. E. Boxford and C. E. Dessent, *Phys. Chem. Chem. Phys.*, 2006, **8**, 5151–5165.
- 43 T. F. M. Luxford, E. M. Milner, N. Yoshikawa, C. Bullivant and C. E. H. Dessent, *Chem. Phys. Lett.*, 2013, **577**, 1–5.
- 44 M. J. Frisch, G. W. Trucks, H. B. Schlegel, G. E. Scuseria, M. A. Robb, J. R. Cheeseman, G. Scalmani, V. Barone, B. Mennucci, G. A. Petersson, H. Nakatsuji, M. Caricato, X. Li, H. P. Hratchian, A. F. Izmaylov, J. Bloino, G. Zheng, J. L. Sonnenberg, M. Hada, M. Ehara, K. Toyota, R. Fukuda, J. Hasegawa, M. Ishida, T. Nakajima, Y. Honda, O. Kitao, H. Nakai, T. Vreven, J. A. Montgomery Jr., J. E. Peralta, F. Ogliaro, M. J. Bearpark, J. Heyd, E. N. Brothers, K. N. Kudin, V. N. Staroverov, R. Kobayashi, J. Normand, K. Raghavachari, A. P. Rendell, J. C. Burant, S. S. Iyengar, J. Tomasi, M. Cossi, N. Rega, N. J. Millam, M. Klenc, J. E. Knox, J. B. Cross, V. Bakken, C. Adamo, J. Jaramillo, R. Gomperts, R. E. Stratmann, O. Yazyev, A. J. Austin, R. Cammi, C. Pomelli, J. W. Ochterski, R. L. Martin, K. Morokuma, V. G. Zakrzewski, G. A. Voth, P. Salvador, J. J. Dannenberg, S. Dapprich, A. D. Daniels, Ö. Farkas, J. B. Foresman, J. V. Ortiz, J. Cioslowski and D. J. Fox, *Gaussian 09, Revision D.01*, Gaussian, Inc., Wallingford, CT, 2009.
- 45 A. V. Friderichsen, E.-J. Shin, R. J. Evans, M. R. Nimlos, D. C. Dayton and G. B. Ellison, *Fuel*, 2001, **80**, 1747–1755.
- 46 A. M. Scheer, C. Mukarakate, D. J. Robichaud, G. B. Ellison and M. R. Nimlos, *J. Phys. Chem. A*, 2010, **114**, 9043–9056.
- 47 P. J. Gates and N. P. Lopes, *Int. J. Anal. Chem.*, 2012, 259217.
- 48 J. B. Kim, T. I. Yacovitch, C. Hock and D. M. Neumark, *Phys. Chem. Chem. Phys.*, 2011, **13**, 17378–17383.
- 49 J. H. Richardson, L. M. Stephenson and J. I. Brauman, *J. Chem. Phys.*, 1975, **62**, 1580–1582.
- 50 B. M. Baughman, E. Stennett, R. E. Lipner, A. C. Rudawsky and S. J. Schmidtke, *J. Phys. Chem. A*, 2009, **113**, 8011–8019.
- 51 P. Gago-Ferrero, M. Badia-Fabregat, A. Olivares, B. Pina, P. Blaquez, T. Vicent, G. Caminal, M. S. Diaz-Cruz and D. Barcelo, *Sci. Total Environ.*, 2012, **427–428**, 355–363.
- 52 M. Miyazaki, A. Fujii and N. Mikami, *J. Phys. Chem. A*, 2004, **108**, 8269–8272.
- 53 M. Miyazaki, A. Fujii, T. Ebata and N. Mikami, *Phys. Chem. Chem. Phys.*, 2003, **5**, 1137–1148.
- 54 D. Kuck, *Mass Spectrom. Rev.*, 1990, **9**, 583–630.
- 55 B. Lucas, M. Barat, J. A. Fayeton, C. Jouvet, P. Çarçabal and G. Grégoire, *Chem. Phys.*, 2008, **347**, 324–330.
- 56 W. D. Geppert, C. E. H. Dessent, S. Ullrich and K. Müller-Dethlefs, *J. Phys. Chem. A*, 1999, **103**, 7186–7191.
- 57 U. Justesen, *J. Mass Spectrom.*, 2001, **36**, 169–178.
- 58 D. P. Demarque, A. E. Crotti, R. Vessecchi, J. L. Lopes and N. P. Lopes, *Nat. Prod. Rep.*, 2016, **33**, 432–455.
- 59 D. Serxner, C. E. H. Dessent and M. A. Johnson, *J. Chem. Phys.*, 1996, **105**, 7231–7234.
- 60 N. A. van Dantzig, H. Shou, J. C. Alfano, N. c. C. Yang and D. H. Levy, *J. Chem. Phys.*, 1994, **100**, 7068–7078.
- 61 S. Jiang and D. H. Levy, *J. Phys. Chem. A*, 2002, **106**, 8590–8598.
- 62 A. L. Sobolewski, W. Domcke, C. Dedonder-Lardeux and C. Jouvet, *Phys. Chem. Chem. Phys.*, 2002, **4**, 1093–1100.

# Chapter 3

## Direct Observation of Photochemical Free Radical Production from the Sunscreen 2- Phenylbenzimidazole-5-Sulfonic Acid via Laser- Interfaced Mass Spectrometry

### 3.1 Declaration

This work was first published in *ChemPhotoChem* on 25 July 2019 and formed Volume 3 (Issue 12) published in December 2019.

All experimental and computational work presented within this paper was performed, processed and analyzed by myself.

I wrote a complete first draft of the manuscript, which was subsequently circulated through Dr. Jacob A. Berenbeim and Prof. Caroline E. H. Dessent for modification and proof-reading.



Signed Prof. Caroline E. H. Dessent (University of York, U.K.)

**3.2 Paper II: Direct Observation of Photochemical Free Radical  
Production from the Sunscreen 2-Phenylbenzimidazole-5-Sulfonic  
Acid *via* Laser-Interfaced Mass Spectrometry**

# Direct Observation of Photochemical Free Radical Production from the Sunscreen 2-Phenylbenzimidazole-5-Sulfonic Acid via Laser-Interfaced Mass Spectrometry

Natalie G. K. Wong,<sup>[a]</sup> Jacob A. Berenbeim,<sup>[a]</sup> and Caroline E. H. Dessent<sup>\*,[a]</sup>

The common sunscreen molecule 2-phenylbenzimidazole-5-sulfonic acid (PBSA) is studied in its gas-phase deprotonated form ([PBSA-H]<sup>-</sup>) for the first time as an important step in achieving a better understanding of its behavior as a photosensitizer. UV laser-interfaced mass spectrometry is employed, revealing that [PBSA-H]<sup>-</sup> photofragments into three ionic products (*m/z* 208, 193, and 80) with distinctive wavelength-dependent production profiles. Both the *m/z* 208 and 80 channels produce associated neutral free radical species. Collision-induced dissociation is performed on [PBSA-H]<sup>-</sup>,

showing that its hot ground-state dissociates only into *m/z* 193 (statistical fragment). Therefore, the *m/z* 208 and 80 fragments which are produced strongly through the UVA/UVB are characterized as non-statistical photofragments associated with non-ergodic excited-state decay. Our observation of non-statistical photofragments reveal that [PBSA-H]<sup>-</sup> is not behaving as a model sunscreen molecule. Further, our results indicate that the T<sub>1</sub> state, associated with photosensitization, decays with direct free radical production.

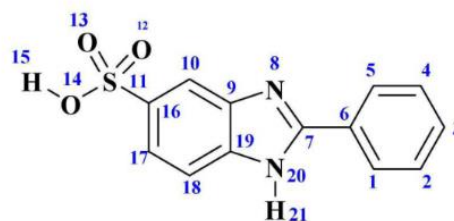
## 1. Introduction

Sunscreens are widely employed to protect human skin from sunburn and the long-term consequences of exposure to the sun. The suitability of a given sunscreen molecule depends on a range of factors, but its effectiveness will clearly be limited if it behaves as a photosensitizer.<sup>[1,2]</sup> (A photosensitizer is a molecule that subsequent to its activation by light, produces a chemical change in another molecule. Commonly, this involves generating reactive oxygen species that initiate further chemical reactions.) Surprisingly, several common organic sunscreen molecules (e.g. octocrylene, octylmethoxycinnamate, and oxybenzone) have been reported to enhance the production of reactive oxygen species.<sup>[3–8]</sup> 2-phenylbenzimidazole-5-sulfonic acid (PBSA) is one such widely-used sunscreen (Scheme 1), which has been found to photogenerate reactive oxygen species and oxidize guanine residues in cellulose under UV radiation.<sup>[9–11]</sup> There is currently a need to better understand the photosensitization mechanisms that occur for UV filters such as PBSA, in order to aid the rational development of future sunscreens.<sup>[1,2]</sup>

In this paper, we adopt a new approach to better understand the photodegradation pathways and hence photosensitization mechanisms that are available to PBSA through applying the novel technique of laser-interfaced photodissociation mass spectrometry.<sup>[12–14]</sup> PBSA exists as a deprotonated species, *i.e.* [PBSA-H]<sup>-</sup>, in solution due to the low p*K*<sub>a</sub> of its sulfonic acid

group. Here, we employ electrospray ionization to transfer [PBSA-H]<sup>-</sup> from solution into the gas phase where the ion is then mass selected and interrogated with laser photons over a wide UV range. This allows us to monitor how the absorbance of the anion varies with wavelength, while simultaneously measuring the production of any photoproducts.<sup>[12,13]</sup> Our laser-based approach is in the spirit of a number of recent studies where advanced spectroscopic techniques have been applied to sunscreen molecules under highly-controlled conditions.<sup>[15–23]</sup>

Recent computational studies by Zhang *et al.* and Shen have been performed on PBSA to better understand its photophysical properties.<sup>[24,25]</sup> Zhang *et al.* used density functional theory to assess the potential for triplet-state electron transfer from different protonation states of PBSA to triplet oxygen.<sup>[24]</sup> They found that deprotonated PBSA could spontaneously transfer an electron to <sup>3</sup>O<sub>2</sub> to generate reactive O<sub>2</sub><sup>-</sup>, with the different protonation states varying in their propensity to effect electron transfer. Shen used time-dependent density functional theory to assess PBSA's photosensitizing potential, finding further evidence that singlet oxygen can be produced from the triplet excited state.<sup>[25]</sup> To date, no computational studies have been performed to calculate the excited-state potential energy surfaces or direct photodegradation products.



Scheme 1. Schematic diagram of PBSA with atom labels.

[a] N. G. K. Wong, Dr. J. A. Berenbeim, Dr. C. E. H. Dessent  
Department of Chemistry  
University of York  
Heslington, York, YO10 5DD (U.K.)  
E-mail: caroline.dessent@york.ac.uk

Supporting information for this article is available on the WWW under <https://doi.org/10.1002/cptc.201900149>

There have also been a number of solution-phase photochemical studies of PBSA, which have confirmed that the T<sub>1</sub> state can generate reactive oxygen species, and that their production is pH dependent.<sup>[10,26–30]</sup> Experiments to track direct photodegradation products in solution are challenging due to secondary reactions and environmental effects. However, such measurements are important outside of the immediate interest in sunscreens, since these molecules are common aquatic pollutants, and a full understanding of potential photoproducts and their toxicity is crucial.<sup>[26–30]</sup>

Gas-phase photochemical studies provide a complementary approach to mapping photodegradation where photoproducts can be directly identified, and experimental results can be straightforwardly compared to theoretical calculations. However, gas-phase laser spectroscopy of the ionic forms of sunscreen molecules are currently sparse,<sup>[12,15]</sup> with only oxybenzone having been studied very recently in its protonated and deprotonated forms.<sup>[15]</sup> Notably, deprotonated oxybenzone was observed to photofragment with production of methyl radicals in the UVB. This result is concerning as it adds to long-standing concerns that some sunscreens can produce free radicals following photoexcitation.<sup>[19]</sup> In the current study on PBSA, we aim to better understand the generality of our recent oxybenzone results, as well as providing a more detailed insight into the photosensitizing behavior of PBSA.

## Experimental and Computational Details

The gaseous ion absorption (photodepletion) and photofragment production spectra of [PBSA-H]<sup>−</sup>, were recorded in vacuo using action spectroscopy. An AmaZon SL mass spectrometer (Bruker Daltonics Inc., Billerica, MA, USA) modified for laser-interfaced mass spectrometry (LIMS), was used as described previously.<sup>[12,13]</sup> PBSA was purchased from Sigma-Aldrich (St. Louis, MA, USA) and used as received. HPLC-grade acetonitrile was purchased from Fisher Scientific, Inc. (Pittsburgh, PA, USA). PBSA solutions (1 × 10<sup>−5</sup> mol dm<sup>−3</sup> in CH<sub>3</sub>CN) were electrosprayed at a capillary temperature 160 °C.

[PBSA-H]<sup>−</sup> was mass-selected (*m/z* 273) and isolated in the ion trap prior to laser irradiation. Photons were produced by an Nd:YAG pumped OPO laser (Surelite™/Horizon™, Amplitude Laser Group, San Jose, CA, USA), giving 0.3 ± 10% mJ across the range 500–216 nm (2.48–5.74 eV), with 2 nm laser step sizes. Photofragmentation experiments were conducted with an ion accumulation time of 10 ms. To minimize the possibility of multiphoton events via sequential absorption, each mass-selected ion packet interacts with only one laser pulse (fragmentation time of 100 ms), and photodepletion restricted to ~40% of the precursor ion at the wavelength of maximum absorption. Multiphoton events via instantaneous absorption of multiple photons in the Frank-Condon region are negligible as the laser beam is only softly focused through the ion-trap region. Photodepletion (PD) of [PBSA-H]<sup>−</sup> was measured as a function of the scanned wavelength, with photofragment production (PF) recorded simultaneously [Eqs. (1a)–(1c)]:

$$\text{Photodepletion Intensity} = \frac{\ln\left(\frac{\text{Int}_{\text{OFF}}}{\text{Int}_{\text{ON}}}\right)}{\lambda \times P} \quad (1a)$$

$$\text{Photofragmentation Intensity} = \frac{\text{Int}_{\text{FRAG}}}{\lambda \times P} \quad (1b)$$

$$\text{Relative Ion Yield} = \text{Int}_{\text{FRAG}}/\text{Int}_{\text{PFT}} \quad (1c)$$

In these expressions, Int<sub>OFF</sub> and Int<sub>ON</sub> are the laser off and on parent ion peak intensities respectively; Int<sub>FRAG</sub> is the fragment intensity with the laser on; λ is the excitation wavelength (nm); P is the laser pulse energy (mJ); and Int<sub>PFT</sub> is the sum of the photofragment ion intensities with the laser on. The photodepletion spectrum is considered to be equivalent to the gaseous absorption spectrum in the limit where excited state fluorescence is negligible.<sup>[13,14,31]</sup> Photodepletion intensities were taken from an average of three runs at each wavelength of the range studied. We note that fragment ions with *m/z* < 50 are not detectable in our mass spectrometer since low masses fall outside the ion-trap mass-window.

Higher-energy collisional dissociation (HCD) was performed to investigate the ground-state thermal fragmentation characteristics of [PBSA-H]<sup>−</sup>, using an Orbitrap™ Fusion Tribrid mass spectrometer (Thermo Fisher Scientific, Waltham, MA, U.S.A.) as described previously.<sup>[32,33]</sup> Solution-phase UV/Vis absorption spectra of PBSA (aqueous solution; 3 × 10<sup>−5</sup> mol dm<sup>−3</sup>) were recorded with a UV-1800 spectrophotometer (Shimadzu, Kyoto, Japan) with a 10 mm UV quartz cuvette, with deionized H<sub>2</sub>O as the baseline solvent.

All calculations were performed using Density Functional Theory (DFT) at the B3LYP/6-31+G\*\* level in Gaussian 09.<sup>[34]</sup> The bulk solvent effect of CH<sub>3</sub>CN was considered by using the integral equation formalism polarized continuum model (IEFPCM) based on the self-consistent-reaction-field (SCRF) method. All reported structures correspond to true minima, as confirmed by frequency calculations.

## 2. Results and Discussion

### 2.1. Identification of the Deprotonation Site in [PBSA-H]<sup>−</sup> via Density Functional Theory Calculations

The sulfonic acid group is a strongly acidic group, so PBSA will be deprotonated at the H15 position (Scheme 1) in aqueous solution to form the sulfonate monoanion.<sup>[29]</sup> Deprotonation is also possible from the H21 position at higher pH.<sup>[29]</sup> Relative energies of the two deprotonomers of [PBSA-H]<sup>−</sup> were calculated in the gas phase and in acetonitrile to reveal which deprotonomer or deprotonomer(s) will be produced following electrospray (Table 1). (Electrospray does not always transfer the most stable

**Table 1.** Calculated relative electronic energies and gaseous vertical detachment energies (VDE) of the deprotonated isomers of PBSA calculated at the B3LYP/6-31+G\*\* level.

Isomer	Relative electronic energy [kJ/mol] <sup>[a]</sup>		VDE [eV] <sup>[b]</sup>
	Gaseous	Acetonitrile	
O14	0	0	4.39
N20	14.3	90.7	4.04

[a] Zero-point energy corrected. [b] VDE = *E* (neutral at optimized anion geometry) − *E* (anion). This is included in the table for comparison with the experimental spectra.

solution-phase ion to the gas phase).<sup>[12,35,36]</sup> In the subsequent discussion, we label the two possible deprotonomers as **O14** and **N20** in line with the excess negative-charge site.

As expected, deprotonation is favored from the sulfonic acid group (**O14**), both in the gas phase and in acetonitrile, although the relative energies of the two deprotonomers are closer in the gas phase. Boltzmann population calculations indicate that the **O14** deprotonomer dominates (> 99.9%) in acetonitrile at 458 K. Since electrospray from acetonitrile solutions maintains the solution-phase ratios of different tautomeric species,<sup>[12,35]</sup> we expect the **O14** deprotonomer to almost entirely dominate the gaseous ion population. Vertical detachment energies (VDE) of the gaseous deprotonomers are also listed in Table 1.

## 2.2. UV Absorption Spectra of [PBSA-H]<sup>-</sup>: Gas Phase versus Solution Phase

Figure 1 shows the electrospray ionization mass spectrum obtained when a solution of PBSA in acetonitrile is sprayed in negative ion mode, showing [PBSA-H]<sup>-</sup> (*m/z* 273) as the dominant peak. The gas-phase absorption spectrum of mass-selected [PBSA-H]<sup>-</sup> across the 2.48–5.74 eV (500–216 nm) range, recorded *via* photodepletion, is shown in Figure 2a. Mass selection is a key advantage of the experimental approach we employ here as it allows us to directly probe the intrinsic properties of the [PBSA-H]<sup>-</sup> anion.

The gaseous absorption spectrum of [PBSA-H]<sup>-</sup> displays strong absorption in the UVA region (with an absorption onset around 3.40 eV) through a band which then reduces in intensity through the UVB range. Absorption again increases to higher energies through the UVC region. To aid discussion of the photofragment production spectra (see Section 2.3), the photodepletion spectrum has been labelled as being composed of features I–IV, with I representing the strong UVA-UVB band. Figure 2b presents an aqueous absorption spectrum of PBSA (pH 7.1) obtained as part of this work for direct comparison with the gas-phase absorption spectrum. The spectrum agrees well with previously-published ones.<sup>[5,11,26–29]</sup> Comparing the gaseous and solution-phase spectra, feature I can be seen to blue-shift significantly on going from the gas-

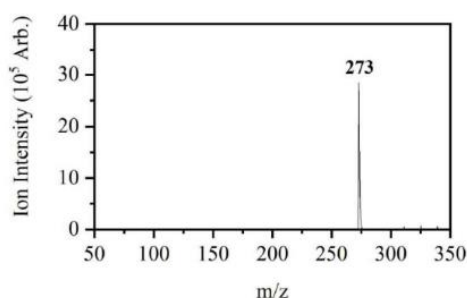


Figure 1. Negative ion electrospray ionization mass spectrum of [PBSA-H]<sup>-</sup> (*m/z* 273).

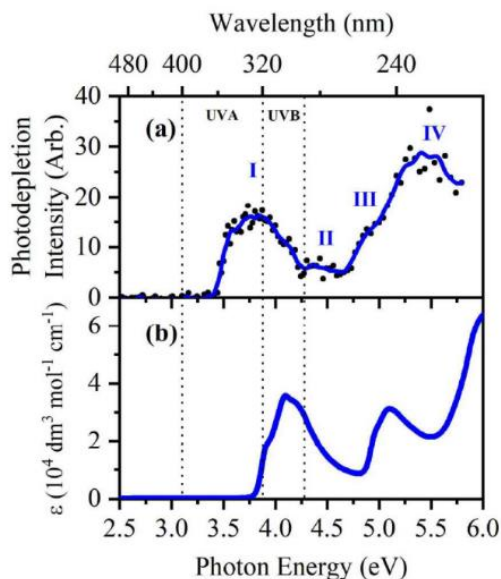


Figure 2. (a) Gas-phase UV absorption (photodepletion) spectrum of [PBSA-H]<sup>-</sup>. (b) Aqueous UV absorption spectrum of PBSA ( $3 \times 10^{-5}$  mol dm<sup>-3</sup>) at pH 7.1.

phase to solution (band maxima at ~340 nm versus 315 nm), a trend which is consistent with the transition displaying charge-transfer character where the excess charge is more localized in the initial ion than in the excited state.<sup>[37]</sup>

Given that the calculated VDE of the **O14** deprotonomer is 4.39 eV, we predict that band I exists within the bound (non-electron-detached) region for this anionic species. Electronic excitations lying above this energy occur within the electron detachment continuum, so that any gas-phase photoexcitation above 4.39 eV is likely to be accompanied by electron detachment.<sup>[38]</sup>

## 2.3. Photofragmentation of [PBSA-H]<sup>-</sup>

We next turn to exploring the photofragment ions that are associated with the excited states evident in the Figure 2a spectrum. Figure 3 displays the difference (laser on – laser off) photofragment mass spectra of [PBSA-H]<sup>-</sup> irradiated at the photoabsorption maxima of features I–IV (3.8, 4.5, 4.9, and 5.3 eV, respectively). Photofragmentation produces *m/z* 80, 193, and 208 as the dominant ionic products, with Equations (2a)–(2c) illustrating the fragmentation pathways associated with their production:



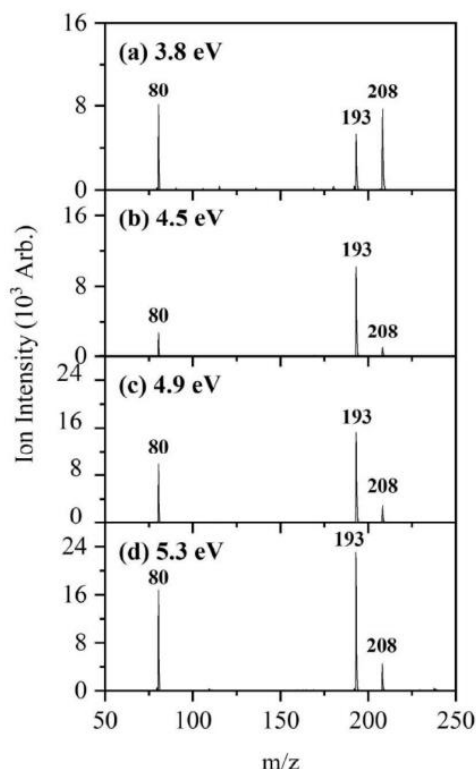


**Figure 3.** Photofragment difference (laser on – laser off) mass spectra of  $[\text{PBSA-H}]^-$ , excited at four photodepletion maxima of (a) 3.8, (b) 4.5, (c) 4.9, and (d) 5.3 eV.

Table 2 lists the proposed structures of the ionic photofragments and their accompanying neutral fragments. Inspection of the structures shown in Table 2 reveals that photofragmentation is localized around the S11–C16 bond, with pathways (2a) and (2b) arising from the fission of this bond with the excess charge moving in two different directions. Photofragment  $m/z$  208 is produced via a less direct pathway, which involves intramolecular rearrangement to eject the  $\text{HSO}_2^-$  neutral. We note that the structures of the lower mass fragments mean that

these ions cannot be produced through fragmentation of higher mass ions, ruling out the possibility that they are produced through a sequential multiphoton processes. The key point of note about the photofragment pathways, is that two of these pathways ((2a) and (2c)) result in the production of free-radical species.

To provide further insight into the nature of the  $[\text{PBSA-H}]^-$  excited states and decay pathways, Figures 4b–4d present the production spectra for the three ionic photofragments  $m/z$  80, 193, and 208, with the parent  $[\text{PBSA-H}]^-$  photodepletion spectrum displayed again in Figure 4a for ease of comparison. The photofragment production spectra highlight that all of the photofragments are produced to some extent across the entire photoexcitation range from 3.40–5.74 eV.

The action spectrum of the lowest mass ionic photofragment,  $m/z$  80, is shown in Figure 4b and is very similar to the  $[\text{PBSA-H}]^-$  gaseous absorption spectrum. This is also largely true for the  $m/z$  208 photofragment (Figure 4d), although this photofragment is produced more weakly across the high-energy III/IV regions. The profile of the high-energy spectral range for the  $m/z$  208 photofragment is similar to other photofragment spectra we have recorded previously, where a higher-mass photofragment dissociates into a lower-mass photofragment at high internal excitation energy.<sup>[12]</sup>

Figure 4c displays the photoproduction spectrum of the most intense ionic photofragment ( $m/z$  193), which is notable compared to the other two photofragments as it is produced much less strongly through region I, with intensity subsequently increasing with excitation wavelength into the UVC region.

It is evident from the data presented in Figures 3 and 4 that the relative production of the three observed photofragments from  $[\text{PBSA-H}]^-$  varies significantly as a function of photon energy. Figure 5 presents a plot of the relative ion yield of the photofragments, providing a concise overview of photofragment production. Within the UVA region (3.5–4.1 eV), the relative ion yields of the  $m/z$  80 and 208 photofragments are larger than that of the  $m/z$  193 ion. At photon energies above 4.1 eV, however, production of the  $m/z$  193 fragment increases strongly, with relative production peaking around 4.5 eV. These

**Table 2.** Proposed structures for the ionic fragments of deprotonated PBSA ( $m/z$  273) produced upon higher-energy collisional dissociation (HCD) and laser photoexcitation.

Ionic fragment mass [ $m/z$ ] [a]	Proposed structure of fragment	Accompanying neutral fragment lost	Observed in HCD [b]	Observed in laser photoexcitation [b]
208		$\text{HSO}_2^-$	Yes (vw)	Yes (w)
193		$\text{SO}_3$	Yes (vs)	Yes (s)
80	$\text{SO}_3^-$		Yes (vw)	Yes (m)

[a] Determined with mass accuracy  $> 0.3$  amu. [b] Very strong (vs), strong (s), medium (m), weak (w), and very weak (vw).

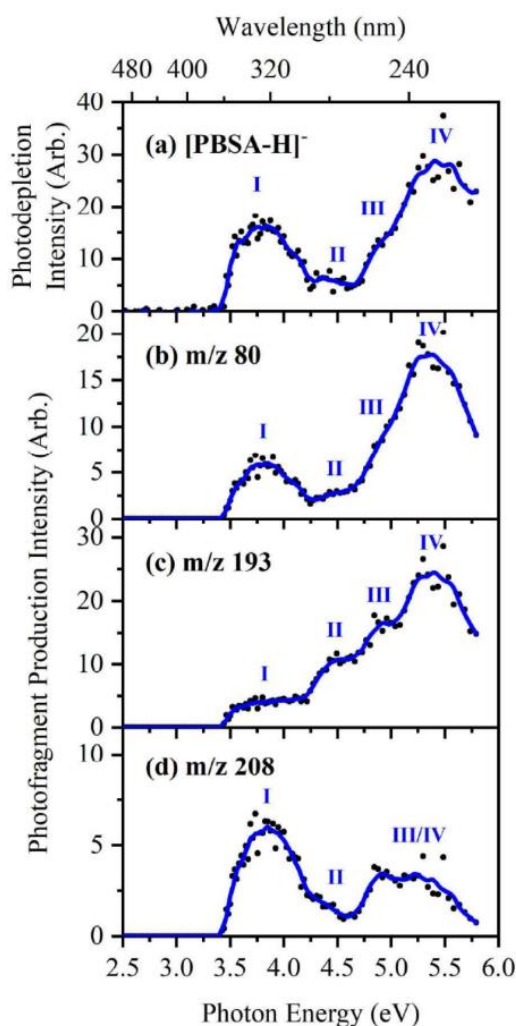
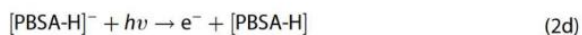


**Figure 4.** (a) Gas-phase UV absorption (photodepletion) spectrum of  $[\text{PBSA-H}]^-$ . (b–d) Photofragment production spectra of the three photofragments with  $m/z$  80, 193, and 208, respectively. The solid line is a five-point adjacent average of the data points.

results are discussed in the context of PBSA's ability to act as an efficient UV filter in the next section.

Electron loss is a dominant photofragmentation channel for  $[\text{PBSA-H}]^-$  as for other gaseous anions [Eq. (2d)].<sup>[15,38]</sup>



Section S2 of the Supporting Information provides an electron detachment yield spectrum, and further details of the extent of electron detachment versus ionic fragmentation. At 224 nm, for example, electron detachment is estimated to constitute 85% of photodepletion compared to 15% branching into ionic fragments. Despite the strong propensity for electron detachment in the gas-phase, it is well established that the propensity of an anionic molecule to photodetach will be

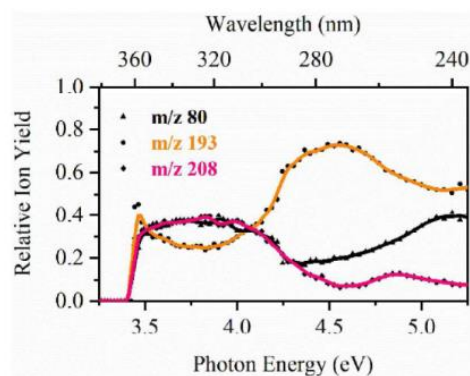


**Figure 5.** Relative ion yield plots for the  $m/z$  80, 193, and 208 photofragments of  $[\text{PBSA-H}]^-$  between 3.25–5.25 eV.

quenched upon solvation,<sup>[39]</sup> so simple electron detachment is likely to be a less important channel compared to ionic fragmentation in solution.

#### 2.4. Thermal Fragmentation versus Photofragmentation

To act as an efficient sunscreen, a molecule must be able to convert the harmful UV radiation it has absorbed into benign thermal energy. This is achieved by the electronic excited state (s) being able to rapidly relax back to the electronic ground state from where excess energy is dissipated by heat loss.<sup>[1,2]</sup> In solution, this thermal energy can be lost to the bulk solvent *via* vibrational relaxation, but in the gas phase, this energy is conserved within the molecular system and the ensuing hot ground state will dissociate across the available fragmentation barriers which are the same as those that are available to the isolated molecule when it is heated (so called "statistical fragmentation"). For molecular ions, a closely comparable "heating" process occurs in collision-induced dissociation.<sup>[40]</sup>  $[\text{PBSA-H}]^-$  was therefore subjected to collisional excitation to allow the fragmentation pathways associated with hot ground-state fragmentation to be identified.

Figure 6 displays the higher-energy collisional dissociation (HCD) fragmentation curves for  $[\text{PBSA-H}]^-$ . Collisional activation reveals that the  $m/z$  193 molecular ion completely dominates the thermal fragmentation profile of  $[\text{PBSA-H}]^-$ , with the  $m/z$  80 and 208 fragments only being seen as extremely minor fragments at the very highest collisional energies (> 50%).<sup>[41]</sup> We can therefore conclude that statistical fragmentation of  $[\text{PBSA-H}]^-$  would proceed with production of only the  $m/z$  193 fragment (pathway (2b)).

The relative ion yield plots shown in Figure 5 are clearly not consistent with a picture where UVA/UVB excitation of isolated  $[\text{PBSA-H}]^-$  leads to the ultrafast decay back to the electronic ground state, followed by statistical fragmentation solely into the  $m/z$  193 fragment. (If this was the case, we would expect to see  $m/z$  193 as the only photofragment with an ion yield profile that follows the absorption spectrum.) Instead, photoexcitation

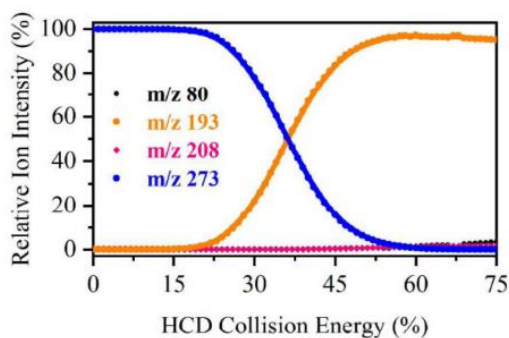


**Figure 6.** Parent ion dissociation curve of  $[\text{PBSA-H}]^-$  along with production curves for the three most intense fragments formed upon HCD between 0–75% energy. The curved lines included with the data points are a five-point adjacent average of such points and are provided as a viewing guide, to emphasize the profile for each individual fragment.

across the UV leads to strong production of the non-statistical fragments ( $m/z$  80 and 208). Such non-statistical (or non-ergodic) processes occur when dissociation proceeds directly from the excited state without significant adiabatic conical-intersection involvement to return the system back to the ground state in the vicinity of the initial geometry.<sup>[42]</sup> This is particularly true in the UVA region where the  $m/z$  193 fragment is the minor fragment, indicating non-statistical excited state decay dominates.

The ion-yield plots displayed in Figure 5 show that statistical dissociation, i.e. dissociation into  $m/z$  193, is enhanced in the UVC region  $< 280$  nm. For deprotonated PBSA as well as neutral PBSA, there are currently no calculations of the excited state potential energy surfaces, so the molecular mechanism that precedes statistical decay is currently unknown. From precedents in other organic molecular systems, it is likely that this could be mediated by a conical intersection involving a bond rotation of the bridging C–C linking the imidazole and benzene,<sup>[43]</sup> although it is also possible a conical intersection could be reached by rotation of the sulfonate group to the imidazole instead. Calculations of the excited state surfaces are highly desirable to provide further insight into the mechanism(s) involved.<sup>[43]</sup>

### 2.5. Implications of the Gas-Phase Results for Solution-Phase Photochemistry

The most detailed solution-phase study of PBSA photochemistry and photophysics conducted to date was that of Inbaraj et al.<sup>[10]</sup> Measurements included the determination of the UVB quantum yield for production of singlet oxygen from deprotonated PBSA (0.05 in  $\text{D}_2\text{O}$ ), as well as the fluorescence quantum yield (0.63). They noted that phosphorescence was also detected, although no quantum yield for this channel was reported. Importantly, the  $T_1$  triplet excited state was found to be sufficiently long-lived at 77 K for the characteristic electron paramagnetic resonance half-field transition to be detectable.

No photofragmentation quantum yields were reported in the study.

It is important at this point to consider how our gas-phase results relate to the photochemistry of PBSA in solution. In Section 2.2, we noted that the region I absorption blue-shifts upon solvation. It is reasonable to assume that the photochemistry we observe across region I in the gas-phase (3.4–4.2 eV), similarly blue-shifts in solution to the 3.8–4.6 eV range. Zhang et al. has calculated the solution-phase  $S_1$  excitation energy of  $[\text{PBSA-H}]^-$  as 4.045 eV,<sup>[24]</sup> an energy which lies in region I (solvated). By analogy, we expect that the  $S_1$  state is reached through gas-phase region I in our experiment. This state is important as it is believed to act as a doorway to the long-lived  $T_1$  state.<sup>[24]</sup> It is notable that the strong production of non-statistical photofragments associated with pathways (2a) and (2c) occurs through region I, leading us to conclude that these are the direct photodegradation products of the  $T_1$  state.<sup>[24,25,29]</sup> Similarly, since the  $T_1$  state has been previously attributed with leading to PBSA's behavior as a photosensitizer,<sup>[24,25,29]</sup> our results suggest that photosensitization by PBSA in solution is not simply associated with electron and energy transfer from the  $T_1$  state, but also through direct formation of free radical products. We note that geminate recombination of any free radical photoproducts may occur in solution, and it will be important in future solution-phase measurements to directly explore whether these direct free radical products can be detected, for example by employing techniques such as spin trapping.<sup>[44]</sup>

### 3. Concluding Remarks

In summary, we report for the first time the gaseous electronic photoabsorption spectrum and direct photofragment production profile spectra of the native form of PBSA, a popular FDA-approved UV filter found within many existing commercial sunscreens. The novelty of our gas-phase experiment is that it allows us to map the direct laser-induced photodegradation products of  $[\text{PBSA-H}]^-$ , away from the complications of bulk mixtures where secondary photoproducts can dominate. Strikingly, we observe evidence for high-yield production of free-radical species at photon energies between 3.5–5.5 eV.  $[\text{PBSA-H}]^-$  is observed to largely photodissociate primarily *via* the heterolytic cleavage of the S11–C16 bond (pathway (2b)); however, competitive homolytic dissociation yielding odd-electron products (pathways (2a) and (2c)) is seen strongly across UVA/UVB absorbance wavelengths. By comparing our gaseous spectra with the solution-phase absorption spectrum, we conclude that the non-statistical odd-electron photofragments (pathways (2a) and (2c)) are the direct photodegradation products of the  $T_1$  state. Indeed, the long-range repulsive interaction inherent in the triplet state is known to aid in the breakdown of such states into such free radical pairs.<sup>[45]</sup> The identification of the direct photoproducts in this work is important as it can guide detection of the direct photolysis products in future condensed-phase studies, as well as informing assessment of the possible toxicity of photoproducts.

Furthermore, our results indicate that future theoretical studies (which are generally performed on gaseous molecules initially) should include this direct photodegradation pathway to provide a more complete understanding of the photosensitizing behavior of PBSA. Such work is highly desirable to guide the rational development of improved UV filters.<sup>[43,46]</sup>

## Acknowledgements

This work was funded through the Leverhulme Trust Research Project Grant RPG-2017-147. We thank the University of York and the Department of Chemistry for provision of funds for the OPO laser system. We are grateful for computational support from the University of York High Performance Computing service, Viking and the Research Computing team. The York Centre of Excellence in Mass Spectrometry, used for the higher-energy collisional dissociation (HCD) work, was created thanks to a major capital investment through Science City York, supported by Yorkshire Forward with funds from the Northern Way Initiative, and subsequently received additional support from the EPSRC. We also thank Mathew Hawkrige for early contributions to this work.

## Conflict of Interest

The authors declare no conflict of interest.

**Keywords:** free radicals · laser spectroscopy · photolysis · photosensitizer · sunscreen molecules

- [1] S. Forestier, *J. Am. Acad. Dermatol.* **2008**, *58*, S133-8.  
 [2] F. Gasparro, *Sunscreen Photobiology*, Springer, Berlin, **1997**.  
 [3] K. M. Hanson, E. Gratton, C. J. Bardeen, *Free Radical Biol. Med.* **2006**, *41*, 1205-1212.  
 [4] V. Brezová, S. Gabčová, D. Dvoranová, A. Staško, *J. Photochem. Photobiol. B* **2005**, *79*, 121-134.  
 [5] N. Serpone, A. Salinaro, A. V. Emeline, S. Horikoshi, H. Hidaka, J. Zhao, *Photochem. Photobiol. Sci.* **2002**, *1*, 970-981.  
 [6] P. J. McHugh, J. Knowland, *Photochem. Photobiol.* **1997**, *66*, 276-81.  
 [7] J. M. Allen, C. J. Gossett, S. K. Allen, *Chem. Res. Toxicol.* **1996**, *9*, 605-609.  
 [8] J. Knowland, E. A. McKenzie, P. J. McHugh, N. A. Cridland, *FEBS Lett.* **1993**, *324*, 309-313.  
 [9] N. Bastien, J.-F. Millau, M. Rouabhia, R. J. H. Davies, R. Drouin, *J. Invest. Dermatol.* **2010**, *130*, 2463-2471.  
 [10] J. J. Inbaraj, P. Bilski, C. F. Chignell, *Photochem. Photobiol.* **2002**, *75*, 107-16.  
 [11] C. Stevenson, R. J. H. Davies, *Chem. Res. Toxicol.* **1999**, *12*, 38-45.  
 [12] E. Matthews, C. E. H. Dessent, *Phys. Chem. Chem. Phys.* **2017**, *19*, 17434-17440.  
 [13] E. Matthews, A. Sen, N. Yoshikawa, E. Bergström, C. E. H. Dessent, *Phys. Chem. Chem. Phys.* **2016**, *18*, 15143-15152.  
 [14] R. Antoine, P. Dugourd, *Phys. Chem. Chem. Phys.* **2011**, *13*, 16494-16509.  
 [15] N. G. K. Wong, J. A. Berenbeim, M. Hawkrige, E. Matthews, C. E. H. Dessent, *Phys. Chem. Chem. Phys.* **2019**, *21*, 14311-14321.  
 [16] N. D. N. Rodrigues, N. C. Cole-Filipiak, M. A. P. Turner, K. Krokidi, G. L. Thornton, G. W. Richings, N. D. M. Hine, V. G. Stavros, *Chem. Phys.* **2018**, *515*, 596-602.  
 [17] L. A. Baker, M. Staniforth, A. L. Flourat, F. Allais, V. G. Stavros, *ChemPhotoChem* **2018**, *2*, 743-748.  
 [18] C. Ma, C. T. L. Chan, R. C. T. Chan, A. K. W. Wong, B. P. Y. Chung, W. M. Kwok, *Phys. Chem. Chem. Phys.* **2018**, *20*, 24796-24806.  
 [19] M. T. Ignasiak, C. Houée-Levin, G. Kciuk, B. Marciniak, T. Pedzinski, C. Houée-Levin, G. Kciuk, B. Marciniak, T. Pedzinski, *ChemPhysChem* **2015**, *16*, 628-633.  
 [20] S. Wang, S. Schatz, M. C. Stuhldreier, H. Böhne, J. Wiese, C. Schröder, T. Raeker, B. Hartke, J. K. Keppler, K. Schwarz, *Phys. Chem. Chem. Phys.* **2017**, *19*, 30683-30694.  
 [21] E. M. M. Tan, M. Hilbers, W. J. Buma, *J. Phys. Chem. Lett.* **2014**, *5*, 2464-2468.  
 [22] J. C. Dean, R. Kusaka, P. S. Walsh, F. Allais, T. S. Zwier, *J. Am. Chem. Soc.* **2014**, *136*, 14780-14795.  
 [23] M.-O. Wingham, J.-P. Yang, M. Kuhn, A.-N. Unterreiner, T. J. A. Wolf, P. D. Dau, H.-T. Liu, D.-L. Huang, W. Klopper, L.-S. Wang, M. M. Kappes, *Phys. Chem. Chem. Phys.* **2013**, *15*, 6726-6736.  
 [24] S. Zhang, J. Chen, X. Qiao, L. Ge, X. Cai, G. Na, *Environ. Sci. Technol.* **2010**, *44*, 7484-7490.  
 [25] L. Shen, *Spectrochim. Acta Part A* **2015**, *150*, 187-189.  
 [26] W. H. M. Abdelraheem, X. He, Z. R. Komy, N. M. Ismail, D. D. Dionysiou, *Chem. Eng. J.* **2016**, *288*, 824-833.  
 [27] Y. Ji, L. Zhou, Y. Zhang, C. Ferronato, M. Brigante, G. Mailhot, X. Yang, J.-M. Chovelon, *Water Res.* **2013**, *47*, 5865-5875.  
 [28] Y. Ji, L. Zhou, C. Ferronato, A. Salvador, X. Yang, J.-M. Chovelon, *Appl. Catal. B* **2013**, *140*, 457-467.  
 [29] Y. Ji, L. Zhou, Y. Zhang, C. Ferronato, M. Brigante, G. Mailhot, X. Yang, J.-M. Chovelon, *Water Res.* **2013**, *47*, 5943-5953.  
 [30] E. De Laurentiis, M. Minella, M. Sarakha, A. Marrese, C. Minero, G. Mailhot, M. Brigante, D. Vione, *Water Res.* **2013**, *47*, 5943-5953.  
 [31] S. K. Sagoo, R. A. Jockusch, *J. Photochem. Photobiol. A* **2011**, *220*, 173-178.  
 [32] R. Cercola, E. Matthews, C. E. H. Dessent, *J. Phys. Chem. B* **2017**, *121*, 5553-5561.  
 [33] J. V. Olsen, B. Macek, O. Lange, A. Makarov, S. Horning, M. Mann, *Nat. Methods* **2007**, *4*, 709-712.  
 [34] M. J. Frisch, G. W. Trucks, H. B. Schlegel, G. E. Scuseria, M. A. Robb, J. R. Cheeseman, G. Scalmani, V. Barone, B. Mennucci, G. A. Petersson, *Gaussian 09, Rev. D.01*, Gaussian Inc. **2009**, Wallingford, CT.  
 [35] D. Schröder, M. Buděšínský, J. Roithová, *J. Am. Chem. Soc.* **2012**, *134*, 15897-15905.  
 [36] E. Matthews, C. E. H. Dessent, *J. Phys. Chem. A* **2016**, *120*, 9209-9216.  
 [37] S. B. Nielsen, M. B. Nielsen, A. Rubio, *Acc. Chem. Res.* **2014**, *47*, 1417-1425.  
 [38] A. Henley, H. H. Fielding, *Int. Rev. Phys. Chem.* **2019**, *38*, 1-34.  
 [39] D. Serxner, C. E. H. Dessent, M. A. Johnson, *J. Chem. Phys.* **1996**, *105*, 7231-7234.  
 [40] P. B. Armentrout, *J. Am. Soc. Mass Spectrom.* **2002**, *13*, 419-434.  
 [41] Whilst we have not quantitatively calibrated the HCD collision energies used in this experiment, earlier work from our group has established that the 20-38% HCD collision energy range closely correlates to internal energies of ~4-6 eV,<sup>[32]</sup> which falls directly into the range of photon energies used within this experiment.  
 [42] B. Lucas, M. Barat, J. A. Fayeton, C. Jouvét, P. Çarçalbal, G. Grégoire, *Chem. Phys.* **2008**, *347*, 324-330.  
 [43] L. A. Baker, B. Marchetti, T. N. V. Karsili, V. G. Stavros, M. N. R. Ashfold, *Chem. Soc. Rev.* **2017**, *46*, 3770-3791.  
 [44] A. Alberti, D. Macciantelli, *Spin Trapping. Electron Paramagnetic Resonance*: John Wiley & Sons, Inc.; **2008**, 285-324.  
 [45] B. Marchetti, T. N. V. Karsili, M. N. R. Ashfold, *Phys. Chem. Chem. Phys.* **2019**, *21*, 14418-14428.  
 [46] R. Losantos, I. Funes-Ardoiz, J. Aguilera, E. Herrera-Ceballos, C. García-Iriepa, P. Campos, D. Sampedro, *Angew. Chem. Int. Ed.* **2017**, *56*, 2632-2635; *Angew. Chem.* **2017**, *129*, 2676-2679.

Manuscript received: May 20, 2019  
 Revised manuscript received: July 10, 2019  
 Accepted manuscript online: July 25, 2019  
 Version of record online: August 12, 2019

# Chapter 4

## Linking Electronic Relaxation Dynamics and Ionic Photofragmentation Patterns for the Deprotonated UV Filter Benzophenone-4

### 4.1 Declaration

This work was originally published in the *Journal of Physical Chemistry Letters* in March 2021.

All the experimental work in this paper was conducted, processed, and subsequently analyzed by myself. Our collaborator, Dr. Conor D. Rankine at the University of Newcastle, performed the high-level *ab initio* calculations and theoretical potential energy surfaces for the ground and excited states of deprotonated benzophenone-4 highlighted within the article.

I wrote a complete first draft of the manuscript, which was subsequently revised and reworked through multiple iterations involving myself, Dr. Conor D. Rankine, and Prof. Caroline E. H. Dessent.



Signed

Prof. Caroline E. H. Dessent (University of York, U.K.)

A handwritten signature in black ink, appearing to be 'd' followed by a long horizontal stroke.

Signed Dr. Conor D. Rankine (University of Newcastle, U.K.)

**4.2 Paper III: Linking Electronic Relaxation Dynamics and Ionic  
Photofragmentation Patterns for the Deprotonated UV Filter  
Benzophenone-4**

# Linking Electronic Relaxation Dynamics and Ionic Photofragmentation Patterns for the Deprotonated UV Filter Benzophenone-4

Natalie G. K. Wong, Conor D. Rankine, and Caroline E. H. Dessent\*

Cite This: *J. Phys. Chem. Lett.* 2021, 12, 2831–2836

Read Online

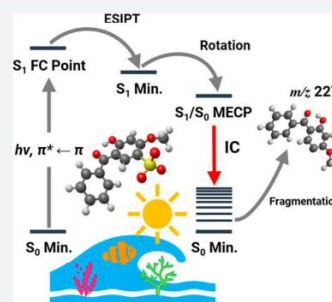
ACCESS |

Metrics & More

Article Recommendations

Supporting Information

**ABSTRACT:** Understanding how deprotonation impacts the photophysics of UV filters is critical to better characterize how they behave in key alkaline environments including surface waters and coral reefs. Using anion photodissociation spectroscopy, we have measured the intrinsic absorption electronic spectroscopy (400–214 nm) and numerous accompanying ionic photofragmentation pathways of the benzophenone-4 anion ( $[\text{BP4-H}]^-$ ). Relative ion yield plots reveal the locations of the bright  $S_1$  and  $S_3$  excited states. For the first time for an ionic UV filter, *ab initio* potential energy surfaces are presented to provide new insight into how the photofragment identity maps the relaxation pathways. These calculations reveal that  $[\text{BP4-H}]^-$  undergoes excited-state decay consistent with a statistical fragmentation process where the anion breaks down on the ground state after nonradiative relaxation. The broader relevance of the results in providing a basis for interpreting the relaxation dynamics of a wide range of gas-phase ionic systems is discussed.



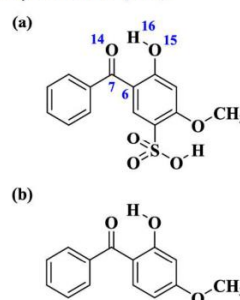
Laser spectroscopy has been increasingly applied over recent years to characterize the intrinsic photophysics of UV filters to provide a more robust understanding of molecular-level sunscreen action.<sup>1</sup> Both solution and gas-phase experiments have been performed, and while the solution phase can constitute an environment closer to that of a commercial sunscreen mixture,<sup>1–5</sup> gas-phase studies are of particular value in providing data that can readily be interpreted by high-level theory.<sup>5–9</sup> While several neutral sunscreens have been the subject of gas-phase investigations, protonated and deprotonated analogues have been studied much more sparsely.<sup>5</sup> These experiments are important given that a number of aquatic environments are alkaline (e.g., surface water and coral reefs),<sup>10,11</sup> so that the understanding of how deprotonation affects photostability has important environmental implications.

Very recently, laser-interfaced mass spectrometry (LIMS) has been used to probe the photophysics of several ionic sunscreen systems in detail.<sup>12–16</sup> These studies reveal that protonation and deprotonation can dramatically affect the sunscreen's UV absorption profile. Information on decay dynamics (and hence the intrinsic sunscreen efficiency), however, has only been inferred indirectly in these experiments, through attempting to match the photofragmentation products against the corresponding thermal fragmentation products to elucidate whether excited-state decay is statistical or nonstatistical.<sup>17,18</sup> This is a general problem for gaseous studies of ionic systems that extends well beyond the specific field of sunscreens,<sup>17,19–23</sup> since there are currently few

experiments where direct time-resolved measurement of ionic photofragments is possible.<sup>24,25</sup>

Here, we present the first laser spectroscopy study of benzophenone-4, BP4 (Scheme 1), in its deprotonated form. BP4 is structurally similar to oxybenzone (OB; Scheme 1), which is one of the most widely investigated sunscreens, both experimentally and theoretically.<sup>5,7,26–29</sup> Studies have revealed

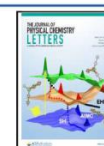
**Scheme 1. Molecular Structures of (a) Benzophenone-4 (BP4) and (b) Oxybenzone (OB)**



Received: February 5, 2021

Accepted: March 2, 2021

Published: March 15, 2021



that the sunscreen action of OB arises from excited-state intramolecular proton transfer (ESIPT) yielding the *keto* form of neutral oxybenzone, which then undergoes ultrafast internal conversion (IC) from the excited- to ground-state potential energy surface and efficiently thermalizes the excess energy.<sup>27–29</sup> Notably, for both deprotonated and protonated OB, the observed photofragmentation patterns were interpreted as indicative of nonstatistical excited-state decay, due to disruption of the *keto–enol* moiety.<sup>15</sup> BP4 provides an important analogue to study in this respect, since it contains a strongly acidic sulfonic acid group in addition to the OB *keto–enol* site. Deprotonation of BP4 will therefore produce the sulfonate monoanion, leaving the crucial *keto–enol* site intact for uninterrupted operation of the ultrafast nonradiative relaxation mechanism. Our aim here is to compare the photofragmentation behavior of deprotonated OB and BP4 to investigate whether excited-state decay is in fact nonstatistical and statistical, respectively. For the first time for a deprotonated UV filter, we apply quantum chemical calculations to obtain *ab initio* potential energy surfaces and hence gain direct physical insight into how the photofragment identity maps the nonradiative relaxation channels.

LIMS action spectroscopy was used to record gaseous ion photodepletion and photofragment spectra of  $[\text{BP4-H}]^-$  (Section S1).<sup>12–16</sup> The photodepletion spectrum can be considered to be equivalent to the gaseous absorption spectrum in the limit where radiative decay is absent. Figure 1a displays the photodepletion spectrum of mass-selected  $[\text{BP4-H}]^-$  ( $m/z$  307) over the range 3.1–5.8 eV (400–214 nm), displaying strong absorption across the UV. To aid in the discussion of the photofragment production spectra, the key spectral features are labeled I–IV, with bands I and II being the two distinct UVA and UVB absorption bands, peaking at 3.5 and 4.1 eV, respectively. Band III increases gradually in intensity in the UVC between 4.5 and 5.0 eV, and leads into band IV which is a strong, broad feature (onset *ca.* 5.0 eV) that extends further into the UVC.

We next turn to the photofragment ions produced following photoabsorption by  $[\text{BP4-H}]^-$ . Photofragmentation is extensive, with over 20 photofragments being observed. Figure 1b–i display the action spectra of the most prominent photofragments, with minor photofragments being reported in Section S3. The most intense photofragment ion is observed at  $m/z$  227 (eq 1d), corresponding to loss of neutral  $\text{SO}_3$  via a heterolytic cleavage mechanism of the C–S bond of the parent anion.  $m/z$  227 is produced with high intensity across the UVA and lower-energy UVC regions. The other major photodissociation channels of  $[\text{BP4-H}]^-$  are given in eqs 1a–1h, with the fragmentation channels discussed further in Section S6. We note that free radical formation is dominant.

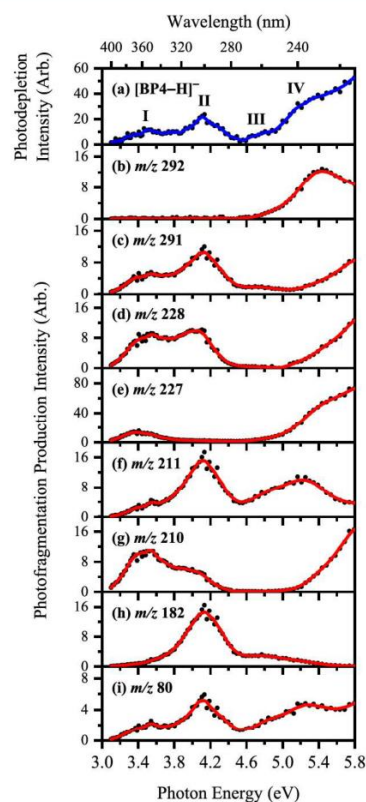
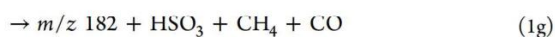
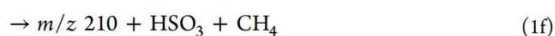


**Figure 1.** (a) Gas-phase absorption (photodepletion) spectrum of  $[\text{BP4-H}]^-$  ( $m/z$  307). (b–i) Photofragment production spectra of the eight major photofragments of  $[\text{BP4-H}]^-$ :  $m/z$  292, 291, 228, 227, 211, 210, 182, and 80. The solid line is a five-point adjacent average of the data points.



In Figure 1b–i, several distinctive spectral profiles are evident for the various photofragment ions. All the photofragment action spectra, except for those of  $m/z$  292 and 182 fragments, show a prominent peak in the UVA (*ca.* 3.5 eV), corresponding to the photodepletion feature I. A subsequent band, peaking at 4.1 eV, is also evident for the  $m/z$  291, 228, 211, 182, and 80 fragments, in the region of feature II. The growth in production of several of the photofragment ions ( $m/z$  291, 228, 227, 210, and 80) beyond 5.0 eV traces the profile of feature IV (Figure 1a). We note that the vertical detachment energy (VDE) for  $[\text{BP4-H}]^-$  is calculated as 5.19 eV, so that most of the spectral range lies below the electron detachment threshold. It is interesting to note that, for the  $m/z$  292 photofragment, production peaks at 5.4 eV, possibly indicating that a dipole-bound excited state is accessed in this region that decays with formation of  $m/z$  292.<sup>30,31</sup> Section S4 discusses electron detachment further.

Figure 2a presents the relative photofragment ion yields of  $[\text{BP4-H}]^-$  as a function of photoexcitation energy, highlighting several maxima that can be attributed to photoexcitation into different electronic states. It is evident that, in both the UVA and low UVC regions, the relative ion yield of the  $m/z$  227 photofragment is *ca.* 50% larger than other photoproduct ions. Conversely, within the range 3.8–5.0 eV, the production of fragment ions  $m/z$  211 and 182 (and to a

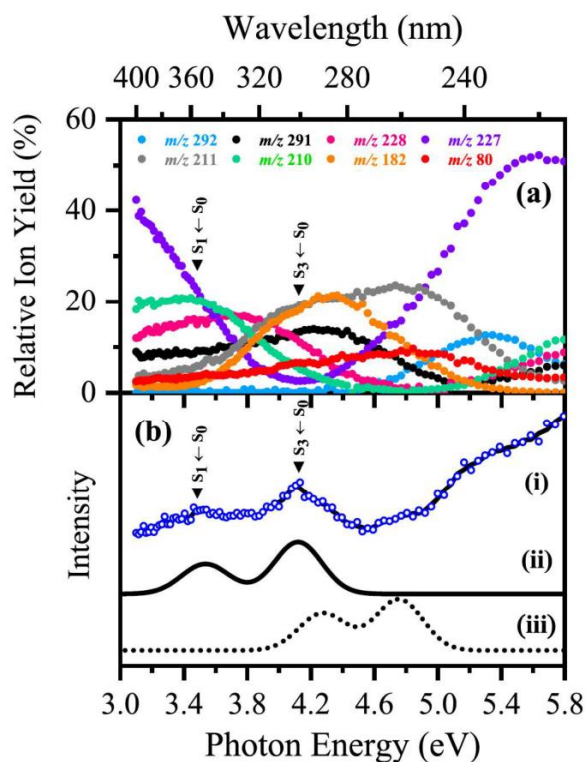


**Figure 2.** (a) Relative ion yield plot highlighting the eight most intense photofragments of  $[\text{BP4-H}]^-$  seen upon laser excitation between 3.1 and 5.8 eV. (b) Gas-phase experimental photodepletion spectrum (i) vs theoretical UV absorption spectra calculated at the (ii) ADC(2)/MP2/ma-def2-SV(P) and (iii)  $\omega\text{B97X-D/ma-def2-SV(P)}$  levels. The optically bright  $S_1 \leftarrow S_0$  and  $S_3 \leftarrow S_0$   $\pi\pi^*$  transitions are indicated.

lesser extent  $m/z$  291) increases significantly in comparison to the remaining ionic photofragments.

To probe the thermal fragmentation pathways of  $[\text{BP4-H}]^-$  on its electronic ground state, higher-energy collisional dissociation (HCD) was employed (Table 1, Figure 3, and Section S5).<sup>14,21</sup> These measurements are essential to identify which ions are secondary products, formed as a precursor species fragments at high internal energy.<sup>32</sup> They are also important, as any photofragments not observed in HCD can be identified as purely photochemical products. At relatively low collisional energies (20–42% HCD), the most intense fragment ion is  $m/z$  227, with  $m/z$  291, 228, and 210 also being produced in significant quantities. This indicates that thermal breakdown of the electronic ground state of  $[\text{BP4-H}]^-$  is associated with the molecule fragmenting along a number of different pathways. Production of the  $m/z$  227, 228, and 291 ions all decreases at higher energies, concomitant with the  $m/z$  211 fragment increasing. (We note that the  $m/z$  291 fragment persists to higher collisional energies than  $m/z$  227 and 228, indicating higher relative stability.) The HCD results therefore reveal that  $m/z$  211 is a secondary fragment from  $m/z$  227, 228, and 291 at higher internal energy. Similarly,  $m/z$  210 appears to decrease as the  $m/z$  182 ion increases.

Since the  $m/z$  227, 228, 291, and 211 fragments dominate both the UV photofragmentation of  $[\text{BP4-H}]^-$  and thermal (HCD) fragmentation, photofragmentation of the anion can

**Table 1.** Summary of the Ionic Fragments of Deprotonated BP4 ( $m/z$  307) Produced upon UV Laser Photoexcitation and Higher-Energy Collisional Dissociation (HCD) at 40% and 70% HCD Energies (Proposed Structures Are Outlined in Table S1)

Ionic mass fragment ( $m/z$ ) <sup>a</sup>	Observed in HCD <sup>b</sup>		Observed in UV laser photoexcitation <sup>b</sup>
	40%	70%	
292	√(xw) <sup>c</sup>	–	√(m)
291	√(m)	√(w)	√(m)
228	√(m)	√(vw)	√(m)
227	√(s)	√(vw)	√(vs)
211	√(w)	√(vs)	√(m)
210	√(m)	√(vw)	√(m)
182	√(m)	√(m)	√(m)
80	√(w)	√(m)	√(w)

<sup>a</sup>Determined with mass accuracy >0.3 amu. <sup>b</sup>Very strong (vs), strong (s), moderate (m), weak (w), very weak (vw), and extremely weak (xw). <sup>c</sup>HCD fragment  $m/z$  292 is observed to peak at 34% HCD energy, with a relative ion intensity of <2%.

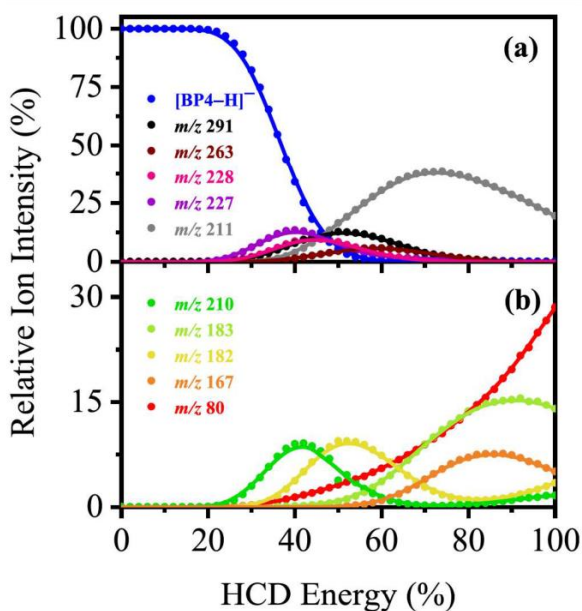


**Figure 3.** Parent ion dissociation curves for  $[\text{BP4-H}]^-$  highlighting its ten most intense thermal fragments between 0% and 100% HCD energy. The curved lines are a five-point adjacent average of such data points and are provided as a viewing guide, to emphasize the profile for each individual fragment.

be categorized as predominantly statistical (ergodic) over the spectral range studied.<sup>17,18</sup> Section S5 discusses the more minor HCD fragments and branching between the minor fragmentation pathways in more detail.

To explore whether this picture of statistical photofragmentation for  $[\text{BP4-H}]^-$  is credible, quantum chemical calculations were performed to characterize the excited-state potential energy surfaces (Section S1). The  $C_1$ -symmetric  $S_0$  minimum-energy geometry of  $[\text{BP4-H}]^-$  was located at the  $\omega\text{B97X-D}$  level (Table S2), with key excited-state parameters ( $\omega\text{B97X-D}$  and ADC(2) levels) summarized in Table 2.

**Table 2. Summary of Vertical Excitation Energies,  $\Delta E$ , Oscillator Strengths,  $f$ , and Characters of the  $S_n \leftarrow S_0$  ( $n = 1, 2, 3$ ) States As Evaluated at the  $\omega$ B97X-D/ma-def2-SV(P) and ADC(2)/MP2/ma-def2-SV(P) Levels**

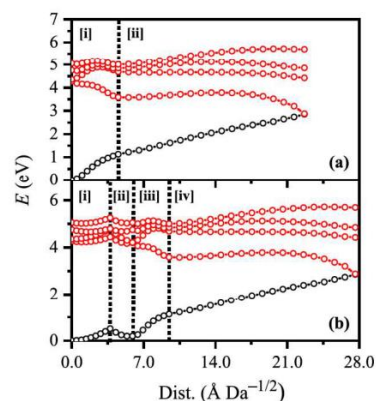
State	Char.	$\omega$ B97X-D		ADC(2)	
		$\Delta E$ (eV)	$f$	$\Delta E$ (eV)	$f$
$S_1$	$\pi\pi^*$	4.272	0.256	3.533	0.156
$S_2$	$n\pi^*$	4.357	0.010	3.701	0.004
$S_3$	$\pi\pi^*$	4.756	0.365	4.120	0.273

Figure 2b displays the calculated UV absorption spectra of [BP4-H]<sup>-</sup>, along with the experimental photodepletion spectrum. We assign the two bands observed in the UVA/UVB regions of the experimental [BP4-H]<sup>-</sup> photodepletion spectrum (I and II) as the optically bright  $S_1 \leftarrow S_0$  and  $S_3 \leftarrow S_0$   $\pi\pi^*$  transitions, respectively. The excellent agreement between the calculated spectra at both the  $\omega$ B97X-D and ADC(2) levels and the experimental spectrum (Figure 2b) is notable, both in terms of state identities, relative peak positions, and intensities. At the ADC(2) level, quantitative agreement with experiment is obtained ‘out of the box’, whereas, at the  $\omega$ B97X-D level, the vertical excitation energies of the  $S_n \leftarrow S_0$  ( $n = 1, 2, 3$ ) states are characteristically overestimated (ca. 0.7 eV) but in good qualitative agreement.

Based on our understanding of the sister molecule, OB,<sup>15,29</sup> [BP4-H]<sup>-</sup> can be expected to relax on the  $S_1$  state via ES IPT. A  $C_1$ -symmetric  $S_1$  minimum-energy geometry for [BP4-H]<sup>-</sup> was located ca. 4.5 Å Da<sup>-1/2</sup> from the Franck–Condon point (Table S3). The  $S_1$  minimum-energy geometry is accessed via ES IPT from the Franck–Condon point, with the H<sub>16</sub> atom bound to O<sub>15</sub> migrating across to O<sub>14</sub>. ES IPT follows a direct excited-state relaxation coordinate and is consequently expected to occur promptly postphotoexcitation to the  $S_1$  state. Post-ES IPT, [BP4-H]<sup>-</sup> can access the  $S_1/S_0$  crossing seam at an  $S_1/S_0$  minimum-energy crossing point (MECP). An  $S_1/S_0$  MECP was located ca. 18.2 and 18.0 Å Da<sup>-1/2</sup> from the Franck–Condon point and  $S_1$  minimum-energy geometry, respectively (Table S4). The  $S_1/S_0$  MECP is accessed via torsion of C<sub>6</sub>–C<sub>7</sub> and is characterized by the aromatic rings being rotated into a near-perpendicular conformation, effectively closing the gap between the  $S_0$  and  $S_1$  states.

To map the  $S_0 \leftarrow S_1$  IC channel, potential energy surfaces have been constructed between the key geometries via linear interpolation of internal coordinates (LIIC). Independent single-point energy calculations have been carried out at each one of 25 interpolated geometries, respectively, with the calculated potential energy surfaces presented in Figure 4a.

The picture to emerge here is similar to that described for OB by Karsili et al.,<sup>29</sup> which is consistent with experiments which identified a subpicosecond lifetime for the IC channel.<sup>27</sup> The quantum-chemical calculations reported here are not able to give information on the time scale that the  $S_1/S_0$  crossing seam is accessed (although they could be readily coupled to excited-state dynamics simulations such as nonadiabatic mixed-quantum-classical or trajectory surface-hopping dynamics, to directly obtain this information). However, given the similar potential energy surface morphologies of [BP4-H]<sup>-</sup> and OB around the key *keto*–*enol* region, it is reasonable to expect that it is ultrafast (i.e., subpicosecond) and, therefore, able to outcompete other processes efficiently, e.g., excited-state fragmentation, radiative decay, and intersystem crossing. (For ISC;  $T_1 \leftarrow S_1$  and  $T_2 \leftarrow S_1$  spin–orbit couplings are on the



**Figure 4.** (a) Energies of the  $S_0$  state (black) and excited singlet states (red) between (i) the  $S_0$  and  $S_1$  minimum-energy geometries and (ii) the  $S_1$  minimum-energy geometry and the  $S_1/S_0$  MECP. (b) Energies of the  $S_0$  state (black) and excited singlet states (red) between (i) the  $S_0$  minimum-energy geometry and the  $S_3/S_2$  MECP, (ii) the  $S_3/S_2$  MECP and the  $S_2/S_1$  MECP, (iii) the  $S_2/S_1$  MECP and the  $S_1$  minimum-energy geometry, and (iv) the  $S_1$  minimum-energy geometry and the  $S_1/S_0$  MECP. Points were generated via linear interpolation of internal coordinates (LIIC). Energies were evaluated at the  $\omega$ B97X-D/ma-def2-SV(P) level.

order of ca. 5–10 cm<sup>-1</sup> along the LIIC channel: Section S8.) The calculations are therefore entirely consistent with our deduction from the experimental results of nonradiative relaxation followed by statistical fragmentation on the hot ground state. This leads to ejection of SO<sub>3</sub> as the initial dominant channel, as the C–S bond is the weakest bond in [BP4-H]<sup>-</sup>.<sup>33</sup> Loss of SO<sub>3</sub> is commensurate with production of the  $m/z$  227 fragment, both from excitation at feature I, i.e., the lowest-energy optically bright state, and, crucially, from the HCD production curves (Figure 3).

For the feature II region, which corresponds to excitation into the optically bright  $S_3$  state, the calculations predict decay pathways that appear similar to those outlined for feature I. Figure 4b shows the  $S_3/S_2$  and  $S_2/S_1$  MECPs that have been located (Tables S5–S6), showing that both lie close to (ca. 3.7 and 2.1 Å Da<sup>-1/2</sup>, respectively), and downhill of, the respective Franck–Condon point. Thus,  $S_3$  excitation is predicted to lead to a prompt  $S_1 \leftarrow S_2 \leftarrow S_3$  cascade of population. After arriving on the  $S_1$  state close to the Franck–Condon point, ES IPT and ultrafast  $S_0 \leftarrow S_1$  IC will proceed as described above. We speculate that  $S_0 \leftarrow S_1$  IC, when the  $S_1$  state is accessed indirectly (from above; i.e., postphotoexcitation into the  $S_3$  state) as opposed to directly (postphotoexcitation to the  $S_1$  state), could be even more efficient, since accessing the  $S_3/S_2$  MECP and the  $S_2/S_1$  MECP directly accesses the proton transfer and torsional coordinates, respectively, that are necessary to subsequently access the  $S_1/S_0$  crossing seam. This could be tested in future work by either excited-state dynamics simulations<sup>34</sup> and/or time-resolved experiments.<sup>24,25</sup>

The differences in fragment production on excitation at features I and II can then be explained as follows. Excitation at feature I (the  $S_1$  state) leads to fission of the C–S bond after nonradiative relaxation (as previously observed for UVB filter 2-phenylbenzimidazole-5-sulfonic acid),<sup>14</sup> producing primarily the  $m/z$  227, 228, and 291 fragments. Excitation at feature II (the  $S_3$  state) will also lead to fission of the C–S bond after nonradiative relaxation and the production of the  $m/z$  227,

228, and 291 fragments. However, as a greater amount of photon energy is pumped into the system (4.1 eV versus 3.5 eV), these fragments possess enough internal energy to undergo secondary fragmentation. The reduction in photofragment intensity can be seen first for  $m/z$  227, then for  $m/z$  228, and finally for  $m/z$  291, exactly mirroring the measured relative stability of these ions from the HCD measurements (Figure 3). (We note that similar arguments can be applied to the  $m/z$  210 and 182 photofragments, where comparison to the HCD data reveals that the  $m/z$  182 ion persists to higher internal energy.) All of these photofragments therefore produce the  $m/z$  211 fragment as a secondary product: indeed, the  $m/z$  211 fragment dominates the medium-high HCD energy range between 42% and 80% HCD energies.

In summary, we have reported the gaseous UV absorption spectrum and photofragmentation profile of [BP4-H]<sup>-</sup> acquired via LIMS. For the first time for an ionic UV filter, *ab initio* potential energy surfaces are presented to provide new insight into the relaxation pathways. The calculations predict that, in the regions of both the optically bright  $S_1 \leftarrow S_0$  and  $S_3 \leftarrow S_0 \pi\pi^*$  transitions, excited state relaxation will occur via nonradiative decay, associated with a statistical excited state decay process. In the photodissociation experiments, the observed photofragments mirror those observed upon thermal breakdown of the electronic ground state. Importantly, the photon-energy dependent production spectra of the numerous photofragments mirror the fragment production curves in the HCD collisional activation measurements. This is clear evidence of statistical decay, driven by fragmentation on a hot ground state surface, which in turn demonstrates that deprotonated BP4 is behaving like an efficient UV filter. However, the results presented here are of broader importance, as they provide a theoretical basis to support the widely adopted argument linking ionic photofragmentation patterns and decay dynamics that has been used for interpreting the behavior of key gaseous ionic systems including nucleobases and nucleotides.<sup>17,19–23,35,36</sup>

## ASSOCIATED CONTENT

### Supporting Information

The Supporting Information is available free of charge at <https://pubs.acs.org/doi/10.1021/acs.jpcllett.1c00423>.

Experimental and computational methodology; photodepletion laser power dependence measurements; additional photofragment action spectra; electron detachment yield versus photodepletion yield interpretation; higher-energy collisional dissociation (HCD) production spectra; further discussion of deprotonated benzophenone-4 fragmentation channels; optimized Cartesian coordinate tables; further computational results; schematic structure of deprotonated benzophenone-4 (PDF)

## AUTHOR INFORMATION

### Corresponding Author

Caroline E. H. Dessent – Department of Chemistry, University of York, York YO10 SDD, U.K.; [orcid.org/0000-0003-4944-0413](https://orcid.org/0000-0003-4944-0413); Email: [caroline.dessent@york.ac.uk](mailto:caroline.dessent@york.ac.uk)

## Authors

Natalie G. K. Wong – Department of Chemistry, University of York, York YO10 SDD, U.K.

Conor D. Rankine – School of Natural and Environmental Sciences, Newcastle University, Newcastle-upon-Tyne NE1 7RU, U.K.

Complete contact information is available at: <https://pubs.acs.org/10.1021/acs.jpcllett.1c00423>

## Notes

The authors declare no competing financial interest.

## ACKNOWLEDGMENTS

This work was funded through the Leverhulme Trust Research Project Grant RPG-2017-147. We thank the University of York and the Department of Chemistry for provision of funds for the OPO laser system. We are grateful for the computational support from the University of York High Performance Computing service, Viking, and the Research Computing team. The York Centre of Excellence in Mass Spectrometry, used for the higher-energy collisional dissociation (HCD) work, was created thanks to a major capital investment through Science City York, supported by Yorkshire Forward with funds from the Northern Way Initiative, and has more recently received additional support from the EPSRC and BBSRC. C.D.R. thanks the Engineering and Physical Sciences Council (EPSRC) and Newcastle University (Newcastle-upon-Tyne, UK) for funding his research via the award of an EPSRC Doctoral Prize Fellowship (EP/R51309X/1). Finally, we thank Prof. Tolga Karsili for useful discussions on benzophenone-4.

## REFERENCES

- Holt, E. L.; Stavros, V. G. Applications of Ultrafast Spectroscopy to Sunscreen Development, from First Principles to Complex Mixtures. *Int. Rev. Phys. Chem.* **2019**, *38*, 243–285.
- Chan, C. T.-L.; Ma, C.; Chan, R. C.-T.; Ou, H.-M.; Xie, H.-X.; Wong, A. K.-W.; Wang, M.-L.; Kwok, W.-M. A Long Lasting Sunscreen Controversy of 4-Aminobenzoic Acid and 4-Dimethylamino-benzaldehyde Derivatives Resolved by Ultrafast Spectroscopy Combined with Density Functional Theoretical Study. *Phys. Chem. Chem. Phys.* **2020**, *22*, 8006–8020.
- Zhao, X.; Luo, J.; Liu, Y.; Pandey, P.; Yang, S.; Wei, D.; Han, K. Substitution Dependent Ultrafast Ultraviolet Energy Dissipation Mechanisms of Plant Sunscreens. *J. Phys. Chem. Lett.* **2019**, *10*, 5244–5249.
- Luo, J.; Liu, Y.; Yang, S.; Flourat, A. L.; Allais, F.; Han, K. Ultrafast Barrierless Photoisomerization and Strong Ultraviolet Absorption of Photoproducts in Plant Sunscreens. *J. Phys. Chem. Lett.* **2017**, *8*, 1025–1030.
- Ignasiak, M. T.; Houee-Levin, C.; Kciuk, G.; Marciniak, B.; Pedzinski, T.; Houee-Levin, C.; Kciuk, G.; Marciniak, B.; Pedzinski, T. A Reevaluation of the Photolytic Properties of 2-Hydroxybenzophenone-Based UV Sunscreens: Are Chemical Sunscreens Inoffensive? *ChemPhysChem* **2015**, *16*, 628–633.
- Iida, Y.; Kinoshita, S.; Kenjo, S.; Muramatsu, S.; Inokuchi, Y.; Zhu, C.; Ebata, T. Electronic States and Nonradiative Decay of Cold Gas-Phase Cinnamic Acid Derivatives Studied by Laser Spectroscopy with a Laser-Ablation Technique. *J. Phys. Chem. A* **2020**, *124*, 5580–5589.
- Domingos, S. R.; Schnell, M. Wet Sunscreens in the Gas Phase: Structures of Isolated and Microsolvated Oxybenzone. *J. Phys. Chem. Lett.* **2018**, *9*, 4963–4968.
- Dean, J. C.; Kusaka, R.; Walsh, P. S.; Allais, F.; Zwier, T. S. Plant Sunscreens in the UV-B: Ultraviolet Spectroscopy of Jet-Cooled

- Sinapoyl Malate, Sinapic Acid, and Sinapate Ester Derivatives. *J. Am. Chem. Soc.* **2014**, *136*, 14780–14795.
- (9) Tan, E. M. M.; Hilbers, M.; Buma, W. J. Excited-State Dynamics of Isolated and Microsolvated Cinnamate- Based UV - B Sunscreens. *J. Phys. Chem. Lett.* **2014**, *5*, 2464–2468.
- (10) Jiang, L.-Q.; Carter, B. R.; Feely, R. A.; Lauvset, S. K.; Olsen, A. Surface Ocean PH and Buffer Capacity: Past, Present and Future. *Sci. Rep.* **2019**, *9*, 18624.
- (11) Stark, J. S.; Langdon, C. Coral Reef PH Altered in Situ. *Nat. Ecol. Evol.* **2019**, *3*, 1380–1381.
- (12) Berenbeim, J. A.; Wong, N. G. K.; Cockett, M. C. R.; Berden, G.; Oomens, J.; Rijs, A. M.; Dessent, C. E. H. Sodium Cationization Can Disrupt the Intramolecular Hydrogen Bond That Mediates the Sunscreen Activity of Oxybenzone. *Phys. Chem. Chem. Phys.* **2020**, *22*, 19522–19531.
- (13) Berenbeim, J. A.; Wong, N. G. K.; Cockett, M. C. R.; Berden, G.; Oomens, J.; Rijs, A. M.; Dessent, C. E. H. Unravelling the Keto–Enol Tautomer Dependent Photochemistry and Degradation Pathways of the Protonated UVA Filter Avobenzene. *J. Phys. Chem. A* **2020**, *124*, 2919–2930.
- (14) Wong, N. G. K.; Berenbeim, J. A.; Dessent, C. E. H. Direct Observation of Photochemical Free Radical Production from the Sunscreen 2-Phenylbenzimidazole-5-Sulfonic Acid via Laser-Interfaced Mass Spectrometry. *ChemPhotoChem.* **2019**, *3*, 1231–1237.
- (15) Wong, N. G. K.; Berenbeim, J. A.; Hawkridge, M.; Matthews, E.; Dessent, C. E. H. Mapping the Intrinsic Absorption Properties and Photodegradation Pathways of the Protonated and Deprotonated Forms of the Sunscreen Oxybenzone. *Phys. Chem. Chem. Phys.* **2019**, *21*, 14311–14321.
- (16) Matthews, E.; Dessent, C. E. H. Experiment and Theory Confirm That UV Laser Photodissociation Spectroscopy Can Distinguish Protomers Formed via Electrospray. *Phys. Chem. Chem. Phys.* **2017**, *19*, 17434–17440.
- (17) Soorkia, S.; Jouvét, C.; Grégoire, G. UV Photoinduced Dynamics of Conformer-Resolved Aromatic Peptides. *Chem. Rev.* **2020**, *120*, 3296–3327.
- (18) Lucas, B.; Barat, M.; Fayeton, J. A.; Jouvét, C.; Çarçabal, P.; Grégoire, G. Statistical versus Non-Statistical Photo-Fragmentation of Protonated GWG Tri-Peptide Induced by UV Excitation. *Chem. Phys.* **2008**, *347*, 324–330.
- (19) Noble, J. A.; Marceca, E.; Dedonder, C.; Phasayavan, W.; Féraud, G.; Inceesungvorn, B.; Jouvét, C. Influence of the N Atom Position on the Excited State Photodynamics of Protonated Azaindole. *Phys. Chem. Chem. Phys.* **2020**, *22*, 27280–27289.
- (20) Uleanya, K. O.; Cercola, R.; Nikolova, M.; Matthews, E.; Wong, N. G. K.; Dessent, C. E. H. Observation of Enhanced Dissociative Photochemistry in the Non-Native Nucleobase 2-Thiouracil. *Molecules* **2020**, *25*, 3157.
- (21) Cercola, R.; Matthews, E.; Dessent, C. E. H. Photoexcitation of Adenosine 5'-Triphosphate Anions in Vacuo: Probing the Influence of Charge State on the UV Photophysics of Adenine. *J. Phys. Chem. B* **2017**, *121*, 5553–5561.
- (22) Marcum, J. C.; Halevi, A.; Weber, J. M. Photodamage to Isolated Mononucleotides—Photodissociation Spectra and Fragment Channels. *Phys. Chem. Chem. Phys.* **2009**, *11*, 1740–1751.
- (23) Nielsen, S. B.; Andersen, J. U.; Forster, J. S.; Hvelplund, P.; Liu, B.; Pedersen, U. V.; Tomita, S. Photodestruction of Adenosine 5'-Monophosphate (AMP) Nucleotide Ions in Vacuo: Statistical versus Nonstatistical Processes. *Phys. Rev. Lett.* **2003**, *91*, 048302.
- (24) Kruppa, S. V.; Bäßler, F.; Klopper, W.; Walg, S. P.; Thiel, W. R.; Diller, R.; Riehn, C. Ultrafast Excited-State Relaxation of a Binuclear Ag(I) Phosphine Complex in Gas Phase and Solution. *Phys. Chem. Chem. Phys.* **2017**, *19*, 22785–22800.
- (25) Nolting, D.; Weinkauff, R.; Hertel, I. V.; Schultz, T. Excited-State Relaxation of Protonated Adenine. *ChemPhysChem* **2007**, *8*, 751–755.
- (26) Baker, L. A.; Grosvenor, L. C.; Ashfold, M. N. R.; Stavros, V. G. Ultrafast Photophysical Studies of a Multicomponent Sunscreen: Oxybenzone–Titanium Dioxide Mixtures. *Chem. Phys. Lett.* **2016**, *664*, 39–43.
- (27) Baker, L. A.; Horbury, M. D.; Greenough, S. E.; Coulter, P. M.; Karsili, T. N. V.; Roberts, G. M.; Orr-Ewing, A. J.; Ashfold, M. N. R.; Stavros, V. G. Probing the Ultrafast Energy Dissipation Mechanism of the Sunscreen Oxybenzone after UVA Irradiation. *J. Phys. Chem. Lett.* **2015**, *6*, 1363–1368.
- (28) Baker, L. A.; Horbury, M. D.; Greenough, S. E.; Ashfold, M. N. R.; Stavros, V. G. Broadband Ultrafast Photoprotection by Oxybenzone across the UVB and UVC Spectral Regions. *Photochem. Photobiol. Sci.* **2015**, *14*, 1814–1820.
- (29) Karsili, T. N. V.; Marchetti, B.; Ashfold, M. N. R.; Domcke, W. Ab Initio Study of Potential Ultrafast Internal Conversion Routes in Oxybenzone, Caffeic Acid, and Ferulic Acid: Implications for Sunscreens. *J. Phys. Chem. A* **2014**, *118*, 11999–12010.
- (30) Matthews, E.; Dessent, C. E. H. Observation of Near-Threshold Resonances in the Flavin Chromophore Anions Alloxazine and Lumichrome. *J. Phys. Chem. Lett.* **2018**, *9*, 6124–6130.
- (31) Harvey, A. J. A.; Yoshikawa, N.; Wang, J.-G.; Dessent, C. E. H. Communication: Evidence for Dipole-Bound Excited States in Gas-Phase I<sup>-</sup> · MI (M = Na, K, Cs) Anionic Salt Microclusters. *J. Chem. Phys.* **2015**, *143*, 101103.
- (32) Cercola, R.; Fischer, K. C.; Sherman, S. L.; Garand, E.; Wong, N. G. K.; Hammerback, L. A.; Lynam, J. M.; Fairlamb, I. J. S.; Dessent, C. E. H. Direct Measurement of the Visible to UV Photodissociation Processes for the PhotoCORM TryptoCORM. *Chem. - Eur. J.* **2020**, *26*, 10297–10306.
- (33) Zhang, X. Mass Spectrometric and Theoretical Studies on Dissociation of the CS Bond in the Benzenesulfonic Acid and Benzenesulfonic Acid Anion Series: Homolytic Cleavage vs Heterolytic Cleavage. *J. Mol. Struct.* **2012**, *1028*, 1–6.
- (34) Mai, S.; González, L. Molecular Photochemistry: Recent Developments in Theory. *Angew. Chem., Int. Ed.* **2020**, *59*, 16832–16846.
- (35) Daly, S.; Porrini, M.; Rosu, F.; Gabelica, V. Electronic Spectroscopy of Isolated DNA Polyanions. *Faraday Discuss.* **2019**, *217*, 361–382.
- (36) Broquier, M.; Soorkia, S.; Pino, G.; Dedonder-Lardeux, C.; Jouvét, C.; Grégoire, G. Excited State Dynamics of Cold Protonated Cytosine Tautomers: Characterization of Charge Transfer, Intersystem Crossing, and Internal Conversion Processes. *J. Phys. Chem. A* **2017**, *121*, 6429–6439.

# Chapter 5

## Photodegradation of Riboflavin under Alkaline

### Conditions: What can Gas-Phase Photolysis Tell Us

### About What Happens in Solution?

#### 5.1 Declaration

This work has been submitted for peer review in *Molecules*.

All the experimental and computational work included in this paper was conducted, processed, and thoroughly analyzed by myself. Whilst the photolysis device built within was conceptualized by myself and the CAD design and eventual assembly/wiring of the cell was carried out by Dr. Chris Rhodes of the University of York Electronics Workshop.

I wrote a complete first draft of the manuscript, which was subsequently revised by myself and Prof. Caroline E. H. Dessent.



Signed Prof. Caroline E. H. Dessent (University of York, U.K.)

**5.2 Paper IV: Photodegradation of Riboflavin under Alkaline Conditions: What can Gas-Phase Photolysis Tell Us About What Happens in Solution?**

Article [Submitted for Peer Review]

# Photodegradation of Riboflavin under Alkaline Conditions: What can Gas-Phase Photolysis Tell Us About What Happens in Solution?

Natalie G. K. Wong<sup>1</sup>, Chris Rhodes<sup>1</sup> and Caroline E. H. Dessent<sup>1,\*</sup>

<sup>1</sup> Department of Chemistry, University of York, Heslington, YO10 5DD, U.K.

\* Correspondence: caroline.dessent@york.ac.uk; Tel.: +44 (0)1904-324092.

**Abstract:** The application of electrospray ionization mass spectrometry (ESI-MS) as a direct method for detecting reactive intermediates is a technique of developing importance in the routine monitoring of solution-phase reaction pathways. Here, we utilize a novel on-line ESI-MS approach to detect the photoproducts of deprotonated riboflavin ( $[\text{RF-H}]^-$ ) in aqueous solution, thus establishing riboflavin as a prototype for such fundamental condensed-phase studies. Development of our on-line setup allows for solution-phase photolysis to occur within a syringe using UV-A LEDs, immediately prior to being introduced into the mass spectrometer *via* ESI. Gas-phase laser photofragmentation studies *via* laser-interfaced mass spectrometry of  $[\text{RF-H}]^-$  are presented alongside the solution-phase photolysis and illustrate the extent to which such methods can inform our understanding of the corresponding solution-phase photochemistry. Results from collision-induced dissociation experiments are also presented and show that  $[\text{RF-H}]^-$  dissociates solely into the  $m/z$  255 ion. We reveal that the solution-phase photofragmentation observed for  $[\text{RF-H}]^-$  closely mirrors the gas-phase photochemistry, with the  $m/z$  241 ion being the only major condensed-phase photoproduct. Further gas-phase photoproducts are observed at  $m/z$  255, 212, and 145. The value of exploring both the gas- and solution-phase photochemistry to characterize photochemical reactions is discussed.

**Citation:** Wong, N.G.K.; Rhodes, C.; Dessent, C.E.H. Photodegradation of Riboflavin under Alkaline Conditions: What can Gas-Phase Photolysis Tell Us About What Happens in Solution? *Molecules* **2021**, *26*, x. <https://doi.org/10.3390/xxxxx>

**Keywords:** laser spectroscopy; online photolysis; solution-phase photolysis; vitamin; flavins; mass spectrometry

Academic Editor: Firstname Last-name

Received: date

Accepted: date

Published: date

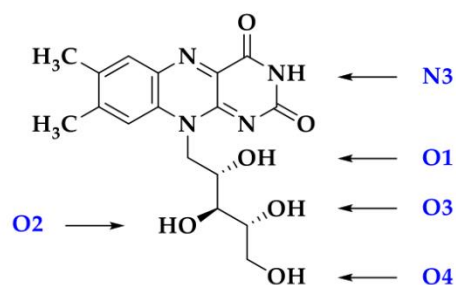
**Publisher's Note:** MDPI stays neutral with regard to jurisdictional claims in published maps and institutional affiliations.



**Copyright:** © 2021 by the authors. Submitted for possible open access publication under the terms and conditions of the Creative Commons Attribution (CC BY) license (<http://creativecommons.org/licenses/by/4.0/>).

## 1. Introduction

Riboflavin (RF; Scheme 1) is one of the most well-studied members of the flavin family to date and is a vital water-soluble vitamin ( $B_2$ ) naturally found in some food products (*e.g.*, milk, cheese, and green vegetables) or added to fortified foods (*e.g.*, cereals, bread, and beer). As a precursor of all biologically-significant flavins, riboflavin is further regarded to form an integral component of the (flavo)coenzymes flavin adenine dinucleotide (FAD) and flavin mononucleotide (FMN), both of which are active within several metabolic enzyme reactions.



**Scheme 1.** Schematic diagram of the structure of riboflavin (RF). Typical labelling conventions have been applied to illustrate the possible deprotonation sites of a mono-anion deprotomer (*i.e.*, [RF-H]<sup>−</sup>).

Riboflavin shows broad absorption across the UV-visible regions in aqueous solution and has been observed to photodegrade *via* intramolecular and/or intermolecular photo-reduction, photoaddition, and photodealkylation mechanisms to, in turn, form an array of photoproducts including formylmethylflavin (FMF), lumichrome (LC), lumiflavin (LF), carboxymethylflavin (CMF), cyclodehydroriboflavin (CDRF), and 2,3-butanedione, as has been reviewed in detail elsewhere [1]. Still, it is notable that the formation of such intermediates is heavily dependent on various reaction conditions (*i.e.*, pH, solvent, and light intensity) and the intermediates also have the capacity to degrade into further (secondary) products [1].

In the body, riboflavin has an absorption maximum of *ca.* 447 nm. Human skin can thereby photodegrade upon exposure to blue (visible) light, causing red-cell lysis and generalized tissue riboflavin deficiencies within the body. Earlier work on riboflavin has shown that it can act as an avid photosensitizer, yielding reactive oxygen species (ROS) such as the superoxide anion, hydroxy radical, hydrogen peroxide, as well as singlet oxygen. Such radicals can in turn promote the decomposition of other ingredients within food, pharmaceuticals, and cosmetics. Recent work investigating the influence of UV radiation on the photochemical mechanisms has shown that riboflavin directly produces singlet oxygen at wavelengths of 308, 330, 355, and 370 nm [2], rationalizing why riboflavin levels in food can rapidly degrade upon exposure to natural/artificial light, ultimately curbing its shelf-life. Given its prominence within many metabolic processes, it has become ever more crucial to explore the photochemistry behind riboflavin and to work towards a means of better stabilizing the vitamin *in vivo* and within consumer products.

The condensed-phase photostability of riboflavin at various pH values (*i.e.*, (de)protonation state) has previously been addressed: under acidic/neutral conditions riboflavin photodegrades to LC whereas, under alkaline conditions, riboflavin photodissociates to both LC and LF. Whilst LC is formed *via* a riboflavin excited singlet state (<sup>1</sup>RF\*), both LF and LC can be formed *via* intramolecular photoreduction from an excited triplet state (<sup>3</sup>RF\*). Naturally, with pK<sub>a</sub> values of 1.7 and 10.2, riboflavin kinetics have also been greatly studied, with rates shown to increase by *ca.* 80 folds in alkaline media (correlated with the increase reactivity of the triplet state) until pH 10, at which the anion is formed [3].

Unsurprisingly, the extensive solution-phase photochemical behavior of riboflavin has accrued much experimental attention over the years; however, analogous to many other flavins (*e.g.*, lumichrome), there has been an overarching lack of exploration into the intrinsic excited-state properties of isolated (*i.e.*, gas-phase) flavins until of late [4–11]. This strikingly appears to be in spite of gas-phase work typically aligning more closely with the findings of most computational efforts. Nevertheless, in the spirit of exploring the anionic behavior of flavin systems, Matthews *et al.* have compared the intrinsic electronic behavior of deprotonated LC and its related chromophore alloxazine (AL) to reveal near-threshold transient anion resonance states for the first time in flavins at ~3.8 eV, which the authors assign to dipole-bound excited states [4]. Recent efforts by Bull *et al.* have further

utilized tandem ion mobility spectrometry and action spectroscopy to bring to light the influence deprotonation sites have on the electronic absorption properties and photochemistry of the FAD anion [6], following on from earlier experimental work assigning probable sites of (de)protonation of flavins in the gas phase [7–12]. Non-statistical (*i.e.*, transpires during the excited-state lifetime) lumichrome formation of the FAD mono-anion is also found to proceed through the photo-induced, intramolecular proton-coupled electron transfer of riboflavin [7].

In this article, we present the first UV-visible electronic gas-phase study of the anionic (*i.e.*, deprotonated) form of riboflavin. We employ the technique of gas-phase laser photodissociation action spectroscopy on  $[\text{RF-H}]^-$  through forming the riboflavin anion as an isolated gas-phase species *via* electrospray ionization (ESI), and then obtaining the electronic absorption spectrum and action spectra of its resultant photofragment ions. Our gas-phase measurements are complemented by on-line photolysis in a UV-LED photolytic cell (365 nm) with ESI mass spectrometry (ESI-MS) [13]. This experimental approach provides a “one-pot” tool for characterizing the gas-phase and solution-phase photochemistry of a chosen system. The technique builds on other recent experiments which have employed on-line photolysis, with subsequent mass spectrometric detection [14–18]. The benefit of this approach is that the solution-phase measurements probe a more real-world environment for the riboflavin vitamin (*e.g.*, when it is in milk or a cosmetic formulations), while the gas-phase measurements can greatly aid the understanding of the solution-phase photochemical mechanisms. In the solution-phase, direct photoproducts can undergo secondary reactions and are subject to environmental factors, *i.e.*, pH, solvent, and aggregation [14–18]. This two-step method provides a new approach that could be widely applied to characterize the photochemical breakdown of food, beauty, and pharmaceutical products.

## 2. Results

### 2.1. Gas-Phase Absorption Spectroscopy of $[\text{RF-H}]^-$

Figure 1 shows the electrospray ionization mass spectrum of a solution of riboflavin obtained in negative ion mode.  $[\text{RF-H}]^-$  appears as the dominant ion in the mass spectrum, with  $m/z$  375 (Figure 1), along with a second intense fragment ion with  $m/z$  255 which can be assigned as deprotonated lumiflavin,  $[\text{LF-H}]^-$ . (Intriguingly, its corresponding protonated species is not observed at all in positive ion mode, as reiterated in Section S5; Figure S9.) The dimer complex, *i.e.*  $[\text{RF-H}]^- \cdot \text{RF}$  is observed at  $m/z$  751.

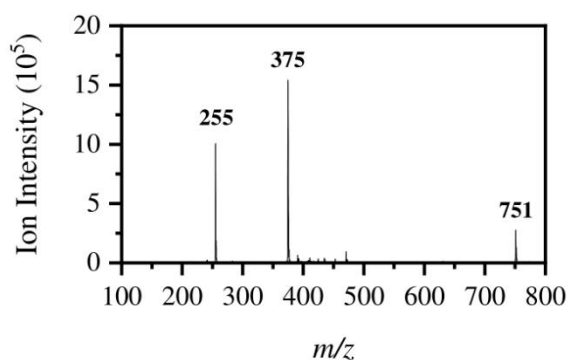


**Figure 1.** Negative ion mode ESI mass spectrum of deprotonated riboflavin ( $[\text{RF-H}]^-$ ).

Laser-interfaced mass spectrometry (LIMS) was used to characterize *in vacuo* the wavelength-dependent photoabsorption and photofragmentation properties of  $[\text{RF-H}]^-$ .

The spectra are acquired by action spectroscopy as described in Section 4 and in References [19–21]. Figure 2a displays the gas-phase photodepletion spectrum of  $[\text{RF-H}]^-$ , which can be considered to be the gas-phase UV-visible absorption spectrum of the ion, subject to the limitations discussed in References [20,22–24]. The absorption spectrum displays an absorption onset at 2.0 eV (620 nm), followed by five bands labeled I–V. Bands I–III (at ca. 3.0, 3.5, and 4.2 eV, respectively) are medium intensity, broad bands, with band I observed in the visible region, centered around 3.0 eV (414 nm). Absorption continues to extend across into the UVC region, where band IV appears as a relatively strong feature between 4.5–5.2 eV, peaking at 5.0 eV (246 nm). The rising edge of band V is at the high-energy spectral edge and extends beyond 5.74 eV (216 nm).

The absorption profile of  $[\text{RF-H}]^-$  in aqueous solution is shown in Figure 2b, for comparison with the gaseous spectrum (Figure 2a). RF has multiple acidic protons, and its reported  $\text{pK}_a$  values of 1.7 and 10.2 [25] indicate that it will be deprotonated in aqueous solution at neutral pH. Drössler *et al.* have demonstrated that the solution-phase UV absorption spectra of RF in aqueous solution is unchanged between the pH values of 7.0, 9.3, 10.25, and 13.35 [26].

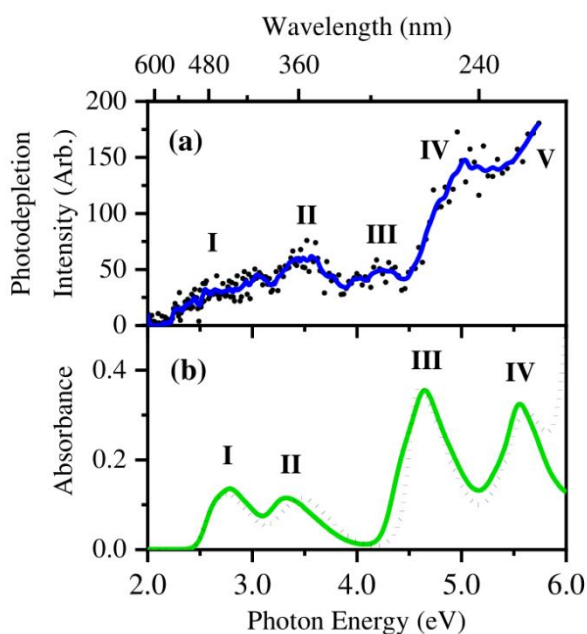


**Figure 2.** (a) Gas-phase photodepletion (absorption) spectrum of  $[\text{RF-H}]^-$  and (b) static solution-phase absorption spectrum of RF in aqueous solution (pH ~ 5.5; solid green line) and RF in aqueous solution with trace amounts of  $\text{NH}_3$  (pH ~ 11.2; dotted black line).

On comparing the experimental gaseous and solution-phase spectra in Figures 2a and 2b, respectively, both spectra are seen to display relatively low absorption across the visible-UVB regions, with the two dominant gas-phase UV bands IV and V likely to correspond to the strong III and IV features seen in the solution phase. It is striking that the intense solution-phase transition band III seems to appear much less strongly in the gas-phase spectrum (4.3 eV) as observed in the gas phase. This effect can arise from fluorescence decay of the electronic states associated bands which are observed more weakly in gas-phase action spectroscopy than in solution [24]. Indeed, riboflavin is known to exhibit fluorescence, with its anionic form in particular, found to exhibit a low fluorescence quantum yield of  $1.2 \times 10^{-3}$  in aqueous solution [26].

## 2.2. Gas-Phase Photofragmentation of $[RF-H]^-$

We next turn to exploring the gas-phase photofragment ions that are associated with the excited states evident in the gaseous absorption spectrum. Figures 3a-e display the photofragment mass spectra of  $[RF-H]^-$  obtained following excitation at 2.5, 3.5, 4.2, 4.7, and 5.0 eV. The spectra show that  $m/z$  255 and 241 are observed as the dominant and minor ionic fragments respectively, corresponding to a loss of 120 and 134 Da from  $[RF-H]^-$  to form deprotonated lumiflavin ( $[LF-H]^-$ ) and lumichrome ( $[LC-H]^-$ ), respectively. It has been previously noted that both LF and LC are formed in alkaline media *via* the triplet excited state through the mediation of formylmethylflavin (FMF; 284.27 Da), which is believed to be an intermediate in the photolysis of RF. A number of less intense, minor fragment ions are also observed, *e.g.*, at  $m/z$  145 and 212.

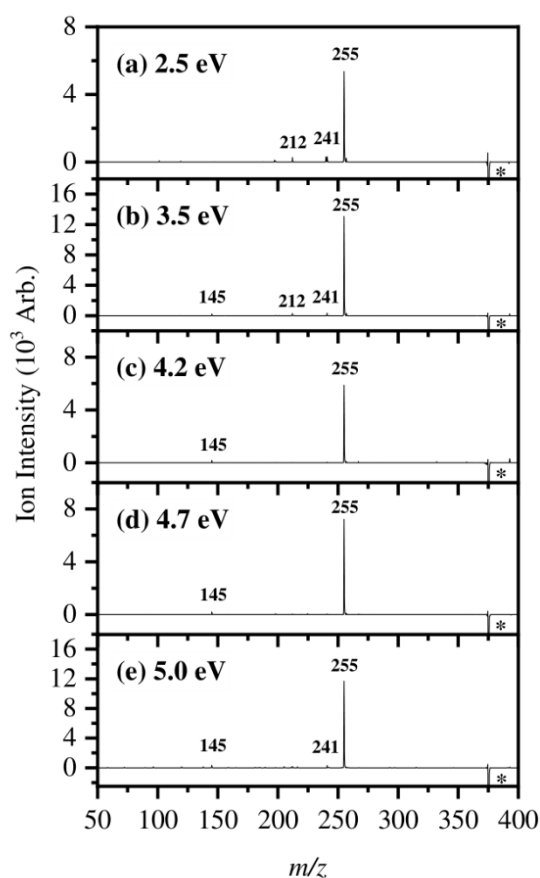
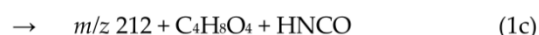


**Figure 3.** Photofragment difference ( $\text{laser}_{\text{ON}} - \text{laser}_{\text{OFF}}$ ) mass spectra of  $[RF-H]^-$  excited at five photodepletion maxima of (a) 2.5, (b) 3.5, (c) 4.2, (d) 4.7, and (e) 5.0 eV. [\*] indicates the photodepleted parent ion signal at  $m/z$  375.

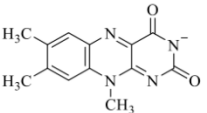
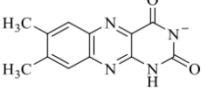
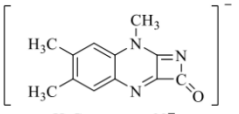
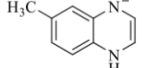
The novelty of our LIMS set-up allows us to monitor the photofragment production intensities at each scanned wavelength to provide further insight into the nature of the excited states. Figure 4b displays the production spectrum of the major photofragment  $[LF-H]^-$  with  $m/z$  255, showing that it is produced across the entire experimental spectral

range from 2.0–5.74 eV (620–216 nm), with significant peaks in production within the band maxima of all bands I–V of the gas-phase photodepletion (absorption) spectrum of  $[\text{RF-H}]^-$  (Figure 4a for ease of comparison). The photofragment production spectra of minor fragments  $m/z$  241 and 212 (Figures 4c and 4d, respectively) also display similar absorption maxima at 3.5, 5.0, and 5.7 eV, but with distinctive absorption profiles in the lower-energy region around 2.5 eV compared to  $m/z$  255. Little to no production of these fragments occurs between 4.0–4.5 eV. The production spectrum of the  $m/z$  145 photofragment (Figure 4e) has a production onset at  $\sim$ 2.75 eV, subsequently peaking at 3.25 eV, 5.0 and 5.7 eV. The major photodissociation channels are summarized in Equations (1a)–(1d) and again in Table 1.



Since  $[\text{RF-H}]^-$  is anionic, any photodepletion that is not associated with photofragment ion production must generally be associated with electron loss processes [4,27,28]. This is discussed further in Section S2.

**Table 1.** Summary of the major ionic fragments of  $[\text{RF-H}]^-$  ( $m/z$  375) observed upon collisional dissociation (CID), higher-collisional dissociation (HCD), gas-phase UV-visible laser photoexcitation, and solution-phase on-line UVA (365 nm) photolysis.

Ionic Fragment Mass ( $m/z$ ) <sup>1</sup>	Proposed Structure of Fragment	Mass of Accompanying Neutral Mass Lost	Observed in CID (via $\text{H}_2\text{O}$ ) <sup>1,2</sup>	Observed in HCD (via EtOH)		Observed in Laser UV-visible Photoexcitation <sup>1,2</sup>	Observed via Solution-Phase On-line UV-A Photolysis <sup>1,2</sup>	
				25%	50%		3 min	6 min
255		120	✓ (vs)	✓ (s) ✓ (m)	✓ (s)	✓ (w) <sup>4</sup>	✓ (vw)	
241		134	-	- ✓ (w)	✓ (w)	✓ (w)	✓ (vs)	
212		163	-	✓ (w) ✓ (m)	✓ (w)	✓ (w)	✓ (w)	
145		230	-	✓ (w) ✓ (w)	✓ (w)	-	-	

<sup>1</sup> Determined with mass accuracy  $> 0.3$  amu. <sup>2</sup> very strong (vs), strong (s), medium (m), weak (w), and very weak (vw). <sup>3</sup> Fragment ions with masses above that of the parent ion at  $m/z$  375 stem from that of the RF dimer complex ( $[\text{RF-H}]^- \text{RF}$ ;  $m/z$  751) and its photofragment (i.e., at  $m/z$  617). The ion at  $m/z$  617 results from the loss of 134 Da ( $\text{C}_5\text{H}_{10}\text{O}_4$ ) from the dimer at  $m/z$  751. <sup>4</sup> Notably, the ion at  $m/z$  255 is thought to be produced via the ESI process of the aqueous RF or via means of in-source dissociation, and is thus intensely observed pre-irradiation.

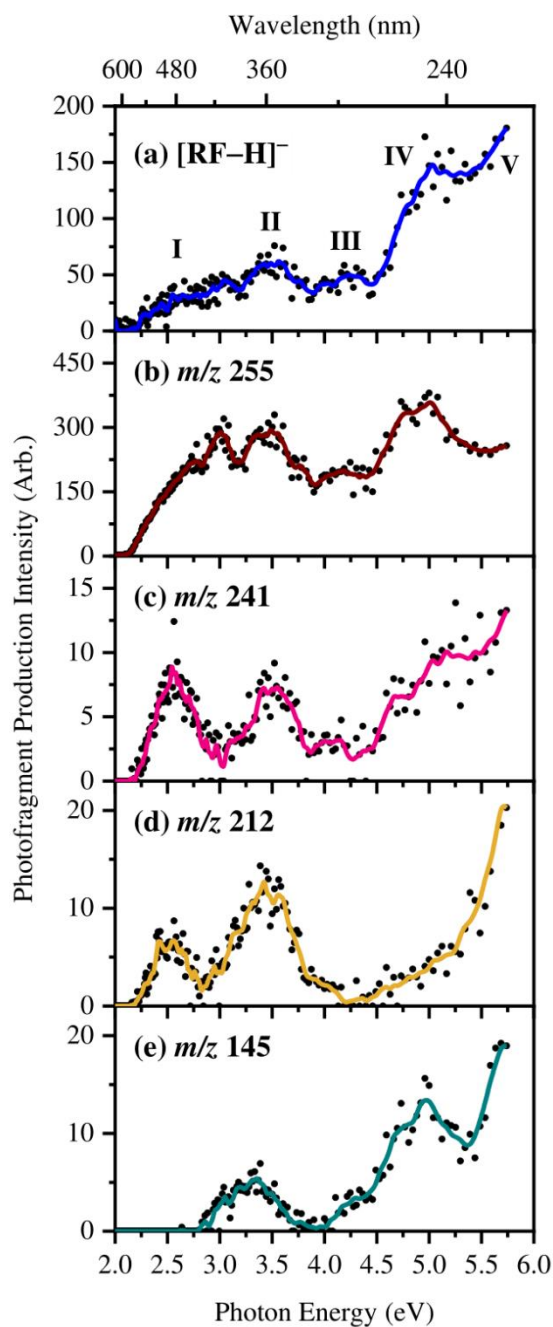


**Figure 4.** (a) Gas-phase photodepletion (absorption) spectrum of  $[RF-H]^-$  ( $m/z$  375). (b–e) Photofragment production spectra of the four major  $[RF-H]^-$  photofragment ions at  $m/z$  255, 241, 212, and 145, respectively. The solid line is a five-point adjacent average of the data points.

Figure 5 presents the relative photofragment ion yields for  $[RF-H]^-$  as a function of excitation energy, highlighting several maxima that can be attributed to photoexcitation into different electronic states [29,30]. It is evident that in the 2.0–3.0 eV region, the  $m/z$  241 and 212 photofragments are dominant, whereas  $m/z$  145 is not produced across this region.

Between 3.0–4.0 eV, all three fragments are produced, with  $m/z$  212 produced at *ca.* 50% larger than that of  $m/z$  145. In contrast, between 4.0–5.74 eV,  $m/z$  145 overtakes  $m/z$  241 and 212 in relative ion intensity, with all three increasing steadily with photon energy towards the high-energy edge.

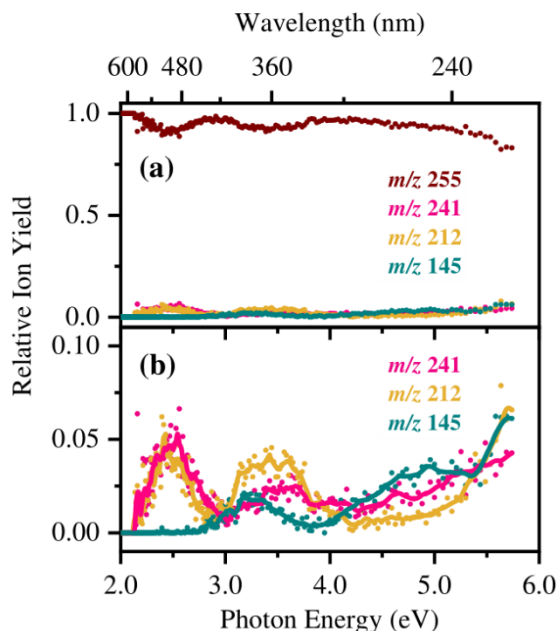


**Figure 5.** (a) Relative ion yield plot highlighting the relative ion yields of the 4 most dominant laser-induced  $[RF-H]^-$  photofragments at  $m/z$  145, 212, 241, and 255 between 2.0–5.74 eV. (b) Zoomed-in depiction of the plot presented in (a), offering a clearer illustration of the events across the 2.0–5.74 eV photon region for the photofragments at  $m/z$  241, 212, and 145.

### 2.3. Collision-Induced Dissociation of $[RF-H]^-$

Low-energy collision-induced dissociation (CID) of  $[RF-H]^-$  electrospayed from aqueous solution gives  $[LF-H]^-$  ( $m/z$  255) as the only ionic product (Figure 6). The CID process is equivalent to thermal heating of ground state  $[LF-H]^-$ , with subsequent fragmentation across the lowest energy fragmentation barrier on the ground state surface [31]. The precursor  $[RF-H]^-$  ion does not dissociate up to ~40% CID, indicating that the ion is stable against spontaneous dissociation. However, as noted in Section 2.1, the ESI-MS of riboflavin produces  $m/z$  255 as well as  $[RF-H]^-$ , and the observation of  $m/z$  255 as a CID fragment indicates that  $[RF-H]^-$  is likely fragmenting into  $m/z$  255 either during ESI or *via* in source dissociation. It is also notable that  $m/z$  255 is the major gas-phase laser photofragment ion.

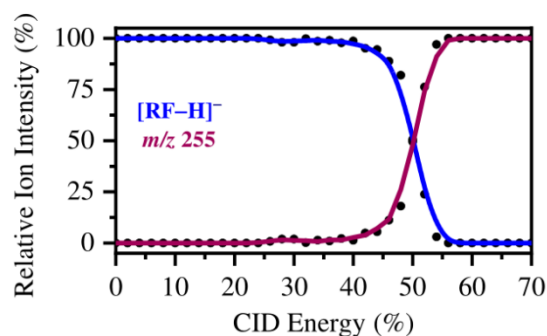


**Figure 6.** Low-energy collision-induced dissociation (CID) fragmentation decay curve for  $[\text{RF-H}]^-$  ( $m/z$  375) upon CID between 0-70% CID energy. The curved lines included with the data points are a three-point adjacent average of such data points.

To further probe the thermal fragmentation pathway(s) of  $[\text{RF-H}]^-$  on its electronic ground state, higher-energy collisional dissociation (HCD) was employed. These measurements are ideal to identify which ions are secondary fragments, formed when a precursor (or intermediate) species fragments at high internal energy. Importantly, any photofragments not observed in these HCD experiments can be identified as purely photochemical products. A HCD plot of  $[\text{RF-H}]^-$  electrosprayed in EtOH in the negative ion mode is shown in Figure 7, highlighting the extent of their thermal degradation products at higher HCD energies. (We note that it was not possible to electrospray from an aqueous solution in these experiments, due to differences in the ionization efficiencies of the two different instruments used.) However, it was possible to electrospray from both EtOH and MeCN in the HCD instrument. The results obtained with both solvents were extremely similar, giving us confidence that this would also be the case if the electrospray had been conducted from an aqueous solution.)

At relatively low collisional energies (0–25% HCD), the most intense fragment ion is  $m/z$  255, with  $m/z$  243 peaking at *ca.* 15% higher relative ion intensity. The production of the  $m/z$  255 ion gradually decreases beyond 25% HCD energy, where the onset of the  $m/z$  212 ion is observed. This secondary ion later peaks at 48% HCD energy. However, since the  $m/z$  255 fragment clearly dominates in both the gas-phase UV-visible laser and the thermal (*i.e.*, CID and HCD) fragmentation experiments, photofragmentation of the  $[\text{RF-H}]^-$  ion can be categorized as predominantly statistical (ergodic) over the spectral range studied in this experiment [29,32].

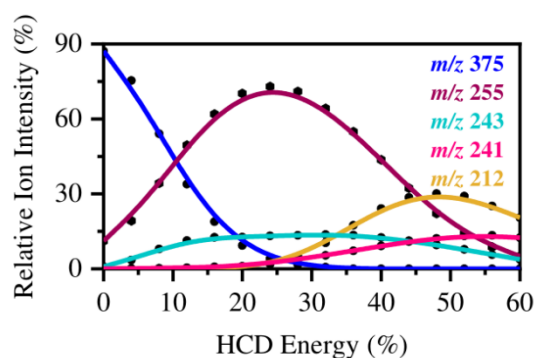
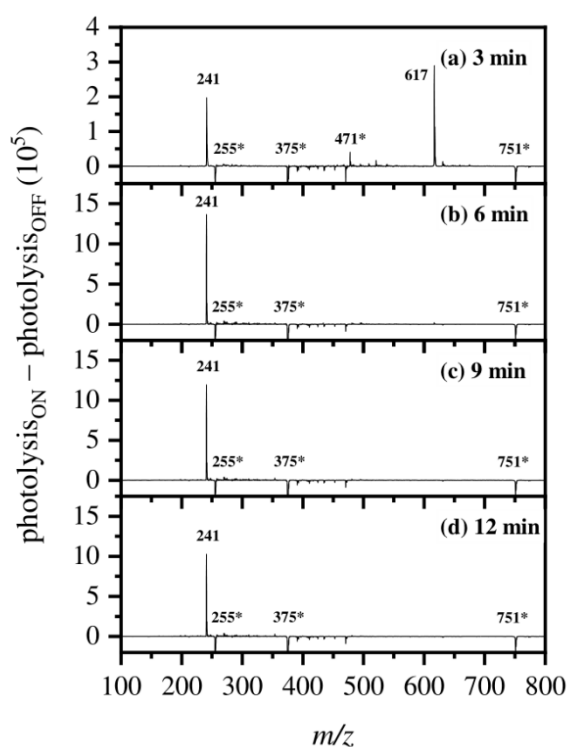


**Figure 7.** Parent ion dissociation curves  $[\text{RF-H}]^-$  ( $m/z$  375) and its four most intense thermal fragments between 0% and 60% HCD energy, as electrosprayed in EtOH. The curved lines are a five-point adjacent average of such data points and are provided as a viewing guide, to emphasize the profile for each individual fragment. A complete HCD plot highlighting the production of the minor fragments of  $[\text{RF-H}]^-$  are available in Section S3.

Overall, the CID and HCD fragmentation experiments reveal that  $[\text{RF-H}]^-$  primarily dissociates into  $m/z$  255, which subsequently dissociates into  $m/z$  212 at higher internal energy, and increasingly into  $m/z$  241 and 145 at the highest internal energies.

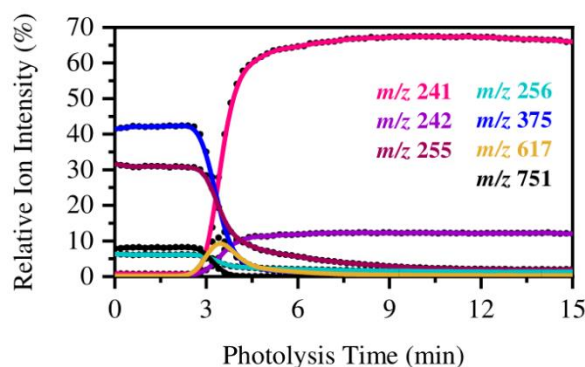
### 2.5 On-Line Solution-Phase Photolysis of $[\text{RF-H}]^-$

Figure 8 shows photolysis<sub>ON</sub> – photolysis<sub>OFF</sub> (difference) ESI mass spectra obtained from the photolysis (UV-A; 365 nm) of aqueous riboflavin at 3, 6, 9, and 12 minutes. The  $[\text{RF-H}]^-$  precursor ion ( $m/z$  375), the primary thermal ion ( $m/z$  255), and the dimer ion ( $m/z$  751) are all seen to be depleted in the difference spectra, indicating that they are photolyzed at this wavelength. Solution-phase photolysis of  $[\text{RF-H}]^-$  dominantly produces the same  $m/z$  241 ion that was observed in the gas-phase irradiation experiments, which corresponds to the production of  $[\text{LC-H}]^-$ . The ion at  $m/z$  617 is again the loss of  $\text{C}_5\text{H}_{10}\text{O}_4$  (134 Da) from the dimer complex  $[\text{RF-H}]^- \cdot \text{RF}$  at  $m/z$  751. The same loss in  $m/z$  is observed in Eq. 1b.



**Figure 8.** (a) Photolysis<sub>ON</sub> – photolysis<sub>OFF</sub> ESI mass spectra of a solution of aqueous RF after irradiation at 365 nm (3.4 eV) at 3, 6, 9, and 12 min. [\*] indicates the photodepleted ions at  $m/z$  255, 375, 471, and 751, where  $m/z$  375 is that of the parent ion.

Figure 9 shows the relative ion intensities of the solution-phase photofragment ions observed through ESI-MS as a function of irradiation time. The relative intensities of the ions which are initially present upon electrospray (*i.e.*,  $m/z$  255, 375, and 751) remained steady until *ca.* 3.0 min (the transit time of the solution that is being photolyzed into the MS), where the sudden production onset of the major  $m/z$  241 fragment ion is then observed. Several relatively minor fragments (<5% relative ion intensity over 30 min of irradiation) are also observed, as outlined in Figure S4.



**Figure 9.** Relative ion intensity plot highlighting the solution-phase photofragment ions of aqueous  $[\text{RF-H}]^-$  produced over a 15 minute interval of irradiation at 365 nm (3.4 eV) when delivered *via* ESI-MS in the negative ion mode. The curved lines included with the data points are a three-point adjacent average of such data points and are extracted from an average of 3 repeat runs. The production curves of the minor solution-phase photofragments are illustrated in Figure S4.

Control experiments run in parallel using routine ESI-MS detection showed that under the same photolytic conditions, solutions of  $[\text{RF-H}]^-$  held within “black-coated” syringes (*e.g.*, to block all transmission of UV light) showed no degradation of the parent ( $m/z$  375) ion, nor the  $m/z$  255, or  $m/z$  375 ions (see Section S6; Figures S10 and S11). The solution-phase photofragment at  $m/z$  241 identified earlier in Figures 8 and 9 was also not observed. This demonstrated that these ions remained unaffected by any several external factors (*e.g.*, heating or hydrolysis).

### 3. Discussion

In this work, gas-phase laser-interfaced photodissociation mass spectrometry has been employed on the native form of riboflavin for the first time to map its intrinsic UV-visible absorption (photodepletion) spectrum and associated photodegradation products. Solution-phase photoproducts were generated *via* photolysis on-line with the MS instrument, and were characterized using ESI-MS and compared with the gas-phase results. Whilst  $[\text{RF-H}]^-$  was found to photodegrade into deprotonated lumichrome ( $m/z$  241) *via* the loss of 134 Da in both the gas and solution phase at 365 nm (3.4 eV), further ions at  $m/z$  255, 212, and 145 were observed to be produced following gas-phase photodissociation of the isolated molecular ion. (Our HCD results revealed that the  $m/z$  255 ion dissociates into  $m/z$  212 and 145 at high internal energies.)

The photoproducts observed in this work mirror those seen in related work by Insińska-Rak *et al.* [15,18], where pH neutral solutions of riboflavin and its derivatives were photolyzed by mercury lamps, and photoproducts detected by HPLC and then electron ionization mass spectrometry (EI-MS). The EI-MS fragmentation pathways of riboflavin proceed with *via* formation of lumichrome and lumiflavin, with major ions observed at  $m/z$  256 (relative intensity of 33%), 213 (43%), 198 (52%), and 170 (25%) *via* the

lumiflavin route, or  $m/z$  242 (12%), 199 (28%), 171 (42%), and 156 (16%) through the lumichrome route [15,18]. (Note that such mass-to-charge ratios are monitored *via* EI-MS). All of the photofragments observed in the work of Insińska-Rak *et al.* are in line with the main photoproducts formed in this work (with the exception of our  $m/z$  145 photofragment, which we know is a secondary fragment).

The results presented herein therefore demonstrate a useful new technique for monitoring solution-phase photodegradation of  $[\text{RF-H}]^-$  and detection of its resulting ionic photodissociation products. The direct and uninterrupted injection of the irradiated contents of the syringe allows for continuous real-time monitoring of the change in ion intensities of select ions over time (see Figure 9). This present work also demonstrates the value of performing the gas-phase photodissociation measurements, even in the absence of on-line solution-phase photolysis, since the gas-phase measurement allows the identification of the major photolysis product for this system, and hence potentially others. The gas-phase measurements have several advantages as they are conducted against zero background, hence allowing straightforward identification of minor photoproducts, as well as allowing the primary photoproducts to be identified away from secondary reactions that can occur in solution. Nonetheless, the combination of on-line solution-phase photolysis coupled with gas-phase photolysis of the mass selected species of interest clearly allows a rapid and straightforward link to be established between the gas-phase measurement and the “real world” environment of the solution photochemistry. This approach has potential for widespread application across photochemical systems of interest, including pharmaceuticals [33] and sunscreens [21,34,35].

#### 4. Materials and Methods

**Laser-Interfaced Photodissociation Mass Spectrometry.** The gaseous ion absorption (photodepletion) and photofragment production spectra of  $[\text{RF-H}]^-$  were recorded *in vacuo* using laser action spectroscopy. An Amazon SL mass spectrometer (Bruker Daltonics Inc., Billerica, MA, USA), modified for laser-interfaced mass spectrometry (LIMS), was used as described previously. RF was purchased from Sigma-Aldrich (St. Louis, MA, USA) and used as received. RF solutions ( $1 \times 10^{-5}$  M) in deionized  $\text{H}_2\text{O}$  were electrosprayed at a capillary temperature  $100^\circ\text{C}$  in the negative ion mode. Trace amounts of  $\text{NH}_3$  (0.4%) was added to the aqueous solution(s) to aid the electrospray process, as the intensity of ions produced without the additive deemed insufficient for later gas-phase measurements.

$[\text{RF-H}]^-$  was mass-selected ( $m/z$  375) and isolated in the ion trap prior to laser irradiation. Photons were produced by an Nd:YAG pumped OPO laser (Surelite™/Horizon™, Amplitude Laser Group, San Jose, CA, USA), giving  $0.1 \pm 15\%$  mJ across the UV-visible range 620–216 nm (2.0–5.74 eV), with 2 nm laser step sizes in the UV and 4 nm steps in the visible. Photofragmentation experiments were conducted with an ion accumulation time of 20 ms. To minimize the possibility of multiphoton events *via* sequential absorption, each mass-selected ion packet interacts with only one laser pulse (corresponding to a fragmentation time of 100 ms), and photodepletion restricted to  $\sim 40\%$  of the precursor ion at the wavelength of maximum absorption. Multiphoton events *via* instantaneous absorption of multiple photons in the Franck-Condon region are negligible as the laser beam is only softly focused through the ion-trap region.

Photodepletion of  $[\text{RF-H}]^-$  was measured as a function of the scanned wavelength, with photofragment production recorded simultaneously [Eq. (2)–(4)]:

$$\text{Photodepletion (PD) Intensity} = \frac{\ln\left(\frac{I_{\text{OFF}}}{I_{\text{ON}}}\right)}{\lambda \times P} \quad (2)$$

$$\text{Photofragment (PF) Production Intensity} = \frac{\text{Int}_{\text{FRAG}}}{\lambda \times P} \quad (3)$$

$$\text{Relative Ion Yield} = \frac{\text{Int}_{\text{FRAG}}}{\text{Int}_{\text{PFT}}} \quad (4)$$

In these expressions,  $\text{Int}_{\text{OFF}}$  and  $\text{Int}_{\text{ON}}$  are the laser off and on parent ion peak intensities respectively;  $\text{Int}_{\text{FRAG}}$  is the fragment intensity with the laser on;  $\lambda$  is the excitation wavelength (nm);  $P$  is the laser pulse energy (mJ); and  $\text{Int}_{\text{PFT}}$  is the sum of the photofragment ion intensities with the laser on. The photodepletion spectrum is considered to be equivalent to the gaseous absorption spectrum in the limit where excited state fluorescence is negligible.

Electron detachment yield ( $\text{ED}^*$ ) spectra were calculated by assuming that any depleted ions not detected as ionic photofragments are decaying *via* means of electron detachment, as determined using Eq. 5. This analysis assumes that both the parent ions and photofragments are detected equally in the mass spectrometer. In Figure S2 where we present  $\text{ED}^*$  spectra, we overlay such data with the photodepletion yield ( $\text{PD}^*$ ).  $\text{PD}^*$  is the normalized photodepletion ion count (Eq. 6), which provides the most straightforward comparison to the electron detachment yield (Eq. 5).

$$\text{Electron detachment yield (ED}^*) = \frac{(\text{Int}_{\text{OFF}} - \text{Int}_{\text{ON}}) - \text{Int}_{\text{PFT}}}{\lambda \times P} \quad (5)$$

$$\text{Photodepletion yield (PD}^*) = \frac{\text{Int}_{\text{OFF}} - \text{Int}_{\text{ON}}}{\lambda \times P} \quad (6)$$

**Analysis.** Photodepletion intensities were taken from an average of three repeat runs at each wavelength of the range studied. We note that fragment ions with  $m/z < 50$  are not detectable in our mass spectrometer since low masses fall outside the ion-trap mass window.

**Collision-Induced Dissociation Energy.** Low-energy collision-induced dissociation (CID) was performed to investigate the ground-state thermal fragmentation characteristics of  $[\text{RF-H}]^-$ , using the aforementioned Bruker AmaZon mass spectrometer. Here, an excitation AC folder was applied to the end caps of the ion trap to induce low-energy collisions of the trapped anions with the helium buffer gas, as has been described in detail previously [31,36]. Precursor ion excitation within the quadrupole ion trap occurs through multiple low-energy collisions with helium. Resonance excitation amplitudes for thermal decomposition of molecular ions within a quadrupole ion trap have been shown to correlate with literature critical dissociation energies. However, given that is no direct conversion from the resonance excitation voltage to absolute CID energies, such CID energies are therefore quoted as a percentage of the 2.5 V excitation voltage, in line with other standard practices [31,36–38].

**Higher-energy Collisional Dissociation.** Higher-energy collisional dissociation (HCD) was performed on  $[\text{RF-H}]^-$ , electrosprayed from solutions of EtOH and MeCN using an Orbitrap Fusion Tribid mass spectrometer (Thermo Fisher Scientific, Waltham, MA, USA) with an ESI source, run in the negative ion mode between 0% and 60% collisional energy. This technique provides tandem mass spectrometry and was operated at a flow rate of 3.0  $\mu\text{L}/\text{min}$ , with the following parameters: spray voltage: -2000 V; sheath gas flow rate: 10; aux. gas flow rate: 2.0; ion transfer tube temperature: 290  $^\circ\text{C}$ ; vaporizer temperature: 20  $^\circ\text{C}$ ;  $\text{MS}^2$  detector: Orbitrap; scan rate: enhanced;  $\text{MS}^2$  injection time: 100 ms; and RF lens: 60%.

**Solution-Phase UV-A Photodissociation.** For sample irradiation, four UV-A light emitting diodes (LEDs; 365 nm {3.4 eV}, LZ1-00UV00, LED Engin, Inc., San Jose, CA, USA) were employed. The four LEDs were connected in series and powered with a 500 mA constant current power source. Each of the LEDs were situated onto each face of the square (23 mm × 23 mm) interior of the custom designed aluminum cell, surrounding the barrel of the UV-transmitting borosilicate glass of the syringe (model 1002LTN; 2.5 mL; needle size: 22 ga [blunt tip]; needle length: 51 mm; Hamilton®, Reno, Nevada, USA). A syringe-pump set to inject solution at 0.33 mL/hr was fitted to hold the cell and syringe, allowing for direct on-line measurement of the contents *via* ESI-MS (see Section S5). The design of the cell allows for a designated volume (*i.e.*, >2.5 mL) of the contents of the syringe to be continually irradiated in chorus for a set time (*i.e.*, 15 minutes). The cell is adapted to permit greater volumes of solution(s), and thus alternate syringes, to be continuously irradiated. A fitted shield has also been added to protect the contents of the syringe from latent photodegradation resulting from that of standard laboratory lighting.

The stability of all RF solutions involved were also monitored *via* static solution-phase UV-visible absorption spectroscopy over a 4-hour window (See Section S5; Figure S6). Similarly, as depicted in Figures S7 and S8, static UV-visible absorption spectra of the irradiated aqueous RF samples (with/without NH<sub>3</sub>, respectfully) were taken by manually transferring the irradiated solution(s) from the syringe in which the solution(s) were irradiated in (model 1002LTN; 2.5 mL; Hamilton®) into a far-UV quartz (macro)cuvette (10 mm path-length; Hellma® UK Ltd., Essex, UK) for measurement *via* a conventional spectrophotometer (GENESYS 180; Thermo Fisher Scientific, Waltham, MA, USA). Notably, deionized H<sub>2</sub>O was used as the baseline solvent, with solutions being irradiated in 1-minute intervals up to 20 minutes.

In an effort to differentiate any photoproducts from that of any consequential potential thermal (*i.e.*, heat) products generated from the array of LEDs, an opaque black cloth was wrapped around the fitted syringe in a separate set of studies (see Section S5; Figures S10 and S11), to remove the influence of the UV-A light from the LEDs, with a temperature probe fitted to review the temperature of the experiment over time (Figure S12).

To mirror the deprotonated solutions used for gas-phase LIMS, on-line solution-phase UV photodissociation was primarily carried out on aqueous RF with NH<sub>3</sub> (0.4%). But for completeness, the solution-phase experiments were comprehensively repeated with and without the influence of NH<sub>3</sub>. High-resolution measurements were additionally performed on a Thermo Fisher Orbitrap mass spectrometer to allow for adequate differentiation of any (photo/thermal) product ions from that of contaminants typically found in the negative ion mode. Further analysis of the high-resolution monitoring of the reaction(s) is available within Section S6.

**Supplementary Materials:** Figure S1: Power dependence measurements for [RF-H]<sup>-</sup>; Figure S2: Electron detachment yield *vs.* photodepletion yield of [RF-H]<sup>-</sup>; Figure S3: Parent ion dissociation curves [RF-H]<sup>-</sup> (*m/z* 375) and the extent of the minor thermal fragments produced between 0% and 60% HCD energy, as electrosprayed in EtOH; Figure S4: Relative ion intensity plot highlighting the solution-phase photofragment ions of aqueous RF produced over a 15 minute interval of irradiation at 365 nm when delivered *via* ESI-MS in the negative ion mode; Figure S5: Various cross-sectional views of the custom-made on-line syringe photolysis cell; Figure S6: Static UV-visible absorption spectra monitoring the absorption spectrum of riboflavin, prepared in aqueous solution with trace amounts of NH<sub>3</sub> (0.4% v/v), between 0–240 min; Figure S7: Static UV-visible absorption spectra monitoring the changes in the absorption spectrum of riboflavin, prepared in aqueous solution with trace amounts of NH<sub>3</sub> (0.4% v/v), between 0–20 min upon irradiation (365 nm); Figure S8: Static UV-visible absorption spectra monitoring the changes in the absorption spectrum of riboflavin, prepared in aqueous solution, between 0–20 min upon irradiation (365 nm); Figure S9: Positive ion mode electrospray ionization (ESI) mass spectrum of protonated riboflavin ([RF+H]<sup>+</sup>) at *m/z* 377; Figure S10: Representative total ion chromatogram and extracted ion chromatogram for ions at *m/z* 751, 617, 375, 255, and 241; Figure S11: Relative ion intensity plot highlighting the solution-phase ions of aqueous [RF-H]<sup>-</sup> produced over a 30 minute interval of irradiation at 365 nm (3.4 eV) when

delivered *via* ESI-MS in the native ion mode when the syringe is covered with a black cloth, preventing UV-A light to be transmitted into the solution for irradiation; and Figure S12: Plot of the data obtained *via* use of a thermocouple employed to monitor the temperature within the photolysis cell at two separate locations within the on-line syringe photolysis cell.

**Author Contributions:** Conceptualization, C.E.H.D. and N.G.K.W.; methodology, C.E.H.D., C.R., and N.G.K.W.; software, C.E.H.D. and N.G.K.W.; validation, C.E.H.D. and N.G.K.W.; formal analysis, N.G.K.W.; investigation, N.G.K.W.; resources, C.E.H.D. and C.R.; data curation, N.G.K.W.; writing—original draft preparation, N.G.K.W.; writing—review and editing, C.E.H.D. and N.G.K.W.; visualization, C.E.H.D.; supervision, C.E.H.D.; project administration, C.E.H.D.; funding acquisition, C.E.H.D. All authors have read and agreed to the published version of the manuscript.

**Funding:** This research was funded through the Leverhulme Trust Research Project Grant RPG-2017-147. We thank the University of York and the Department of Chemistry for provision of funds for the OPO laser system.

**Conflicts of Interest:** The authors declare no conflict of interest.

## References

1. Sheraz, M.A.; Kazi, S.H.; Ahmed, S.; Anwar, Z.; Ahmad, I. Photo, thermal and chemical degradation of riboflavin. *Beilstein J. Org. Chem.* **2014**, *10*, 1999–2012, doi:10.3762/bjoc.10.208.
2. Knak, A.; Regensburger, J.; Maisch, T.; Bäuml, W. Exposure of vitamins to UVB and UVA radiation generates singlet oxygen. *Photochem. Photobiol. Sci.* **2014**, *13*, 820–829, doi:10.1039/C3PP50413A.
3. Ahmad, I.; Fasihullah, Q.; Noor, A.; Ansari, I.A.; Ali, Q.N.M. Photolysis of riboflavin in aqueous solution: a kinetic study. *Int. J. Pharm.* **2004**, *280*, 199–208, doi:10.1016/j.ijpharm.2004.05.020.
4. Matthews, E.; Dessent, C.E.H. Observation of Near-Threshold Resonances in the Flavin Chromophore Anions Alloxazine and Lumichrome. *J. Phys. Chem. Lett.* **2018**, *9*, 6124–6130, doi:10.1021/acs.jpcllett.8b02529.
5. Matthews, E.; Cercola, R.; Dessent, C. Protomer-Dependent Electronic Spectroscopy and Photochemistry of the Model Flavin Chromophore Alloxazine. *Molecules* **2018**, *23*, 2036, doi:10.3390/molecules23082036.
6. Bull, J.N.; Carrascosa, E.; Giacomozzi, L.; Bieske, E.J.; Stockett, M.H. Ion mobility action spectroscopy of flavin dianions reveals deprotomer-dependent photochemistry. *Phys. Chem. Chem. Phys.* **2018**, *20*, 19672–19681, doi:10.1039/c8cp03244k.
7. Stockett, M.H. Photo-induced proton-coupled electron transfer and dissociation of isolated flavin adenine dinucleotide mono-anions. *Phys. Chem. Chem. Phys.* **2017**, *19*, 25829–25833, doi:10.1039/C7CP04068G.
8. Günther, A.; Nieto, P.; Müller, D.; Sheldrick, A.; Gerlich, D.; Dopfer, O. BerlinTrap: A new cryogenic 22-pole ion trap spectrometer. *J. Mol. Spectrosc.* **2017**, *332*, 8–15, doi:10.1016/j.jms.2016.08.017.
9. Langer, J.; Günther, A.; Seidenbecher, S.; Berden, G.; Oomens, J.; Dopfer, O. Probing protonation sites of isolated flavins using IR spectroscopy: From lumichrome to the cofactor flavin mononucleotide. *ChemPhysChem* **2014**, *15*, 2550–2562, doi:10.1002/cphc.201402146.
10. Zhang, T.; Papsion, K.; Ochran, R.; Ridge, D.P. Stability of Flavin Semiquinones in the Gas Phase: The Electron Affinity, Proton Affinity, and Hydrogen Atom Affinity of Lumiflavin. *J. Phys. Chem. A* **2013**, *117*, 11136–11141, doi:10.1021/jp406786a.
11. Guyon, L.; Tabarin, T.; Thuillier, B.; Antoine, R.; Broyer, M.; Boutou, V.; Wolf, J.-P.; Dugourd, P. Femtosecond pump-probe experiments on trapped flavin: Optical control of dissociation. *J. Chem. Phys.* **2008**, *128*, 075103, doi:10.1063/1.2828558.
12. Sheldrick, A.; Müller, D.; Günther, A.; Nieto, P.; Dopfer, O. Optical spectroscopy of isolated flavins: Photodissociation of protonated lumichrome. *Phys. Chem. Chem. Phys.* **2018**, *20*, 7407–7414, doi:10.1039/c8cp00590g.
13. Cercola, R.; Wong, N.G.K.; Rhodes, C.; Olijnyk, L.; Mistry, N.S.; Hall, L.M.; Berenbeim, J.A.; Lynam, J.M.; Dessent, C.E.H. A “one pot” mass spectrometry technique for characterizing solution- and gas-phase photochemical reactions by electrospray mass spectrometry. *RSC Adv.* **2021**, *11*, 19500–19507, doi:10.1039/D1RA02581C.

14. Mehara, J.; Roithová, J. Identifying reactive intermediates by mass spectrometry. *Chem. Sci.* **2020**, *11*, 11960–11972, doi:10.1039/D0SC04754F.
15. Insińska-Rak, M.; Prukała, D.; Golczak, A.; Fornal, E.; Sikorski, M. Riboflavin degradation products; combined photochemical and mass spectrometry approach. *J. Photochem. Photobiol. A Chem.* **2020**, *403*, 112837, doi:10.1016/j.jphotochem.2020.112837.
16. Pahl, M.; Mayer, M.; Schneider, M.; Belder, D.; Asmis, K.R. Joining Microfluidics with Infrared Photodissociation: Online Monitoring of Isomeric Flow-Reaction Intermediates. *Anal. Chem.* **2019**, *91*, 3199–3203, doi:10.1021/acs.analchem.8b05532.
17. Chen, S.; Wan, Q.; Badu-Tawiah, A.K. Picomole-Scale Real-Time Photoreaction Screening: Discovery of the Visible-Light-Promoted Dehydrogenation of Tetrahydroquinolines under Ambient Conditions. *Angew. Chemie Int. Ed.* **2016**, *55*, 9345–9349, doi:10.1002/anie.201603530.
18. Insińska-Rak, M.; Golczak, A.; Sikorski, M. Photochemistry of riboflavin derivatives in methanolic solutions. *J. Phys. Chem. A* **2012**, *116*, 1199–1207, doi:10.1021/jp2094593.
19. Matthews, E.; Dessent, C.E.H. Locating the proton in nicotinamide protomers via low-Resolution UV action spectroscopy of electrosprayed solutions. *J. Phys. Chem. A* **2016**, *120*, 9209–9216, doi:10.1021/acs.jpca.6b10433.
20. Matthews, E.; Sen, A.; Yoshikawa, N.; Bergström, E.; Dessent, C.E.H. UV laser photoactivation of hexachloroplatinate bound to individual nucleobases: In vacuo as molecular level probes of a model photopharmaceutical. *Phys. Chem. Chem. Phys.* **2016**, *18*, 15143–15152, doi:10.1039/c6cp01676f.
21. Wong, N.G.K.; Berenbeim, J.A.; Hawkrige, M.; Matthews, E.; Dessent, C.E.H. Mapping the intrinsic absorption properties and photodegradation pathways of the protonated and deprotonated forms of the sunscreen oxybenzone. *Phys. Chem. Chem. Phys.* **2019**, *21*, 14311–14321, doi:10.1039/C8CP06794E.
22. Sen, A.; Luxford, T.F.M.; Yoshikawa, N.; Dessent, C.E.H. Solvent evaporation versus proton transfer in nucleobase–Pt(CN)<sub>4</sub>,6<sup>2-</sup> dianion clusters: a collisional excitation and electronic laser photodissociation spectroscopy study. *Phys. Chem. Chem. Phys.* **2014**, *16*, 15490–15500, doi:10.1039/c4cp00989d.
23. Antoine, R.; Dugourd, P. Visible and ultraviolet spectroscopy of gas phase protein ions. *Phys. Chem. Chem. Phys.* **2011**, *13*, 16494–16509, doi:10.1039/c1cp21531k.
24. Wellman, S.M.; Jockusch, R.A. Moving in on the Action: An Experimental Comparison of Fluorescence Excitation and Photodissociation Action Spectroscopy. *J. Phys. Chem. A* **2015**, *119*, 6333–6338, doi:10.1021/acs.jpca.5b04835.
25. O’Neil, M.J. The Merck Index, 15th edition Available online: <https://www.rsc.org/Merck-Index/monograph/m9595/riboflavin>.
26. Drössler, P.; Holzer, W.; Penzkofer, A.; Hegemann, P. pH dependence of the absorption and emission behaviour of riboflavin in aqueous solution. *Chem. Phys.* **2002**, *282*, 429–439, doi:10.1016/S0301-0104(02)00731-0.
27. Matthews, E.; Cercola, R.; Mensa-Bonsu, G.; Neumark, D.M.; Dessent, C.E.H. Photoexcitation of iodide ion-pyrimidine clusters above the electron detachment threshold: Intracuster electron transfer versus nucleobase-centred excitations. *J. Chem. Phys.* **2018**, *148*, 084304, doi:10.1063/1.5018168.
28. Wong, N.G.K.; Rankine, C.D.; Dessent, C.E.H. Measurement of the Population of Electrosprayed Deprotomers of Coumaric Acids Using UV-Vis Laser Photodissociation Spectroscopy. *J. Phys. Chem. A* **2021**, *XXX*, XXX–XXX, doi:10.1021/acs.jpca.1c04880.
29. Wong, N.G.K.; Rankine, C.D.; Dessent, C.E.H. Linking Electronic Relaxation Dynamics and Ionic Photofragmentation Patterns for the Deprotonated UV Filter Benzophenone-4. *J. Phys. Chem. Lett.* **2021**, *12*, 2831–2836, doi:10.1021/acs.jpcllett.1c00423.
30. Berenbeim, J.A.; Wong, N.G.K.; Cockett, M.C.R.; Berden, G.; Oomens, J.; Rijs, A.M.; Dessent, C.E.H. Unravelling the Keto–Enol Tautomer Dependent Photochemistry and Degradation Pathways of the Protonated UVA Filter Avobenzone. *J. Phys. Chem. A* **2020**, *124*, 2919–2930, doi:10.1021/acs.jpca.0c01295.
31. Boxford, W.E.; Dessent, C.E.H. Probing the intrinsic features and environmental stabilization of multiply charged anions.

- Phys. Chem. Chem. Phys.* **2006**, *8*, 5151–5165, doi:10.1039/b609123g.
32. Cercola, R.; Matthews, E.; Dessent, C.E.H. Photoexcitation of Adenosine 5'-Triphosphate Anions in Vacuo: Probing the Influence of Charge State on the UV Photophysics of Adenine. *J. Phys. Chem. B* **2017**, *121*, 5553–5561, doi:10.1021/acs.jpcc.7b03435.
  33. Furlan, C.; Berenbeim, J.A.; Dessent, C.E.H. Photoproducts of the Photodynamic Therapy Agent Verteporfin Identified via Laser Interfaced Mass Spectrometry. *Molecules* **2020**, *25*, 5280, doi:10.3390/molecules25225280.
  34. Wong, N.G.K.; Berenbeim, J.A.; Dessent, C.E.H. Direct Observation of Photochemical Free Radical Production from the Sunscreen 2-Phenylbenzimidazole-5-Sulfonic Acid via Laser-Interfaced Mass Spectrometry. *ChemPhotoChem* **2019**, *3*, 1231–1237, doi:10.1002/cptc.201900149.
  35. Berenbeim, J.A.; Wong, N.G.K.; Cockett, M.C.R.; Berden, G.; Oomens, J.; Rijs, A.M.; Dessent, C.E.H. Sodium cationization can disrupt the intramolecular hydrogen bond that mediates the sunscreen activity of oxybenzone. *Phys. Chem. Chem. Phys.* **2020**, *22*, 19522–19531, doi:10.1039/D0CP03152F.
  36. Luxford, T.F.M.M.; Milner, E.M.; Yoshikawa, N.; Bullivant, C.; Dessent, C.E.H. Complexation of carboxylate anions with the arginine gas-phase amino acid: Effects of chain length on the geometry of extended ion binding. *Chem. Phys. Lett.* **2013**, *577*, 1–5, doi:10.1016/j.cplett.2013.05.040.
  37. Zhang, J.; Brodbelt, J.S.; Wang, J. Threshold dissociation and molecular modeling of transition metal complexes of flavonoids. *J. Am. Soc. Mass Spectrom.* **2005**, *16*, 139–151, doi:10.1016/j.jasms.2004.10.005.
  38. Wan, K.X.; Gross, M.L.; Shibue, T. Gas-phase stability of double-stranded oligodeoxynucleotides and their noncovalent complexes with DNA-binding drugs as revealed by collisional activation in an ion trap. *J. Am. Soc. Mass Spectrom.* **2000**, *11*, 450–457, doi:10.1016/S1044-0305(00)00095-7.

# Chapter 6

## The Present and the Future

### 6.1 Contributions

One key consideration that has been largely overlooked, particularly in fundamental studies, is the way the performance of a sunscreen is affected by the pH environment (*i.e.*, its protonation/deprotonation state). Gas-phase laser spectroscopic studies of the ionic analogues of sunscreen molecules have been studied much more sparsely, with only the protonated and deprotonated forms of OB, protonated AB, deprotonated PBSA, and most recently, deprotonated BP4, having been very recently explored within the author's Ph.D. at the University of York using laser-interfaced mass spectrometry. These experiments have proven to be important, especially considering the number of aquatic environments that are alkaline (*i.e.*, swimming pools and oceans) and with the pH of human skin being mildly acidic. Gaining a fundamental understanding of how ionization affects the photostability of UV filters has therefore provided important fundamental information to better understand how to optimize organic sunscreen performance, and hence any consequential implications for human health.

OB has been the subject of a number of contemporary studies using advanced laser techniques. Quantum chemical and transient absorption studies of the system in solution have attributed its efficacy as a sunscreen to its ultrafast decay dynamics post-photoexcitation which yield the *keto* form of oxybenzone *via* an ESIPT reaction. OB was therefore an excellent model molecule for our initial investigations of the intrinsic absorption properties of sunscreen molecules and, for the first time, has been used very successfully to demonstrate the utility of LIMS for mapping its photodegradation pathways as a function of protonation state. Deprotonated OB was observed to

photofragment with production of methyl radicals in the UV-B, which more concerningly adds to long-standing apprehensions that some sunscreens can produce free radicals following excitation.

Owing to its potential phototoxic effect, the photosensitizing nature of PBSA has also been of great interest to many. To this end, we reveal that the  $T_1$  state of deprotonated PBSA decays with direct free radical production, and therefore, photosensitization by PBSA in solution cannot just simply be associated with electron and energy transfer from the aforementioned  $T_1$  state. This is particularly concerning as the native form of an ideal sunscreen should not only absorb broadly across the UV-A and UV-B regions but should also be capable of dissipating the excess UV energy harmlessly, and without forming any potentially harmful photoproducts (*e.g.*, free radicals).

Notably, we report the gas-phase UV absorption spectra and associated photofragmentation pathways of deprotonated BP4 acquired *via* LIMS. Extensive wavelength-dependent ionic photofragmentation is observed upon photoexcitation within the UV spectral region, which aligns excellently with the results of our accompanying ground state collisional dissociation measurements. This study additionally offers an unparalleled insight into the relaxation channels available to this system, with theoretical insights revealing excited-state relaxation to occur *via* non-radiative decay, associated with a statistical excited-state decay process, at both the optically-bright  $S_1 \leftarrow S_0$  and  $S_3 \leftarrow S_0$   $\pi\pi^*$  transitions. Statistical decay is also evident throughout, visible in the fragmentation pattern on a hot ground state surface. Such experiments, supported by advanced theory, on deprotonated BP4 exemplify brilliantly the mechanisms desired for an efficient UV filter.

The application of UV laser-interfaced electrospray photodissociation mass spectrometry has previously been well established across a range of biological molecular systems and has now, through the Ph.D. work outlined herein and within other parallel publications, been used to successfully probe the photochemistry of organic sunscreen systems. The comparison between the gas- and solution-phase photofragmentation channels of our prototype system riboflavin has since validated the utility of the author's newly-developed on-line UV photolysis device. It will now be of great interest to further apply this methodology to investigate the photostability of UV filters upon solvation and aggregation, both of which are events that commonly occur within all 'bulk' suncreening formulations found extensively on the market.

## 6.2 Future directions

Whilst this Thesis stresses the importance of recognizing just how well common organic sunscreen molecules function at the molecular level, it is now evident that there is a need for future studies of these systems in the solution phase, where the environment is much closer to the “real life” application of commercial suncreening formulations. In the first instance, the ultimate potential of the newly-built UV photolysis cells alone, developed in line with Chapter 5, will undoubtedly set a heavy precedent in what could be an ideal means of detecting reactive intermediates and interpreting the solution-phase data of organic sunscreen systems in the future so as to consequently form a strong basis for a future standardized photostability index for commercial sunscreen testing. Further integration of electron paramagnetic resonance (EPR) spectroscopy with the author’s photolysis techniques will no doubt prove to be the best-suited technique available to track, capture, detect, and quantify the free radicals generated from the breakdown of these systems.

As of late, much attention has rightfully been focused on the issue surrounding cosmetic sunscreen products as emerging aquatic pollutants with potential ecological consequences on the coastal marine ecosystem. As the cosmetic community has started to delve into utilizing more natural bioactive alternatives (*e.g.*, mycosporines and mycosporine-like amino acids), collectively, the biosynthesis of new ingredients, supported by the application of gas-phase UV laser action spectroscopy and the author’s on-line photolysis cells, will again no doubt offer a more innovative and insightful means of understanding how their intrinsic behaviors can be influenced by acidic and alkaline environments.

Modern sunscreens typically contain a handful of organic and inorganic UV filters so it might be expected that crosslinks between one or more sunscreen molecules lead to dimerization. The binding of alkali metal cations to prototypical organic sunscreens (*i.e.*, oxybenzone) has already accrued much interest within the past year, so there is no doubt that an advanced understanding of the synergistic effect(s) between chemical sunscreens themselves or the eclectic array of active ingredients typically found within commercially-available formulations (*e.g.*, solvents, fragrances, emollients, emulsifiers, thickeners, and stabilizers) will also prove valuable for the optimization of the SPF of more ‘becoming’ sunscreens in the years to come.

### 6.3 Final remarks

In late 2017, in order to address a critical issue had been almost entirely ignored to date, this Ph.D. project set out to investigate the key question of how the basic photochemical properties of common UV filters can be affected by protonation or deprotonation. Over the course of her Ph.D., the author of this thesis has carried out a succession of novel experiments utilizing UV laser photodissociation mass spectrometry to explore the basic photophysical behaviors of a series of key active sunscreen components (Chapters 2-4). Using riboflavin as a model photoactive system (Chapter 5), the author leaves behind a solid foundation for the future solution-phase studies that are necessary to fully understand how combining organic and inorganic sunscreens together can modify their intrinsic organic sunscreen spectra and their resultant photoproducts. Further co-authored works in recent years have also mapped the photophysical properties of protonated avobenzene and have more so revealed how sodium cationization can perturb the mechanisms that mediate the sunscreens abilities of UV filters like oxybenzone.

To close this Thesis, the author reminisces in the words of Amy Poehler – “*It doesn't matter how much you get; you are left wanting more.*” It is extremely gratifying that within just three short years, our modern-day understanding of commercial organic sunscreen molecules has advanced so dramatically. But whilst there has been increasing interest in such publications over the years, the author ultimately acknowledges that even with the sheer volume of data accrued to date, there will *always* be more to be uncovered and therefore hopes that this thesis can all in all equip the next generation of researchers within the research group with the tools needed to further optimize the “sunscreens” as we know them today.

# **Appendices**

**A1 Supplementary Information – Mapping the Intrinsic Absorption Properties and Photodegradation Pathways of the Protonated and Protonated Forms of the Sunscreen Oxybenzone**

## Supplementary Information

### Mapping the Intrinsic Absorption Properties and Photodegradation Pathways of the Protonated and Deprotonated Forms of the Sunscreen Oxybenzone

Natalie G. K. Wong, Jacob A. Berenbeim, Mathew Hawkrige, Edward Matthews  
and Caroline E. H. Dessent\*

Department of Chemistry, University of York, Heslington, York, YO10 5DD, UK.

\* Corresponding author: E-mail [caroline.dessent@york.ac.uk](mailto:caroline.dessent@york.ac.uk)

#### Supplementary Material:

- S1. Electron Detachment Spectrum of Deprotonated Oxybenzone
- S2. Geometries of Deprotonated and Protonated Oxybenzone and Selected Physical Properties
- S3. Collision-Induced Dissociation of Deprotonated and Protonated Oxybenzone
- S4. Additional Photofragment Action Spectra for Protonated Oxybenzone
- S5. Solution-Phase UV Absorption Spectra of Oxybenzone in Variable Methanol-Aqueous Mixtures at Known Acidic, Neutral, and Basic pH

## S1. Electron Detachment Spectrum of Deprotonated Oxybenzone

Relative electron detachment was determined according to the following equation:

$$\% \text{ Electron Detachment} = \left( 1 - \frac{\sum \text{Int}_{\text{FRAG}}}{(\text{Int}_{\text{OFF}} - \text{Int}_{\text{ON}})} \right) \times 100 \quad [1]$$

The remaining percent of raw photodepletion signal ( $\text{Int}_{\text{OFF}} - \text{Int}_{\text{ON}}$ ) once the contribution of all photofragments are removed is the electron detachment intensity.  $\text{Int}_{\text{FRAG}}$  is the signal intensity for a unique  $m/z$  fragment where all are summed to account for a total ( $> 50 m/z$ ) photofragment intensity.

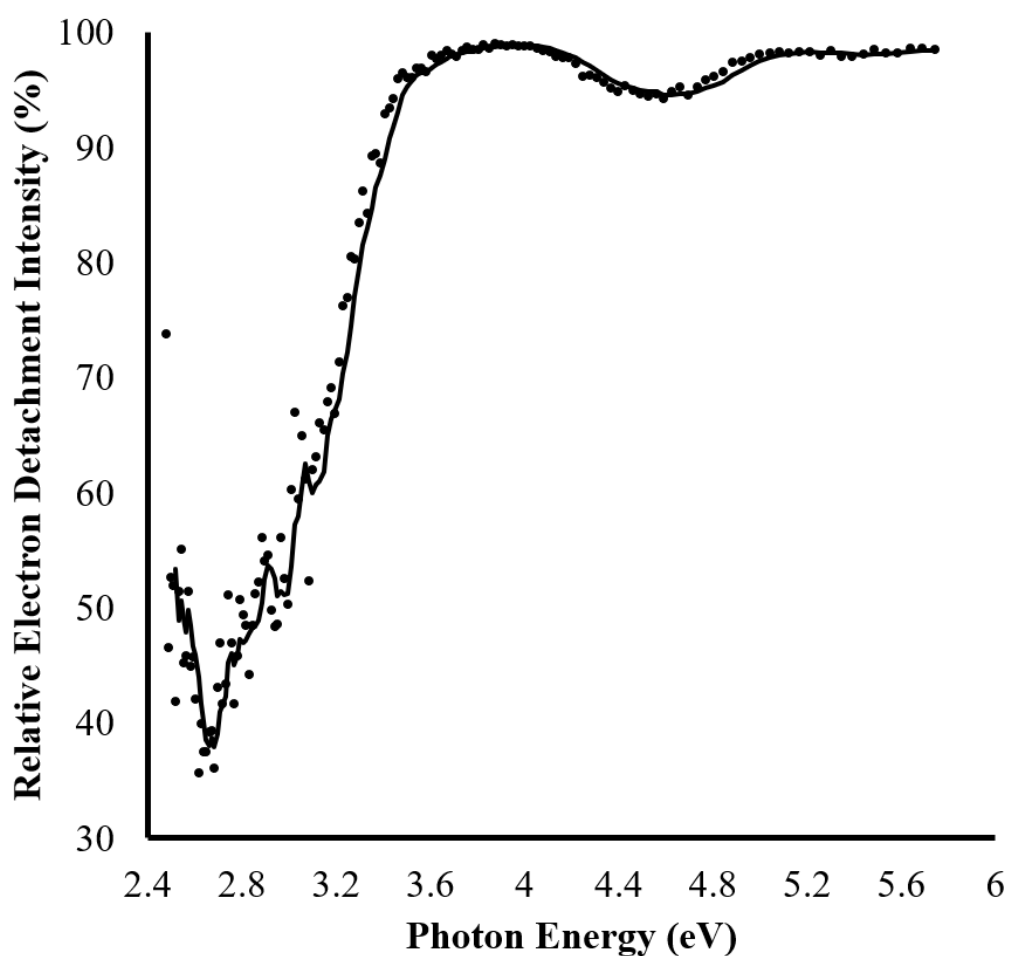


**Figure S1.** Relative electron detachment intensity of photodissociation of deprotonated oxybenzone ( $[\text{OB-H}]^-$ ).

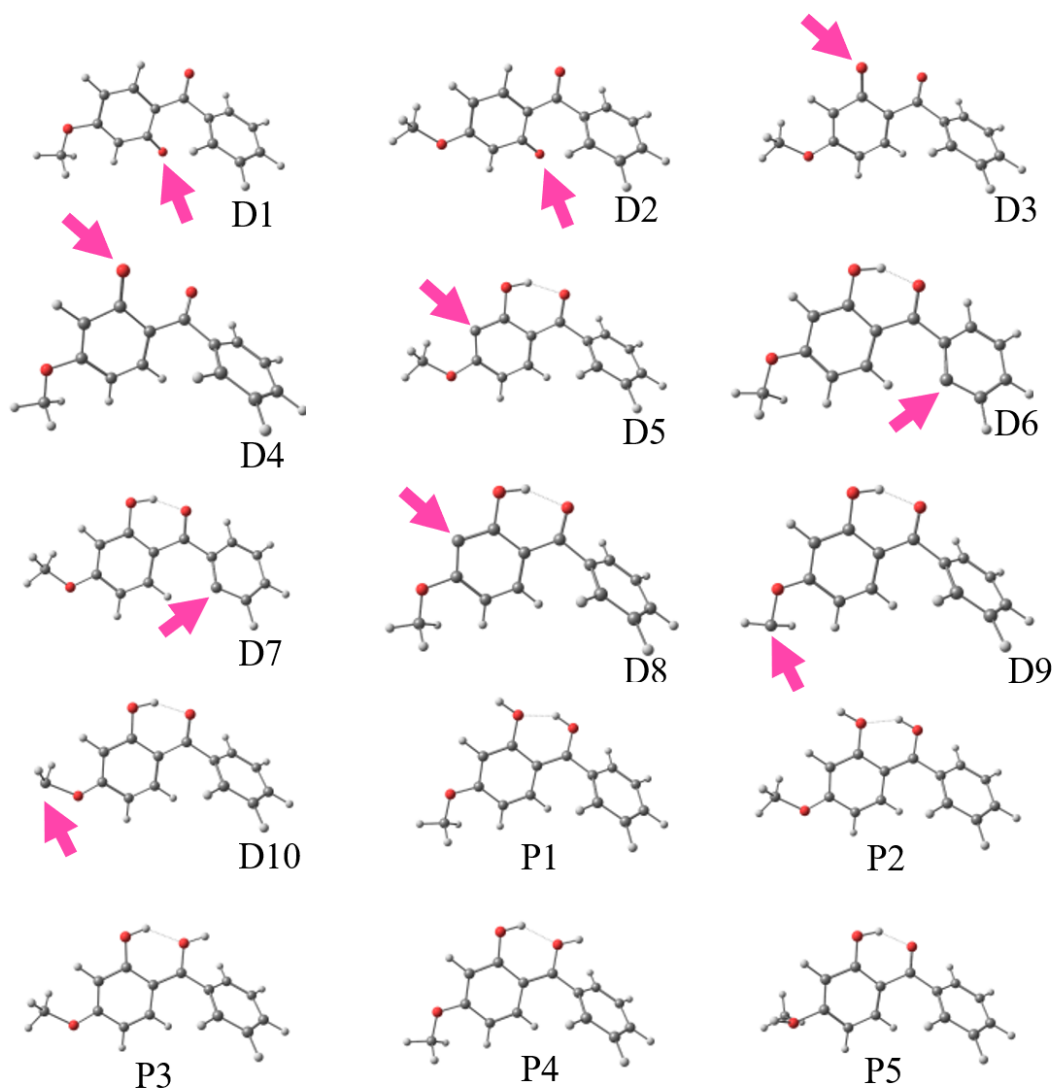
## S2. Extensive Geometries of Deprotonated and Protonated Oxybenzone and Selected Physical Properties

Only the lowest energy structures were listed within the manuscript. Here are all inspected structures which include high-energy deprotonation site and protomer species. Table S1 includes the energies relative to the lowest energy deprotonated (**D**) or protonated (**P**) structure. Scheme S1 shows the structures found in Table S1.

**Table S1.** Calculated relative energies and physical properties of OB dependent on pH. Calculated at the  $\omega$ B97XD/6-311++G\*\* level.

Structure	Relative Energy (kJ mol <sup>-1</sup> ) <sup>a,b</sup>	VDE (eV) <sup>c</sup>	Vertical Dipole Moment (D)
<b>D1</b>	0.0 (0.0)	3.00	4.2
<b>D2</b>	8.2 (5.1)	3.00	4.7
<b>D3</b>	21.0 (3.8)	2.89	6.0
<b>D4</b>	29.8 (8.7)	2.87	7.9
<b>D5</b>	159 (150)	2.45	3.4
<b>D6</b>	175 (181)	2.21	5.2
<b>D7</b>	175 (179)	2.17	2.5
<b>D8</b>	191 (158)	2.25	5.9
<b>D9</b>	191 (198)	1.75	5.2
<b>D10</b>	210 (201)	1.94	2.9
<b>P1</b>	0.0 (1.0)		
<b>P2</b>	1.8 (0.0)		
<b>P3</b>	9.9 (9.8)		
<b>P4</b>	16.6 (12.7)		
<b>P5</b>	139 (92)		

**Scheme S1.** All the structures from Table S1. Arrows indicate the deprotonation site for all **D** structures.



### S3. Collision-Induced Dissociation of Deprotonated and Protonated Oxybenzone

Low-energy collision-induced dissociation (CID) was performed on isolated deprotonated and protonated oxybenzone to determine the thermal fragments. Figures S2 and S3 present the relative intensities of the deprotonated and protonated OB parent ion respectively, and the corresponding fragment ions as a function of applied CID energy.

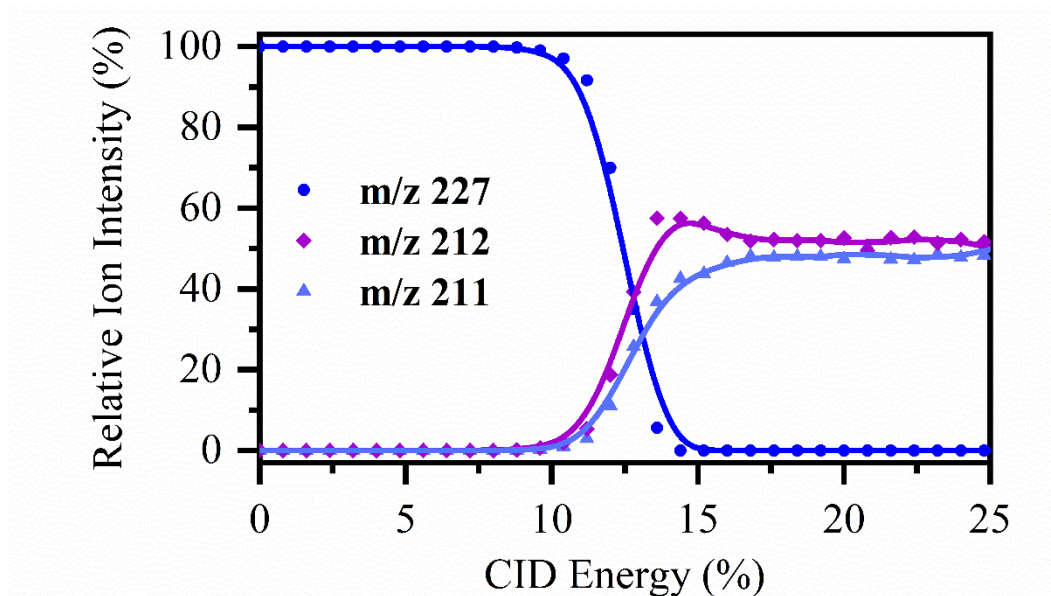


**Figure S2.** CID fragmentation decay curve for deprotonated oxybenzone ( $m/z$  227) upon low energy CID. Onset plots for production of the associated fragment ions ( $m/z$  212 and  $m/z$  211) are also shown. The curved lines included with the data points are a three-point adjacent average of such data points and are provided as a viewing guide, to emphasize the profile for an individual fragment.

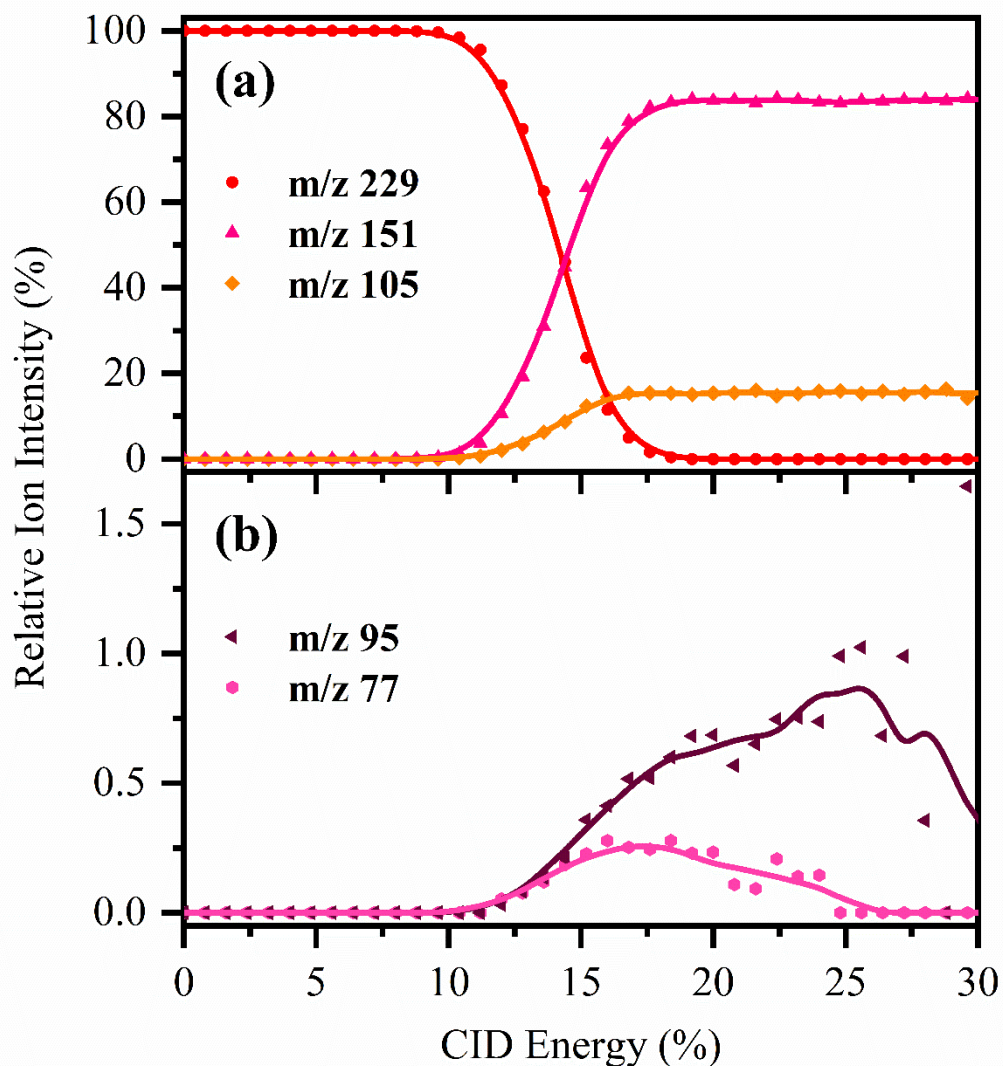


**Figure S3.** CID fragmentation decay curve for protonated oxybenzone ( $m/z$  229) upon low energy CID. Onset plots for production of the associated fragment ions **(a)**  $m/z$  151 and 105, and **(b)**  $m/z$  95 and 77 are also shown. The curved lines included with the data points are a three-point adjacent average of such data points and are provided as a viewing guide, to emphasize the profile for an individual fragment.

#### S4. Additional Photofragment Action Spectra for Protonated Oxybenzene

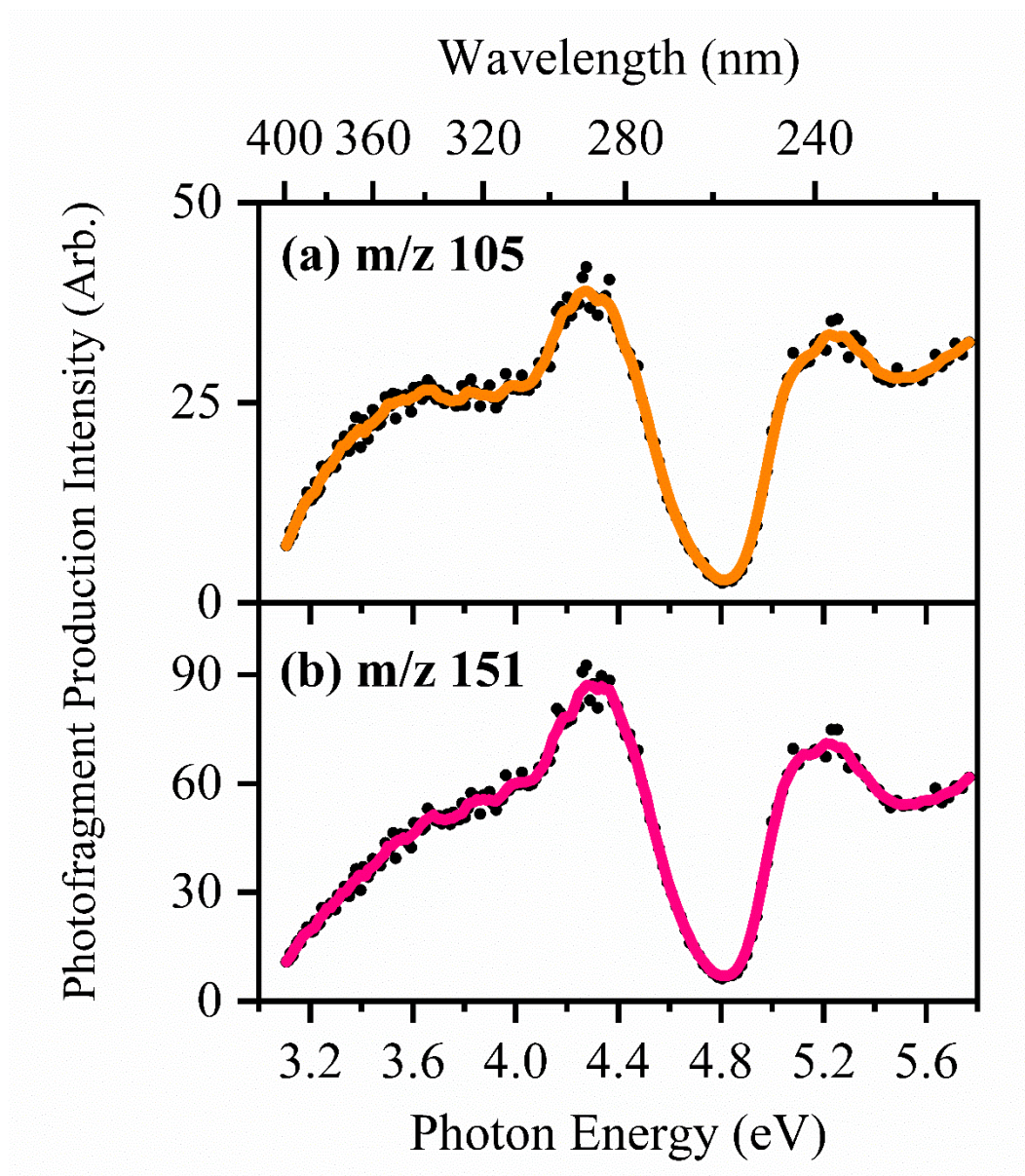


**Figure S4.** Protonated oxybenzene photofragmentation action spectra of (a)  $m/z$  105 and (b)  $m/z$  151. The solid line is a five-point adjacent average of the data points.

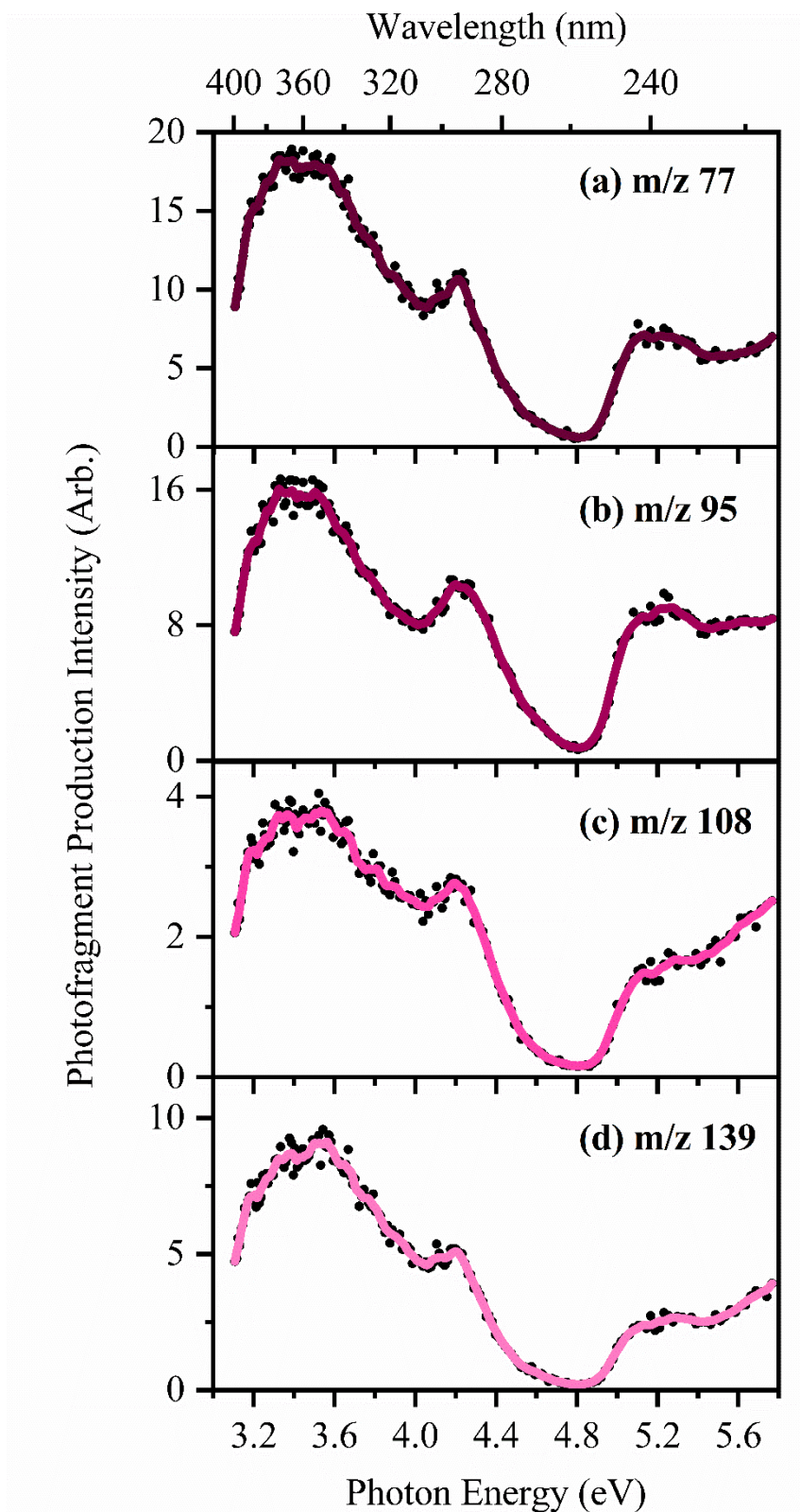


**Figure S5.** Protonated oxybenzone photofragmentation action spectra of (a)  $m/z$  77, (b)  $m/z$  95, (c)  $m/z$  108, and (d)  $m/z$  139. The solid line is a five-point adjacent average of the data points.

### **S5. Solution-Phase UV Absorption Spectra of Oxybenzone in Variable Methanol-Aqueous Mixtures at Known Acidic, Neutral, and Basic pH**

Solution-phase UV absorption spectra of oxybenzone (OB;  $1 \times 10^{-5}$  mol dm<sup>-3</sup>) in methanol-aqueous mixtures were recorded using a UV-1800 UV-Visible spectrophotometer (Shimadzu, Kyoto, Japan) with a 10 mm UV quartz cuvette. The mass-percent composition of methanol to buffered aqueous solution was varied while the pH and [OB] were held constant. Mixtures were prepared using HPLC-grade MeOH and required the use of NIST standard pH = 7.0 (phosphate) buffer solutions to provide the aqueous component. Here, HCl (3.0 M) and NaOH (2.0 M) were added to pH = 7.0 buffer solutions to achieve the desired protonated and deprotonated forms of OB at pH = 2.95 and 13.0, respectively. Basic mixture solutions > 10% MeOH are not shown due to the precipitation of phosphate buffer under those conditions. OB is poorly soluble in water therefore a 0% MeOH mixture is not shown.

Acidic, neutral, and basic methanol solution conditions shown in Figures S6a-c yield UV spectra are comparable to those methanol-aqueous mixtures of pH = 2.95, 7.0, and 13.0 buffered solutions, respectively. These results are consistent with previously published OB spectra by Li *et al.* (26) and by Baughman *et al.* (50), references found in main article. Issues of miscibility likely account for small shifts of absorbance intensity.

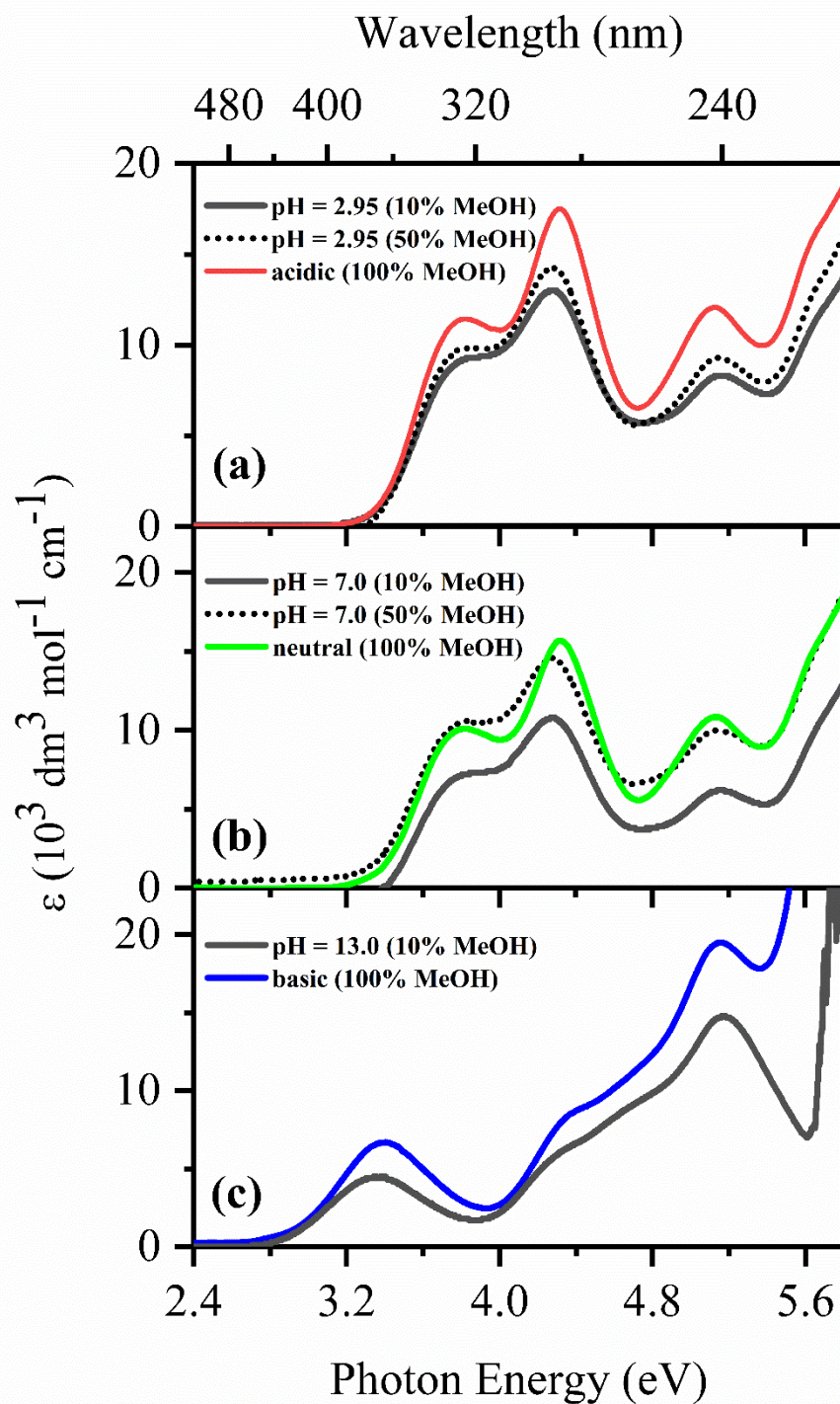


**Figure S6.** (a) Solution-phase absorption spectrum of OB mixture at pH = 2.95. (b) Solution-phase absorption spectra of OB mixture at pH = 7.0. (c) Solution-phase absorption spectrum of OB mixture at pH = 13.0.

**A2 Supplementary Material – Direct Observation of Photochemical Free Radical Production from the Sunscreen 2-Phenylbenzimidazole-5-Sulfonic Acid *via* Laser-Interfaced Mass Spectrometry**

## Supporting Information

### Direct Observation of Photochemical Free Radical Production from the Sunscreen 2-Phenylbenzimidazole-5-Sulfonic Acid via Laser-Interfaced Mass Spectrometry

Natalie G. K. Wong, Jacob A. Berenbeim and Caroline E. H. Dessent\*

Department of Chemistry, University of York, Heslington, York, YO10 5DD, U.K.

\* Corresponding author: Email: [caroline.dessent@york.ac.uk](mailto:caroline.dessent@york.ac.uk)

#### Supporting Information:

S1. Laser Power Measurements

S2. Electron detachment action spectra

## Section S1. Laser Power Measurements

Laser power measurements were conducted on [PBSA-H]<sup>-</sup> at two photon energies, 3.8 and 5.3 eV, to test for the presence of multiphoton effects. The plots displayed in Figures S1-S2 include measurements of the power dependence of photodepletion, electron detachment (see Section S2), and the  $m/z$  80, 193 and 208 photofragments.

The ln-ln of the data has been plotted and overlain with a pseudolinear fit. The resultant slope is proportional to the number of absorbed photons.<sup>1</sup> The slopes at both photon energies measure less than 1 (see Figures S1-S2 for values). This result indicates that the action response is not multiphoton in nature. Additionally, that the pseudolinear slope is less than one over the fitted region likely indicates saturation of the linear transition.

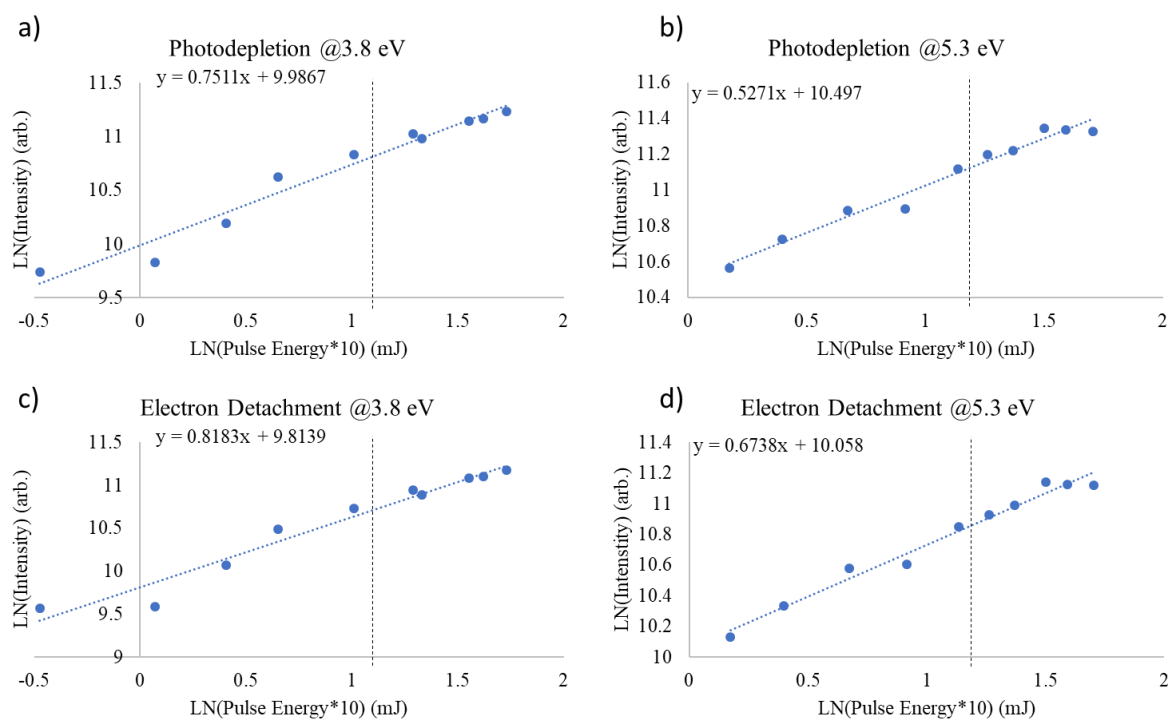


**Figure S1.** Power Dependence Spectra of photodepletion signal at **(a)** 3.8 eV and **(b)** 5.3 eV and of photoelectron signal at **(c)** 3.8 eV and **(d)** 5.3 eV. Plots are presented as LN-LN where the slope (shown) indicates the power dependence with respect to pulse energy used. Vertical line indicates pulse energies used during the experiment.

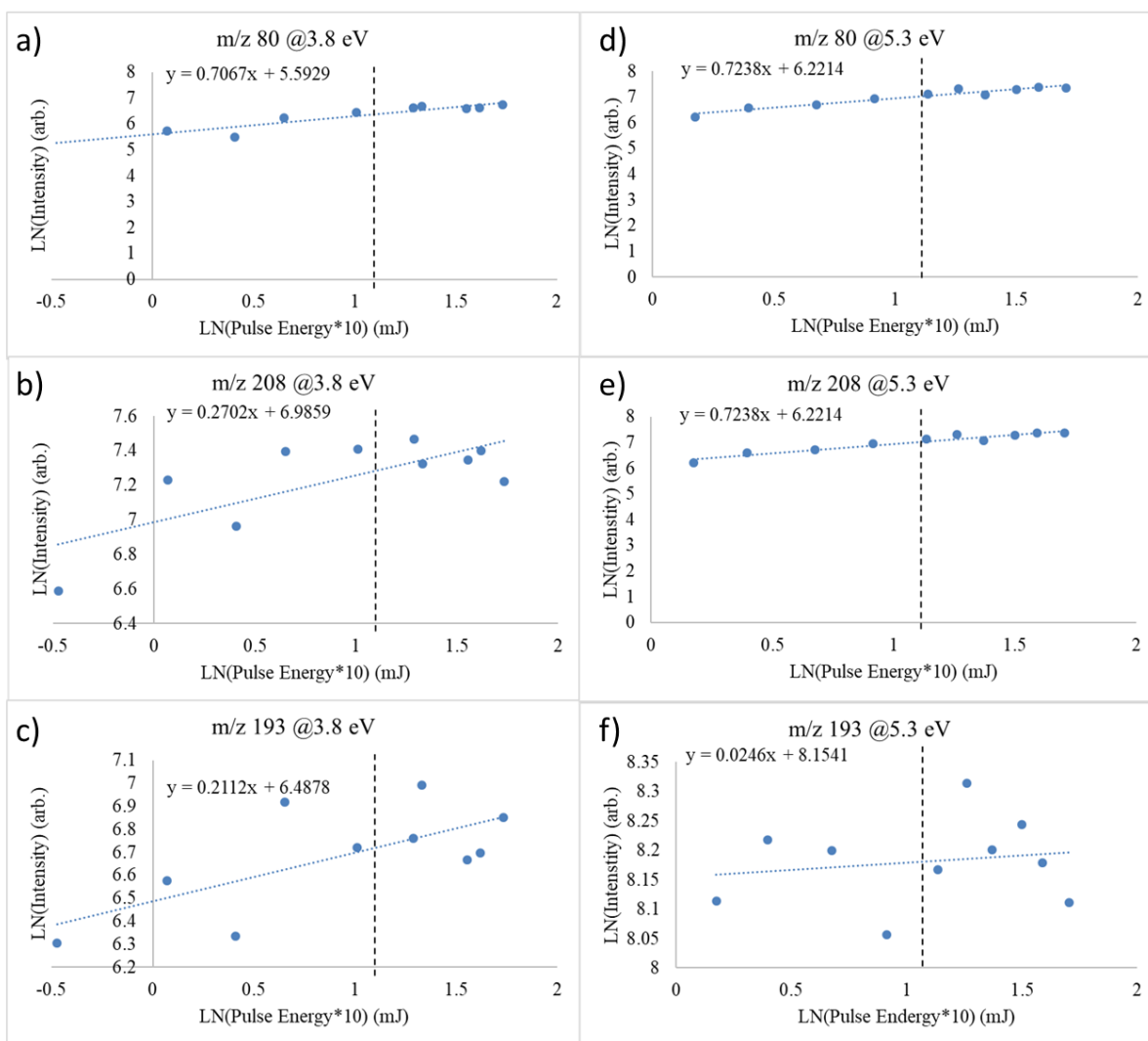


**Figure S2.** Power dependence spectra of ion photofragments at  $m/z$  80,  $m/z$  208, and  $m/z$  193 at photon energies of (a-c) 3.8 eV and (d-f) 5.3 eV. Plots are presented as LN-LN where the slope (shown) indicates the power dependence with respect to pulse energy used. Vertical line indicates pulse energies used during the experiment.

## Section S2. Electron detachment action spectra

The electron detachment yield of  $[\text{PBSA-H}]^-$  is given in Figure S3. The electron loss is not directly measurable within our instrument, thus these spectra are calculated assuming that any depleted ions that are not detected as ionic photofragments are, instead, losing an electron, *i.e.*, the electron detachment yield = photodepletion ion count –  $\Sigma$  photofragment ion counts. This assumes that both the parent ions and photofragments are detected equally in the mass spectrometer, a reasonable assumption for the systems studied here where the parent ions and fragment ions are reasonably close in  $m/z$ .

Compared with the photodepletion spectrum displayed in the main text (Figure 2a), the electron detachment yield curve displays a similar profile, indicating that the electron detachment is the main photodepletion pathway. (Note that we have not adjusted the scans presented in Figure S3 by  $\lambda$  (see Experimental section in main text), whereas the spectrum in Figure 2a of the main text are. Due to this, the spectral intensity in the higher energy region is moderately reduced in the spectra displayed in Figure S3.)

As discussed in the main text, our calculations indicate that the vertical detachment energy (VDE) of  $[\text{PBSA-H}]^-$  is  $\sim 4.4$  eV. From the electron detachment yield spectrum shown in Figure S3, this suggests that electrons are being detached below the VDE for  $[\text{PBSA-H}]^-$ . We have seen similar effects in deprotonated adenosine monophosphate anions,<sup>[1]</sup> and this observation suggests that upon electronic excitation, the excess electron has access to a pathway that allows it to detach at energies below the VDE.

To give some further information about the relative extent of electron detachment versus ionic fragmentation, Table S1 provides ion counts measured in a typical experimental run conducted in this work. These numbers again show that electron detachment is the major excited state decay channel for gaseous  $[\text{PBSA-H}]^-$  is electron detachment.

**Table S1.** Percent electron depletion of [PBSA-H]<sup>-</sup> calculated directly from precursor and ionic photofragment intensities.

Ion	Intensity (ion counts)		
	3.8 eV	4.36 eV	5.5 eV
Precursor Ion Depletion	215362	63784	213055
<i>m/z</i> 80	8105	2150	11960
<i>m/z</i> 193	5298	7946	17991
<i>m/z</i> 208	7665	1586	1598
<b>% electron depletion</b>	<b>90.2</b>	<b>81.7</b>	<b>85.2</b>

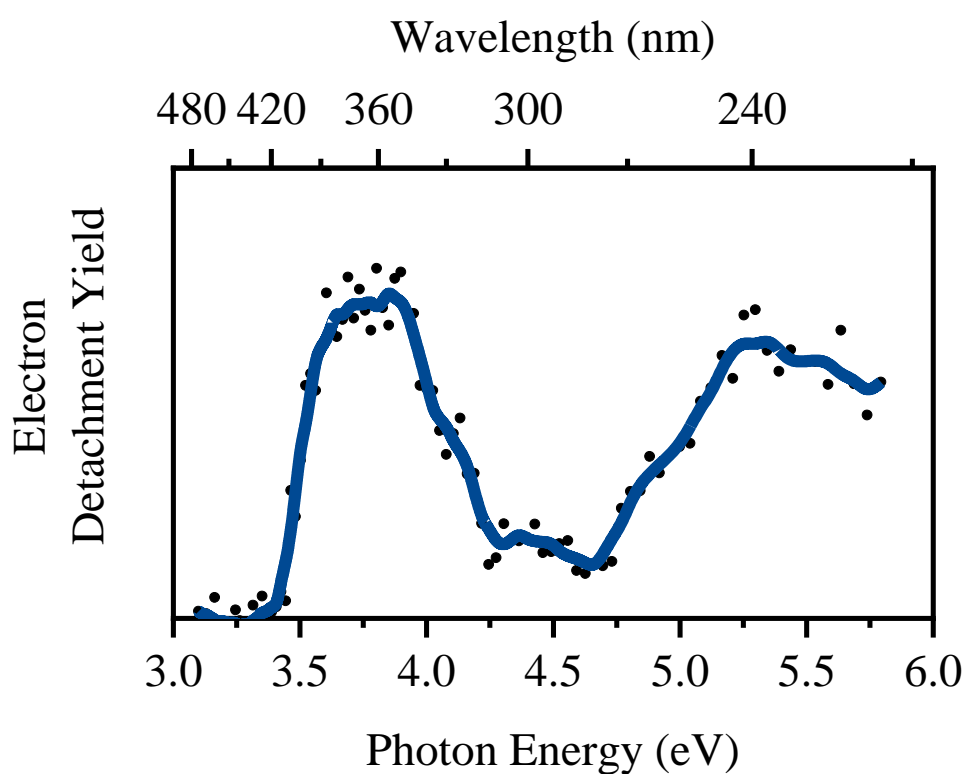


**Figure S3.** Electron detachment yield of [PBSA-H]<sup>-</sup>. The solid blue line is a five-point adjacent averages of the data points.

## References

- [1] R. Cercola, E. Matthews, C. E. H. Dessent, *J. Phys. Chem. B* **2017**, *121*, 5553–5561.

**A3 Supporting Information – Linking Electronic Relaxation  
Dynamics and Ionic Photofragmentation Patterns for the  
Deprotonated UV Filter Benzophenone-4**

## Supporting Information

### Linking Electronic Relaxation Dynamics and Ionic Photofragmentation Patterns for the Deprotonated UV Filter Benzophenone-4

Natalie G. K. Wong,<sup>a</sup> Conor D. Rankine,<sup>b</sup> and Caroline E. H. Dessent<sup>a\*</sup>

<sup>a</sup> Department of Chemistry, University of York, Heslington, York, YO10 5DD, UK.

<sup>b</sup> School of Natural and Environmental Sciences, Newcastle University, Newcastle-upon-Tyne, NE1 7RU, UK.

\* Corresponding author: Email: [caroline.dessent@york.ac.uk](mailto:caroline.dessent@york.ac.uk)

#### Supporting Information:

- S1. Experimental and computational methodology
- S2. Photodepletion laser power dependence measurements
- S3. Additional photofragment action spectra
- S4. Electron detachment yield versus photodepletion yield interpretation
- S5. Higher-energy collisional dissociation (HCD) production spectra
- S6. Further discussion of deprotonated benzophenone-4 fragmentation channels
- S7. Optimized Cartesian coordinate tables
- S8. Further computational results
- S9. Schematic structure of deprotonated benzophenone-4

## S1. Experimental and computational methodology

Gas-phase UV photodissociation experiments were conducted in an AmaZon SL electrospray ionization quadrupole ion-trap (ESI-QIT) mass spectrometer (Bruker Daltonics Inc., Billerica, MA, USA), which was modified to allow for laser-interfaced mass spectrometry (LIMS). This instrument has the advantages of a commercial mass spectrometer, coupled with the ability to record UV-visible photodissociation spectra in a routine manner.

Benzophenone-4 (2-hydroxy-4-methoxybenzophenone-5-sulfonic acid; sulisobenzene; BP4) was purchased from Sigma Aldrich, Inc. (St. Louis, MO, USA). Solutions of BP4 ( $\sim 10^{-4}$  M) in HPLC-grade acetonitrile (Fisher Scientific, Inc., Pittsburgh, PA, USA) were introduced into the mass spectrometer by ESI using typical instrumental parameters in the negative ion mode: nebulizing gas pressure: 14.0 psi; injection rate: 0.33 mL/hr; drying gas flow rate: 10.0 L/min; and capillary temperature: 160 °C.

Deprotonated BP4 ( $[\text{BP4-H}]^-$ ) was mass selected and isolated in the ion trap prior to laser irradiation. Photons were produced by a 10 Hz Nd:YAG (Surelite™, Amplitude Laser Group, San Jose, CA, USA) pumped OPO (Horizon™, Amplitude Laser Group) laser, giving  $\sim 0.3$  mJ across the range 400-214 nm (3.1-5.8 eV). A laser step size of 2 nm was used, and the laser beam was focused as has been described previously.<sup>1-4</sup> Photofragmentation experiments were conducted with an ion accumulation time of 2 ms and a fragmentation time of 100 ms, thereby ensuring that each ion packet interacted with one laser pulse to minimize the likelihood of multiphoton events. A laser power dependence study for  $[\text{BP4-H}]^-$  is outlined in Section S2. As fluorescence is also negligible here,<sup>1-3,5,6</sup> the UV-excited gaseous ion will fragment upon excited state relaxation, yielding an action absorption spectrum by photodepletion (see Figures 1b-i and Section S3). Photodepletion was measured as a function of the scanned wavelength, with photofragment production recorded simultaneously (see Eqs. S1-3):

$$\text{Photodepletion intensity} = \frac{\ln\left(\frac{\text{Int}_{\text{OFF}}}{\text{Int}_{\text{ON}}}\right)}{\lambda \times P} \quad (\text{Eq. S1})$$

$$\text{Photofragmentation intensity} = \frac{\left(\frac{\text{Int}_{\text{FRAG}}}{\text{Int}_{\text{OFF}}}\right)}{\lambda \times P} \quad (\text{Eq. S2})$$

$$\text{Relative ion yield} = \text{Int}_{\text{FRAG}}/\text{Int}_{\text{PFT}} \quad (\text{Eq. S3})$$

where  $\text{Int}_{\text{OFF}}$  and  $\text{Int}_{\text{ON}}$  are the peak parent ion intensities with laser off and on, respectively;  $\text{Int}_{\text{FRAG}}$  is the fragment intensity with the laser on;  $\lambda$  is the excitation wavelength (nm);  $P$  is the tunable laser pulse energy (mJ); and  $\text{Int}_{\text{PFT}}$  is the sum of the photofragment ion intensities with the laser on.

Higher-energy collisional dissociation (HCD) was performed on  $[\text{BP4-H}]^-$  using an Orbitrap™ Fusion Tribrid mass spectrometer (Thermo Fisher Scientific, Waltham, MA, USA) with an ESI source, run in the negative ion mode between 0-100% collisional energy.<sup>2,7,8</sup> This technique provides tandem mass spectrometry and was operated at a flow rate of 3.0  $\mu\text{L}/\text{min}$ , with the following parameters: spray voltage: -2500 V; sheath gas flow rate: 10; aux. gas flow rate: 2.0, ion transfer tube temperature: 290 °C; vaporizer temperature: 20 °C;  $\text{MS}^2$  detector: ion trap; scan rate: enhanced;  $\text{MS}^2$  AGC target: 10,000;  $\text{MS}^2$  max. injection time: 100 ms; and RF lens: 60%.

All density functional theory (DFT) calculations were carried out using ORCA (v4.2.1).<sup>9,10</sup> All second-order algebraic diagrammatic construction/Moller-Plesset perturbation theory [ADC(2)/MP2] calculations were carried out using TURBOMOLE (v6.3.1).<sup>11</sup>

DFT and time-dependent DFT (TDDFT) calculations employed the  $\omega\text{B97X-D}$  density functional of Head-Gordon *et al.*<sup>12</sup> and used the resolution-of-identity (RI) approximation for Coulomb and Hartree-Fock exchange integrals (RI-JK). ADC(2)/MP2 calculations employed the CC2 routines implemented in TURBOMOLE,<sup>13-16</sup> and used the frozen-core approximation; the 25 lowest-energy core orbitals were frozen in all ADC(2)/MP2 calculations. A tightened SCF convergence criterion of  $1.0 \times 10^{-8}$  a.u. was used in all calculations; tightened convergence criteria of  $1.0 \times 10^{-6}$  and  $3.0 \times 10^{-5}$  a.u. were used for the energy change and RMS gradient, respectively, in all geometry optimizations. The proper convergence of all geometry optimizations to real minima was verified *via* vibrational frequency inspection. Minimum-energy crossing points (MECP) between electronic states were located *via* a home-built external optimizer following the approach of Martinez *et al.*<sup>17</sup>

The minimally-augmented (*ma-def2*-SV(P) basis set of Truhlar *et al.*<sup>18</sup> was used throughout; where required for RI-(TD)DFT, a density-fitting auxiliary basis set was generated following the approach of Neese *et al.*<sup>19</sup>

## S2. Photodepletion laser power dependence measurements

Laser power measurements were conducted on  $[\text{BP4-H}]^-$  at four absorption maxima: 3.5 eV (354 nm), 4.1 eV (300 nm), 5.3 eV (234 nm), and 5.4 eV (230 nm). The plot displayed in Figure S1 shows that of the parent ion photodepletion intensities ( $\text{Int}_{\text{OFF}} - \text{Int}_{\text{ON}}$ ) at such photon energies. Following standard protocol, such data has been plotted and fit to a power function.<sup>1,2,20</sup> The resultant slope is thereby proportional to the number of absorbed photons implicated in the experiment. Multiphoton events *via* instantaneous absorption of multiple photons in the Franck-Condon region are negligible as the laser beam is only softly focused through the ion-trap region. The slopes at all four photon energies measure at less than 1, confirming that photodepletion of  $[\text{BP4-H}]^-$  at 0.3 mJ is evidently not multiphoton in nature.

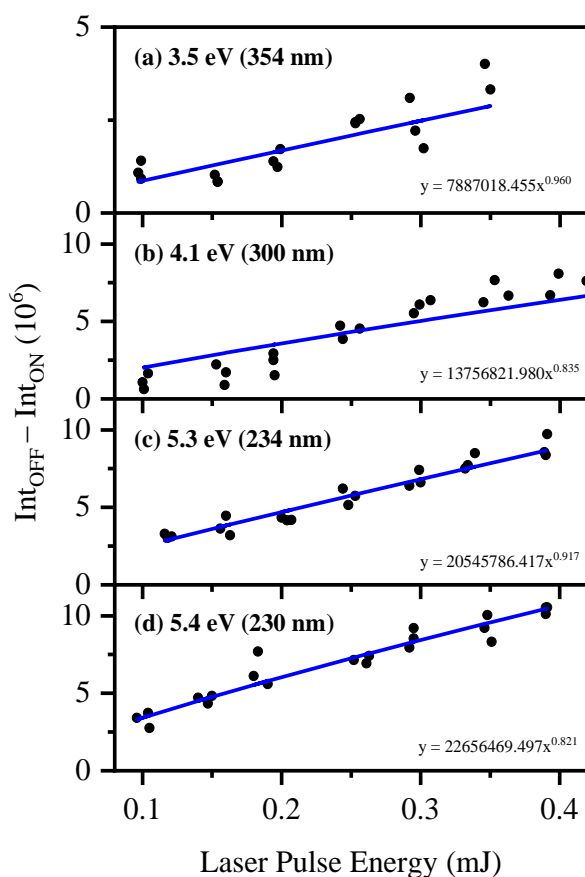


**Figure S1.** Power dependence measurements for  $[\text{BP4-H}]^-$  at four absorption maxima of (a) 3.5 eV (354 nm), (b) 4.1 eV (300 nm), (c) 5.3 eV (234 nm), and (d) 5.4 eV (230 nm).

### S3. Additional photofragment action spectra

It is apparent that the UV photofragmentation of  $[\text{BP4-H}]^-$  is extensive. To provide a comprehensive assessment of the majority of the photofragments observed, Figures S2-3 show the photofragment action spectra of the next 11 most intense photofragments, all deemed relatively minor in comparison to those presented in the main text (Figures 1b-i).

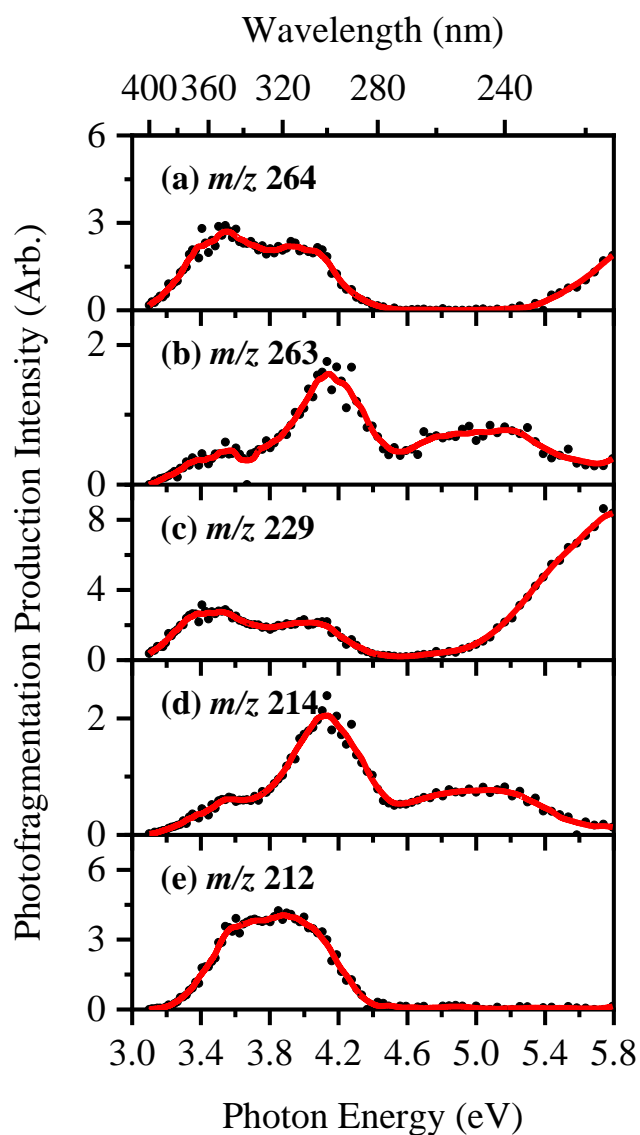


**Figure S2.** Additional photofragment action spectra for the first set of minor  $[\text{BP4-H}]^-$  fragments observed at  $m/z$  264, 263, 229, 214, and 212. The solid line is a five-point adjacent average of the data points.

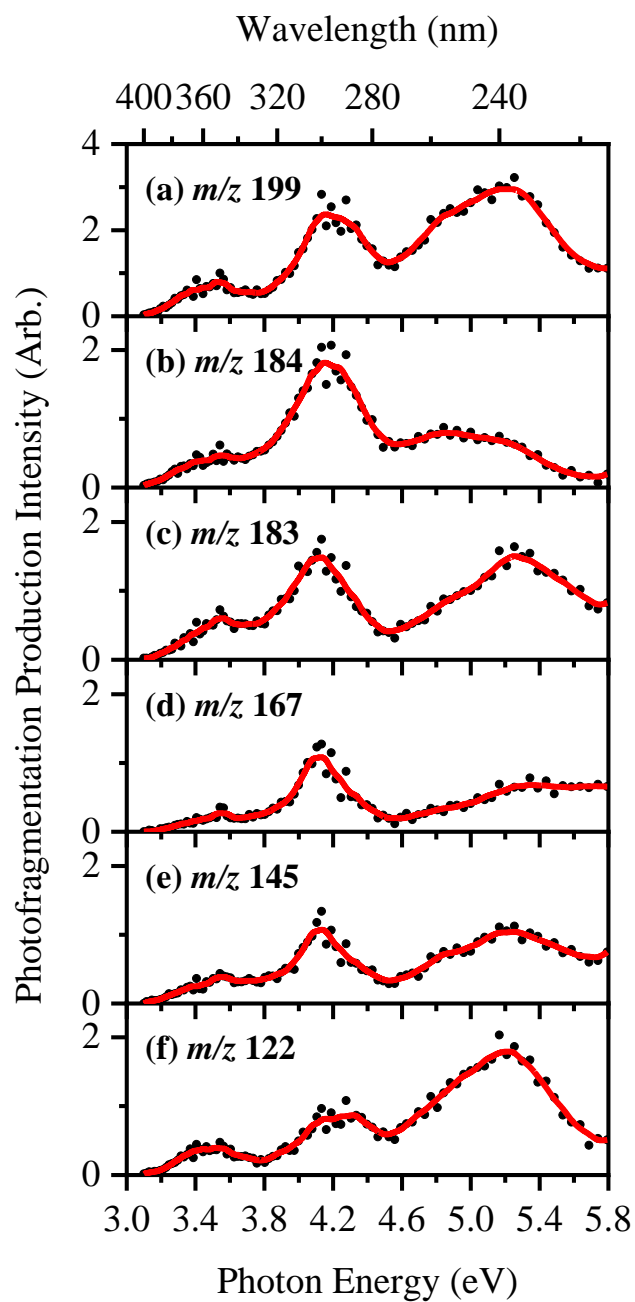


**Figure S3.** Additional photofragment action spectra for the second set of minor [BP4-H]<sup>-</sup> fragments observed at  $m/z$  199, 184, 183, 167, 145, and 122. The solid line is a five-point adjacent average of the data points.

#### S4. Electron detachment yield versus photodepletion yield interpretation

Electron loss has been regarded as the most dominant photofragmentation channel for gaseous sunscreen anions previously studied within our group, *e.g.*, 2-phenylbenzimidazole-5-sulfonic acid (PBSA) and oxybenzone (OB), and this has been in line with their calculated vertical detachment energies (VDEs).<sup>1,2</sup> The VDE of [BP4-H]<sup>-</sup> (5.19 eV) indicates, however, that the electrons here are being detached below this. Nevertheless, the decay of [BP4-H]<sup>-</sup> through electron detachment is less concerning, given that photodetachment is quenched on solvation for anionic molecules, *e.g.*, in sunscreen formulations.

Electron loss is not directly measurable within our instrument and thus can only be calculated *via* the use of Eqs. S4-5, assuming that any photodepletion ions that are not detected as ionic photofragments are instead losing an electron. Note that fragment ions with  $m/z < 50$  are not detectable in our mass spectrometer since low masses fall outside the mass window of the ion trap.

Electron detachment yield (ED\*) spectra were calculated by assuming that any depleted ions not detected as ionic photofragments are decaying *via* means of electron detachment, as determined using Eq. S4. This analysis assumes that both the parent ions and photofragments are detected equally in the mass spectrometer. In Figure S4 where we present ED\* spectra, we overlay such data with the photodepletion yield (PD\*) for ease of comparison; PD\* is the normalized photodepletion ion count (Eq. S5), which provides the most straight-forward comparison to the ED\* (Eq. S4):

$$ED^* = \frac{(Int_{OFF} - Int_{ON}) - Int_{PFT}}{\lambda \times P} \quad (Eq. S4)$$

$$PD^* = \frac{Int_{OFF} - Int_{ON}}{\lambda \times P} \quad (Eq. S5)$$

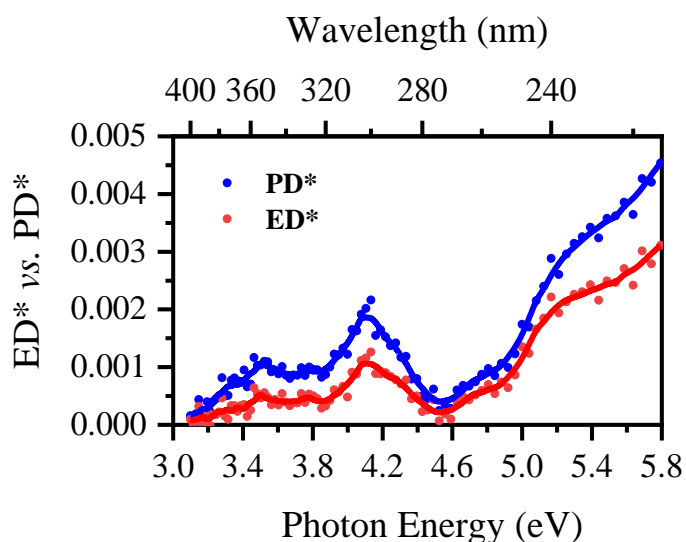


**Figure S4.** Electron detachment yield (ED\*; red) vs. photodepletion yield (PD\*; blue) of  $[\text{BP4-H}]^-$ . The solid line is a five-point adjacent average of the data points.

Such yields do not significantly overlap as greatly within the UVA and UVB regions in comparison to previously studied gas-phase iodide ion-nucleobase clusters,<sup>21</sup> but does strongly suggest that  $[\text{BP4-H}]^-$  decays predominantly through means of electron detachment. Similar effects have also been observed in the case of the adenosine monophosphate anions.<sup>7</sup>

## S5. Higher-energy collisional dissociation production spectra

Figures 3 and S5 display the major and minor HCD fragmentation curves for [BP4-H]<sup>-</sup>, respectively, illustrating a clear onset of thermal fragment production at 20% HCD energy. Hereafter, a great number of thermal fragment ions can be observed. The identifiable thermal fragment ions are summarized in Table 1, and their postulated structures presented in Section S6.

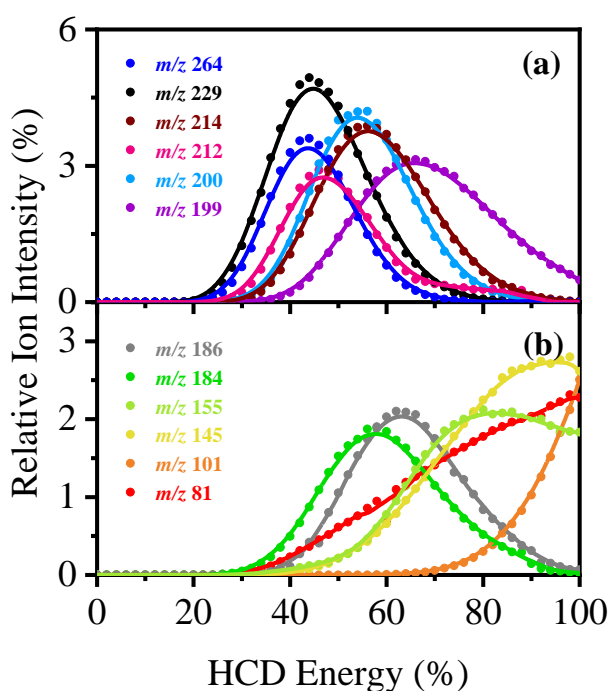


**Figure S5.** Photofragment action spectra for the minor [BP4-H]<sup>-</sup> HCD fragments observed at (a)  $m/z$  264, 229, 214, 212, 200, and 199, and at (b)  $m/z$  186, 184, 155, 145, 101, and 81. The solid lines are a five-point adjacent average of the data points.

## S6. Further discussion of deprotonated benzophenone-4 fragmentation channels

The main text presents and discusses the implications of the major photofragments of  $[\text{BP4-H}]^-$  observed for  $m/z$  292, 291, 228, 227, 211, 210, 182, and 80 in Figures 1b-i of the main text.

The major dissociation channels of  $[\text{BP4-H}]^-$  are again given in Eqs. 1a-h and their proposed structural assignments outlined in Table S1. A condensed version is available in the main text (Table 1).

**Table S1.** Proposed structures for the major ionic fragments of  $[\text{BP4-H}]^-$  ( $m/z$  307) produced upon UV laser photoexcitation and higher-energy collisional dissociation (HCD) at 40% and 70% HCD energies.

Ionic mass fragment ( $m/z$ ) <sup>a</sup>	Proposed structure of fragment	Accompanying neutral fragment lost	Observed in HCD <sup>b</sup>		Observed in UV laser photoexcitation <sup>b</sup>
			40%	70%	
292		CH <sub>3</sub>	✓ (xw) c	-	✓ (m)
291		O	✓ (m)	✓ (w)	✓ (m)
228		SO <sub>2</sub> + CH <sub>3</sub>	✓ (m)	✓ (vw)	✓ (m)
227		SO <sub>3</sub>	✓ (s)	✓ (vw)	✓ (vs)

Ionic mass fragment ( $m/z$ ) <sup>a</sup>	Proposed structure of fragment	Accompanying neutral fragment lost	Observed in HCD <sup>b</sup>		Observed in UV laser photoexcitation <sup>b</sup>
			40%	70%	
211		SO <sub>3</sub> + CH <sub>4</sub>	✓ (w)	✓ (vs)	✓ (m)
210		HSO <sub>3</sub> + CH <sub>4</sub>	✓ (m)	✓ (vw)	✓ (m)
182		HSO <sub>3</sub> + CH <sub>4</sub> + CO	✓ (m)	✓ (m)	✓ (m)
80			✓ (w)	✓ (m)	✓ (w)

<sup>a</sup> Determined with mass accuracy > 0.3 amu. <sup>b</sup> Very strong (vs), strong (s), moderate (m), weak (w), very weak (vw), and extremely weak (xw). <sup>c</sup> HCD fragment  $m/z$  292 is observed to peak at 34% HCD energy, with a relative ion intensity of <2%.

The loss of 15 Da from [BP4-H]<sup>-</sup> is consistent with the loss of a methyl group to form the phenoxy radical ion at  $m/z$  292 (Eq. 1a), an observation in line with previous work mapping degradation of anisole<sup>22</sup> and deprotonated OB.<sup>[108]</sup> The assignment of fragments  $m/z$  291 (Eq. 1b) and  $m/z$  228 (Eq. 1c) (Table S1) was informed using results from the dissociation of benzenesulfonic acid and benzenesulfinic acid.<sup>23-25</sup> This leads us to assign the  $m/z$  291 fragment as loss of an oxygen atom from the SO<sub>3</sub><sup>-</sup> moiety of [BP4-H]<sup>-</sup>,<sup>23</sup> with the  $m/z$  228 fragment arising from SO<sub>2</sub> ejection from a rearranged Ph-O-SO<sub>2</sub><sup>-</sup>.<sup>23-25</sup> Finally, the observed  $m/z$  80 fragment ion can be assigned as a radical SO<sub>3</sub><sup>-</sup>, arising from homolytic cleavage of the C-S bond.<sup>23</sup>

## S7. Optimized Cartesian coordinate tables

**Table S2.** Optimized Cartesian coordinates in Å and ground-state SCF energies,  $E_{\text{SCF}}$ , in atomic units (a.u.) for the  $S_0$  minimum-energy geometry of  $[\text{BP4-H}]^-$  at the  $\omega\text{B97X-D/ma-def2-SV(P)}$  level.

---

$E_{\text{SCF}} = -1388.57549345$			
C	-0.221823	-2.474803	-0.169963
C	-1.603388	-2.356399	-0.219380
C	-2.259796	-1.123178	-0.067627
C	-1.484431	0.055007	0.140452
C	-0.108941	-0.087281	0.191964
C	0.571665	-1.307683	0.017039
C	2.025734	-1.417411	0.021824
C	2.899645	-0.195327	-0.020550
C	2.630324	0.898969	-0.851174
C	3.504442	1.984836	-0.884751
C	4.648867	1.988961	-0.088816
C	4.929039	0.895032	0.732993
C	4.064432	-0.195648	0.757314
O	2.587897	-2.521916	0.052048
O	0.327076	-3.686993	-0.304755
H	1.297719	-3.570681	-0.177224
O	-3.587198	-1.247939	-0.152467
C	-4.551797	-0.261584	0.198804
H	-4.562619	0.554397	-0.535452
H	-4.339858	0.165119	1.188310
H	-5.510208	-0.797412	0.204407
S	-2.077745	1.780564	0.268760
O	-0.833317	2.577668	0.277872
O	-2.840145	1.849913	1.535092
O	-2.900647	1.970580	-0.947346
H	-2.211392	-3.250037	-0.365031
H	0.449074	0.831265	0.379763
H	1.736785	0.908418	-1.478744
H	3.277387	2.836745	-1.529973
H	5.325067	2.848219	-0.107212
H	5.826649	0.892962	1.357408
H	4.277982	-1.065224	1.383514

---

**Table S3.** Optimized Cartesian coordinates in Å and ground-state SCF energies,  $E_{\text{SCF}}$ , in atomic units (a.u.) for the  $S_1$  minimum-energy geometry of  $[\text{BP4-H}]^-$  at the  $\omega\text{B97X-D/ma-def2-SV(P)}$  level.

$E_{\text{SCF}} = -1388.53218793$			
C	-0.189887	-2.426716	-0.233872
C	-1.606019	-2.331474	-0.281191
C	-2.324692	-1.113947	-0.165787
C	-1.599187	0.064941	0.008142
C	-0.174595	-0.048337	0.168476
C	0.555785	-1.188063	-0.071235
C	2.003609	-1.274848	0.103742
C	2.927667	-0.173048	0.037203
C	2.617097	1.065700	-0.580650
C	3.548424	2.098697	-0.603340
C	4.815817	1.933596	-0.038266
C	5.147897	0.705490	0.550083
C	4.228189	-0.331991	0.585643
O	2.492968	-2.446416	0.477174
O	0.412608	-3.544054	-0.316546
H	1.777166	-3.133830	0.234764
O	-3.651000	-1.277169	-0.268088
C	-4.582317	-0.388119	0.332754
H	-4.783715	0.467847	-0.324290
H	-4.200977	-0.009801	1.292572
H	-5.493557	-0.979943	0.494090
S	-2.201953	1.778049	-0.070194
O	-0.963458	2.541880	-0.332798
O	-2.798417	2.043326	1.256794
O	-3.168326	1.780022	-1.185847
H	-2.172039	-3.249083	-0.451719
H	0.323851	0.872478	0.479737
H	1.654761	1.219162	-1.070791
H	3.277453	3.043470	-1.081528
H	5.542335	2.750217	-0.061557
H	6.139370	0.561014	0.989200
H	4.485846	-1.286263	1.048441

**Table S4.** Optimized Cartesian coordinates in Å and ground-state SCF energies,  $E_{\text{SCF}}$ , in atomic units (a.u.) for the  $S_1/S_0$  minimum-energy crossing point (MECP) geometry of [BP4-H]<sup>-</sup> at the  $\omega$ B97X-D/ma-def2-SV(P) level.

$E_{\text{SCF}} = -1388.47789110$			
C	0.098901	-1.703817	-0.565039
C	-1.249833	-1.554745	-1.029099
C	-2.109776	-0.566300	-0.580780
C	-1.659739	0.396392	0.390894
C	-0.359016	0.286148	0.858399
C	0.510869	-0.716302	0.415234
C	1.884679	-0.824794	0.884651
C	3.008411	-0.159316	0.281227
C	2.793649	0.685637	-0.826691
C	3.868155	1.330639	-1.429542
C	5.162399	1.144602	-0.940788
C	5.385528	0.306863	0.159411
C	4.321868	-0.342700	0.767981
O	2.139570	-1.588874	1.926902
O	0.886961	-2.608407	-0.938601
H	1.310192	-2.008128	2.199135
O	-3.319152	-0.575875	-1.178898
C	-4.527231	-0.289773	-0.491325
H	-4.737852	0.787871	-0.501176
H	-4.481177	-0.627495	0.553941
H	-5.312333	-0.840128	-1.030006
S	-2.606833	1.805020	1.052783
O	-1.584311	2.626500	1.735867
O	-3.594272	1.201615	1.977215
O	-3.206772	2.449690	-0.135337
H	-1.618144	-2.267074	-1.769837
H	-0.024901	1.047551	1.569068
H	1.776496	0.824392	-1.199201
H	3.692840	1.984267	-2.287068
H	6.004449	1.653683	-1.417350
H	6.400235	0.161722	0.538828
H	4.488319	-1.001980	1.621976

**Table S5.** Optimized Cartesian coordinates in Å and ground-state SCF energies,  $E_{\text{SCF}}$ , in atomic units (a.u.) for the  $S_3/S_2$  minimum-energy crossing point (MECP) geometry of [BP4-H]<sup>-</sup> at the  $\omega$ B97X-D/ma-def2-SV(P) level.

$E_{\text{SCF}} = -1388.55672076$			
C	-0.216422	-2.390303	-0.111570
C	-1.593661	-2.324942	-0.086102
C	-2.324128	-1.079635	0.005214
C	-1.582372	0.182503	0.091030
C	-0.213951	0.082074	0.078711
C	0.547004	-1.174665	0.000344
C	2.040585	-1.320049	0.028151
C	2.928073	-0.164084	-0.000516
C	2.697411	1.066569	-0.679471
C	3.667929	2.064910	-0.706511
C	4.895165	1.883028	-0.059912
C	5.150639	0.666463	0.601377
C	4.198891	-0.337591	0.615215
O	2.516073	-2.481575	0.064032
O	0.381178	-3.574135	-0.168873
H	1.371607	-3.345732	-0.065739
O	-3.616329	-1.359282	-0.029218
C	-4.726082	-0.510661	0.189307
H	-4.832668	0.191994	-0.657868
H	-4.573297	0.092385	1.100123
H	-5.587699	-1.184181	0.274385
S	-2.235971	1.888404	0.147822
O	-1.055768	2.753766	0.040630
O	-2.948256	1.998819	1.440878
O	-3.136039	1.951477	-1.031455
H	-2.174969	-3.246544	-0.134323
H	0.335971	1.021220	0.169809
H	1.758745	1.236792	-1.211973
H	3.461677	2.999647	-1.236418
H	5.648439	2.676565	-0.069982
H	6.108634	0.512083	1.108302
H	4.396065	-1.296180	1.101702

**Table S6.** Optimized Cartesian coordinates in Å and ground-state SCF energies,  $E_{\text{SCF}}$ , in atomic units (a.u.) for the  $S_2/S_1$  minimum-energy crossing point (MECP) geometry of  $[\text{BP4-H}]^-$  at the  $\omega\text{B97X-D/ma-def2-SV(P)}$  level.

$E_{\text{SCF}} = -1388.56833379$			
C	-0.219164	-2.412488	-0.131418
C	-1.592658	-2.343300	-0.181351
C	-2.293985	-1.123884	-0.059205
C	-1.545477	0.098324	0.126022
C	-0.153326	0.012608	0.195625
C	0.554534	-1.195808	0.028546
C	2.020393	-1.333623	0.036033
C	2.926768	-0.169089	-0.005386
C	2.677223	0.980167	-0.786303
C	3.605108	2.017422	-0.825789
C	4.799015	1.932346	-0.102671
C	5.062461	0.787860	0.659287
C	4.144334	-0.255334	0.704828
O	2.508344	-2.506877	0.163209
O	0.359011	-3.620672	-0.265178
H	1.328799	-3.543557	-0.200660
O	-3.615193	-1.300650	-0.141628
C	-4.616089	-0.351422	0.186665
H	-4.648630	0.452745	-0.562850
H	-4.421592	0.104500	1.168498
H	-5.554818	-0.920160	0.196469
S	-2.213083	1.796418	0.223094
O	-1.018025	2.657553	0.223690
O	-2.979747	1.831915	1.489847
O	-3.047373	1.922783	-0.992988
H	-2.170142	-3.259513	-0.308048
H	0.382846	0.944843	0.378172
H	1.754132	1.062901	-1.364353
H	3.388708	2.903789	-1.428155
H	5.520659	2.753436	-0.132703
H	5.994848	0.710926	1.226667
H	4.348593	-1.155017	1.289134

## S8. Further computational results

**Table S7.** Summary of vertical excitation energies,  $\Delta E$ , oscillator strengths,  $f$ , and transition characters evaluated at the  $S_0$  minimum-energy geometry. Tabulated values are at the  $\omega$ B97X-D/ma-def2-SV(P) level; values in parentheses are at the ADC(2)/MP2/ma-def2-SV(P) level.

Transition	Transition	$\Delta E$ (eV)	$f$
$T_1 \leftarrow S_0$	$\pi\pi^*$	3.183	0.000
$T_2 \leftarrow S_0$	$\pi\pi^*$	3.745	0.000
$T_3 \leftarrow S_0$	$n\pi^*$	3.872	0.000
$T_4 \leftarrow S_0$	$n\pi^*$	4.139	0.000
$S_1 \leftarrow S_0$	$\pi\pi^*$	4.272 (3.533)	0.256 (0.156)
$S_2 \leftarrow S_0$	$n\pi^*$	4.357 (3.701)	0.010 (0.004)
$S_3 \leftarrow S_0$	$\pi\pi^*$	4.756 (4.120)	0.365 (0.273)

We note that the lowest energy  $\pi/\sigma^*$  and  $n/\sigma^*$  states appear  $>8$  eV at the Franck-Condon point.

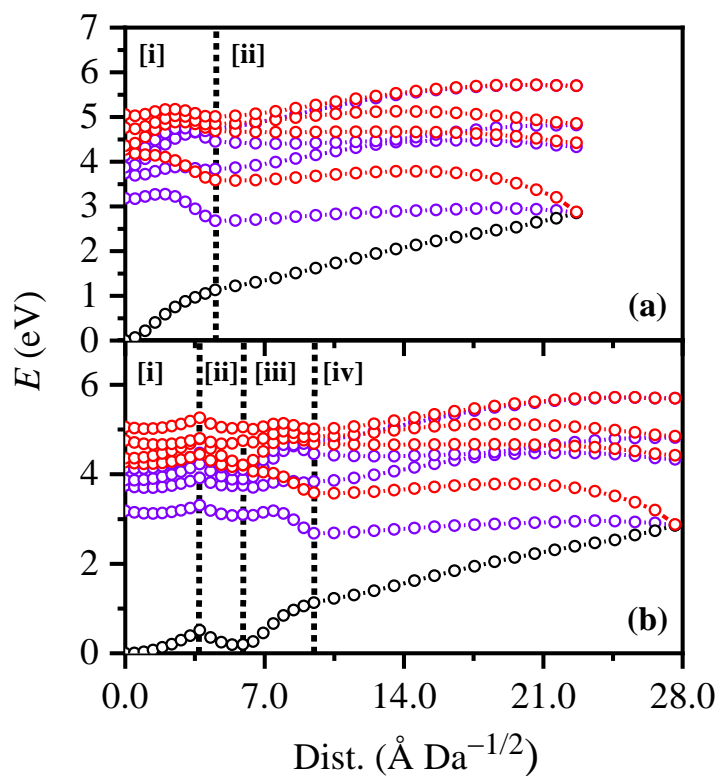


**Figure S6.** (a) Energies of the  $S_0$  state (black) and excited singlet (red) and triplet (violet) states between (i) the  $S_0$  and  $S_1$  minimum-energy geometries, and (ii) the  $S_1$  minimum-energy geometry and the  $S_1/S_0$  MECP. (b) Energies of the  $S_0$  state (black) and excited singlet states (red) between (i) the  $S_0$  minimum-energy geometry and the  $S_3/S_2$  MECP, (ii) the  $S_3/S_2$  MECP and the  $S_2/S_1$  MECP, (iii) the  $S_2/S_1$  MECP and the  $S_1$  minimum-energy geometry, and (iv) the  $S_1$  minimum-energy geometry and the  $S_1/S_0$  MECP. Points were generated *via* linear interpolation of internal coordinates (LIIC). Energies were evaluated at the  $\omega$ B97X-D/ma-def2-SV(P) level.

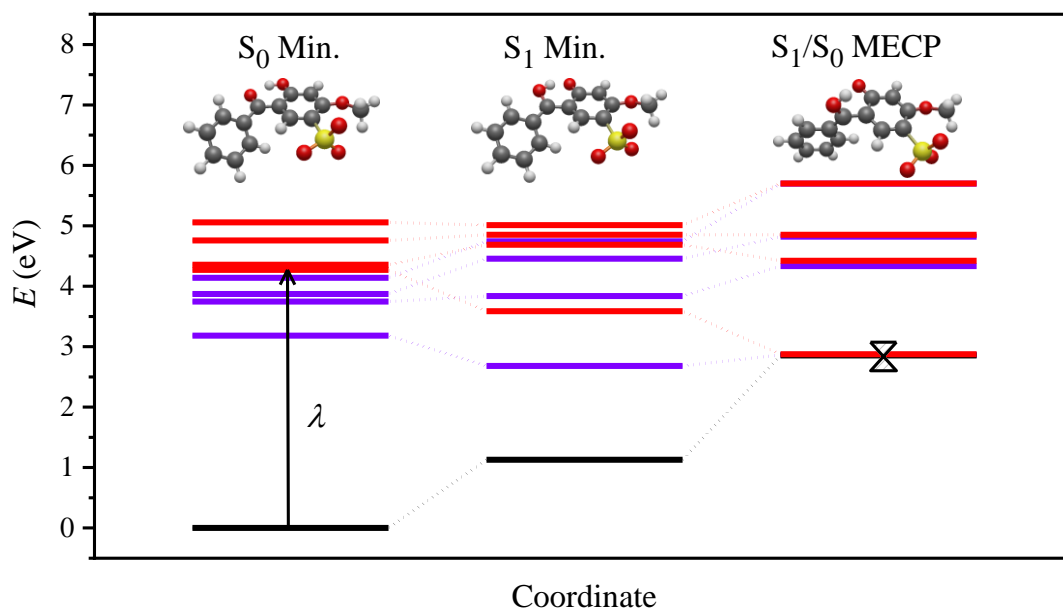


**Figure S7.** Energies of the  $S_0$  state (black) and excited singlet (red) and triplet (violet) states at key geometries for the  $S_1$  excitation scheme. MECP are denoted *via* a diablo. Energies were evaluated at the  $\omega$ B97X-D/ma-def2-SV(P) level.

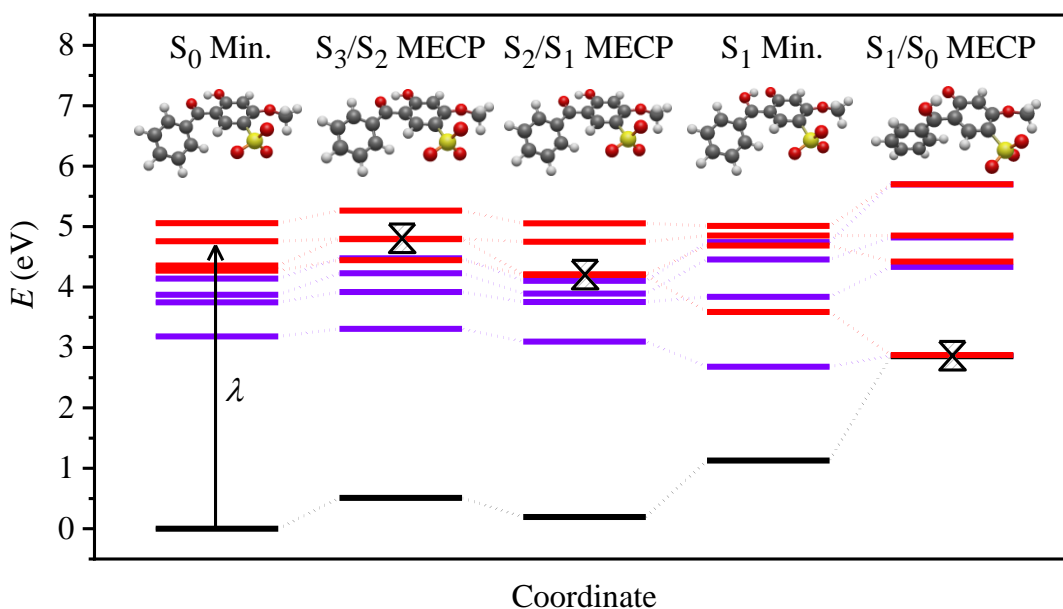
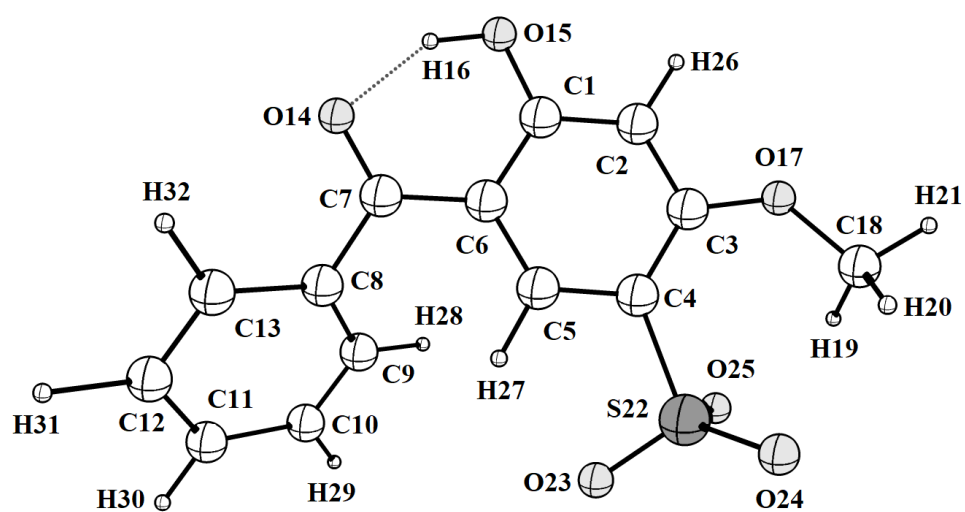


**Figure S8.** Energies of the  $S_0$  state (black) and excited singlet (red) and triplet (violet) states at key geometries for the  $S_3$  excitation scheme. MECP are denoted *via* a diablo. Energies were evaluated at the  $\omega$ B97X-D/ma-def2-SV(P) level.

### S9. Schematic structure of deprotonated benzophenone-4



**Scheme S1.** Structure of deprotonated benzophenone-4 ( $[\text{BP4-H}]^-$ ). All atoms are labelled.

## References

1. Wong, N. G. K.; Berenbeim, J. A.; Hawkrigde, M.; Matthews, E.; Dessent, C. E. H. Mapping the Intrinsic Absorption Properties and Photodegradation Pathways of the Protonated and Deprotonated Forms of the Sunscreen Oxybenzone. *Phys. Chem. Chem. Phys.* **2019**, *21*, 14311–14321.
2. Wong, N. G. K.; Berenbeim, J. A.; Dessent, C. E. H. Direct Observation of Photochemical Free Radical Production from the Sunscreen 2-Phenylbenzimidazole-5-Sulfonic Acid via Laser-Interfaced Mass Spectrometry. *ChemPhotoChem* **2019**, *3*, 1231–1237.
3. Matthews, E.; Sen, A.; Yoshikawa, N.; Bergström, E.; Dessent, C. E. H. UV Laser Photoactivation of Hexachloroplatinate Bound to Individual Nucleobases: In Vacuo as Molecular Level Probes of a Model Photopharmaceutical. *Phys. Chem. Chem. Phys.* **2016**, *18*, 15143–15152.
4. Sen, A.; Luxford, T. F. M.; Yoshikawa, N.; Dessent, C. E. H. Solvent Evaporation versus Proton Transfer in Nucleobase–Pt(CN)<sub>4</sub>,<sub>62</sub><sup>–</sup> Dianion Clusters: A Collisional Excitation and Electronic Laser Photodissociation Spectroscopy Study. *Phys. Chem. Chem. Phys.* **2014**, *16*, 15490–15500.
5. Antoine, R.; Dugourd, P. Visible and Ultraviolet Spectroscopy of Gas Phase Protein Ions. *Phys. Chem. Chem. Phys.* **2011**, *13*, 16494–16509.
6. Sagoo, S. K.; Jockusch, R. A. The Fluorescence Properties of Cationic Rhodamine B in the Gas Phase. *J. Photochem. Photobiol. A Chem.* **2011**, *220*, 173–178.
7. Cercola, R.; Matthews, E.; Dessent, C. E. H. Photoexcitation of Adenosine 5'-Triphosphate Anions in Vacuo: Probing the Influence of Charge State on the UV Photophysics of Adenine. *J. Phys. Chem. B* **2017**, *121*, 5553–5561.
8. Olsen, J. V.; Macek, B.; Lange, O.; Makarov, A.; Horning, S.; Mann, M. Higher-Energy C-Trap Dissociation for Peptide Modification Analysis. *Nat. Methods* **2007**, *4*, 709–712.
9. Neese, F. The ORCA Program System. *WIREs Comput. Mol. Sci.* **2012**, *2*, 73–78.
10. Neese, F. Software Update: The ORCA Program System, Version 4.0. *WIREs Comput. Mol. Sci.* **2018**, *8*, e1327.
11. Ahlrichs, R.; Bär, M.; Häser, M.; Horn, H.; Kölmel, C. Electronic Structure Calculations on Workstation Computers: The Program System Turbomole. *Chem. Phys. Lett.* **1989**, *162*, 165–169.

12. Chai, J.-D.; Head-Gordon, M. Long-Range Corrected Hybrid Density Functionals with Damped Atom–Atom Dispersion Corrections. *Phys. Chem. Chem. Phys.* **2008**, *10*, 6615–6620.
13. Hättig, C.; Weigend, F. CC2 Excitation Energy Calculations on Large Molecules Using the Resolution of the Identity Approximation. *J. Chem. Phys.* **2000**, *113*, 5154–5161.
14. Hättig, C.; Köhn, A. Transition Moments and Excited-State First-Order Properties in the Coupled-Cluster Model CC2 Using the Resolution-of-the-Identity Approximation. *J. Chem. Phys.* **2002**, *117*, 6939–6951.
15. Hättig, C. Geometry Optimizations with the Coupled-Cluster Model CC2 Using the Resolution-of-the-Identity Approximation. *J. Chem. Phys.* **2003**, *118*, 7751–7761.
16. Köhn, A.; Hättig, C. Analytic Gradients for Excited States in the Coupled-Cluster Model CC2 Employing the Resolution-of-the-Identity Approximation. *J. Chem. Phys.* **2003**, *119*, 5021–5036.
17. Levine, B. G.; Coe, J. D.; Martínez, T. J. Optimizing Conical Intersections without Derivative Coupling Vectors: Application to Multistate Multireference Second-Order Perturbation Theory (MS-CASPT2) †. *J. Phys. Chem. B* **2008**, *112*, 405–413.
18. Zheng, J.; Xu, X.; Truhlar, D. G. Minimally Augmented Karlsruhe Basis Sets. *Theor. Chem. Acc.* **2011**, *128*, 295–305.
19. Stoychev, G. L.; Auer, A. A.; Neese, F. Automatic Generation of Auxiliary Basis Sets. *J. Chem. Theory Comput.* **2017**, *13*, 554–562.
20. Berenbeim, J. A.; Wong, N. G. K.; Cockett, M. C. R.; Berden, G.; Oomens, J.; Rijs, A. M.; Dessent, C. E. H. Unravelling the Keto–Enol Tautomer Dependent Photochemistry and Degradation Pathways of the Protonated UVA Filter Avobenzone. *J. Phys. Chem. A* **2020**, *124*, 2919–2930.
21. Cercola, R.; Matthews, E.; Dessent, C. E. H. Near-Threshold Electron Transfer in Anion-Nucleobase Clusters: Does the Identity of the Anion Matter? *Mol. Phys.* **2019**, 1–10.
22. Scheer, A. M.; Mukarakate, C.; Robichaud, D. J.; Ellison, G. B.; Nimlos, M. R. Radical Chemistry in the Thermal Decomposition of Anisole and Deuterated Anisoles: An Investigation of Aromatic Growth. *J. Phys. Chem. A* **2010**, *114*, 9043–9056.

23. Zhang, X. Mass Spectrometric and Theoretical Studies on Dissociation of the CS Bond in the Benzenesulfonic Acid and Benzenesulfinic Acid Anion Series: Homolytic Cleavage vs Heterolytic Cleavage. *J. Mol. Struct.* **2012**, *1028*, 1–6.
24. Ben-Ari, J.; Etinger, A.; Weisz, A.; Mandelbaum, A. Hydrogen-Shift Isomerism: Mass Spectrometry of Isomeric Benzenesulfonate and 2-, 3- and 4-Dehydrobenzenesulfonic Acid Anions in the Gas Phase. *J. Mass Spectrom.* **2005**, *40*, 1064–1071.
25. Binkley, R. W.; Flechtner, T. W.; Tevesz, M. J. S.; Winnik, W.; Zhong, B. Rearrangement of Aromatic Sulfonate Anions in the Gas Phase. *Org. Mass Spectrom.* **1993**, *28*, 769–772.

**A4 Supplementary Information – Photodegradation of Riboflavin  
under Alkaline conditions: What can Gas-Phase Photolysis Tell Us  
About What Happens in Solution?**

## Supplementary Materials

### **Photodegradation of Riboflavin under Alkaline Conditions: What can Gas-Phase Photolysis Tell Us About What Happens in Solution?**

Natalie G. K. Wong,<sup>a</sup> Chris Rhodes,<sup>a</sup> and Caroline E. H. Dessent<sup>a\*</sup>

<sup>a</sup> Department of Chemistry, University of York, Heslington, York, YO10 5DD, U.K.

\* Corresponding author: Email: caroline.dessent@york.ac.uk

#### **Supporting Information:**

- S1. Photodepletion laser power dependence measurements
- S2. Electron detachment yield vs. photodepletion yield interpretation
- S3. Higher-energy collisional dissociation of [RF-H]<sup>-</sup>
- S4. Solution-phase photofragment production curves
- S5. Design of custom-made on-line syringe cell
- S6. Control solution-phase studies

## S1. Photodepletion laser power dependence measurements

Laser power measurements were conducted on  $[\text{RF-H}]^-$  at several of its respective absorption maxima when electrosprayed in deionized  $\text{H}_2\text{O}$ . The plot displayed in Figure S1 shows the parent ion photodepletion intensities ( $\text{Int}_{\text{OFF}} - \text{Int}_{\text{ON}}$ ) at the selected photon energies. Following standard protocols, the data has been plotted and fit to a power function.[1-3] The resultant slope is thereby proportional to the number of absorbed photons implicated in the experiment(s).

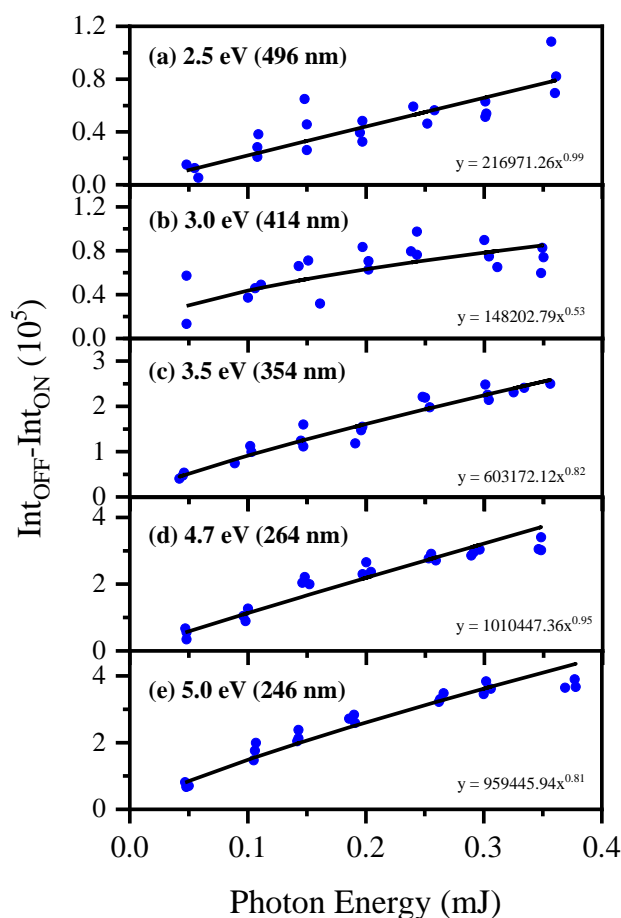


**Figure S1.** Power dependence measurements for  $[\text{RF-H}]^-$  at five absorption maxima of (a) 2.5 eV (496 nm), (b) 3.0 eV (414 nm), (c) 3.5 eV (354 nm), (d) 4.7 eV (264 nm), and (e) 5.0 eV (246 nm).

Multiphoton events *via* instantaneous absorption of multiple photons in the Franck-Condon region are negligible as the laser beam is only softly focused through the ion-trap

region. The slopes of all photon energies are less than 1.0, confirming that photodepletion [RF-H]<sup>-</sup> at 0.1 mJ are evidently not multiphoton in nature.

## S2. Electron detachment yield vs. photodepletion yield interpretation

In Figure S2 where we present ED\* spectra, we overlay such data with the photodepletion yield (PD\*) for ease of comparison; PD\* is the normalized photodepletion ion count (Eq. 6), which provides the most straight-forward comparison to ED\* (Eq. 5). Previous work on the vertical detachment energies (VDEs) of flavins have shown predicted VDEs of *ca.* 4.0 and 3.8 eV for deprotonated alloxazine and *ca.* 4.6 and 4.7 eV for deprotonated structures of lumichrome [4] with deprotonation on the ribose side chain likely giving a VDE close to that of an alkoxide [5].

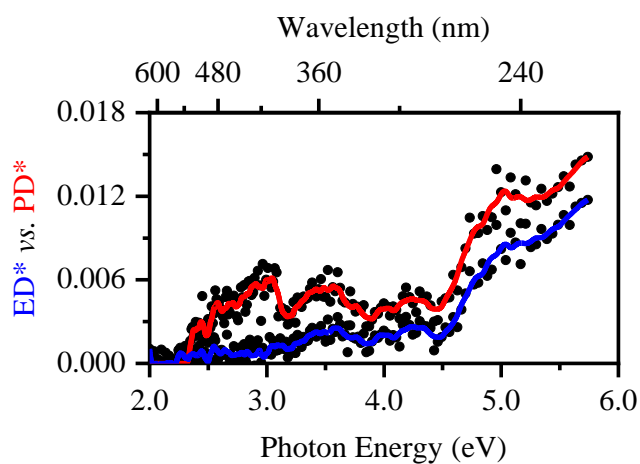


**Figure S2. (a)** Electron detachment yield (ED\*; blue) vs. photodepletion yield (PD\*; red) of [RF-H]<sup>-</sup>. The solid lines are a five-point adjacent average of the data points.

### S3. Higher-energy collisional dissociation of [RF-H]<sup>-</sup>

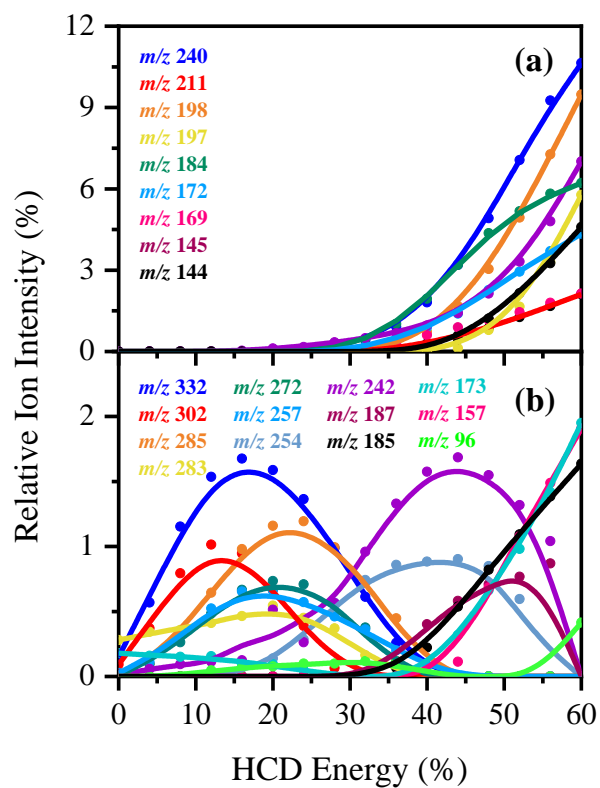


**Figure S3.** Parent ion dissociation curves [RF-H]<sup>-</sup> (*m/z* 375) and the extent of the minor thermal fragments produced between 0% and 60% HCD energy, as electrosprayed in EtOH. The curved lines are a five-point adjacent average of such data points and are provided as a viewing guide, to emphasize the profile for each individual fragment.

#### S4. Solution-phase photofragment production curves

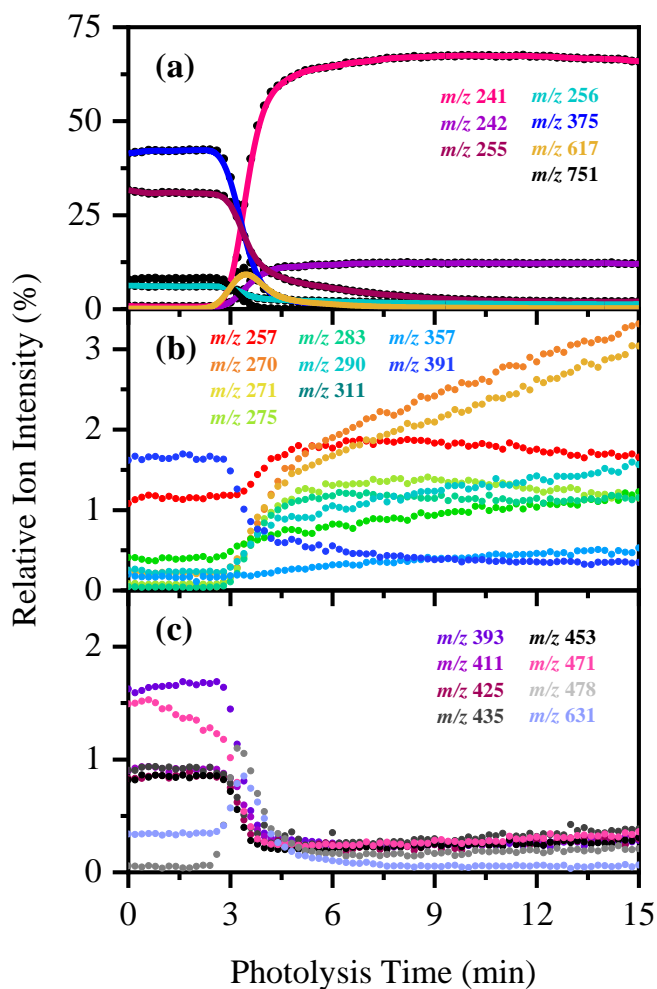


**Figure S4.** (a) Relative ion intensity plot highlighting the solution-phase photofragment ions of aqueous RF produced over a 15 minute interval of irradiation at 365 nm when delivered *via* ESI-MS in the negative ion mode. (b-c) Linked inset plot highlighting the relative ion intensities of the minor photofragments observed upon the solution-phase irradiation of aqueous RF. The curved lines included with the data points are a three-point adjacent average of such data points and are extracted from an average of 3 repeat runs.

## S5. Design of custom-made on-line syringe cell

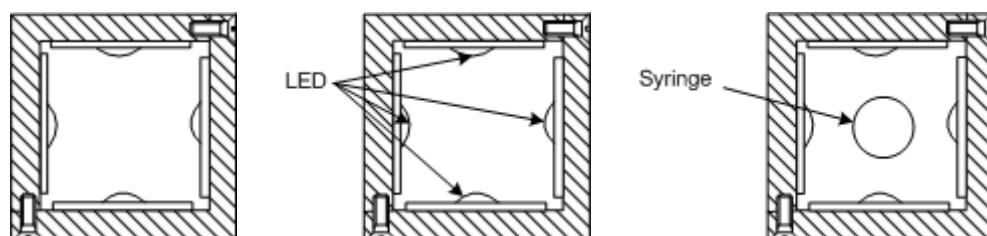


**Figure S5.** Various cross-sectional views of the custom-made on-line syringe photolysis cell.

## S6. Control solution-phase studies

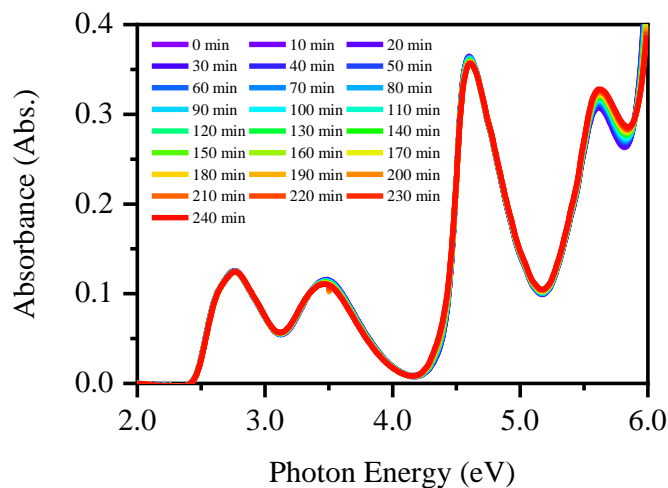


**Figure S6.** Static UV-visible absorption spectra monitoring the absorption spectrum of riboflavin, prepared in aqueous solution with trace amounts of  $\text{NH}_3$  (0.4% v/v), between 0–240 min. The overall stability of the spectra depicted support the idea that hydrolysis does not occur on this time scale.

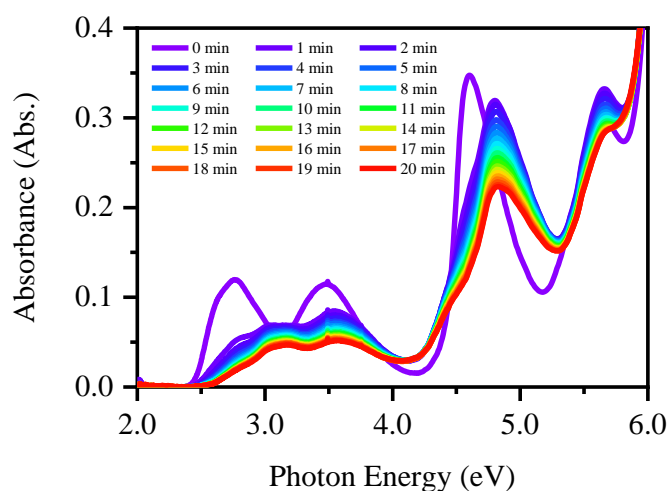


**Figure S7.** Static UV-visible absorption spectra monitoring the changes in the absorption spectrum of riboflavin, prepared in aqueous solution with trace amounts of  $\text{NH}_3$  (0.4% v/v), between 0–20 min upon irradiation (365 nm).

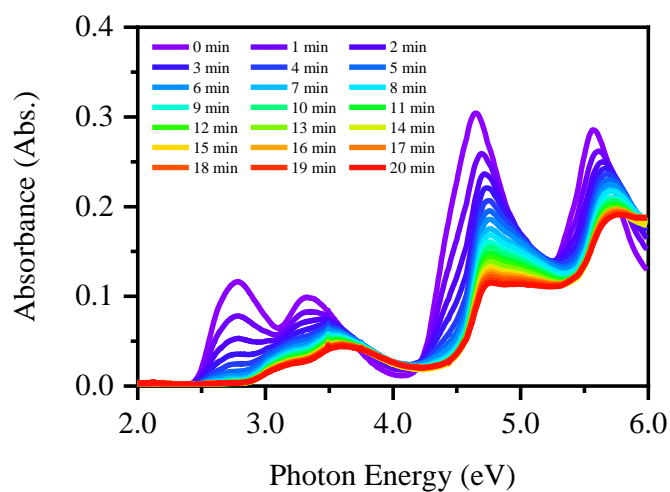


**Figure S8.** Static UV-visible absorption spectra monitoring the changes in the absorption spectrum of riboflavin, prepared in aqueous solution, between 0–20 min upon irradiation (365 nm).

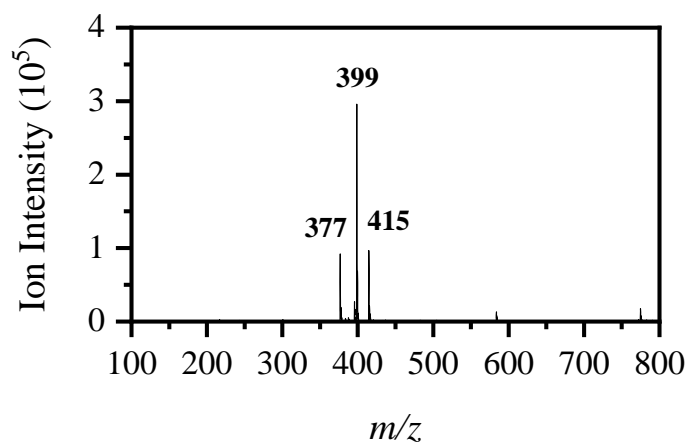


**Figure S9.** Positive ion mode electrospray ionization (ESI) mass spectrum of protonated riboflavin ( $[\text{RF}+\text{H}]^+$ ) at  $m/z$  377. Note that the ions at noted at  $m/z$  399 and 415 represent its  $[\text{RF}+\text{Na}]^+$  and  $[\text{RF}+\text{K}]^+$  systems, respectively.

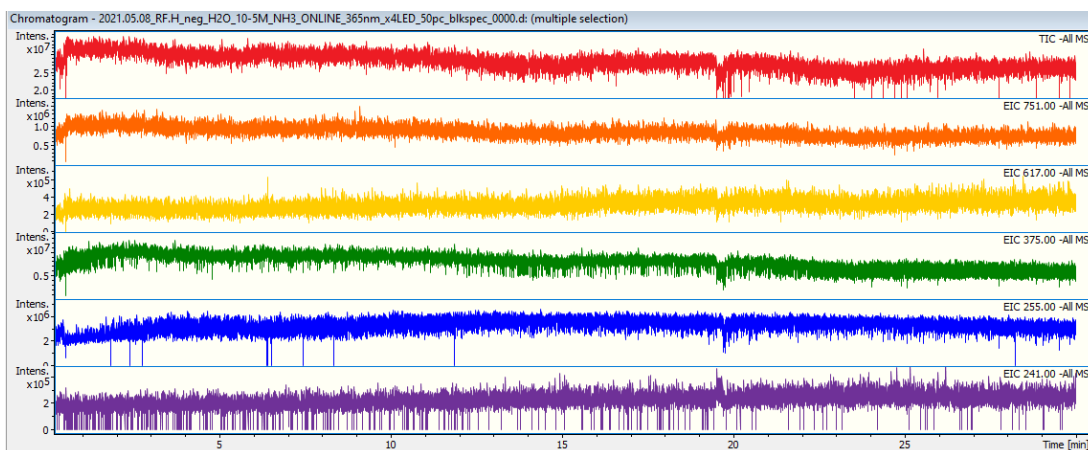


**Figure S10.** Representative total ion chromatogram and extracted ion chromatogram for ions at  $m/z$  751, 617, 375, 255, and 241. Note that the ion intensities of the  $m/z$  751, 617, 375, and 255 ions barely fluctuate relative to one another across the 0–30 min time period of irradiation. Notably the production of the major photofragment ion in the solution phase at  $m/z$  241 (as identified previously in Figures 8 and 9 of the main text) is not induced when the syringe is covered, and where UV-A light is not transmitted through to the solution.

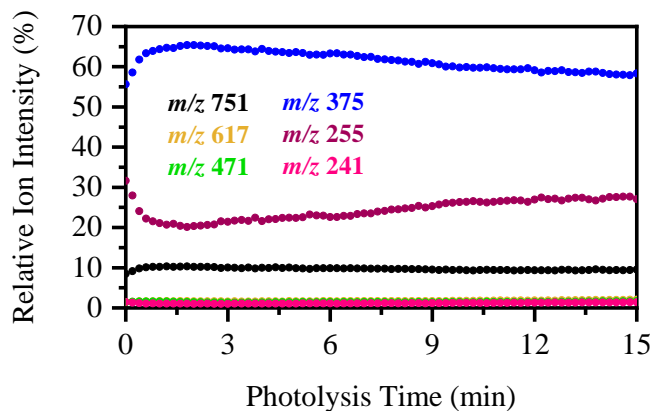


**Figure S11.** Relative ion intensity plot highlighting the solution-phase ions of aqueous  $[\text{RF-H}]^-$  produced over a 30 minute interval of irradiation at 365 nm (3.4 eV) when delivered *via* ESI-MS in the native ion mode when the syringe is covered with a black cloth, preventing UV-A light to be transmitted into the solution for irradiation. The curved lines included with the data points are a three-point adjacent average of such data points and are extracted from an average of 3 repeat runs.

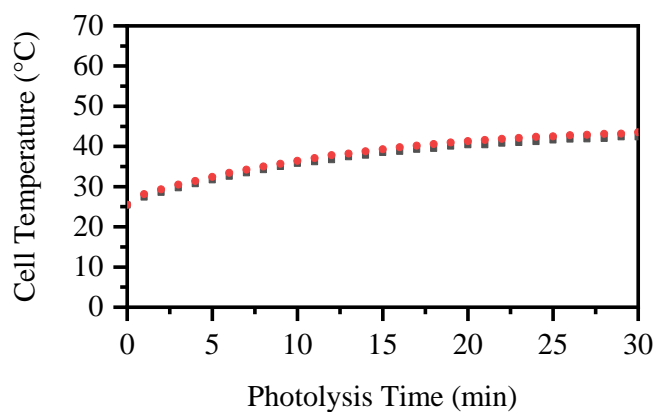


**Figure S12.** Plot of the data obtained *via* use of a thermocouple (Six Channel Handheld Temperature Data Logger; Omega RDXL6SD, Serial No. 003308) employed to monitor the temperature within the photolysis cell at two separate locations within the on-line syringe photolysis cell.

## References

1. Wong, N.G.K.; Rankine, C.D.; Dessent, C.E.H. Linking Electronic Relaxation Dynamics and Ionic Photofragmentation Patterns for the Deprotonated UV Filter Benzophenone-4. *J. Phys. Chem. Lett.* **2021**, *12*, 2831–2836, doi:10.1021/acs.jpcllett.1c00423.
2. Berenbeim, J.A.; Wong, N.G.K.; Cockett, M.C.R.; Berden, G.; Oomens, J.; Rijs, A.M.; Dessent, C.E.H. Unravelling the Keto–Enol Tautomer Dependent Photochemistry and Degradation Pathways of the Protonated UVA Filter Avobenzene. *J. Phys. Chem. A* **2020**, *124*, 2919–2930, doi:10.1021/acs.jpca.0c01295.
3. Wong, N.G.K.; Berenbeim, J.A.; Dessent, C.E.H. Direct Observation of Photochemical Free Radical Production from the Sunscreen 2-Phenylbenzimidazole-5-Sulfonic Acid via Laser-Interfaced Mass Spectrometry. *ChemPhotoChem* **2019**, *3*, 1231–1237, doi:10.1002/cptc.201900149.
4. Matthews, E.; Dessent, C.E.H. Observation of Near-Threshold Resonances in the Flavin Chromophore Anions Alloxazine and Lumichrome. *J. Phys. Chem. Lett.* **2018**, *9*, 6124–6130, doi:10.1021/acs.jpcllett.8b02529.
5. Stokes, S.T.; Bartmess, J.E.; Buonaugurio, A.; Wang, Y.; Eustis, S.N.; Bowen, K.H. Anion photoelectron spectroscopy of the linear  $C_nH_{2n+1}O^-$  ( $n = 1-9$ ) alkoxides. *Chem. Phys. Lett.* **2019**, *732*, 136638, doi:10.1016/j.cplett.2019.136638.